Fabrication of Two-Dimensional Polymers and Two-Dimensional Materials

Dissertation zur Erlangung des Grades

„Doktor der Naturwissenschaften“

am Fachbereich Chemie, Pharmazie und Geowissenschaften

der Johannes Gutenberg-Universität Mainz

vorgelegt von

Martin Gerhard Christian Pfeffermann

geboren in Offenbach am Main

Mainz, 2016

Dekan:

1. Berichterstatter
2. Berichterstatter

Tag der mündlichen Prüfung:

Die vorliegende Arbeit wurde in der Zeit von Mai 2013 bis April 2016 am Max-Planck-Institut für Polymerforschung in Mainz im Arbeitskreis von [redacted] angefertigt.

D77

Meiner Familie

Table of Contents

Abbreviations IX

1. Motivation 1

2. Two-Dimensional Supramolecular Polymers 7

2.1. Introduction 7

2.1.1. CB[8] complexes 8

2.1.2. Metal-Ligand Complexes 11

2.1.3. Two-Dimensional Supramolecular Polymers 11

2.1.4. Analysis of Two-Dimensional Supramolecular Polymers 13

2.2. Target Objective 16

2.3. Two-Dimensional Supramolecular Polymers Based on Host-Guest Enhanced Donor-Acceptor Interactions 17

2.3.1. Assembly in Aqueous Medium 17

2.3.2. Assembly at the Toluene-Water Interface 29

2.3.3. Assembly at the Air-Water Interface 74

2.3.4. Summary 79

2.4. Two-Dimensional Supramolecular Polymers Based on Metal-Organic Interactions 81

2.4.1. Synthesis 82

2.4.2. General Procedure for the Self-Assembly of Metal-Organic Layers at the Water-Air Interface 83

2.4.3. Morphological Characterization 84

2.4.4. Structural Characterization 86

2.4.5. Application as Active Material in the Hydrogen Evolution Reaction 95

2.4.6. Summary 98

3. Hollow Carbon Tubes 101

3.1. Introduction 101

3.1.1. Structure and Conductivity of Graphite 103

3.1.2. Raman Spectroscopy on Graphite Materials 105
3.2. Results and Disscussion 106
3.2.1. Solution-Based Approaches 106
3.2.2. Vapor-Based Approach 108
3.3. Summary 123
4. Disulfide-Bridged Coronenes for Li-S batteries 125
4.1. Introduction 125
4.2. Results and Discussion 128
4.2.1. Per(disulfide)coronene as Small Molecule Cathode Material in Li-S Batteries 128
4.2.2. Randomly Disulfide-Bridged Persulfocoronene as Polymer Cathode Material in Li-S Batteries 138
4.3. Summary 146
5. Conclusion and Outlook 147
6. Experimental Part 155
6.1. Materials 155
6.2. Methods 155
6.3. Synthesis 167
7. References 188
8. List of Publications 207
9. Curriculum Vitae 209
10. Acknowledgement 211

Abbreviations

2D	two-dimensional
2DP	two-dimensional polymer
2DSP	two-dimensional supramolecular polymers
AFM	atomic force microscopy
BET	Brunauer-Emmett-Teller
CB[n]	cucurbit[n]uril
CNT	carbon nanotube
D-A-CB[8]	donor-acceptor-cucurbit[8]uril
DCM	dichloromethane
DLS	dynamic light scattering
DME	1,2-dimethoxyethane
DOL	1,3-dioxolane
DOSY	diffusion-ordered spectroscopy
EDX	energy dispersive X-ray spectroscopy
GIWAXS	grazing incidence wide angle X-ray scattering
HBB	hexabromobenzene
HBC	hexa-*peri*-hexabenzocoronene
HER	hydrogen evolution reaction
HETCOR	heteronuclear correlation spectroscopy
HOPG	highly oriented pyrolytic graphite
HSQC	heteronuclear single quantum coherence
IR	infrared spectroscopy
ITC	isothermal titration calorimetry
LB	Langmuir-Blodgett
LG	Lee-Goldberg
LiTFSI	lithium bis-trifluoromethanesulfonylimide

NMR	nuclear magnetic resonance spectroscopy
NOESY	nuclear Overhauser enhancement spectroscopy
OM	optical microscopy
PAH	polycyclic aromatic hydrocarbon
PCC	perchlorocoronene
PTFE	poly(tetrafluoro)ethylene
PXRD	powder X-ray diffraction
Ref.	reference
REPT-HDOR	recoupled polarization transfer heteronuclear dipolar order
RHE	reference hydrogen electrode
SAED	selected area electron diffraction
SAXS	small-angle X-ray scattering
SEM	scanning electron microscopy
STM	scanning tunneling microscopy
TEM	transmission electron microscopy
UV/Vis	ultraviolet-visible spectroscopy
XPS	X-ray photoelectron spectroscopy
XRD	X-ray diffraction

1. Motivation

In 2004, Novoselov and Geim received the Nobel Prize for “groundbreaking experiments regarding the two-dimensional material graphene”[1]. Prior to the isolation of single-layer graphene sheets, it was believed that two-dimensional polymers (2DPs) were not achievable, as a layer spread into two dimensions appears entropically unfavored.[2] Even more important than the general accessibility of 2DPs were the outstanding properties measured in graphene, namely a high electron mobility of 200 000 $cm^2 V^{-1} s^{-1}$,[3-4] ballistic electron transport over ~0.4 µm,[5] a quantum Hall effect at room temperature,[6-7] a large specific surface area of 2630 $m^2 g^{-1}$,[8] a Young’s modulus of ~1.0 TPa,[9] and a high thermal conductivity of ~5000 $W m^{-1} K^{-1}$.[8] Most of these properties were traced back to its two-dimensionality, triggering research in the field of both inorganic as well as organic two-dimensional (2D) materials, which is steadily increasing ever since.

When discussing 2D structures, it is important to define and distinguish the terminology used in literature, as it includes an extensive number of different structural occurrences, morphologies, properties, and applicabilities, all correlated to the dimensionality of the apparent material. Although their expressions are sometimes randomly used throughout the literature, 2D monolayers will be addressed as two-dimensional polymers, and two-dimensional supramolecular polymers (2DSPs) as subcategory, respectively, according to the definition of *Schlüter* et al.[10] This definition implicates the presence of a well-ordered structure of connected monomer units in only two orthogonal directions. The remaining materials, consisting of an ensemble of lamellar structures of bi-, tri-, or multilayers will be referred to with the general term 2D material as conventionalized by *Feng* et al[11] or *Payamyar* et al.[12] When discussing both 2DPs and 2D materials, the generalizing term 2D structures will be used.

The field of 2D materials is well-developed and includes a large number of materials, both naturally occurring and synthetically produced. For example, both graphite and mica can be found in nature and exhibit lamellar structures.[13] After removing the first layers with a scotch tape, they provide a homogeneously flat surface for scanning tunneling microscopy (STM) and atomic force microscopy (AFM), respectively. Graphite is further used in electronics, as lubricant or as heat-resistant material.[14] Mica on the other hand is chemically inert and used as pearlescent pigment.[15] Although these applications are diverse, the advantageous utilization of these 2D materials can be traced back to their lamellar structure. Synthetically produced

inorganic 2D materials exemplarily include MoS_2, WS_2, $MoSe_2$, $NbSe_2$, and BN, and were reported to exhibit unique intrinsic properties for application in electronics or energy storage.[16-17] Organic 2D materials on the other hand are predominantly represented by layered, 2D covalent organic frameworks and are provided as promising material in applications like gas storage, catalysis, or optoelectronic applications.[18-19]

In addition to structurally confining molecules into a layered material, the category of 2DPs and 2DSPs faces the challenge to furnish monomolecular-thick sheets, which can only be made artificially and cannot be found in nature. In this regard, a variety of inorganic 2DPs were synthesized, including perovskites,[20] selenide nanosheets,[21] zeolites,[22] metal layers,[23-24] metal sulfides,[25] and metal oxides.[2, 26] These efforts resulted in chemically and thermally stable 2DPs, exhibiting beneficial semiconducting or electrically insulating properties.[27] Although applicable in sensing,[28] photovoltaics or electronics[29], these inorganic 2DPs feature the general disadvantage of rigidity.[30] In contrast, ambitious work was reported on organic molecules, covalently polymerized to flexible 2DPs using an appropriate monomer design. Exemplarily, surface-templated 2D formations were studied. *Bieri* et al. deposited hexaiodo-substituted cyclohexa-*m*-phenylene onto Cu(111), Ag(111), and Au(111) surfaces and cross-linked the monomers thermally. With this method, several nanometer-sized, atomically defined structures were obtained.[31] This concept was followed by e.g. *Abel* et al. with the polymerization of phthalocyanines on Ag(111) surfaces, being able to achieve 2DPs with lateral dimensions of ~50 nm.[32] *Zwaneveld* et al. were not able to exceed these layer sizes, but they showed the versatility of such chemistry by varying the pore sizes from 1.5 nm to 2.9 nm.[33] Although the surface-templated approaches provided an outstanding regularity of the structure, the insuperable disadvantage remained the small layer sizes. Thus larger sheets were achievable with an approach based on the well-established covalent organic framework chemistry. *Bunck* et al. used hydrothermal conditions to connect triphenylbenzene with diethoxybenzene in solution by a Schiff-base reaction. Although micrometer-sized flakes were obtained, exfoliation predominantly resulted in few-layer material rather than the desired monolayers.[34] With this achievement using dynamic covalent bonds, further approaches were based on photo-polymerization, owing their successful 2DP formation to the certain degree of equilibrium a photo reaction provides. In this regard *Baek* et al. reported on cucurbit[6]uril substituted with allyloxy groups, which were cross-linked with ethane dithiol in a solution-based thiol-ene click reaction towards a 2D material, consisting of an unspecified numbers of layers. Addition of protonated spermine as guest molecules

incorporated into the cavity of the cucurbit[6]uril hosts and resulted in delamination of the multilayers by electrostatic repulsion forces. With this method, sheets with dimensions of up to several µm² were achieved. Notwithstanding this impressive rational design, few-layer species were predominantly found over the desired monolayers.[35] To exclusively obtain monolayers, *Kissel* et al. designed a cup-shaped molecule bearing both anthracene and acetylene units. After growing single-crystalline 2D material from these monomers, [4+2] solid-state photopolymerization of the anthracene with an adjacent acetylene unit allowed for an intermolecular cross-linking in-plane. The resulting single-crystalline material was subsequently exfoliated by solvent-induced delamination to obtain monolayers with sizes limited to the lamellar crystallite precursor to ~100 µm.[36] The circumstantial synthesis of the cup-shaped molecule was simplified by *Bhola* et al., using a triptycene core with each benzene unit extended to anthracene moieties, which reacted in a [2+2] photopolymerization in solid state. However, opposing to the trend of producing larger layer sizes, this approach reduced the size of obtainable 2D monolayers to 300 nm.[37] Just recently, this concept was further enhanced by *Murray* et al., substituting one side of the triptycene core with an ethylene glycol chain as anchor unit for interaction with aqueous solution, thus being able to photopolymerize the anthracene units at the air-water interface. This approach made the time-consuming and size-limiting step of growing single-crystals redundant and resulted in obtaining 2DPs up to the mm² range.[38] Regardless of this outstanding achievement, the production of this monomer still requires extensive work with seven synthetic steps as well as an additional photopolymerization step. Also, the resultant 2DPs lack a possibility of facile functionalization, wherefore they are currently – in accordance to the theoretical calculation of *Brockway* et al. suggesting a high selectivity of e.g. noble gas separation for nanoporous 2DPs[39] – only considered as possible candidates for gas separation.[12]

Besides revealing outstanding intrinsic properties, these examples demonstrate the major weaknesses currently being faced in the area of 2D structures. As there already exists a variety of beneficial 2D materials, challenges cover mainly processing procedures in combination with producing advantageous applications. In contrast, the major issues in the research area of 2DPs deal with rationally constructing big scales and large areas of monolayered, functionalized, organic 2DPs being free-standing, which implies the ability to sustain over certain gap sizes without collapsing or breaking.

In this work, three separate approaches towards 2D structures are studied and discussed.

The first project concentrates on fabricating new monolayered 2DPs based on supramolecular interactions. Of course, challenges to overcome include the choice of appropriate supramolecular interactions. These are supposed to feature three properties: a strong aggregation force for interconnecting the individual molecules, a directed interaction for a spatially restricted polymerization into two dimensions, and should exhibit a molecular recognition pattern for a controlled expansion. In addition, a rational molecular design of monomers provides the backbone between the functional moieties and is eligible for enhancing the supramolecular properties. During the preparation of layers from these molecules, a deliberate adjustment of the external conditions assures control of the polymerization. As the area of research on 2DPs and 2DSPs is still in its early stages, one of the main foci is the elaboration of an appropriate analytical sequence. The project is divided into two molecular designs. The first ensemble of molecules provides an intrinsically new polymerization motif towards 2DSPs with the target of implementing this assembly method with a reliable protocol to this area of research. The second 2DSP of this project then proceeds with a different structural motif. Based on a literature known approach, the advantages of this material lie within entailing optimized structural properties and processing parameters, as well as utilization in an application.

The second project disregards the main aspects of the first topic, which is a monomolecular thickness and structural precision, and rather approaches two-dimensionality from a material's point-of-view. Based on the multilayered material graphite with its advantageous properties, the target is set to producing hollow tubes. Typically, components made from graphite are fabricated by abrasive cutting or grinding. Thus achievable dimensions are in the macroscopic scale and limited to a lower level of millimeters or centimeters, wherefore microscopic structures remain elusive. For lowering this limit, the tubes are accessed from small molecules. To control the shape, wire templates are introduced. They concurrently offer the possibility to influence the generation of graphite, e.g. to optimize the intrinsic order, or to lower the reaction temperature. Furthermore, using appropriate templates gives an opportunity to produce forms, exclusively accessible with this approach, like hollow toroids or any other shape deviating from linearity. Naturally, the preparation procedure has to involve removing of the template to assure hollowness.

Within the third project, the two-dimensionality is limited to the intrinsic structure of a small molecule. With the target of producing cathode material for a lithium-sulfur battery, the periphery of the 2D core has to contain disulfide as active species. To keep the ratio of active material and thus the battery capacity high, the dimension of the 2D subunit is restrained to coronene. Nevertheless, the two-dimensionality of the molecule is essential for this approach, as it provides the necessary ability to stabilize and transport occurring charges. Due to the localization of sulfur atoms to the 2D matrix, performance decreasing effects like solvation of polysulfide in the electrolyte are presumed to be avoided. Apart from providing and characterizing such novel material, the difference in performance between the small molecule and its randomly crosslinked allotrope is to be examined.

2. Two-Dimensional Supramolecular Polymers

2.1. Introduction

Although concepts of supramolecular chemistry can be found in the history of chemistry as early as the work of Sir Humphrey Davy in 1810, it was Nobel-prize winner Jean-Marie Lehn who defined supramolecular chemistry as “chemistry of molecular assemblies and of the intermolecular bond” in 1978.[40] While conventional chemical synthesis provides the power to generate novel materials based on new molecules with new properties, it is supramolecular chemistry which exceeds the examination and influence of characteristics based on covalent bonds on a molecular level, and expands the field of chemistry by rational consideration of its non-covalent bonds.[41] According to the wide spectrum of possibilities and specifications this definition addresses, the broad field of supramolecular chemistry has been classified into three major categories:[42]

1) The chemistry of molecular recognition, generally including only small systems and describing interactions between few molecules.
2) The chemistry of molecular assemblies, distinguishing from molecular recognition by the number of molecules involved, which is not limited in the case of assemblies.
3) Building specific macroscopic structures, utilizing the knowledge of the first two categories to generate, influence, and customize macroscopic structures.

As the general target of this work comprises structurally confined frameworks, the third category is of particular interest, whereby the desired structure is a 2DP. To achieve latter, both molecular recognition and self-assembly of molecules have to be considered and utilized. In principle, molecular recognition uses complementary interactions for a precise and selective aggregation behavior, a concept which has already been suggested by *Emil Fisher* in 1894.[43] As an example, the interaction behavior of DNA is based on the molecular recognition of the complementary base pairs adenine with thymine, and guanine with cytosine, respectively.[44] This principle can be adapted for obtaining 2DSPs to constrain supramolecular polymerization in two dimensions, which will be explicated in the subsections 2.1.1 and 2.1.2, respectively. Self-assembly as second concept is defined as “spontaneous assembly of molecules

into structured, stable, noncovalently joined aggregates".[45] The reversibility of this process provides the ability to eliminate mismatches from the structure, thus providing an intrinsic driving force for the formation of an ordered system.[46] Fundamentally, this concept involves the aggregation strength of the respective interaction motif. Typically, strong interactions are able to produce mechanically stable structures, but exhibit a lower degree of reversibility. Chemistry provides a variety of different non-covalent interactions, such as coordination forces,[47] hydrogen bonding,[48] π-π-stacking,[49] or halogen bonding.[50] Two of the strongest supramolecular interactions currently known in literature are inclusion complexes with cucurbit[n]uril (CB[n]; n is an integer and represents the number of glycol uril repetition units in the macrocycle), and metal-ligand coordination complexes (Figure 1).[51] As these interactions additionally feature certain possibilities of molecular recognition and were already reported in literature to build macroscopic structures, they were individually considered to facilitate the formation of 2DSPs.

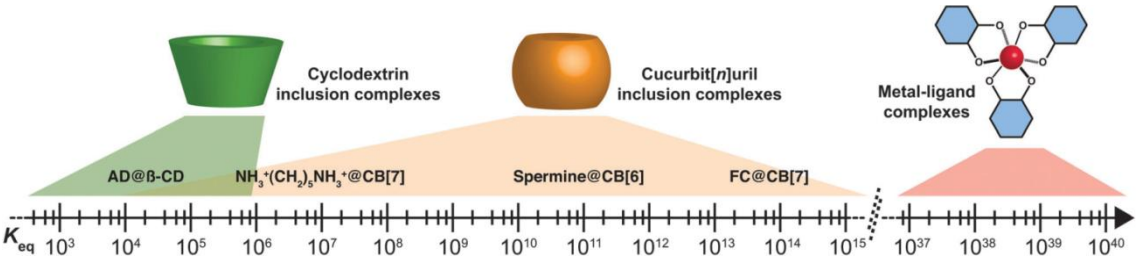

Figure 1: Selected examples of different supramolecular binding motifs, highlighting the respective areas of aggregation constants K_{eq}.[51]

2.1.1. CB[8] complexes

The well-known line "One Ring to rule them all, One Ring to find them, One Ring to bring them all, and […] bind them",[52] although not chemically intended, fundamentally describes host-guest driven supramolecular interactions featuring CB[8] as host molecule. This phrase well addresses its ability of molecular recognition to bind two guest molecules inside its cavity as well as stabilizing and enhancing their interaction. The synthesis and isolation of CB[8] was first reported in 2000 together with its smaller homologues CB[5] and CB[7],[53] driven by outstanding properties of the already known CB[6], exhibiting a remarkable supramolecular host behavior.[54-58] Immediately after

the preparation of CB[5], CB[7], and CB[8], extensive research followed the lead of CB[6]. The decisive factors of cucurbit[n]urils resulting in molecular recognition and binding affinities as high as $3 \cdot 10^{15}$ M^{-1}[59] were successively elucidated to be mainly influenced by a combination of hydrophobic effects, ion-dipole and/or dipole-dipole interactions. Providing a high polarity at the carbonyl oxygens, as illustrated by the electrostatic potential map in Figure 2, the interior of the ring remains unpolar. This unpolarity is the result of three factors: no bonds or lone electrons point to the inside of the molecule; cucurbit[n]urils are not aromatic; and residual electron density is mesomerically delocalized at the nitrogen atoms.[60] Thus, the CB[n] family features a polar-unpolar-polar structured environment of the cavity, being able to selectively recognize and bind analogous structures.

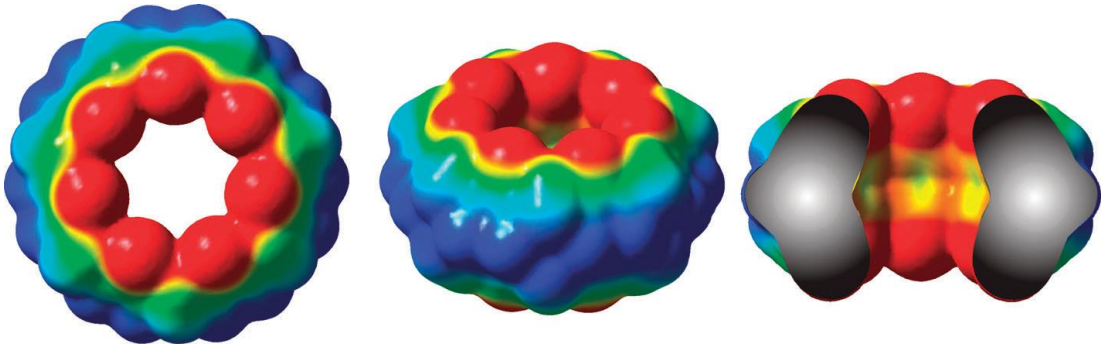

Figure 2: Electrostatic potential map of cucurbit[7]uril, presenting the polar aperture and the unpolar interior of its cavity.[61]

Considering relatively large inner cavities with diameters of 0.44 nm, 0.58 nm, 0.73 nm, and 0.88 nm for CB[5], CB[6], CB[7], and CB[8], respectively, solvent molecules like H_2O can be found inside their interiors. Because of the unfavorable, hydrophobic environment, H_2O molecules trapped inside the cavities are referred to as high-energy water molecules.[53] In accordance to the size of the individual cavities, CB[5], CB[6], CB[7], and CB[8] hold 2, 4, 8, and 12 high-energy water molecules, respectively.[61] Upon inclusion of a hydrophobic guest molecule inside the ring, these H_2O molecules are replaced (Figure 3) and release a potential energy of -41.5, -51.1, -102.4, and -66.2 $kJ \cdot mol^{-1}$, respectively, resulting in a significant driving force towards complexation.[62]

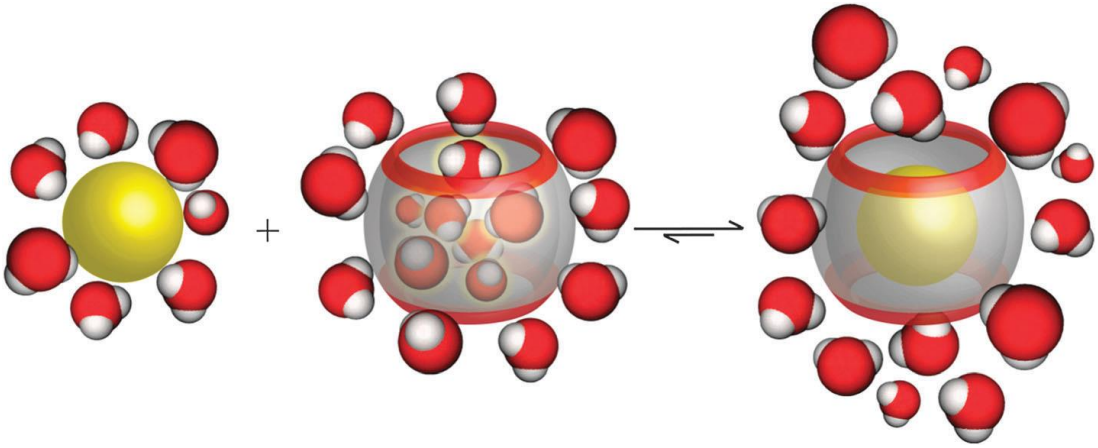

Figure 3: Schematic complexation of a hydrophobic guest inside the hydrophobic cavity of cucurbit[n]uril, visualizing the release of high-energy water molecules as driving force for complexation.[60]

In addition to the similarities within the members of the CB[n] family, CB[8] takes precedence over the other homologues, as the size of its inner cavity allows for the complexation of two guest molecules at the same time. Therefore, a number of different complexation motifs are possible with this macrocycle, remaining elusive to other CB[n] species, namely host-guest enhanced interactions in ternary complexes. In this regard, dipole-dipole dimers, radical cation dimers, and donor-acceptor dimers were reported to build ternary complexes with CB[8], whereby CB[8] significantly enhanced the binding affinity in all cases. It is important to mention that these ternary complexes were of course structurally limited to functional molecules, providing the molecular recognition motif of two polar regions in the area of the carbonyl oxygens, while at the same time featuring a hydrophobic center. Dipole-dipole and radical cation ternary complexes used only one kind of guest molecule with CB[8]. Donor-acceptor approaches on the other hand were advantageous and more versatile due to the possibility of enhancing the complexation strength with increasing the electron-donating and –withdrawing effect of the guest donor and acceptor, respectively.[63] Even more, with the possibility to connect a donor and an acceptor unit, this concept allows the preparation of materials incorporating two different functionalities, e.g. for supramolecular formation of block copolymers.[64]

2.1.2. Metal-Ligand Complexes

Typically, metal-ligand complexes occur due to the attraction of an electron accepting metal ion with the electron donating effect of a ligand. Since the discovery of this effect by *Pedersen* et al. on the complexation of metal salts by cyclic polyethers,[65-66] this interaction motif has been extensively transferred and adapted to building supramolecular structures and is the basis for the extensive and promising research area on metal-organic frameworks.[67] Metal-organic interactions feature extraordinary aggregation constants and are able to form distinguished coordination geometries, making them promising candidates for assembling 2DSPs with mechanically and electrically advantageous properties.[51] Typically, σ-orbitals of electron-donating ligands interact with d-orbitals of metals. Depending on e.g. d-orbital population or ligand properties,[68] hybridization induces a degeneration of d-fragment orbitals. This energy of electrons occupying low energy orbitals can be larger than the electron pairing energy, thus resulting in different coordination geometries like linear, tetragonal, square planar, hexagonal or octahedral assemblies.[69] Although the planarity of a square planar coordination geometry rationally facilitates 2D self-assembly, mainly hexagonally coordinating metal ions like Co^{2+}, Ru^{2+}, Zn^{2+}, Pb^{2+}, or Fe^{2+} were successfully applied for the formation of 2DSPs. Using such nonplanar geometries essentially made providing an interface for achieving two-dimensionality indispensable, which is supposed to be in contrast to utilizing an intrinsically 2D-favoring coordination geometry.[70]

2.1.3. Two-Dimensional Supramolecular Polymers

2D polymers fundamentally rely on the absence of structural defects. Thus utilization of supramolecular assemblies with their ability to reorganize towards structurally perfect 2DSPs is a promising approach in this field of research to obtain large-area 2DPs in the mm^2 or cm^2-range. This could pave the way for applying bulk 2DSPs in membranes, sensing, (opto-)electronic devices biotechnology, and catalysis.[10-11, 71-72]

Several reports on successfully achieving 2DPs with the use of supramolecular interactions were published. *Vybornyi* et al. applied the self-assembly of phosphodiester-bridged pyrenes by intermolecular π-π-stacking and hydrophilic-hydrophobic interactions towards a 2DSP. The resulting monolayers featured limited

lateral sizes up to 300 nm.[73] A similar work was done by *Shin* et al., also providing an amphiphilic monomer, which assembled towards a sheet structure in aqueous solution. Although separation of monolayers from the solution failed, an additional switching to a helical arrangement by coordination of pyridine subunits with a transition metal was shown.[74] Utilizing hydrogen bonding instead of π-π-stacking for yielding a 2DSP, *Hou* et al. prepared a C_3-symmetric carbamate. Layers obtained with hydrogen bonds were rather small, reaching only several µm².[75] Before this work was started, CB[8] enhanced complexation motifs were not reported in the field of 2DSPs. However recently several 2DSPs were achieved. *K. Zhang* et al. provided a C_3-symmetric triphenylbenzene equipped with water-solubilizing bis(2-hydroxyethyl)carbamoyl groups at the core molecule and dipolar 4,4'-bipyridin-1-ium units in the periphery together with CB[8] in a 2:3 ratio in water. They confirmed the successful complexation with ^{1}H NMR studies and with a weak spherical diffraction corresponding to the hexagonal pore size in small-angle X-ray scattering (SAXS) measurements. Dynamic light scattering (DLS) experiments suggested fragment sizes of 69 nm, which was in good agreement with small, monolayered particles exhibited in AFM studies. Processing, however, remained challenging and featured multilayer material in transmission electron microscopy (TEM) measurements.[76] *L. Zhang* et al. used the identical monomer, but further methylated the terminating pyridine units, providing the electron poor 1'-methyl-4,4'-bipyridin-1,1'-diium moiety. Its ability to form radical cations allowed for the interaction of two radical-cationic species to a dimer, whereat this interaction was stabilized by a ternary complexation with CB[8] in water. Again, DLS and AFM measurements revealed only small particle sizes of <100 nm for this approach.[77] Further protocols were reported by *Xu* et al. and *Zhou* et al., varying the spacer molecule and assembling one kind of molecule with CB[8] in water, obtaining only small particles in the submicrometer range.[78-79] These results in literature demonstrate the major problem of 2DSPs consisting of organic molecules without using transition metals, which is the limited size of resulting monolayers, thus demanding for elaboration of extensive and reliable preparation methods. Additionally, applications in this area of research still remain elusive and represent the challenges of current research.

2D metal-organic hybrid materials on the other hand appear more intensively investigated. Thus, in addition to sophisticated assembly protocols, these materials were already used in different applications. Exemplarily for preparation of 2DSPs using metal-organic interactions, *Bauer* et al. self-assembled a hexa(terpyridine) hexaphenylbenzene with metal ions. An air-water interface was provided to avoid out-

of-plane polymerization to yield 2DSP-sizes of 0.25 mm².[70] *Yue* et al. just recently reported on a 2D network, providing ethylene glycol-connected and pyridinium-capped azobenzene units as guest molecule for cyclodextrin hosts, being able to build a single-layer structure via synergistic ion self-assembly with a polyoxometalate cluster. The resulting 2DSP was further processed and used for the separation of quantum dots.[80] Another example for a possible application of a 2DSP was provided by *Sakamoto* et al. After synthesizing a dipyrrin-substituted triphenylbenzene, this monomer was complexed with a Zn^{2+}-species using an interface reaction to obtain lateral layer sizes up to 10 µm. After deposition onto a SnO_2 working electrode, the 2DSP was applied in photoelectric conversion experiment, yielding conversion efficiencies of 0.86%.[81] One of the most promising results from literature – however without an application – was the polymerization of benzene hexathiol with a Ni^{2+} species, as prepared by *Kambe* et al. The square planar coordination motif facilitated a 2D structure, which was further enhanced by the assembly at the air-water interface.[82]

2.1.4. Analysis of Two-Dimensional Supramolecular Polymers

The analysis of 2DSPs can be basically divided into two different aspects, which both have to be fulfilled to designate a material as 2DSP. The first aspect covers the macroscopic occurrence as flat, homogeneous, single-molecule thick layer. The second one concerns the elucidation of the structure and thus the necessary proof of the interconnection of monomers within the 2DSP in regards to a proposed design. As it remains elusive to meet both requirements with only one method, it is conventionalized to use a combination of different analytical measurements.

For determining the thickness of a layer, atomic force microscopy (AFM) or scanning tunneling microscopy (STM) of the layers processed on flat substrates, such as mica, Si/SiO_2-wafer, highly oriented pyrolytic graphite, or Au(111) surfaces were found to be suitable. Both methods were typically carried out by providing a scratch through the surface and scanning the height difference between the coating and the substrate. The number of present layers was then verified by comparing measured thicknesses with the thickest component of the 2DSP. Reported values ranged from 0.5 to 1.0 nm for monoatomic thick layers,[5, 83-84] and featured up to several nanometers with molecules aligned vertically to the 2DP-expansion.[36, 73, 85] Accompanying these measurements,

usually the area of the monolayers in combination with its homogeneity was investigated, e.g. by scanning electron microscopy (SEM), transmission electron microscopy (TEM), or – when sufficient in size – with optical microscopy (OM). Within these methods, appearing characteristics like a continuous contrast of the layer or the absence of split edges help with the identification of monolayered material and substantiate its presence. Additional high resolution measurements of AFM, STM, or TEM further provide the possibility to visualize the molecular structure on an atomic scale and build a connection between the analysis of the morphology and the structure elucidation.

Analyzing supramolecular interactions is an unequally more challenging task than characterizing covalently bound molecules, considering the dynamic properties of noncovalent bonds. Depending on the nature of the interaction, direct effects can be visible, like a change in color or viscosity, or indirect ones by differences in the response behavior, e.g. peak broadening and peak shifting in nuclear magnetic resonance (NMR) spectroscopy. To trace such effects back to the noncovalent interaction, it is necessary to start from an assembled complex and to compare the relevant measurements with and without the supramolecular interaction. The one method being able to unambiguously prove the molecular structure and its ordering is an X-ray diffraction (XRD) measurement of a single-crystal. For example, such analyses were already applied to retrieve information about supramolecular interactions influencing the structure and folding of proteins.[86-87] In case of one donor and one acceptor molecule in CB[8], *Kim* et al. were able to grow a single-crystal from the complex, which allowed them to provide proof of the successful complexation.[53] Based on this accomplishment, a number of different phenomena occurring in other analytical methods, such as nuclear magnetic resonance (NMR) spectroscopy, ultraviolet-visible (UV/Vis) spectroscopy, photoluminescence (PL) spectroscopy, iterative titration calorimetry (ITC) or dynamic light scattering (DLS), were assigned to the interaction of this ternary complex. In NMR spectroscopy, measurements of different combinations of the three components in water and their direct comparison were conventionalized as indication of successful complexation.[64, 88-91] In this regard, the bare donor and acceptor spectra were measured and compared with the combination of these molecules in solution for the investigation of effects caused by donor-acceptor interactions and to distinguish them from the ternary complex. Subsequently, a measurement of the acceptor molecule with CB[8] in water typically revealed two characteristics: minor up-field shifts and peak broadenings of the acceptor signals due to the interaction of the CB[8] units with the acceptor molecule,

and additional distinct and intensive signals of CB[8] molecules, which correspond to a significantly enhanced water-solubility of CB[8], facilitated by the water-soluble acceptor molecule inside the cavity. Mixing all three components together in water then showed a complex spectrum. Upon comparison to the preceding measurements, the donor and acceptor signals typically experienced down- and up-field shifts in addition to peak broadening, respectively, each affect to a greater extent than in the donor-acceptor mixture without CB[8]. The CB[8] signals mostly remained unaltered in the ternary complex, presumably due to a compensation of donor and acceptor effects inside the cavity. In UV/Vis spectroscopic measurements, a variety of donor-acceptor-CB[8] (D-A-CB[8]) combinations was reported to exhibit an additional broad signal in the bathochromic region to the absorption of the single components, verified by comparison with the respective spectra. This phenomenon was identified by *Scherman* et al. and assigned to the formation of charge-transfer (CT) complexes of generally electron poor with electron rich molecules inside CB[8], e.g. by correlation of the polarizability of the solvent with the wavelength maximum of the CT absorption.[92] For related PL spectroscopies, the particular fluorescence bands were reported to be visible, however relatively small in intensity compared to the single components' spectra. Such fluorescence quenching was assigned to an additional non-radiant transition caused by the interaction within the ternary complex.[88, 90] This behavior was in contrast to a fluorescence enhancing effect of binary complexes of CB[8] with only one guest molecule.[93] Although these examples were carried out for small molecules in solution, these particular measurements comprise the possibility to measure solid state samples. Remaining measurements reported to indicate or prove complexation of guest molecules with CB[8] were sensitive to precipitation, or not applicable to large molecules and were therefore not considered to be appropriate for analyzing 2DSPs. These examples include e.g. iterative titration calorimetry (ITC), electrospray ionization mass spectrometry (ESI-MS), or nuclear Overhauser effect spectroscopy (NOESY) and diffusion ordered spectroscopy (DOSY).

Apart from these examples in solution, there exist a few analytical methods for structure elucidation in a thin film or monolayer. Selected area electron diffraction (SAED) utilizes the diffraction of emitted electrons for analyzing the internal structure of a film, which is orthogonal to the incident beam. The resulting characteristic pattern can be analyzed using the Bragg equation to obtain packing parameters.[94-95] This method requires a regular ordering of the molecules in the layer, a low thickness to allow the electrons to pass through the material, and stability against electron irradiation. Grazing incidence wide angle X-ray scattering (GIWAXS) is another

possibility for measuring the packing parameters of a thin layer. This two-dimensional variation of a single-crystal XRD measurement uses the total reflection of an X-ray beam on a flat surface to prevent diffraction signals occurring from the substrate but exclusively originating by the covering film. Although being beneficial for thin layers, which cannot grow large single-crystals, it has to be mentioned, that this method results in a projection of the two-dimensional information of the molecular order in-plane into one dimension, and thus remains with a minor ambiguity of the diffraction pattern analysis.[96-97]

If the supramolecular interaction is a metal-ligand complex, further methods become available due to the high binding strength. Exemplarily, infrared (IR) spectroscopy can reveal additional coordination signals[98-99] and X-ray photoelectron spectroscopy (XPS) is able to give information about the metal-ligand binding situation and composition of the material.[100-101] These measurements, however, cannot solely prove the material's structure, but give strong indications about the molecular connection and can elucidate the internal structure in combination with above-mentioned measurements.

2.1.5. Target Objective

In this project, two different supramolecular approaches towards the formation of 2DSPs are investigated. One method utilizes the strong host-guest enhanced donor-acceptor interactions, which, although being studied intensively, have not been applied as binding motif between individual molecules for the self-assembly of a two-dimensional polymer. After investigating structural behaviors and the general achievability of host-guest enhanced ternary complexes as pivotal building blocks for the production of 2DSPs, appropriate molecular designs are expected to facilitate molecular ordering and maximize binding affinities towards formation of large-area monolayer sheets, exceeding comparable state-of-art in literature. For accomplishing this target, different processing protocols are tested for applicability and are being optimized. Subsequently, the effects of different molecular structures on the morphology and ordering of the polymers are to be examined.

The second approach uses a literature-reported metal-organic interaction, but with a different organic monomer for an enlarged π-system. The main target there lies within an optimization of the processing procedure towards large-area monolayer sheets, exceeding the benchmarks of comparable literature. Subsequent application in an

energy technology should be accomplished, taking advantage of the regular distribution of transition metal atoms in the polymer.

2.2. Two-Dimensional Supramolecular Polymers Based on Host-Guest Enhanced Donor-Acceptor Interactions

2.2.1. Assembly in Aqueous Medium

To elaborate a basis for utilizing host-guest enhanced donor-acceptor interactions in the field of 2DSPs, the first approaches were made in aqueous medium, considering complexes with **CB[8]** being exclusively reported from water. Hence, the general achievability and a protocol for analyzing the resulting structures had to be developed.

The 2DSP was designed to consist of a hexagonal structure. To increase the control over the polymerization and in respect to the planned transfer to an interface approach being augmented by orthogonal solubilities, a copolymerization of two types of monomers was selected. With these requirements, a hexagonal structure could be obtained involving an A_3B_2-type supramolecular polymerization with one molecule bearing a C_3 symmetry and the other one being linear. Additionally, the individual molecules should minimize self-assembly within one kind of monomers to avoid structural defects. Therefore, a donor-acceptor combination was to be complexed inside **CB[8]**, as both donors and acceptors were supposed to provide a high interaction force to its respective counter piece. As donor molecule, synthesis of the C_3-symmetric triphenylbenzene molecule with 6-methoxynaphthyl units in the periphery was planned. Solubility in water was introduced to the molecule by modification of the benzene core with three carboxylate groups (Scheme 1). The acceptor monomer was based on an electron deficient naphthalene diimide, substituted with *N*-methyl-4,4'-bipyridin-1-ium as acceptor units at the imide position. Between the naphthalene diimide and the acceptor group, ethyl spacers were introduced to provide a certain degree of flexibility for enhancing the mechanic stability (Scheme 2).

2.2.1.1. Synthesis of the Water-Soluble Donor Molecule 7

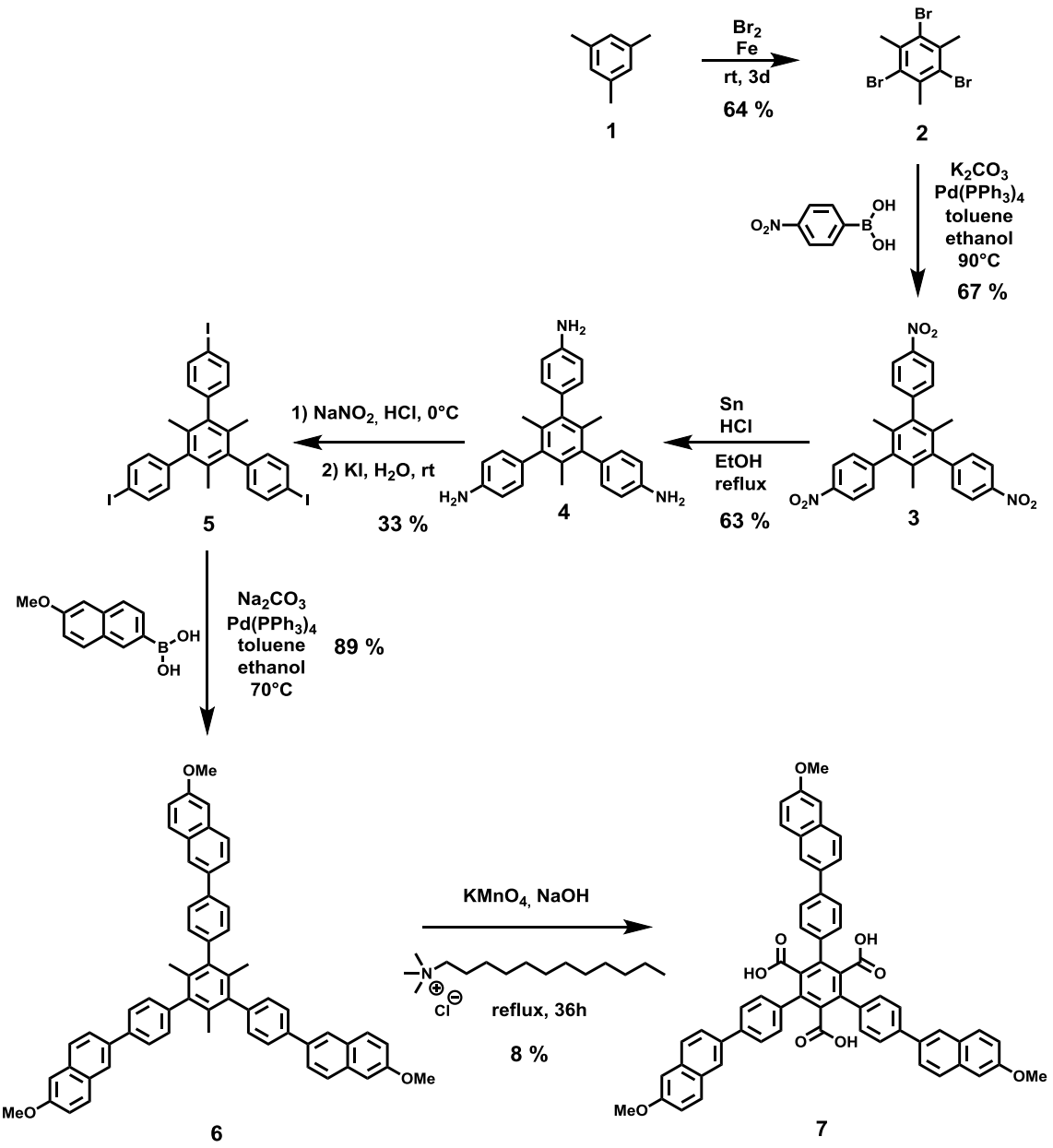

Scheme 1: Synthetic route to obtain the water-soluble C_3-donor molecule triphenylbenzene **7**.

Synthesis of the water-soluble donor molecule **7** was performed through a six-step synthesis, starting with commercially available mesitylene **1**. By bromination of the benzene core using bromine and iron, tribromomesitylene **2** was obtained in 64% (63.4 g) yield. Further reaction of **2** with commercially available 4-nitrophenylboronic acid under Suzuki coupling conditions yielded **3** in 67% (3.64 g). Subsequent reduction of the nitro groups by means of tin in acidic medium gave the triamino compound **4** in

yields of 63% (0.51 g). The Ullman-like reaction of **4** successfully provided **5** by 33% (879 mg). Molecule **5** was functionalized with methoxynaphthyl groups in the periphery by Suzuki coupling with 6-methoxy-2-naphthaleneboronic acid to obtain **6** in 89% (807 mg) yield. Introducing carboxylic acids at the core was possible by oxidation of the central methyl groups with potassium permanganate and trimethyldodecyl-ammonium chloride as phase-transfer catalyst, giving target molecule **7** in 8% yield (30.2 mg). The solubility of **7** after deprotonation in 35 mM KOH solution was found to be sufficient for further assembly in water.

2.2.1.2. Synthesis of the Water-Soluble Acceptor Molecule 10

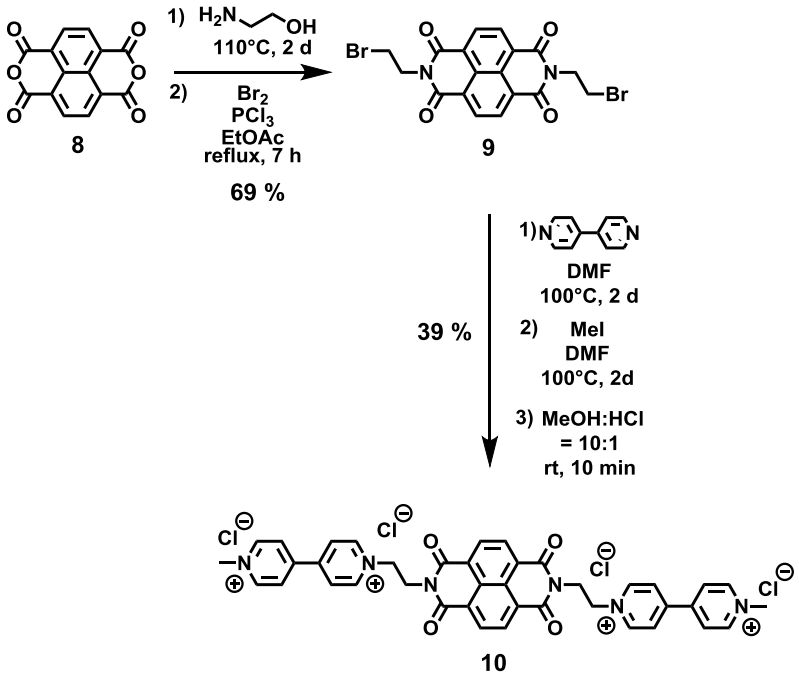

Scheme 2: Reaction path to the water-soluble acceptor molecule **10**.

Synthesis of the acceptor molecule **10** was started with an imidization reaction of commercially available 2-aminoethanol with 1,4,5,8-naphthalenetetracarboxylic anhydride **8**. The resulting intermediate was reacted without further work-up by bromination of the hydroxy substituents with bromine and phosphorous trichloride to yield *N*,*N*-bis(2-bromoethyl)naphthalene diimide **9** in 69% (12.4 g). The *N*-methyl-4,4'-bipyridin-1-ium substituents were introduced in the periphery by first reacting **9** with 4,4'-bipyridine by a nucleophilic substitution. Subsequent methylation of the crude

intermediate with methyl iodide, and counterion exchange in hydrochloric acid resulted in **10** with 39% yield (3.49 g).

2.2.1.3. Protocol for the Self-Assembly of the Molecules 10, CB[8], and 7 in Water

For a typical self-assembly experiment of **10**, **CB[8]**, and **7** in water, two solutions were prepared. In one solution, **CB[8]** ($c_{CB[8]}$ = 1.00·10^{-4} mol/L) and **10** (c_{10} = 5.00·10^{-5} mol/L) were provided in a 3.5 M aqueous potassium hydroxide solution and let at rest to self-assemble for 24 h. The other solution contained the third compound **7** (c_7 = 3.33·10^{-5} mol/L), dissolved in a 3.5 M aqueous potassium hydroxide solution. Both solutions were mixed at room temperature in a 1:1 volume ratio.

2.2.1.4. Structural Characterization in Water

^{1}H-^{13}C HSQC NMR spectra were measured of the monomers in different combinations of **10**, **CB[8]**, and **7** in a 10% KOD solution in D_2O to prove the complexation of **7** and **10** inside **CB[8]** according to literature (2.1.4).

Combining **7** and **10** resulted in a precipitation inside the NMR tube. The spectrum of **7+10** is shown in Figure 4, blue, and is compared to the spectrum of bare **10** (Figure 4, red). As all blue and red signals overlapped and no additional ones were found, the occurring precipitation of the mixture was identified as **10**, indicating a negligible complexation of **7** and **10** under the present conditions.

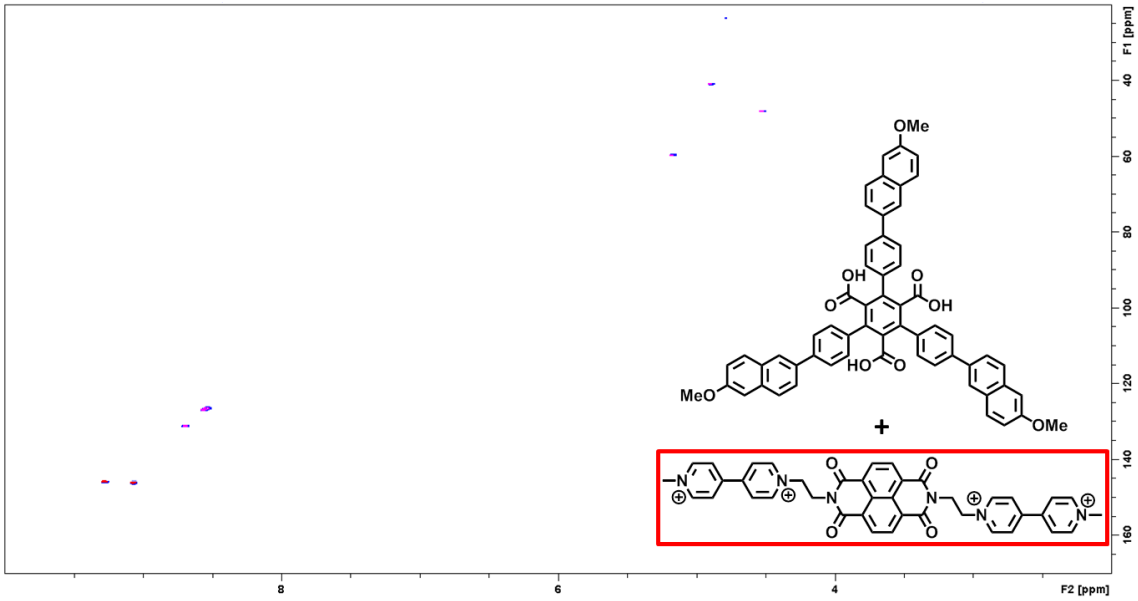

Figure 4: ^{1}H-^{13}C HSQC NMR spectrum of the combination of **7+10** (blue) in respect to the spectrum of **10** (red).

Upon mixing **10** and **CB[8]** in the ratio 1:2, three additional cross signals were visible compared to the bare spectrum of **10**, corresponding to the proton signals of **CB[8]** (Figure 5, yellow circles). The protons of the methyl bridge connecting the glycol uril units of **CB[8]** appear degenerated due to rotational inhibition, hence the signal of the proton facing towards the outside of the ring is shifted upfield compared to the one facing towards the inner side of the ring. Apart from the visibility of **CB[8]** signals, which were not detectable in the bare **CB[8]** measurement due to its low solubility, the

complexation of **10** inside **CB[8]** was further indicated by the broadening of the signals on the proton axis.

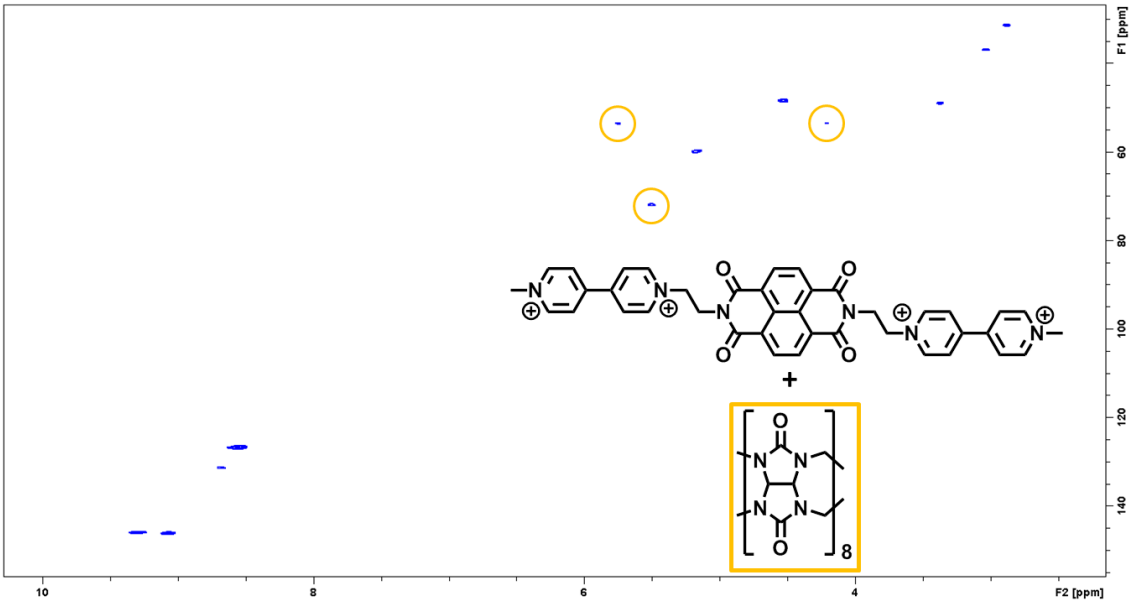

Figure 5: ^{1}H-^{13}C HSQC NMR spectrum of the combination **10+CB[8]** (blue). The additional signals of **CB[8]** are highlighted in orange.

In contrast to the combination of **10** and **7**, mixing all three precursors **10+CB[8]+7**, no precipitation occurred. The spectrum of **10+CB[8]+7** revealed both peak broadenings and peak shifts (Figure 6, blue). For comparison, the monomer spectra of **7**, and **10+CB[8]** were included (Figure 6, red and green, respectively). Comparing the donor-acceptor-CB[8] (D-A-CB[8]) complex with the signals of **10+CB[8]**, the **CB[8]** peaks revealed no shifting behavior in the D-A-CB[8] assembly, but only a peak broadening (Figure 6, yellow). This absence of a proton shifting behavior for **CB[8]** is in accordance to comparable complexes reported in literature.[53, 88, 102] In contrast, the aromatic region of **10+CB[8]+7** between 7.25-8.6 ppm in the ^{1}H dimension and 120-140 ppm in the ^{13}C dimension revealed significant peak shifts compared to its monomeric spectra. Interestingly, the peaks deriving from the benzene spacers of **7**, which were found in the uncomplexed spectrum at 7.6 ppm in the ^{1}H dimension and 129 ppm in the ^{13}C dimension, remained unaltered in the complex. This was in accordance to the expectation, as they were applied as spacer moieties without electron donating or withdrawing properties. The aromatic signals of the methoxynaphthyl unit of **7**, found between 7.8-8.2 ppm in the ^{1}H dimension and 126-

130 ppm in the ^{13}C dimension, experienced a significant down-field shift upon complexation to 7.8-8.6 ppm in the ^{1}H dimension and to 127-132 ppm in the ^{13}C dimension, indicating an electron withdrawing effect on this functional group. The aromatic signals of the 1'-methyl-[4,4'-bipyridine]-1,1'-diium unit of **10** were observed in the area between 8.5-9.4 ppm in the ^{1}H dimension and 124-146 ppm in the ^{13}C dimension for precomplexed **10+CB[8]** and revealed an upfield shift of all signals upon complexation with **7** to 7.3-7.9 ppm in the ^{1}H dimension and 123-130 ppm in the ^{13}C dimension. This behavior gave proof for a successful donor-acceptor interaction of the methoxynaphthyl and 1'-methyl-[4,4'-bipyridine]-1,1'-diium moieties inside **CB[8]**.

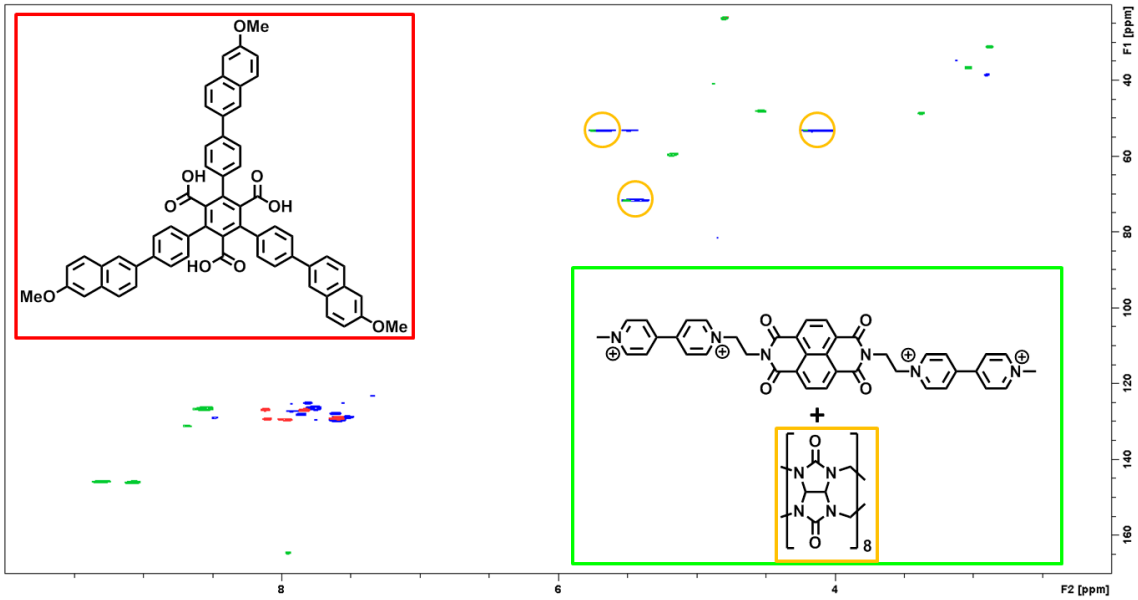

Figure 6: ^{1}H-^{13}C HSQC NMR spectrum of the combination of **10+CB[8]+7** (blue) in respect to the monomer spectra of **7** (red), and **10+CB[8]** (green). The signals of **CB[8]** are highlighted in orange.

The combination of **10+CB[8]+7** showed a behavior in NMR spectroscopic measurements as anticipated qualitatively from literature, wherefore a complexation is probable. Additionally, comparison of the spectra of **10+CB[8]+7** with the precursors **10+CB[8]** and **7** provided quantitative information about the peak shifts of both donor and acceptor monomers upon complexation with **CB[8]** and act as benchmark for solid-state measurements.

In accordance to UV/Vis spectroscopy measurements in literature, providing strong indication about D-A-CB[8] complexations, the solution of **7**, and the assembled

solution of **10+CB[8]** were measured and compared to the mixture of **10+CB[8]+7** (Figure 7). In case of a successful complexation, an additional broad signal can be visible, bathochromically shifted to the absorption of the monomers, which was assigned as charge-transfer band of the donor and acceptor monomer being sterically forced to a closer distance in CB[8].[92] This characteristic behavior was displayed for the spectrum of **10+CB[8]+7**, displaying the superposition of the individual spectra with the expected stoichiometry of **7:10:CB[8]** = 2:3:6, but with an additional broad absorption at λ_{max} = 617 nm.

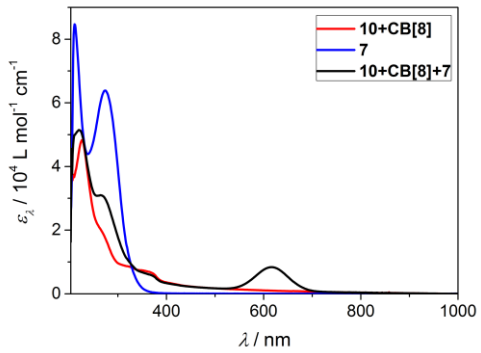

Figure 7: UV/Vis spectrum of **10+CB[8]** (red), **7** (blue), and **10+CB[8]+7** (black). The black spectrum reveals the expected stoichiometric superposition of monomeric **10**, **CB[8]**, and **7** as well as an additional broad absorption at λ_{max} = 617 nm.

It was further tried to perform UV/Vis spectroscopic measurements in solvents with different polarizations as conventional way of proving the presence of a charge-transfer interaction in such system in accordance to literature.[92] However, in less polar solvents or solvent-additions precipitation occurred, resulting in the spectra not being comparable anymore. Nevertheless, as solely the occurrence of this peak was conventionally accounted for successful complexation,[64, 88, 90, 92, 103-106] the designation of this peak as CT band was neglected.

Although showing an additional absorption band, typically the fluorescence intensity decreased upon complexation. Therefore, the fluorescence spectrum of **10+CB[8]+7** was measured and plotted against the monomeric spectra of **10+CB[8]**, and **7**, respectively (Figure 8). **10+CB[8]+7** reveals a superposition of the monomer spectra in the range of 300 – 500 nm. An additional small and broad fluorescence can be found in the range of 600 – 900 nm. This increased fluorescence appears most likely due to the

additional absorption at λ_{max} = 617 nm in the UV/Vis spectrum. The existence of this peak corroborates the complexation of **10** and **7** inside **CB[8]**. The fluorescence in this this area however is quite low, suggesting an efficient nonradiative relaxation motif of the complex.

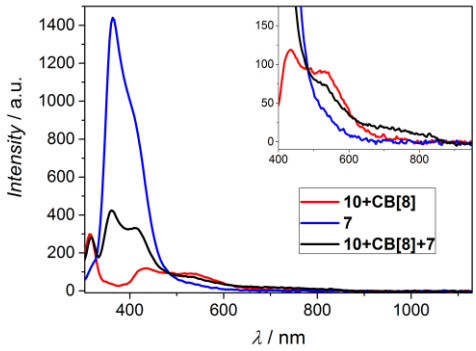

Figure 8: Fluorescence spectra of **10+CB[8]** (red), **7** (blue), and **10+CB[8]+7** (black). The inset shows a magnified area of the region between 400 – 950 nm and has the same units.

2.2.1.5. Morphological Characterization

Besides acquiring overlapping characteristic behaviors of structural analyses for subsequent interpretability of solid-state measurements, the **10+CB[8]+7** was supposed to reveal sheet formation upon complexation. Therefore, the morphology was analyzed by OM and TEM after investigating the macroscopic time-dependency of the assembly process with DLS. Therefore, DLS studies were performed on solutions of **10+CB[8]+7**. First, an aqueous 35 mM KOH solution was provided with $7 \cdot 10^{-5}$ M **7**, $1 \cdot 10^{-4}$ M **10**, and $2 \cdot 10^{-4}$ M **CB[8]** and measured after a time of 3 d. The result revealed a multimodal distribution, suggesting the presence of aggregates larger than 3 µm, in respect to the detector limit. Indeed, the formation of aggregates was visible by the eye, hence the sample was investigated by optical microscopy (OM) (Figure 9). The optical microscopy pictures revealed sizes of the aggregates of more than 2500 µm². Of course, control experiments were performed of the individual solutions and the combinations of only two components, which resulted in no layer formation.

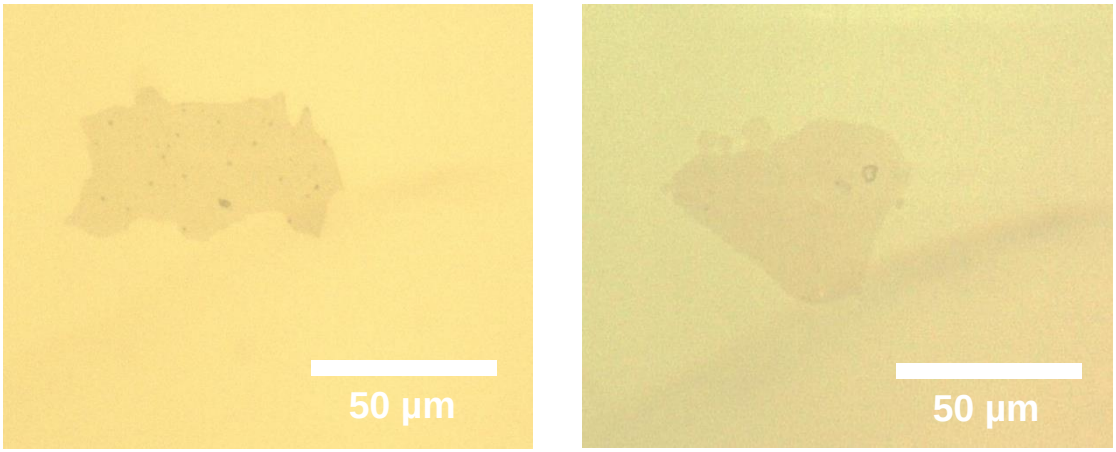

Figure 9: Optical microscopy pictures of aggregates found in the solution. The left picture shows a layer after drying, the right picture reveals a sheet in aqueous medium.

Thus to give an idea about the duration of the aggregation in solution, time-dependent DLS studies were performed. A fresh solution was provided with the precursors and measured after incremental time-intervals. The sizes of the measured hydrodynamic radii were plotted against time and intensity (Figure 10). The plot revealed a clear growth of aggregates with passing time. At the beginning of the assembly, small aggregates between 8-40 nm were formed, which increased in size to 80-200 nm after the first 100 min. During the subsequent 300 min, the aggregates grew to a range between 200-3000 nm. After a total time of 400 min, a continuous decrease in the total intensity was visible, corroborating the formation of layers larger than 3 µm exceeding the DLS detection range.

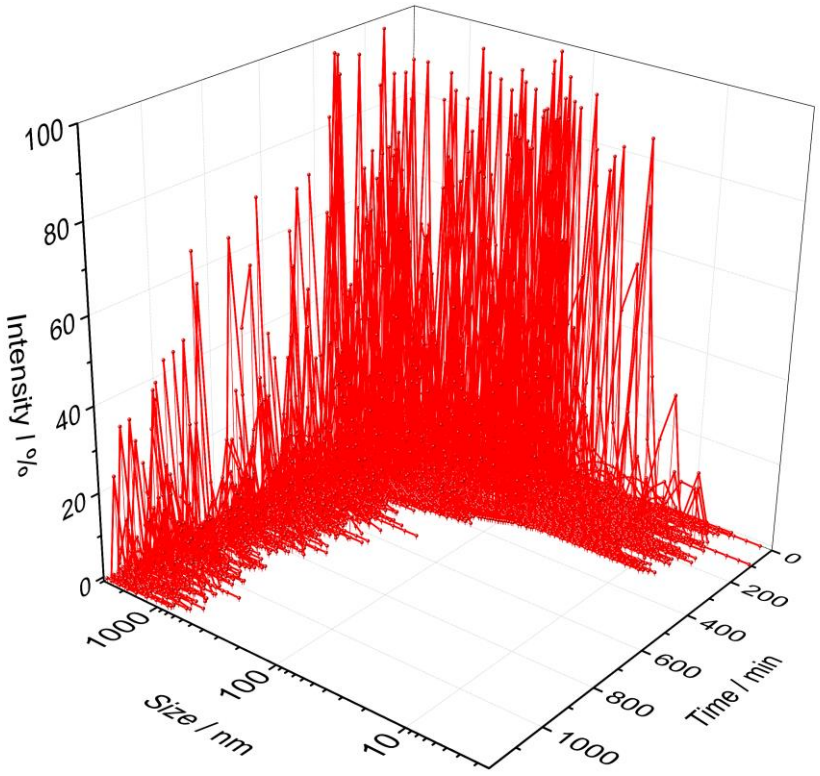

Figure 10: Time-dependent DLS measurement. The sizes of the hydrodynamic radii were plotted against their relative intensity and the assembly time. With continuing time, the intensity maximum increased from 8 nm to the measurable maximum of 3000 nm after 400 min. Eventually, the total intensity decreased due to a continuative growth of the particles.

For further characterization of the assembled layers of **10+CB[8]+7**, they were transferred from the solution onto Lacey carbon coated copper TEM grids by horizontal dip-coating. Subsequent rinsing with water and ethanol removed residual precursors.

TEM analysis of these copper grids revealed a large number of layers free-standingly covering the holes in the Lacey framework up to ~10 µm² (Figure 11a). This mechanical stability exceeded comparable work in literature, which revealed fragments of 2DSPs with lateral sizes between 200 nm and 2 µm, supported on a substrate without the free-standing ability (Chapter 2.1). However, the obtained layers of **10+CB[8]+7** seemed to be lacking homogeneity covering the Lacey carbon support, which was reasonable due to the absence of a stabilizing interface. This was corroborated at higher magnifications (Figure 11b), where multilayer structures within the covered areas were visible, typically occurring in a one phase reaction due to rupturing, folding, or layer-stacking.

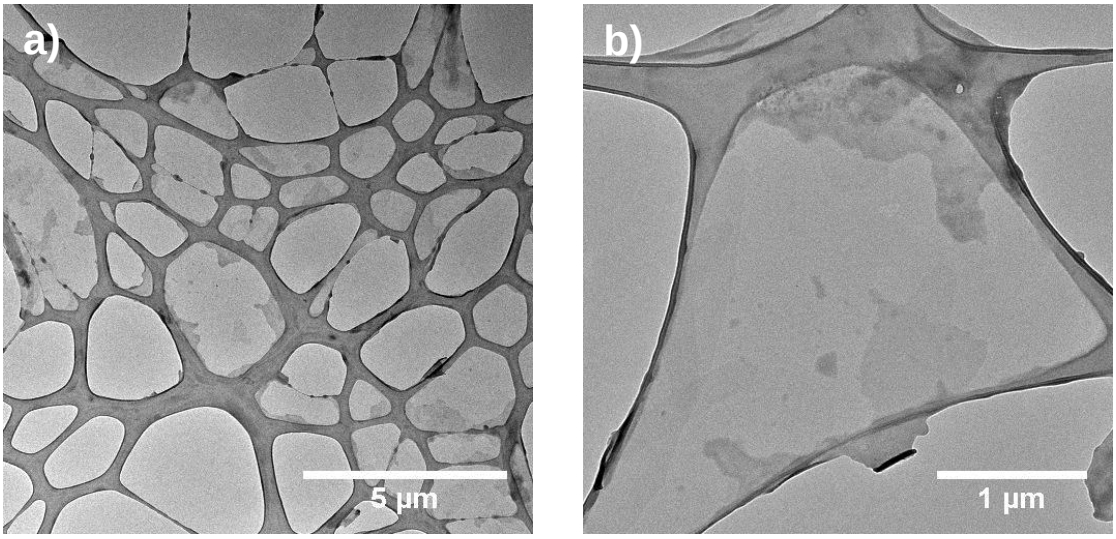

Figure 11: TEM-pictures of **10+CB[8]+7** layers after dip-coating Lacey carbon grids through an aqueous solution bearing the three precursors.

To investigate the possibility of multilayer formation resulting during dip-coating by transferring several layers successively, the appearance of the layers as monolayers or as multilayers in solution was examined by cryo-TEM measurements. Those were performed in collaboration with [redacted]. A Lacey carbon coated TEM grid was wetted with an aqueous solution of **10+CB[8]+7**, frozen, and subjected to a cryo-TEM device. Comparing the dip-coated layers of Figure 11 with the cryo-TEM images in Figure 12, the presence of corrugated single layers in latter is evident. The crumbled appearance is not surprising as it should be the general case of a dissolved 2D layer without template support due to Brownian motion and diffusion and does not refute the presence of monolayers. The additional crystals visible were identified as frozen solvent residues.

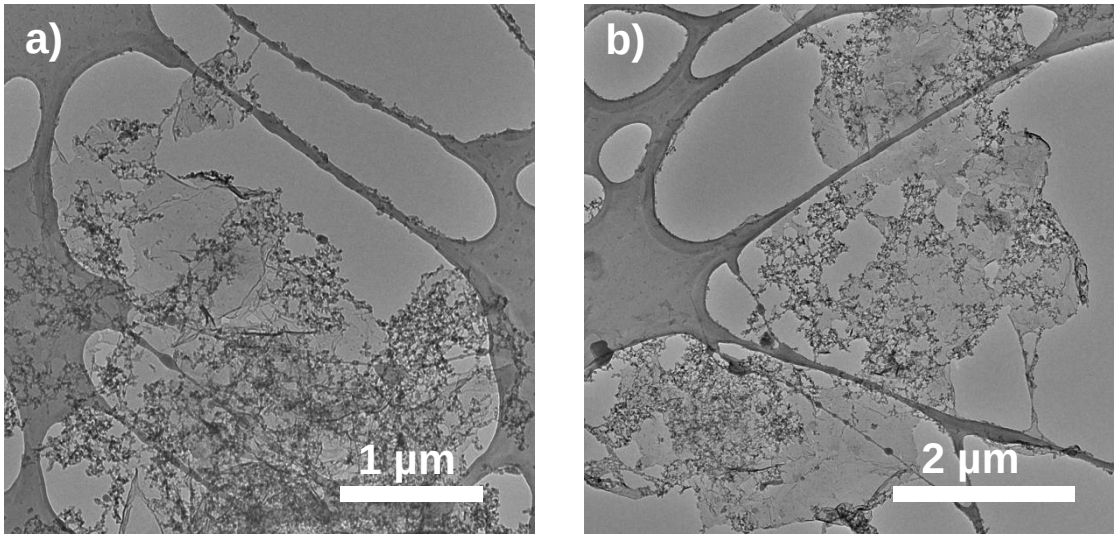

Figure 12: Cryo-TEM images of an aqueous solution of **10+CB[8]+7**.

These preliminary investigations of NMR, UV/Vis, Fluorescence, OM, DLS, and TEM measurements proved several microscopic and spectroscopic methods feasible for examining assembled 2DSPs. They further showed the successful assembly of the precursors and gave benchmarks in terms of assembly time, free-standing ability, and layer sizes. Based on the thus gained knowledge, the approach was subsequently transferred to a liquid-liquid interface.

2.2.2. Assembly at the Toluene-Water Interface

The D-A-CB[8] combination in water showed the general possibility to form a layered assembly of all three participants, donor, acceptor, and **CB[8]**. However, obtained TEM images revealed, that the lateral interactions inside the layer are too weak to support the 2D monolayer in solution spread in only two dimensions. As a result, the 2DSP appeared corrugated and gave multilayers upon processing. Thus, to achieve single-layer 2DSPs, the interaction motif was transferred to a liquid-liquid interface, utilizing its stabilizing effect and its ability to support self-assembly in only two dimensions, restraining out-of-plane polymerization.

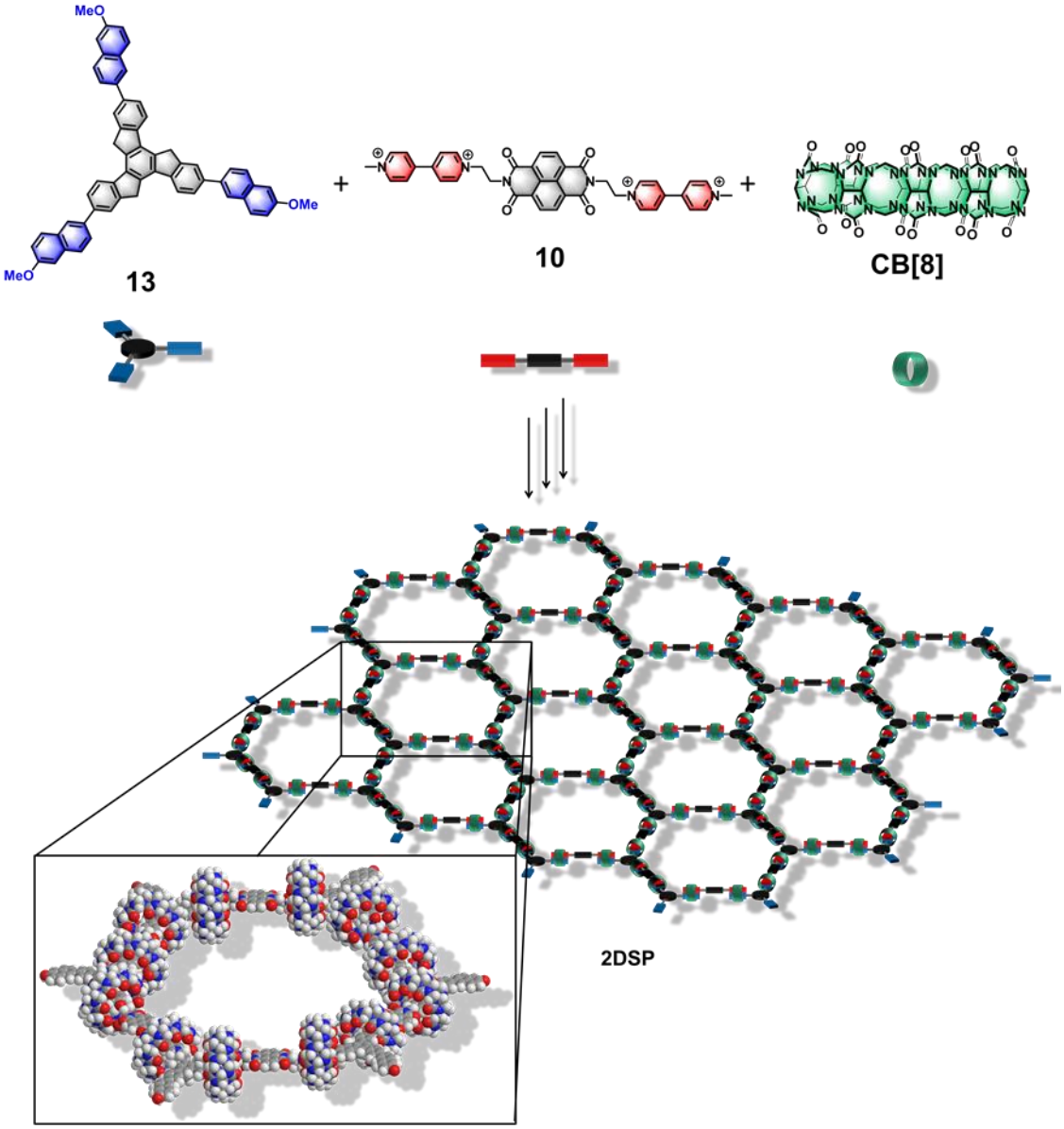

Figure 13: Schematic assembly of the C_3-symmetric, planar donor molecule **13**, the linear acceptor molecule **10**, and the host-molecule **CB[8]** towards the hexagonal superstructure of a 2DSP. The molecular structures of **13** (top), **10** (middle) and **CB[8]** (bottom) are shown at the left. Below each molecule, a schematic representation is visible with blue and red parts representing the donor and acceptor moieties, respectively. The proposed hexagonal superstructure based on these schemes is visible on the right. The inset represents a molecular model of one hexagon of the superstructure (geometry optimized by UFF method[107]).

To apply the host-guest enhanced donor-acceptor interaction to an air-liquid-, or liquid-liquid interface approach, the molecular design had to bear orthogonal solubilities of at least two of the three components. Furthermore, this particular interaction is fundamentally dependent on the donor and acceptor strength. Therefore, strong donor

and acceptor moieties were combined with spacer units, which should enhance the respective function of the monomers in order to maximize the appearing supramolecular interactions, hence making the resulting 2DSP more robust.

Notwithstanding the necessity to introduce small, water-solubilizing groups as in the case of **7**, the electron rich, hydrophobic molecule truxene was chosen as spacer moiety for the donor monomer. This spacer is advantageously compared to a triphenylbenzene core in terms of providing a larger π-system, as the peripheral benzene units are being forced into the plane of the central benzene by methylene bridges. The design of the truxene donor monomer **13** featured the same three strong methoxynaphthyl donor units in its periphery (Scheme 3) as they already furnished 2DSP formation in water. Furthermore, this design of monomers located their solubilizing moieties at the donor and acceptor units. This allowed for insolubility of the 2DSP after assembly due to spatial isolation of the donor and acceptor groups in the cavity of CB[8]. The anticipated structure of the resulting hexagonal 2DSP assembly from the toluene-water interface is schematically shown in Figure 13.

2.2.2.1. Synthesis of Donor Molecule 13

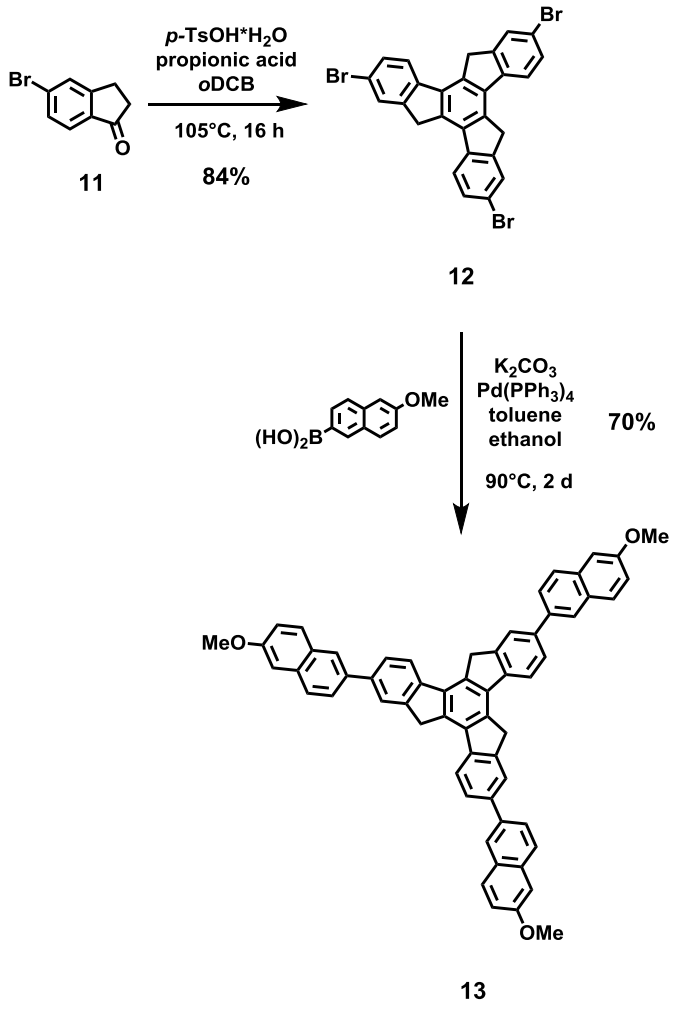

Scheme 3: Reaction scheme for the synthesis of the donor monomer **13**.

The truxene derivative **13** was synthesized in a two-step reaction, starting from the commercially available 5-bromo-1-indanone **11**. Two acid catalyzed aldol condensations of three molecules of **11**, followed by an electrocyclization and a subsequent condensation[108] led to the cyclotrimerization product 2,7,12-tribromotruxene **12** in 84% yield. The boronic acid unit of the commercially available 6-methoxy-2-naphthaleneboronic acid was reacted with the bromo-functionalized truxene derivative **12** by means of a Suzuki reaction to give the truxene donor **13** in 70% (1.00 g) yield.

2.2.2.2. General Procedure for the Self-Assembly of Monolayers at the Toluene-Water Interface

In literature, the air-water interface was preferably used for the assembly of 2D layers due to beneficial properties, namely the large, homogeneous area of the surface, the possibility to adjust the lateral surface pressure of the monomers prior to polymerization, and the processability of the assembled layer from the interface onto a variety of substrates.[70] The air-water interface was initially expected to furnish larger and more homogeneous layers in contrast to layer formations at a liquid-liquid interface, due to avoiding a mixed phase between the two solutions.[70, 82]

Thus a solution of **10+CB[8]** was provided in the aqueous subphase of an air-water Langmuir trough and **13** was deposited onto the water surface by evaporating it from a toluene solution. After compressing the barriers, the water-covering layer was horizontally deposited onto a SiO_2/Si wafer and a Lacey carbon coated TEM grid. After the deposition, the substrates were washed two times with water, ethanol, toluene, and again ethanol. Layers were neither found on the SiO_2/Si-wafer surface, nor on the TEM grid (Figure 14).

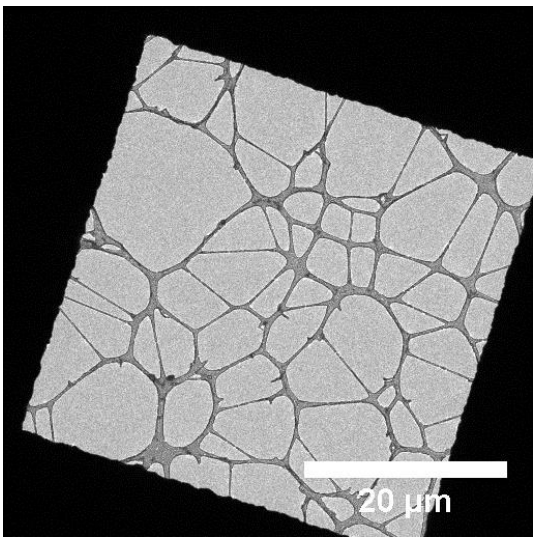

Figure 14: TEM image of an empty TEM grid covered with Lacey carbon support after deposition from the air-water interface. The image revealed no sign of a layer formation.

Repeatedly failed attempts to obtain layered material from the air-water interface suggested the absence of self-assembly of the monomer species, for which a number

of reasons can be assumed. On the one hand, considering a favored face-on orientation of **13** molecules onto the water surface,[82, 109] the truxene core can be so hydrophobic that the repulsive interaction between the molecules and the water surface spatially prevents the overlayed molecules to self-assemble with the molecules in the sub-phase. On the other hand, the dipole moments of the peripheral methoxy substituents could interact with the aqueous subphase rather than the hydrophobic truxene core. This in combination with the increasing concentration of **13** upon evaporation of the toluene supporting π-π-stacking of the aromatic truxene cores, could obviate a preferred face-on orientation of the molecules to the interface and support a horizontal orientation of columnar stacked molecules to the surface.

Hence, the assembly process was transferred to a toluene-water interface. Notwithstanding the immiscibility of both solvents, the small diffusion area at the interface was expected to enhance the interaction of **13** with the aqueous subphase to allow for the self-assembly of **13**, **10**, and **CB[8]**. Furthermore, the possibility to work with diluted solutions was expected to suppress homo-molecular stacking of **13** and to support the face-on arrangement of the aromatic cores to the interface. Thus, the assembly of **13**, **10**, and **CB[8]** was performed at a liquid-liquid Langmuir trough (Figure 15).

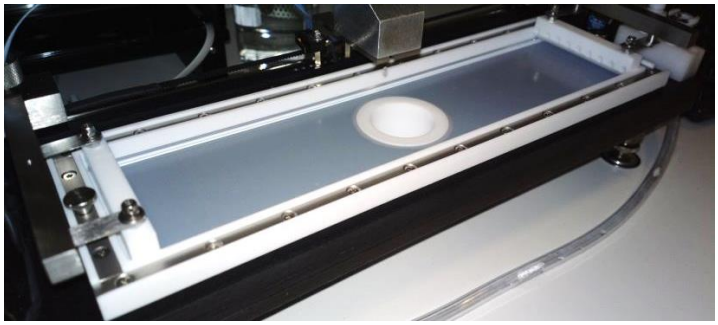

Figure 15: Picture of the liquid-liquid Langmuir trough, used for the assembly of **13**, **10**, and **CB[8]** at the toluene-water interface.

Prior to processing, a $1.00 \cdot 10^{-5}$ M solution of **10** in water was preassembled with 2 eq. of **CB[8]**. The donor molecule was dissolved in toluene with a concentration of $5.00 \cdot 10^{-6}$ M. For self-assembling, the aqueous solution of **10** with **CB[8]** was provided as subphase and the respective quartz, Si/SiO_2, or Lacey carbon coated TEM substrates were placed on the bottom of the trough. The subphase was subsequently overlayed

with the solution of **13** in toluene. After an assembly time of 5 h, the interfacial layer was deposited onto substrates and subsequently washed two times with water, ethanol, toluene, and again ethanol.

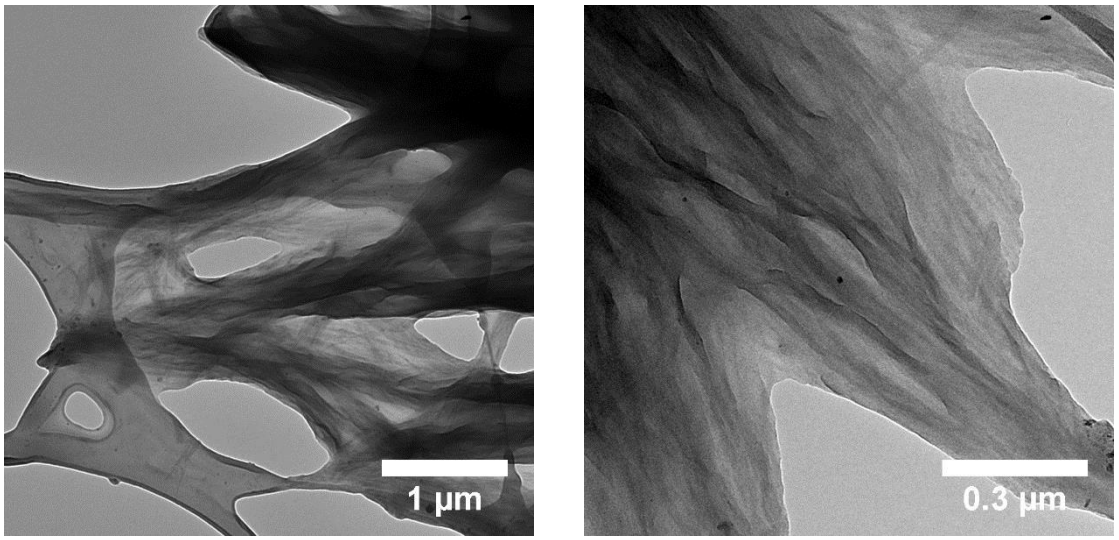

Figure 16: TEM pictures of assembled layers of **10+CB[8]+13** on a Lacey carbon supported TEM grid.

The deposition of the layers from the interface was initially performed by vertical dip-coating of the layer with the Langmuir-Blodgett (LB) technique. Resulting films with dimensions of up to 1 µm² and several layers were visible by TEM (Figure 16), whereas the films seemed to be gathered and rolled around the Lacey support. Holes occurred in the layer, indicating a certain fragility and instability of the film if free-standing over a gap. Ruptures were presumably caused by lateral stress due to the orthogonal deposition direction to the propagation of the polymer. For the purpose of minimizing this stress, copper grids were placed on a slightly inclined plane in the aqueous phase and the interface slowly lowered on the substrate by draining the aqueous phase from the bottom by suction with a pump through a cannula.

The horizontally prepared TEM substrates revealed domains of the Lacey carbon support, being covered more homogeneously with thin layers of 2DSPs from the interface (Figure 17). These layers appeared free-standing over gaps of over 4 µm², although ruptured and corrugated over larger gaps. Those confirm the fragility of the assembled film, but intact domain sizes were already comparable to covalently bound 2DPs reported in literature by *Schlüter* et al.[36]

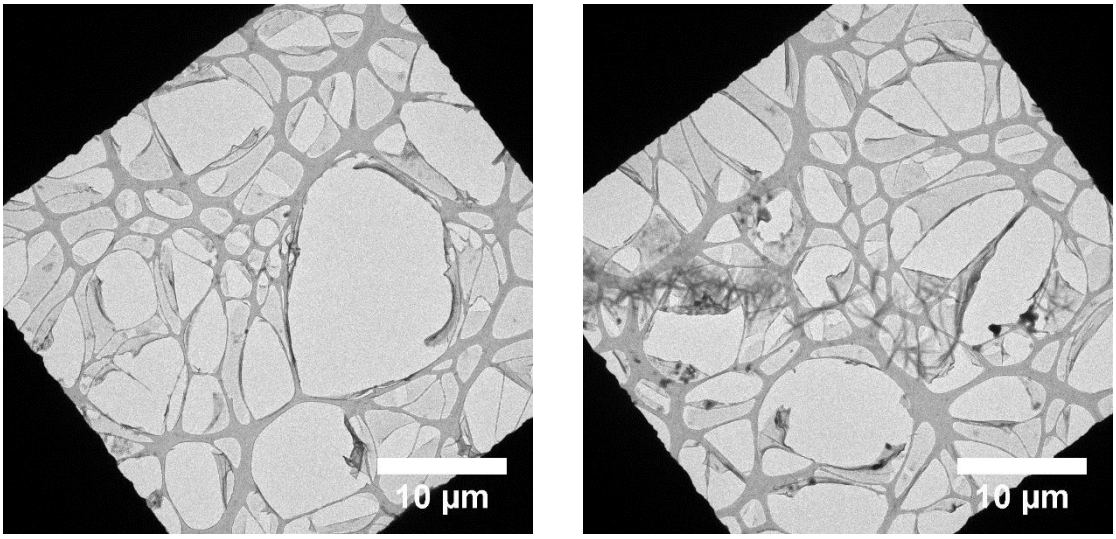

Figure 17: TEM pictures of **10+CB[8]+13** layers, assembled at the liquid-liquid Langmuir trough from a toluene-water interface.

For enhancing the homogeneity and to further avoid rupturing, the deposition procedure was altered as it featured several disadvantages. On the one hand, draining the solution from the bottom was only possible with a pump, which had to pierce the interface and thus the assembled film. Additionally, the running pump induced vibrations possibly causing stress and hence rupturing the layer. Furthermore, as the volume of the lower solution was fixed by the trough design to a small thickness of 3 mm, the weight of the overlaying toluene layer was frequently able to suppress the aqueous phase to a half-ellipsoid. This collapsing of the interface was irreversible due to an increased interaction of toluene and the trough's PTFE-surface compared to water and PTFE. Due to the suppression of the water, the water-toluene interface was changed from planar to convex, causing the self-assembled layer to break, whereby only very few and small layers could be deposited. In addition, the trough provided a high surface area, causing – in combination with the long assembly time of 5 h and the low vapor pressure of toluene – the evaporation of a significant amount of toluene. To keep the concentration constant and to avoid precipitation of components, permanent addition of toluene was necessary, limiting the reproducibility and again causing vibrations.

Figure 18: Picture of the new trough design (left) and the same trough with an air-tight cover in a trough-holder (right) for processing the donor-acceptor-**CB[8]** polymers.

Taking these disadvantages into account, a new trough was designed (Figure 18). A porous glass bottom as substrate holder in combination with a valve underneath made it possible to drain the solutions through the bottom without piercing the layer at the interface and preventing excessive vibrations. The trough was manufactured from glass to avoid the aqueous layer being suppressed from overlayed toluene and contained an air-tight cover to prevent evaporation of toluene.

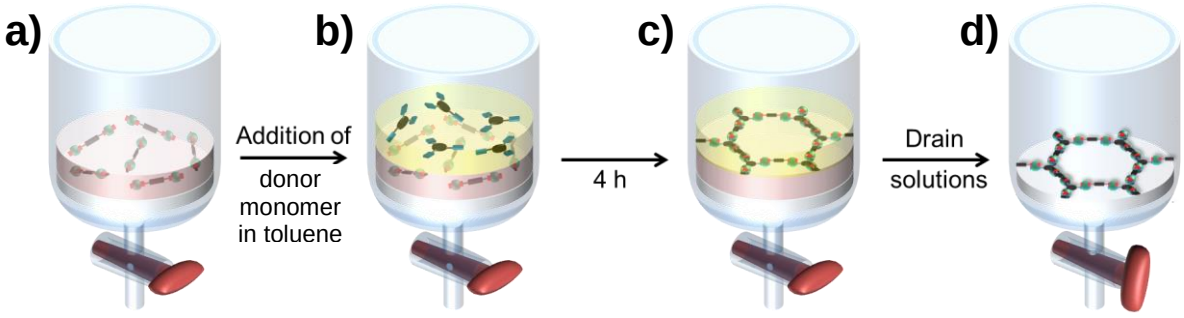

Figure 19: Schematic representation of a self-assembly experiment of donor- and acceptor molecules with **CB[8]** at the toluene-water interface in the custom-made glass trough. The pictures show the trough during different states of the trough. a) A preassembled solution of acceptor molecules and **CB[8]** is provided. b) The donor molecules, dissolved in toluene, are overlayed. c) After an assembly time of 4 h, the supramolecular 2D layer was formed at the interface. d) The valve at the bottom of the trough was opened and the solutions were drained through the porous bottom, leaving behind the insoluble, assembled polymer.

Additionally, the area of the interface was reduced to ~15 cm² to minimize the amount of applied molecules in respect to the substrate's area. Eventually, the trough was placed inside a cork frame, itself being positioned onto an active vibration isolation platform, standing on a passive vibration isolation table, to minimize environmental stress to the interface.

To further optimize the assembly process, different ratios of concentrations were applied. Thus, the preassembled solution of **10+CB[8]** was provided in excess, and the concentration of **13** in toluene was varied. Keeping the concentration lower than $8 \cdot 10^{-6}$ mol/L resulted in no continuous layer, but rather in a perforated film. Concentrations higher than $4 \cdot 10^{-5}$ mol/L revealed many small multilayers as a result of a layered stacking of small aggregates before the interconnection could take place. It was possible to obtain homogeneous monolayers in the concentration range between $8 \cdot 10^{-6}$ mol/L and $4 \cdot 10^{-5}$ mol/L. the concentration of $2 \cdot 10^{-5}$ mol/L were found to be most suitable for reproducibly obtaining monolayers in a relatively short assembly time of 4 h.

The glass trough however deprived a possibility to follow the assembly process during the complexation like it is well-established for a Langmuir trough for instance with a Wilhelmy balance. Therefore, the assembly at the interface was deposited after incremental time-intervals on Si/SiO_2-wafers. The surface of the wafers was analyzed by AFM. After 1 h, small and randomly distributed particles were found with a height difference of 1.6 nm (Figure 20a). An assembly time of 2 h resulted in the separated aggregates to accumulate to larger domains (Figure 20b). Again, the height difference of these aggregates was 1.6 nm, suggesting the presence of the same kind of aggregation. After 3 h, the substrate was completely covered with a layer, being yet interspersed with many nanometer-sized holes and cracks (Figure 20c).

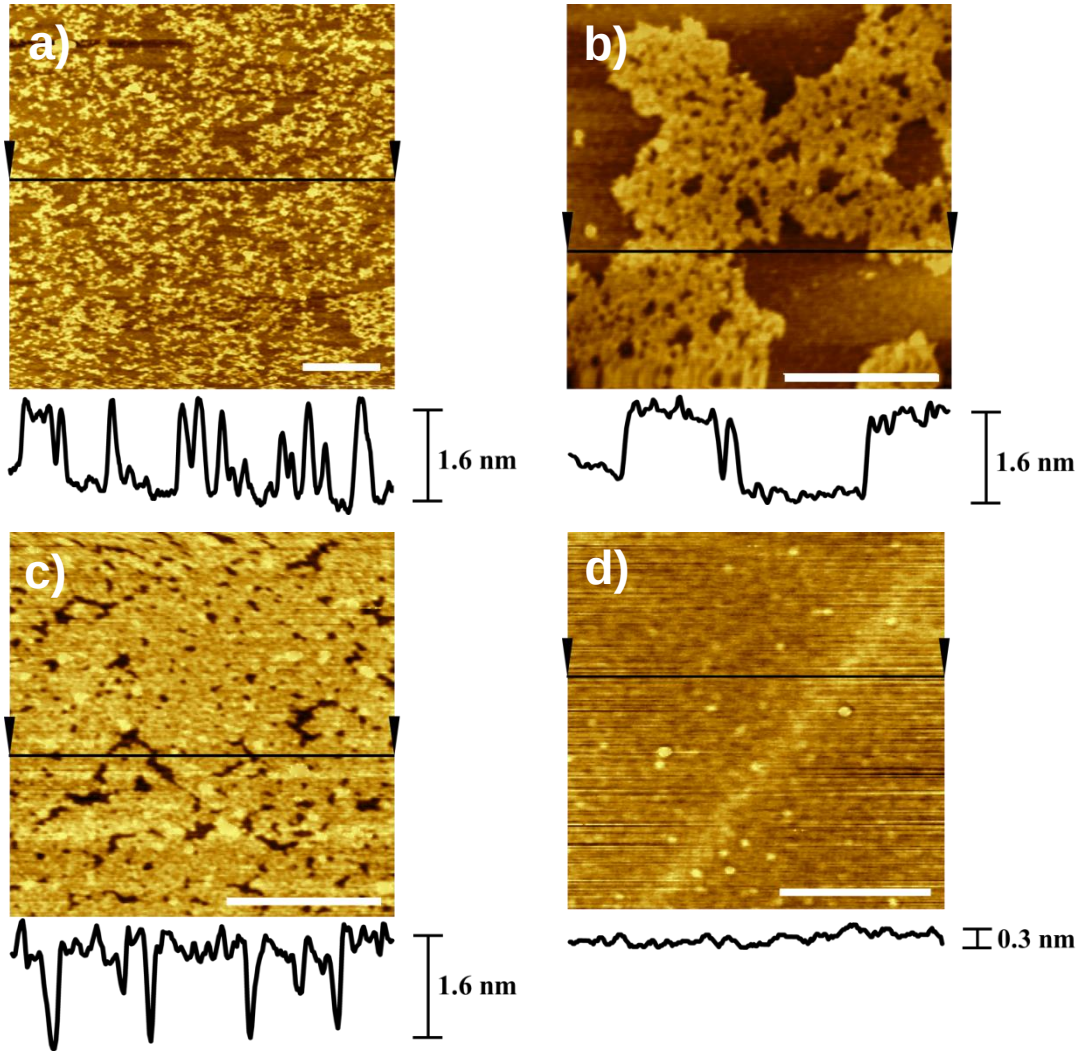

Figure 20: Tapping-mode AFM pictures of the assembled layer of **10+CB[8]+13** deposited from the toluene-water interface after a) 1 h, b) 2 h, c) 3 h, and d) 4 h, respectively. Below each picture, a cross section of the position, marked with a black line and two triangles, is shown. The inset scale bars are 400 nm.

Again the height difference was 1.6 nm, although due to small hole diameters, minor depths were found. Those were a result of the conical cantilever tip, which necessarily had to contact the bottom to reveal the correct height. If holes feature smaller diameters, the cone of the cantilever tip contacts the edge, resulting in analyzing a minor depth. After 4 h, a flat layer covered the substrate with height differences of 0.3 nm, being rougher than the bare SiO_2 surface and therefore revealing the assembled layer of **10+CB[8]+13** without major defects. In every step, there was only one thickness of particles or layers visible, substantiating the formation of a monolayer.

Comparing the assembly time of the water-soluble monomers of more than 5 h to produce 3 µm sized layers with the assembly time at the toluene-water interface, the latter is with a total time of 4 h significantly faster and in fact created larger self-assembled films. Both effects were traced back to the influence of the templating effect of an interface due to several reasons. Considering the approach only in water, all molecules were present in a homogeneous solution, enabling an assembly of molecules in accordance to their statistical concurrence. In contrast, the assembling monomers are more likely to meet at the interface, comprising the adsorption face-on of aromatic groups to an interface and thus promoting dynamics in only two-dimensions.[82, 109] This effect was assumed to further stimulate layer growth at the interface by connecting small aggregates. After initial assembly to small flakes they were presumed to accumulate at the interface considering the solubilizing moieties to be complexed and protected from peripheral solution by the cavity of **CB[8]**. Due to the insolubility assembling monomers were withdrawn from the chemical equilibrium and were not available for the reverse reaction. This is in contrast to the solution-based assemblies, which showed solubility up to certain sizes of flakes, as visible e.g. in UV/Vis spectroscopy or NMR studies, indicating the possibility of a certain degree of reverse reactions, thus slowing down the growth of the assembled polymer. The dynamics of those insoluble flakes at the interface was then expected to be restrained to two dimensions, enabling different flakes to combine and build larger layers. Contrary to that, the experiment in solution rather built many flakes with layer-growth only resulting from assembly with dissolved molecules in the peripheral solution. These flakes were less likely to connect at some point, as the edges are not necessarily oriented to each other. The assembly at the interface however leads to a two-dimensional confinement of the growth direction and of the assembled layer. This minimizes the possibility of the edges of two layers not facing each other and being ripped apart during the generation by lateral stress, and additionally stabilizes evolving larger structures to result in the formation of large layers.

2.2.2.3. Morphological Characterization of Layers Processed From The Toluene-Water Interface

The reproducibly observed height difference of 1.6 nm was in accordance to the outer diameter of **CB[8]** of 1.75 nm (Figure 21).[53] Considering **CB[8]** standing vertically on the substrate due to the parallel aggregation of donor and acceptor surfaces to the substrate's plane, this thickness revealed a monomolecular arrangement and complied with **CB[8]**-based supramolecular polymer monolayers in literature.[76-78, 110] The slightly larger height difference of 1.8 nm, which was measured after scratching the surface, presumably occurred due to a marginal damage of the surface, as indicated by the slightly tilted bottom of the cross section (Figure 21a).

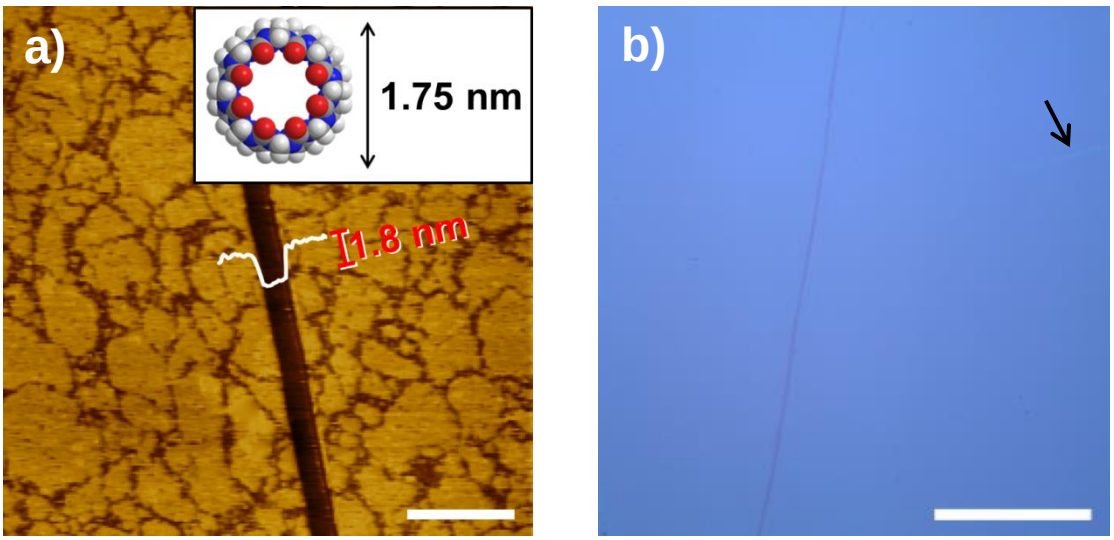

Figure 21: a) Tapping-mode AFM picture of a monolayer of **10+CB[8]+13**, scratched with a needle. The scale bar is 1 µm. The inset shows a cross-section orthogonal to the scratching direction. The height difference of the scratch was measured to be 1.8 nm. The molecular structure of **CB[8]** is depicted for comparison on the upper right, revealing an outer diameter of 1.75 nm.[53] b) Optical microscopy image of a wafer surface, covered with assembled **10+CB[8]+13** after deposition from the toluene-water interface. A slightly tilted, vertical scratch in the middle of the sample serves as contrast for the bare surface. The arrow indicates a small wrinkle of the layer. The scale bare is 150 µm.

The applied procedure was also found to further cover large areas of wafer surfaces homogeneously. In this regard, layers covering whole Si/SiO_2 wafer pieces with surface areas of 1.5 cm^2 were found. As it was not possible to visualize a monolayer in

such dimensions, a representative picture of a covered wafer area was shown by OM in Figure 21b, indicating a homogeneous layer of over 0.25 cm². The layer was scratched with a needle to show the contrast between the bare wafer surface and the covered area. Additionally, the homogeneity of the layer was corroborated by a small wrinkle (Figure 21b, arrow), demonstrating the visibility of an inhomogeneous area.

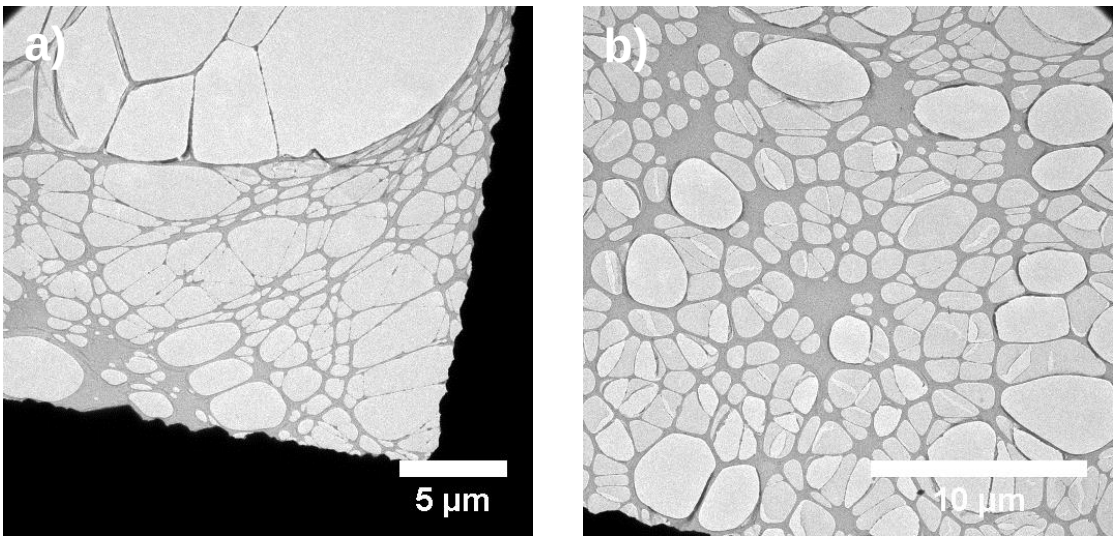

Figure 22: TEM-pictures of **10+CB[8]+13** layers after deposition with the custom made glass trough.

Comparing the free-standing layers of **10+CB[8]+13** on Lacey carbon supported copper grids, deposited with a Langmuir trough (Figure 17) and those obtained with the procedure utilizing the custom-made glass trough (Figure 22), similarities and differences can be found. Although both procedures featured free-standing layers over gaps in the support, the homogeneity of the layers from the glass trough exceeded the one of the Langmuir approach by far. Where the latter revealed many broken, separated films, it was possible to obtain a continuous layer lying over a large area of the support in the case of the improved procedure. This was probably the result of the reduced stress to the interface and the milder deposition of the assembled product onto the substrate's surface. In both cases, however, the layers appeared broken upon covering holes larger than 10 µm². This stability exceeded the results obtained with the combination of **7** with **10** and **CB[8]**. The reason for the larger layers can be traced back to two phenomena. First, the increased planarity of the truxene core of **13** causes a stronger donor behavior compared to triphenylbenzene in **7**. Second, the advantageous preparation method minimizes the stress exposed to the layer, thus

promoting larger layers. However, the layers broke upon covering a certain gap size in both preparation methods. It was assumed that an intrinsic parameter of the molecular structure caused the collapse. Therefore, the layers probably ruptured upon the stress of their own weight.

2.2.2.4. Structural Characterization

The resulting layers were found to be insoluble, demanding for characterization methods different from those typically used in literature for comparable systems, e.g. concentration dependent UV/Vis and fluorescence spectroscopy, NMR titration spectroscopy, diffusion-ordered spectroscopy (DOSY) and nuclear Overhauser enhancement spectroscopy (NOESY), isothermal titration calorimetry (ITC), DLS, or single crystal X-ray diffraction (XRD).[64, 76-79, 103, 110-114]

UV/Vis absorption studies of **10+CB[8]+13** in solid state were performed in reflection mode on covered quartz wafer substrates by means of an Ulbricht sphere. For comparison, samples of the monomers **13**, and **10+CB[8]** were prepared by drop-casting the respective solution onto quartz wafers. In solution, UV/Vis studies showed an intensive, bathochromically shifted charge-transfer band visible upon the complexation of one donor and one acceptor molecule inside **CB[8]**.[64, 88, 92] Comparing the solid-state UV/Vis absorption spectra of **13** (Figure 23, blue) and **10+CB[8]** (Figure 23, red) with **10+CB[8]+13** (Figure 23, black), the spectrum of **10+CB[8]** exhibited no visible absorption in the range between 575 – 1150 nm. **13** in contrast showed a very small and not significant, broad absorption. Notwithstanding the absorption range between 575 – 1150 nm, the spectrum of **10+CB[8]+13** appeared as an superposition of both monomeric spectra **13** and **10+CB[8]**. In the absorption range between 575 – 1150 nm, however, an additional, bathochromically shifted, broad absorption with an unambiguously increased absorbance was visible. This absorption was assigned to a charge-transfer band of interacting donor and acceptor moieties inside **CB[8]** in accordance to literature.[92] In view of the fact that the system in the solid state should be immobilized, the donor-acceptor overlap inside **CB[8]** was expected to exist in different extents, resulting in more energetic states and therefore a broader absorption. Contrary to that, the flexibility in solution allowed the system to move and rearrange, demonstrating a statistically higher presence of the optimal overlap during the measurement and visualizing a more distinct peak. Notably, the characteristic absorption of the naphthalene diimide spacer between 330 – 400 nm remained

unshifted upon the complexation, corroborating the interaction of the *N*-methyl-4,4'-bipyridin-1-ium acceptor moieties instead of the naphthalene diimide spacer core, with the methoxynaphthyl donor groups. Therefore, the bathochromic shift in combination with the increased absorption indicated the successful complexation of donor moieties of **13** with acceptor moieties of **10** in the cavity of **CB[8]**.

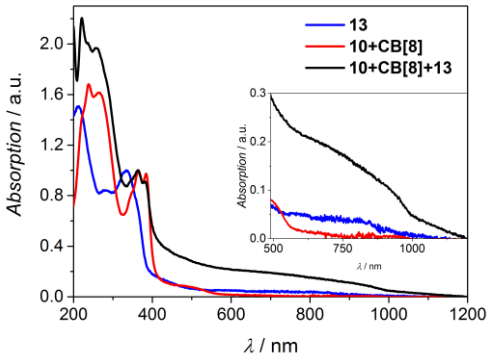

Figure 23: UV/Vis absorption spectra of the monomers **13** (blue), **10+CB[8]** (red), as well as the self-assembled layer **10+CB[8]+13** (black). The spectra were normalized to the local absorption maximum of 333 nm for **13**, and to the 0 → 1 absorption of the naphthalene diimide spacer at 365 nm in the case of **10+CB[8]**, respectively, to be comparable. The inset shows the magnified area between 500 – 1150 nm.

In contrast to UV/Vis spectroscopy, infrared (IR) spectroscopy was not expected to be sufficiently sensitive to changes in the rotational-vibrational structure upon this noncovalent interaction motif. Therefore, the IR spectrum of **10+CB[8]+13** was supposed to reveal a stoichiometric superposition of the monomeric spectra of **13**, **10**, and **CB[8]**. The precursors were measured in solid state and a superposition of the theoretical composite was generated from the precursors' spectra in a ratio of **CB[8]**:**10**:**13** = 6:3:2 (Figure 24, blue). This theoretical composite was in good agreement with the spectrum of **10+CB[8]+13** (Figure 24, black), assuming a quantitative presence of the individual monomers in the self-assembled species.

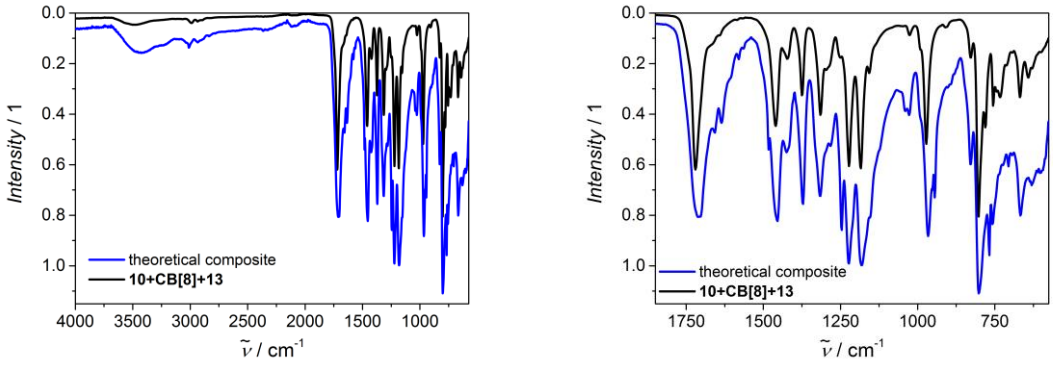

Figure 24: IR spectra of **10+CB[8]+13** (black), and of the theoretical composite (blue). Latter was formed by stoichiometric superposition of the monomers' IR spectra. The right plot shows the magnified area of the left spectrum between 575-1850 cm^{-1}.

$^{13}C\{^{1}H\}$ Lee-Goldburg (LG) heteronuclear correlation (HETCOR) NMR spectra were measured in collaboration with [redacted] of the supramolecular network as well as of its precursors. As the amount of material necessary for the measurement exceeded the processable amount of **10+CB[8]+13** with a layer-by-layer deposition of the general procedure by far, an alternative preparation method was chosen. Thereby, an aqueous solution of preassembled **10+CB[8]** was vigorously stirred with a solution of **13** in toluene. The permanently regenerating interface was therefore able to prevent the formation of an impenetrable layer at the interface. The bulk material for the measurement was collected by filtration and purified by washing with water, ethanol, and toluene. The occurring ruptures of the layer into small flakes was considered not to be obstructive to the measurement, as the expected chemical shift upon complexation was not depending on the orientation of the flakes in the measurement chamber. The $^{13}C\{^{1}H\}$ LG-HETCOR NMR spectra in Figure 25 displays **10+CB[8]+13** in comparison with its precursors. The correlation signals of the complex **10+CB[8]+13** were observed to be shifted in respect to the corresponding signals of uncomplexed **13**, **10**, and **CB[8]**. Considering an interaction of donor and acceptor inside **CB[8]**, the observed nuclear spin sites were expected to modulate their respective local electron density. As a result, stronger electron shielding should originate in decreasing chemical shift values and vice versa. The expectation of the signals of donor molecule **13** experiencing a down-field shift upon complexation complied with the compared spectra in Figure 25c. Thus, the correlation signals of the **13** $^{13}C\{^{1}H\}$ LG-HETCOR NMR spectra were found between 6-8 ppm in the ^{1}H dimension and 120-130 ppm in the ^{13}C dimension. The respective correlation peaks in the complex **10+CB[8]+13** displayed

the pronounced down-field shift in both ^{1}H and ^{13}C dimensions. The resulting signals were found between 8-10 ppm in the ^{1}H dimension and 125-135 ppm in the ^{13}C dimension. In contrast, the acceptor molecules **10** experienced an up-field shift. The correlation signals of uncomplexed **10** were observed at 9.2 ppm in the ^{1}H dimension, and 144 ppm and 129 ppm in the ^{13}C dimension, whereas **10+CB[8]+13** revealed the peak positions of **10** at 6.7 ppm in the ^{1}H dimension and 130 ppm in the ^{13}C dimension, as well as 6.3 ppm in the ^{1}H dimension, and 116 ppm in the ^{13}C dimension.

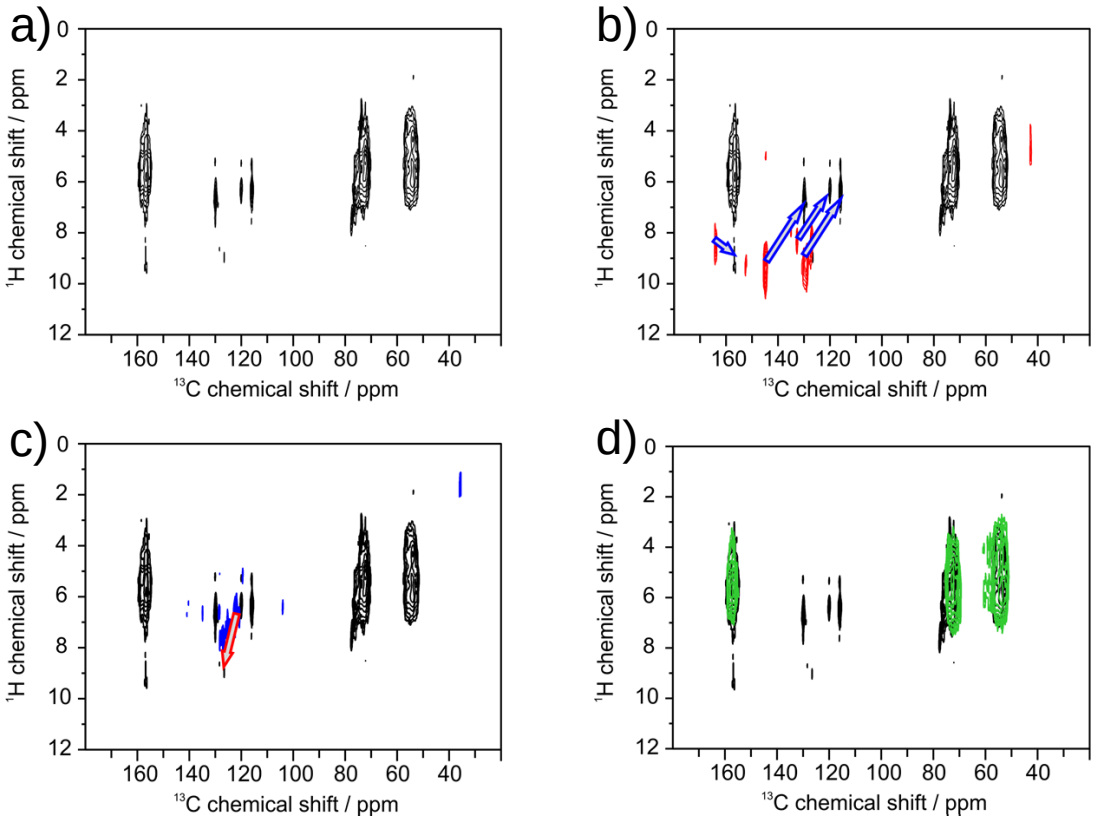

Figure 25: $^{13}C\{^{1}H\}$ Lee-Goldburg (LG) heteronuclear correlation (HETCOR) NMR spectrum of a) the supramolecular network. In order to illustrate changes due to the complexation, superpositions of a) with the corresponding $^{13}C\{^{1}H\}$ LG-HETCOR spectra of the pure precursors b) **10** (red), c) **13** (blue) and d) **CB[8]** (green) are given. Arrows visualize the chemical shifts, appearing due to complexation.

Both peak shifts corresponded to a deshielding effect of **13** at the same time as an increased electronic shielding of **10**. As these shifts were in qualitative agreement with the spectral changes observed with **10+CB[8]+Np-TPB**, they were interpreted by an electron withdrawing effect of the *N*-methyl-4,4'-bipyridyl moiety of **10** in combination

with the electron donating behavior of the methoxynaphthyl group of **13**. In accordance to **10+CB[8]+Np-TPB** and to comparable complexations in literature,[115] **CB[8]** only showed minor shifting behavior as host molecule incorporating two guest molecules. The correlation peaks of **CB[8]** in **10+CB[8]+13**, visible at 55 ppm in the ^{13}C dimension for the CH_2 groups and at 157 ppm in the ^{13}C dimension in case of the carbonyl groups remained almost unaltered compared to bare **CB[8]**. The signal of the **CB[8]**-CH groups at 72 ppm, however, showed a heterogeneous behavior. The main part of the signal remained unshifted, thus being in concordance with the other signals of **CB[8]**, whereas a small contribution of this peak revealed a clear deshielding trend, being shifted 2 ppm in the ^{1}H dimension and 3 ppm in the ^{13}C dimension to the down-field. To further investigate the complexation behavior of **CB[8]** in the complex and to analyze the heterogeneous behavior of the **CB[8]**-CH groups, additional recoupled polarization transfer heteronuclear dipolar order (REPT-HDOR) sideband pattern experiments were performed. REPT-HDOR sideband patterns are able to give information about the local mobility of molecules in solid state.[116-117] These sideband pattern were influenced by the MAS spinning frequency, the excitation and reconversion duration, as well as the effective dipolar coupling strength. REPT-HDOR sideband patterns were generated for each CH site and spectrally resolved in respect to its ^{13}C chemical shift (Figure 26a). From the resulting 2D REPT-HDOR sideband patterns, the motional averaged dipole-dipole coupling of a CH group can be determined by comparing the cross-section of the sideband pattern at particular ^{13}C chemical shift values with a computation of sideband pattern, characteristic for the dynamic behavior of the CH group (Figure 26b and c).

A 2D REPT-HDOR experiment was carried out on the bulk **10+CB[8]+13** powder. Remarkably, the **CB[8]**-CH groups exhibited a heterogeneous behavior in the $^{13}C\{^{1}H\}$ LG-HETCOR NMR spectrum in the region at 72 ppm in the ^{13}C dimension, revealing two different mobilities of the **CB[8]** molecules. The one species of **CB[8]** molecules in the **10+CB[8]+13** powder, being unshifted at 72 ppm compared to the pure **CB[8]** molecules, were rigid with only small angle fluctuations < 13° (Figure 26b). A simple geometric consideration – disregarding thermodynamic influences – accommodating two guests inside the cavity of **CB[8]** was carried out. Taking into account the inner diameter of the cavity of 0.69 nm, a width of the guests of 0.47 nm and a π-π-interaction distance of 0.35 nm, a theoretically possible fluctuation of the two guests of 19° was calculated. Considering attractive and repulsive molecular interactions, resulting in smaller fluctuations, the obtained REPT-HDOR sideband pattern at 72 ppm represented **CB[8]** molecules, incorporating both donor- and acceptor moieties as

guests. In contrast, the down-field shifted signals of **CB[8]**-CH units at 75 ppm exhibited large angle fluctuations of > 40°. Therefore, this **CB[8]** species was less rigid and likely to be located in areas with incomplete complexation, e.g. at grain boundaries or defects. As the molecular packing at these areas was considered to be less restricted compared to the regularly ordered hexagonal pattern of the 2D assembly, these large angle fluctuations can be possible. Calculating the geometrically possible fluctuation of a **CB[8]** molecule incorporating only one guest, a value of 58° was obtained. This value as well was considered to be excessive due neglected molecular interactions or thermal influences in the calculation. However, this estimation corroborated the **CB[8]**-species to enclose only one guest molecule, identified as the acceptor moiety of **10** in regards to the observed down-field shift. The visibility of these defect signals in NMR was antithetical to the homogeneity of the previously shown TEM pictures (Figure 22). However, this can be explained with the deviating preparation method of the **10+CB[8]+13** powder, hence expecting more defects and grain boundaries.

The $^{13}C\{^{1}H\}$ LG-HETCOR NMR spectrum of **10+CB[8]+13** revealed different intensities for the complexed monomers. Although LG-HETCOR is not a quantitative method, the high intensity of **CB[8]** signals, the medium intensity of **10** signals, and the weak signals of **13** were in qualitative agreement with the stoichiometry of the proposed supramolecular assembly, as suggested from IR spectroscopy (Figure 24). Eventually, the visibility of a fine structure in the spectrum of the assembly indicated the presence of a well ordered structure of **10+CB[8]+13** (Figure 25).

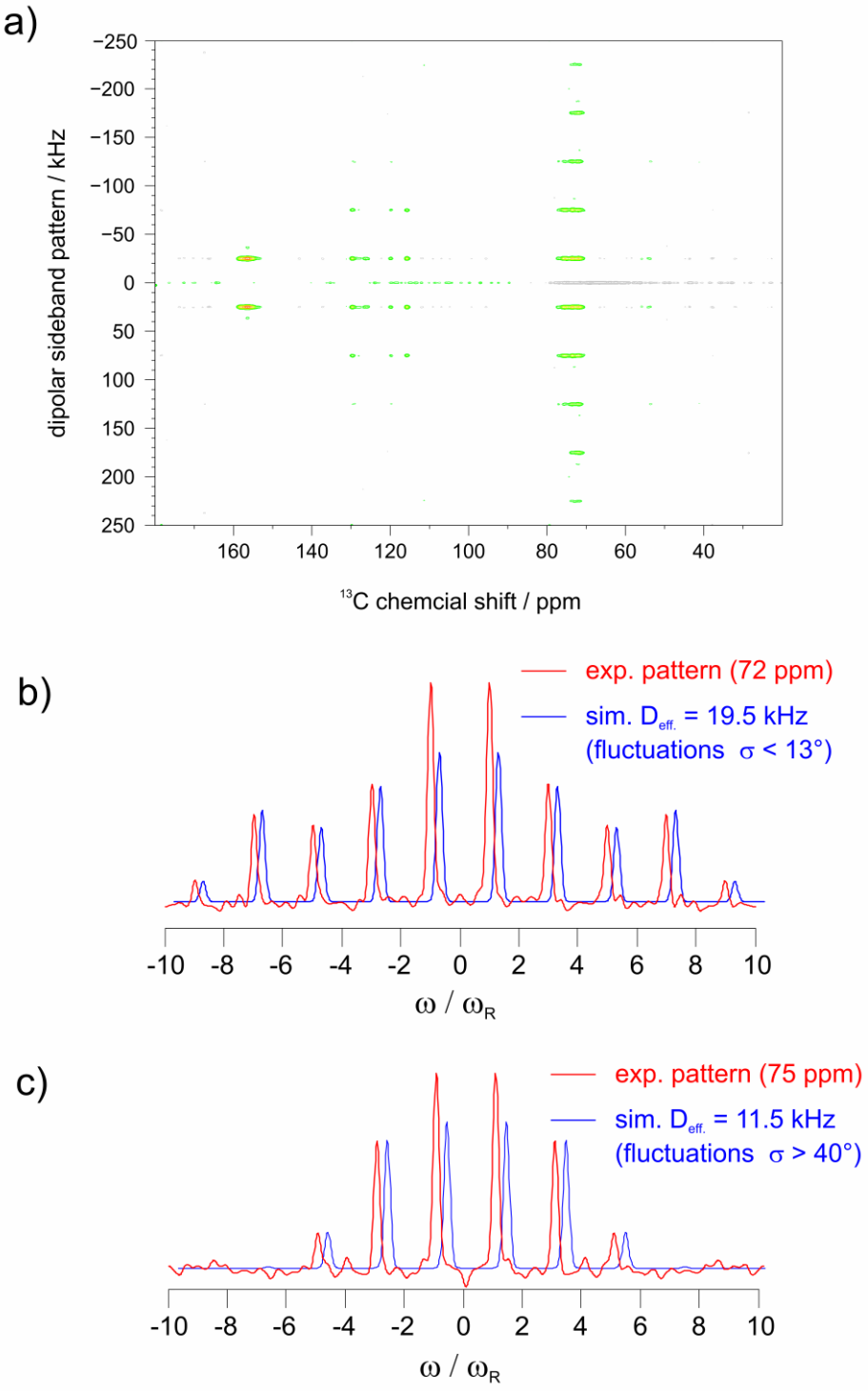

Figure 26: a) 2D REPT-HDOR sideband pattern of **CB[8]** in the supramolecular complex of **Np-10+CB[8]+13**. The effective dipolar coupling value of the **CB[8]**-CH at 72 ppm indicated a rigid environment, whereas the shifted **CB[8]**-CH-signals at 75 ppm originated from molecules in mobile environments undergoing substantial large angle fluctuations on the 100 kHz time scale. b) The experimental cross section of the signal at 72 ppm (red), compared to a simulated sideband pattern of a dipolar coupling value of 19.5 kHz (blue). c) The experimental cross section of the signal at 75 ppm (red), compared to a simulated sideband pattern of a dipolar coupling value of 11.5 kHz (blue).

To elucidate the internal structure of the resulting monolayers, approaches with high-resolution TEM were carried out in cooperation with [redacted].

The assembled layers of **10+CB[8]+13** were unstable against high irradiation doses of over 1000 e/(nm²·s), which were necessary for high magnifications while measuring TEM. Upon small magnifications with low beam intensities, the layers remained stable, whereas holes appeared under higher magnifications due to decomposition (Figure 27a). Further irradiation and intensification of the beam resulted in a structure with a stable pattern in addition to the holes, indicating occurrence of graphitization (Figure 27b). With higher magnifications undulated and rolled-up structures with a multilayer graphene pattern were visible.

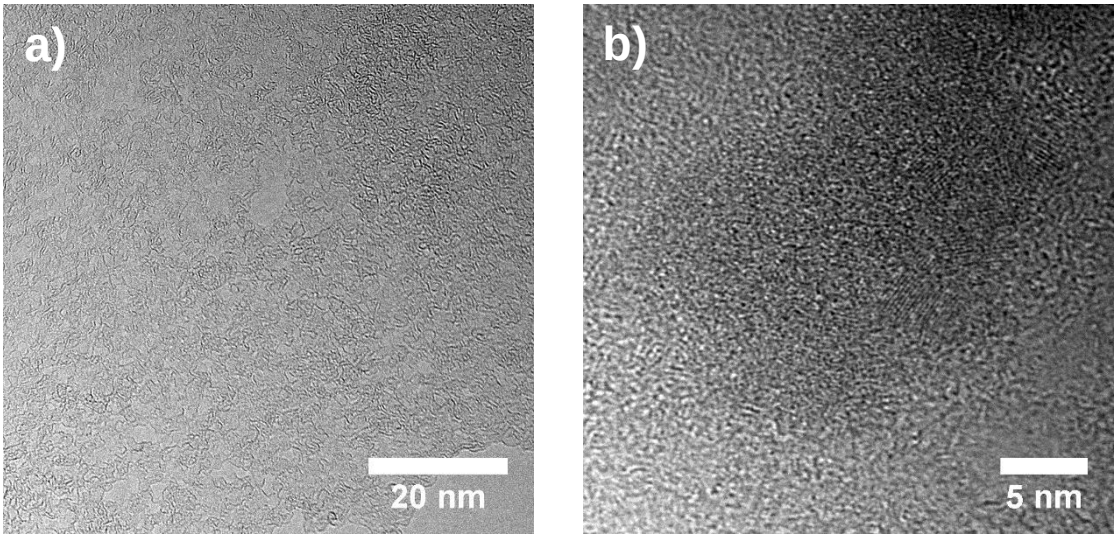

Figure 27: HR-TEM pictures of **10+CB[8]+13**. a) The decomposition of the layer upon high beam intensities was visible by the formation of holes and small flakes. b) Higher magnification of the remaining flakes revealed patterns typical for multilayer graphene.

To enhance the stability of the film against high beam intensities, it was deposited onto CVD-graphene covered Quantifoil grids and subsequently covered with another layer of CVD-graphene to minimize charging effects to the sandwiched polymer. However, as the decomposition of the polymer under high electron beam intensities still occurred, and as the instability against irradiation was in accordance to other reported monolayered material,[70, 118-120] the attempt to visualize the self-assembly by high-resolution TEM was not pursued further.

Instead, STM experiments were carried out in cooperation with [redacted]. Layers of **10+CB[8]+13** were deposited onto highly oriented pyrolytic graphite (HOPG) and Au(111) substrates. Although the successful deposition was confirmed by AFM measurements, STM measurements only revealed the bare HOPG and Au(111) surfaces. This behavior was assumed to be a result of a poor interaction between the layer and the substrate, considering a small contact area of **CB[8]** standing perpendicular to the substrate's surface. Additionally, as the polymer geometry required large distances between the **CB[8]** units, the contact area of the polymer was even smaller. In this case, the layer was not fixed to defined positions in the crystal structure of the substrate but rather moving on the surface. In the time average of the measurement, these dynamics were expected to lead to an invisibility of the layer. As the attempts to visualize the internal structure failed in real space, further experiments were carried out utilizing crystallographic methods in reciprocal space.

In this regard, grazing incidence wide-angle X-ray scattering (GIWAXS) studies were performed in collaboration with [redacted]. GIWAXS is a versatile and powerful method, which can provide information about the molecular orientation of weakly scattering organic materials in thin films.[121] Therefore, in contrast to conventional XRD measurements, information about both in-plane *(q_{xy})* and the out-of-plane *(q_z)* directions in respect to the film surface were obtained. For thin films with lamellar stacking, the *(00l)* diffraction peaks corresponding to the interlayer spacing emerged on the q_z axis and those related to the in-plane organization, *(h00)* and *(0k0)*, appeared on the q_{xy} axis. Materials comprising crystalline orientations typically result in GIWAXS diffraction patterns with a high number of intensive elliptical reflections.[122] The position, shape, and intensity of these diffraction peaks can thereby be used to elucidate the packing behavior within the film.

A monolayer sample of **10+CB[8]+13** was prepared onto a SiO_2/Si-wafer substrate and measured with a solid anode X-ray tube at the DELTA synchrotron facility of the TU Dortmund. The synchrotron irradiation was thereby necessary to obtain a reasonable diffraction signal from the few material a monolayer provides. Remarkably enough, the GIWAXS pattern for the monolayer sample showed very weak, but distinct reflections, indicating the presence of a highly ordered structure (Figure 28c). For comparison and to exclude visible reflections to originate from the precursors, **13** and **10+CB[8]** were deposited by drop casting onto SiO_2/Si-wafer substrates, and measured (Figure 28a,b). Drop casting was chosen as deposition method, since the highest probability of an impurity of the precursors to occur within the preparation and processing of the

assembled layer of **10+CB[8]+13** occurred by drying of residual precursor solutions under ambient conditions. The resulting diffraction pattern of **10+CB[8]+13** differed significantly from the monomeric reflections, therefore excluding the presence of uncomplexed precursor. However, the internal order of **10+CB[8]+13** could not be elucidated from these patterns, because the intensity of the monolayer reflections was too low for interpretation.

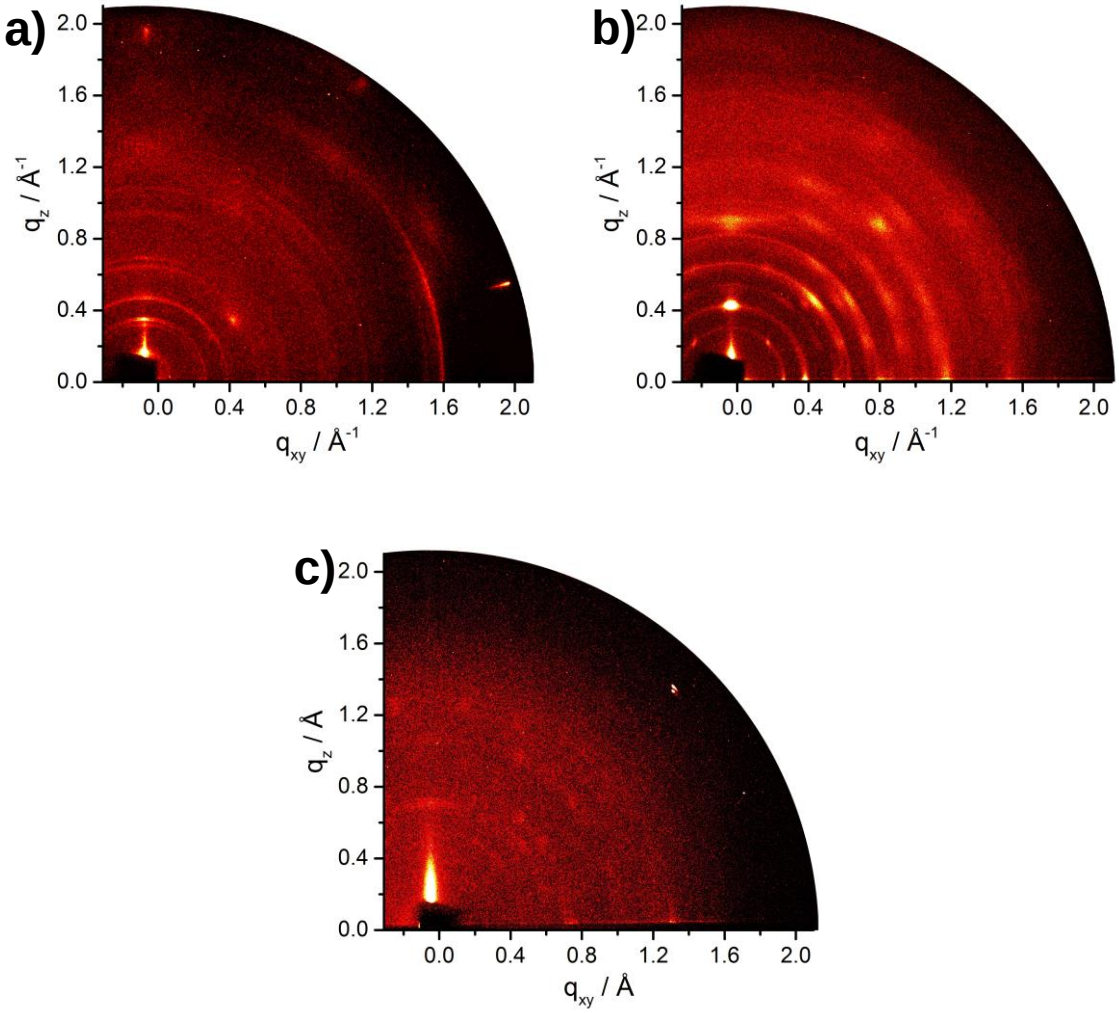

Figure 28: GIWAXS diffraction pattern of a) the monomer **13**, deposited on a SiO_2/Si-wafer by drop-casting, of b) the monomer **10+CB[8]**, deposited on a SiO_2/Si-wafer by drop-casting, and of c) the assembled monolayer of **10+CB[8]+13** after horizontal deposition on a SiO_2/Si-wafer.

To overcome this problem, a thin film of **10+CB[8]+13** was prepared by repeated depositions from the glass trough to form a 122 nm thick material on a SiO_2/Si-wafer. The GIWAXS pattern showed intensive and distinct reflections (Figure 29a), which were in qualitative agreement with the pattern of Figure 28c and corroborated the suggested highly ordered structure. Due to the complexity of the system and the correspondingly high amount of possibilities for signals outside q_z and q_{xy} axis, only the meridional and equatorial reflections were examined for the structure elucidation. The one-dimensional integration of meridional reflections (Figure 29c, top) of **10+CB[8]+13** was in agreement to a lamellar, Bernal-stacked arrangement in respect to the diameter of **CB[8]** with 1.75 nm.[53] The 001 and 001' interlayer planes generated reflections at q_z = 0.395 Å^{-1} and q_z = 0.422 Å^{-1}, corresponding to *d*-spacings of 1.59 and 1.48 nm, respectively. The visibility of these reflections up the 4th order proved the long-range order of this arrangement parallel to the substrate surface. Generally, in a Bernal-stacking, only one interlayer distance was found, being assigned to the smaller *d*-spacing of 1.48 nm. The visible splitting of the reflections on the q_z-axis and the therefore visible *d*-spacing of 1.59 nm indicated a marginally elliptical deformation of the **CB[8]** rings. This deformation relative to the long axis of the **CB[8]** complex, incorporating the donor- and acceptor moieties, was in agreement with REPT-HDOR sideband patterns (Figure 26), showing a restricted rotation of **CB[8]** molecules around its guests. The arrangement of molecules in-plane was retrieved from the equatorial plane on the q_{xy}-axis. To the one-dimensional integration of the equatorial plane (Figure 29c, bottom), theoretical peak distributions of different lattices with different lattice parameters derived from Bragg's law were fitted. The simplicity of the periodic sequence of diffractions suggested a high symmetry of the molecular arrangement in the film. The best agreement with theoretical peak distributions was found with an either cubic structure or a hexagonal symmetry. Considering the structure of the monomers, a cubic structure contradicted with the possible packing motives the symmetry of the monomers allows. The peak distribution in the equatorial plane implied a periodicity of the first visible reflection in the small-angle range at q_{xy}= 0.381 Å^{-1} corresponding to the index (*300*). The *d*-spacing of 1.64 nm corresponded to a first-order reflection with a *d*-spacing of 4.92 nm. Indexing the latter as (*100*) in a hexagonal lattice gave a unit-cell parameter of 5.68 nm. Higher-order scattering intensities even up to 10th order corroborated this fit and indicated a good long-range order of molecules with thus pronounced in-plane crystallinity. With this assignment and considering the meridional reflections, a two-dimensional hexagonal superstructure with lattice parameters of 5.68 nm, 5.68 nm, and 1.5 nm was derived, conforming well to the schematic structure representation (Figure 29b). To validate these results,

different donor and acceptor monomers were synthesized and measured with this method.

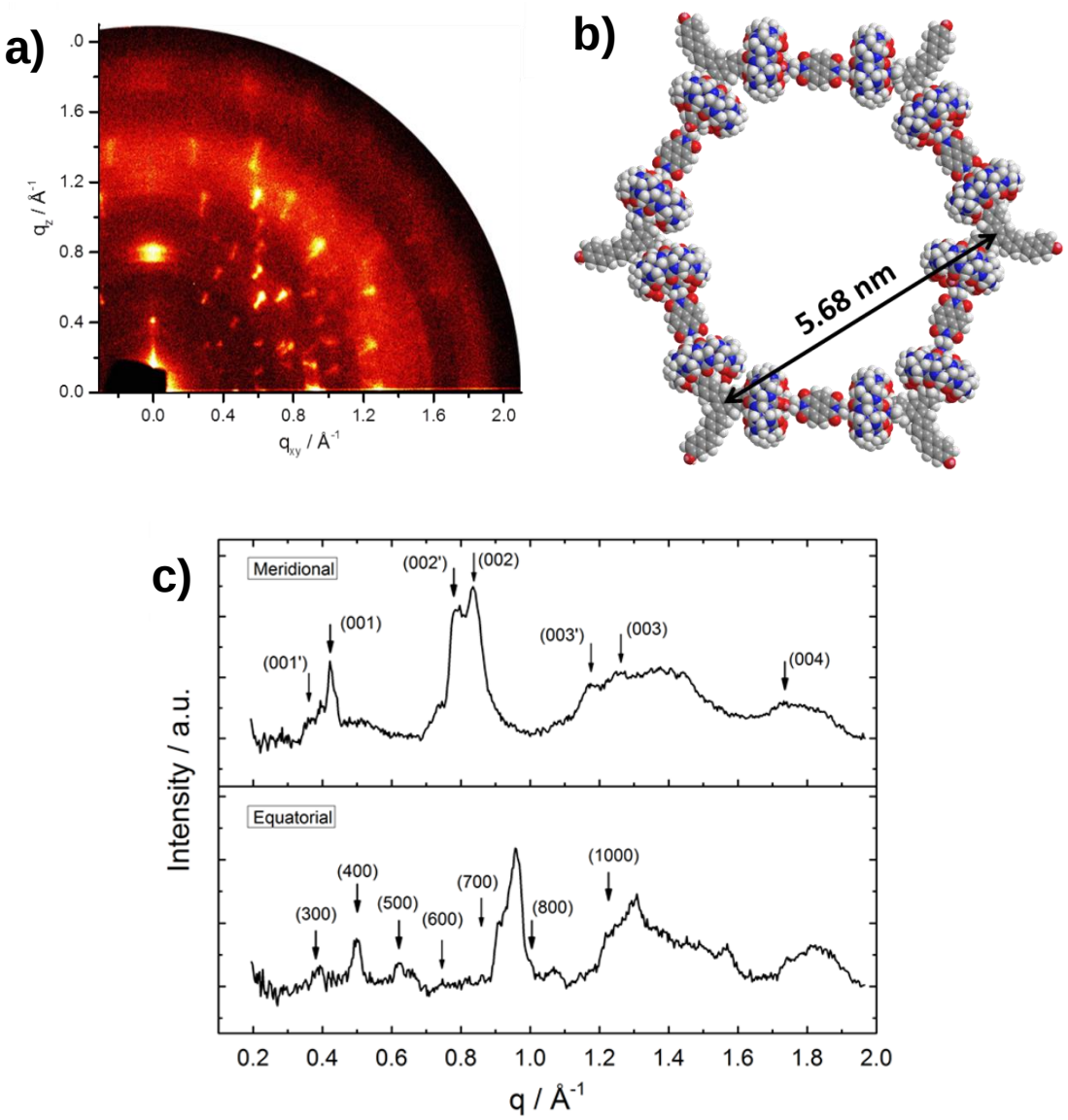

Figure 29: a) GIWAXS diffraction pattern of the 122 nm thick multilayered film of **10+CB[8]+13**. b) Top view of one hexagon of a geometry optimized model structure of **10+CB[8]+13** with the calculated distance revealing a hexagonal unit cell parameter of 5.79 nm. c) One dimensional integrations of the meridional (top) and the equatorial (bottom) diffractions derived from a). The arrows illustrate the positions of the particular *(hkl)* scattering intensities.

2.2.2.5. *Influences of Different Donor and Acceptor Monomers on the Self-Assembly Behavior*

For introducing different functionalities into the supramolecular polymer, different donor and acceptor molecules were synthesized for the self-assembly at the toluene-water interface. The donor and acceptor moieties themselves were left unaltered, whereas the spacer units were varied in size, functionality, and conjugation.

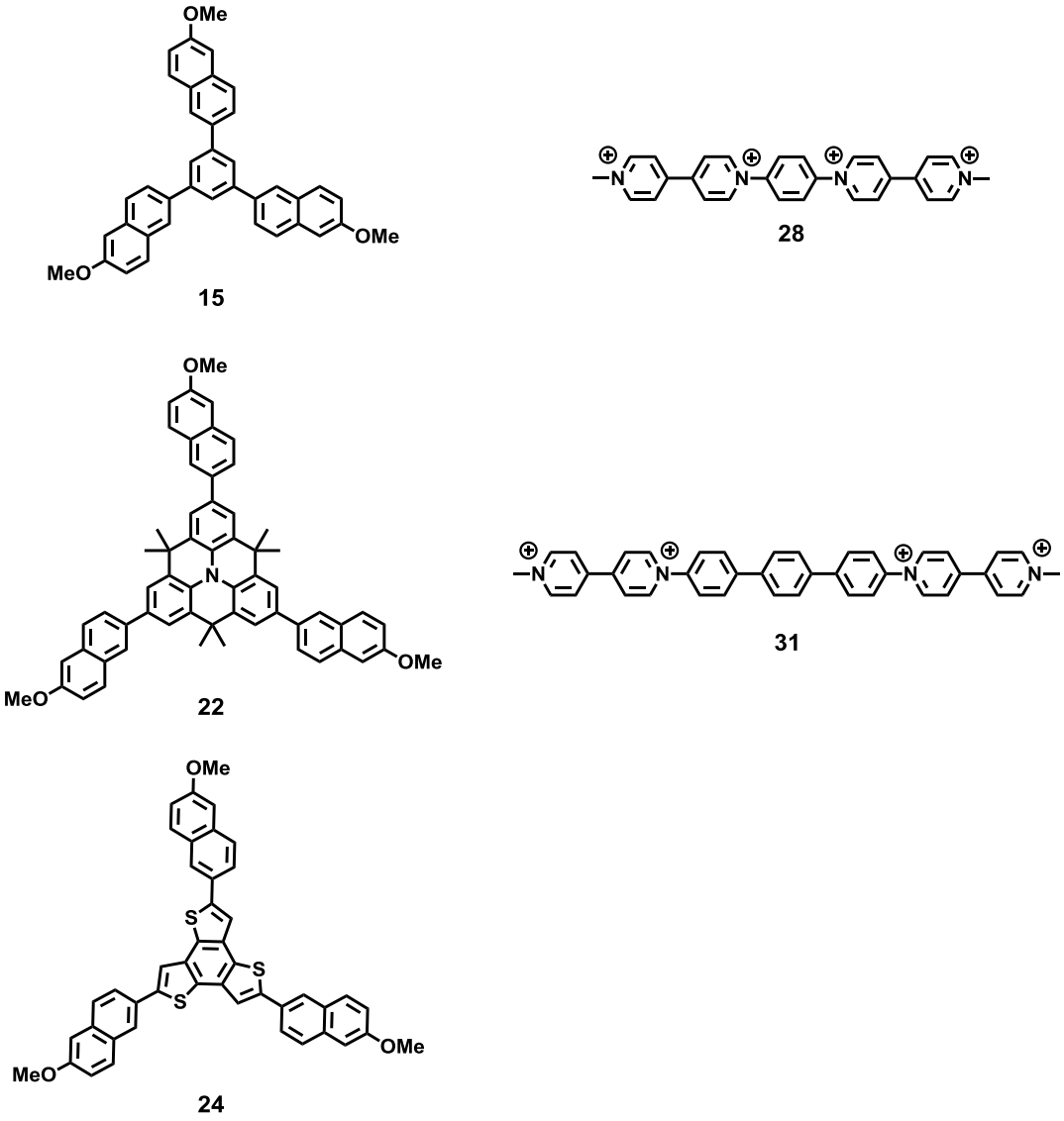

Scheme 4: Molecular structures of the donor molecules **15**, **22**, and **24** (left), and of the acceptor molecules **28**, and **31** (right).

Synthesis of Additional Donor and Acceptor Monomers

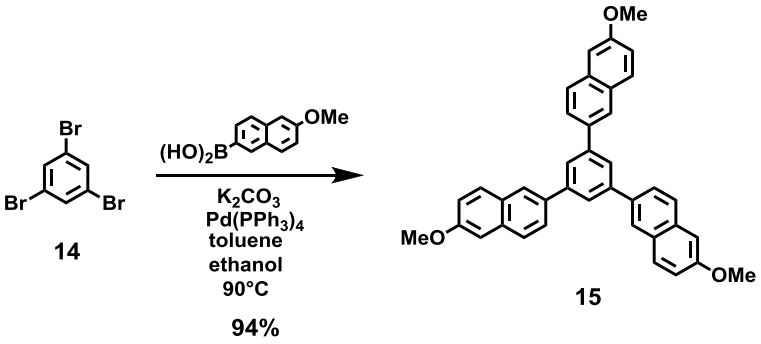

Scheme 5: Reaction scheme for the synthesis of the donor molecule **15**.

15 was synthesized as small donor molecule in one step with a Suzuki reaction of the commercially available compounds 6-methoxy-2-naphthaleneboronic acid and 1,3,5-tribromobenzene **14**. After purification, **15** was obtained in 94% (1.63 g) yield.

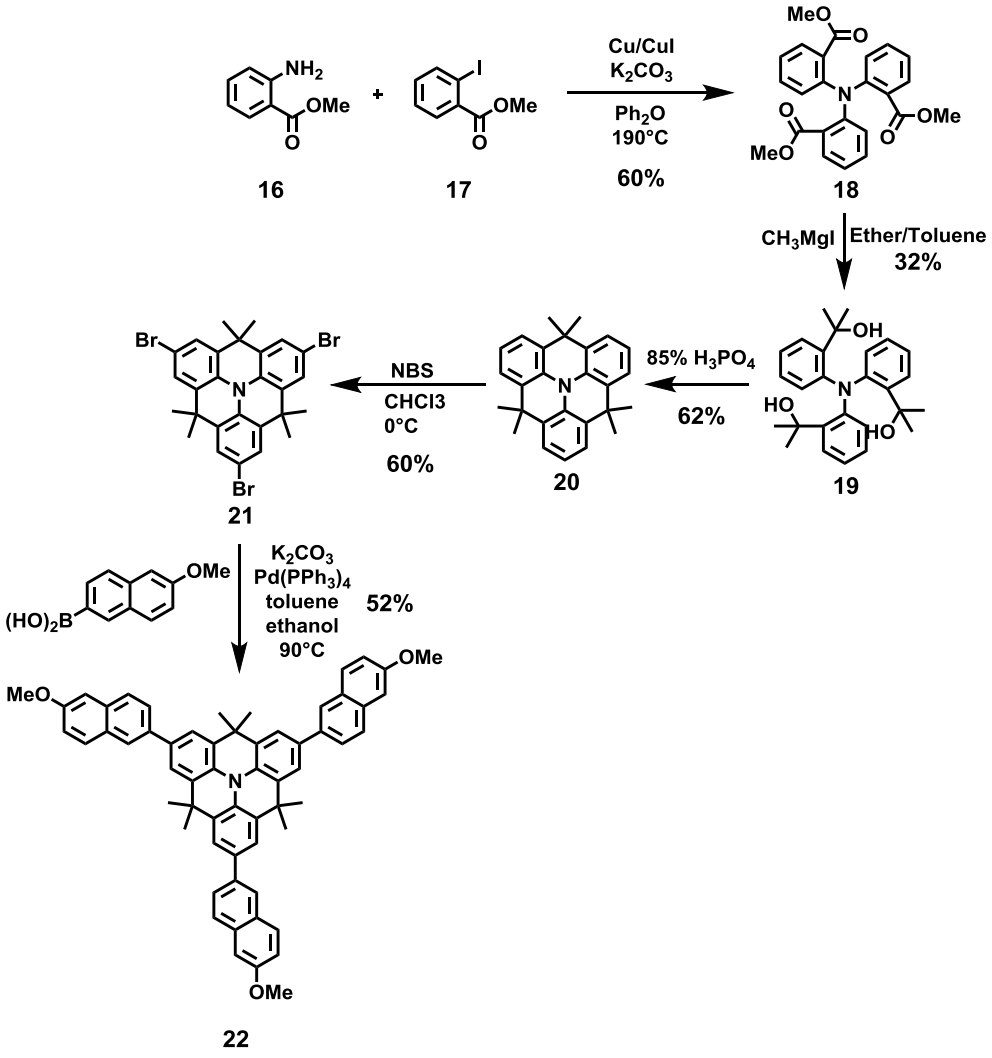

Scheme 6: Reaction scheme for the synthesis of the donor molecule **22**.

Triangulene **20** was synthesized after literature known procedure[123]. Starting from the commercially available **16** and **17**, an Ullmann reaction led to triester **18** in 60% yield (14.23 g). A subsequent Grignard reaction yielded triol **19** in 32% (1.45 g). Triangulene **20** was obtained by a cyclization reaction by means of orthophosphoric acid in yield of 62% (112 mg). Bromination of **20** with NBS gave tribromotriangulene **21** in 60% yield (106 mg). A Suzuki coupling with 6-methoxy-2-naphthaleneboronic acid as final step afforded the triangulene donor **22** in 52% yield (71.6 mg).

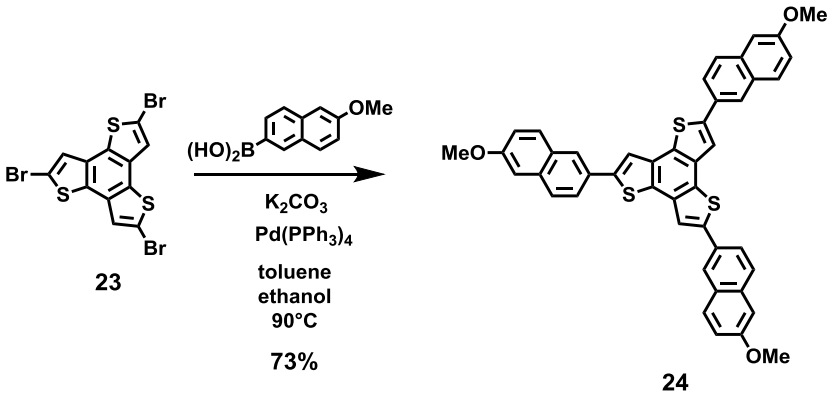

Scheme 7: Reaction scheme for the synthesis of the donor molecule **24**.

For the synthesis of **24** donor monomer, the precursor tribromo-substituted benzotrithiophene **23** was gratefully received from [redacted]. Further Suzuki coupling of **23** with commercially available 6-methoxy-2-naphthaleneboronic acid gave 108.27 mg **24** after column chromatography in 73% yield.

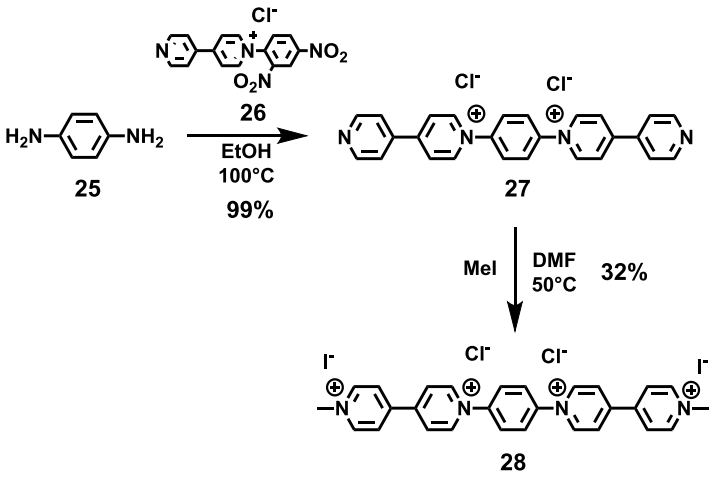

Scheme 8: Reaction scheme for the synthesis of the acceptor molecule **28**.

28 was synthesized starting from the commercially available 1,4-phenylenediamine **25**. 2,4-Dinitrophenyl-4,4'-bispyridinium chloride **26**, necessary for the reaction with 1,4-phenylenediamine was synthesized by electrophilic aromatic substitution of 4,4'-bipyridine with 2,4-dinitrochlorobenzene in 74% yield (8.2 g). The subsequent Zincke reaction of 1,4-phenylenediamine and **26** yielded **27** in 99% (5.92 g) yield. After the methylation of **27** by means of methyl iodide as final reaction step, **28** was isolated in 32% (2.14 g) yield by recrystallization from an acetonitrile/water mixture.

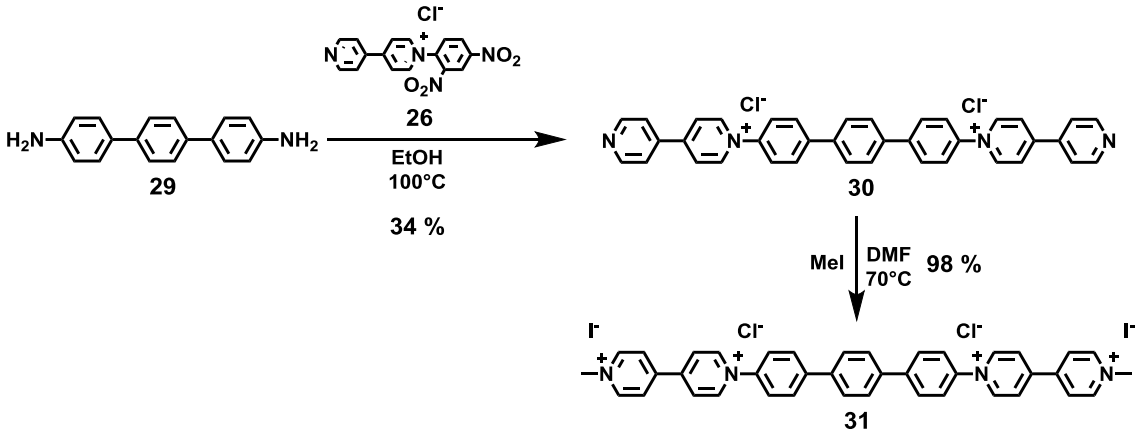

Scheme 9: Reaction scheme for the synthesis of the acceptor molecule **31**.

31 was synthesized as linear, fully conjugated acceptor compound, starting from the commercially available 4,4'-diamino-*p*-terphenyl **22**. The Zincke reaction of **22** with **20** yielded **23** in 34% (1.99 g). After the subsequent methylation of **23** with methyl iodide, 1.44 g (98%) of **31** were isolated as a dark-red powder by reprecipitation from DMF/Et_2O.

TEM Analysis of Processed Layers With Different Donor-Acceptor Combinations

Assemblies of the different combinations of acceptor and donor monomers with **CB[8]** were prepared according to the general procedure (2.2.2.2). In all cases, the solubility in water and toluene was sufficient for application at the established toluene-water interface. For all TEM measurements, Lacey carbon supported copper grids were provided as substrates to obtain information about the free-standing ability over different hole-sizes, indirectly indicating the stability of the supramolecular interaction.

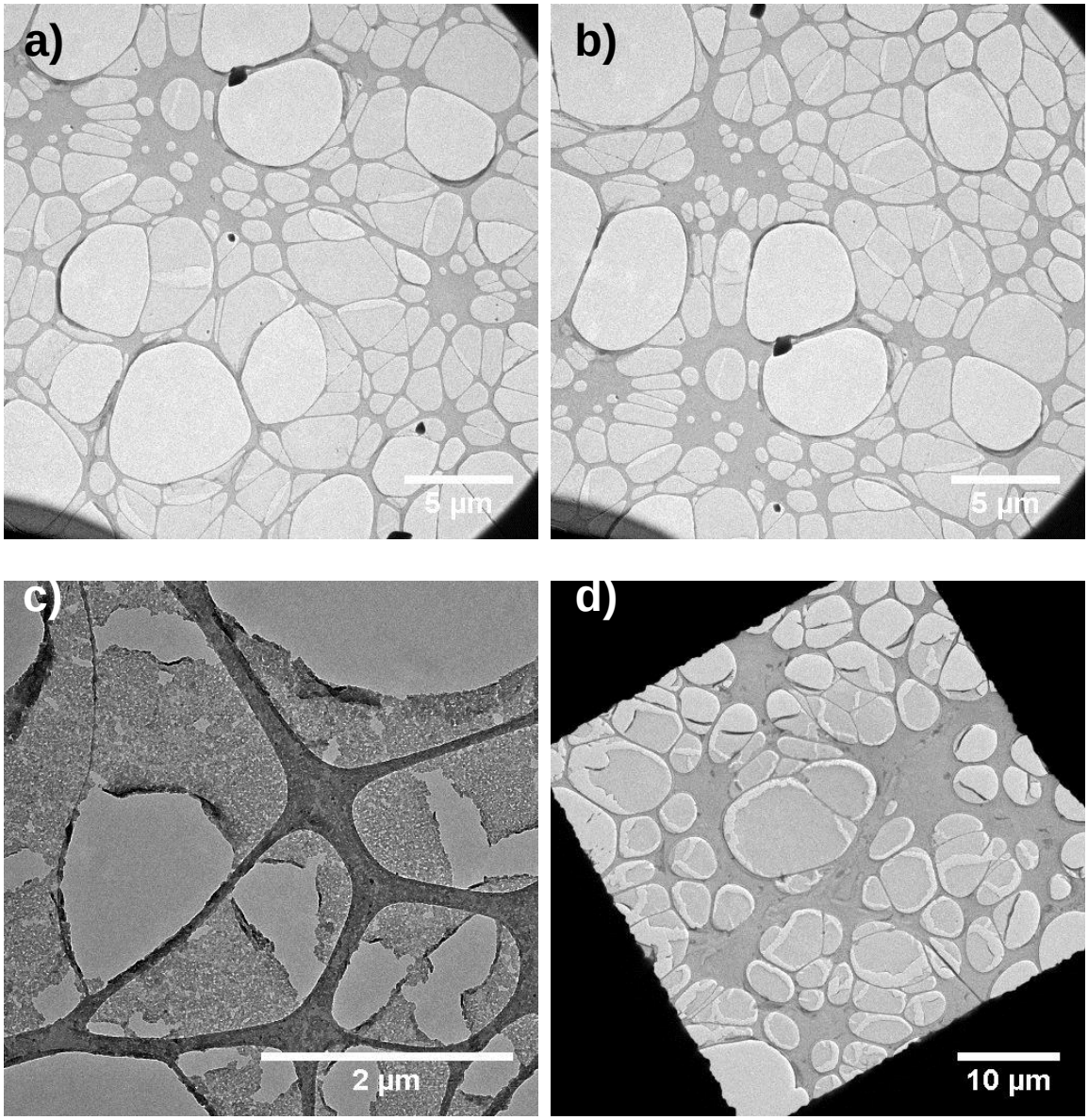

Figure 30: TEM-images of a) **28+CB[8]+15**, b) **28+CB[8]+13**, c) **28+CB[8]+22**, and d) **28+CB[8]+24**.

Monolayers were found for all combinations of different donor and acceptor molecules, judging by the absence of split edges. This assumption of present monolayer material was corroborated with additional AFM measurements of scratched monolayers on Si/SiO_2. TEM-measurements, however, revealed different stabilities of the layers when being free-standing over gaps of the copper grid supports, as well as different morphologies (Figure 30-Figure 32).

In Figure 30, the different combinations of donor molecules with **28+CB[8]** were illustrated. Both **28+CB[8]+15** (Figure 30a) and **28+CB[8]+13** (Figure 30b) achieved regularly arranged layers. Those covered gaps of up to ~4 µm² homogeneously. Holes being basically larger than that appeared empty, whereas rolled-up fragments were found around the edges, indicating a collapse of the layers. The small particles with a high contrast were assumed to be residual precursors. They can appear, as the washing procedure for free-standing monolayers has to be performed in a very mild way to prevent the fragile films from rupturing. The homogeneity of the sheets accounted for a regular order, however the higher fragility indicated a weaker supramolecular interaction than the one present in the case of **10+CB[8]+13** (Figure 22). In contrast to this regularity, **28+CB[8]+22** (Figure 30c) revealed small, randomly connected grains instead of providing a continuous layer. In between these grains, a high number of defects was visible, which indicated a limited internal order. The remaining donor in this ensemble gave films, which homogeneously covered Lacey carbon supports and were free-standing over gaps as big as 80 µm². The grid revealed some ruptures in the sheet of **28+CB[8]+24** (Figure 30d), occurring only at transitions to the carbon supports. These defects were presumably caused by solvent-induced shrinking within the drying process. This was indicated as the layer remained free-standing over the gaps of the support.

The layers obtained with the different donors in combination with **10+CB[8]** revealed a less ambiguous behavior. The already characterized combination of **10+CB[8]+13** was added for comparison with the remaining assemblies (Figure 31b). **10+CB[8]+15** (Figure 31a), **10+CB[8]+22** (Figure 31c), and **10+CB[8]+24** (Figure 31d) furnished sheets, significantly less stable than the benchmark of **10+CB[8]+13**, however quite similar to each other. The homogeneity was comparable with the ones in Figure 30a,b, and d, rather than the one of Figure 30c, and accounted for the presence of regular, but weak interactions. Among these layers, **10+CB[8]+22** produced the highest amount of ruptured layers, which are rolled up and cover only gaps up to 1 µm².

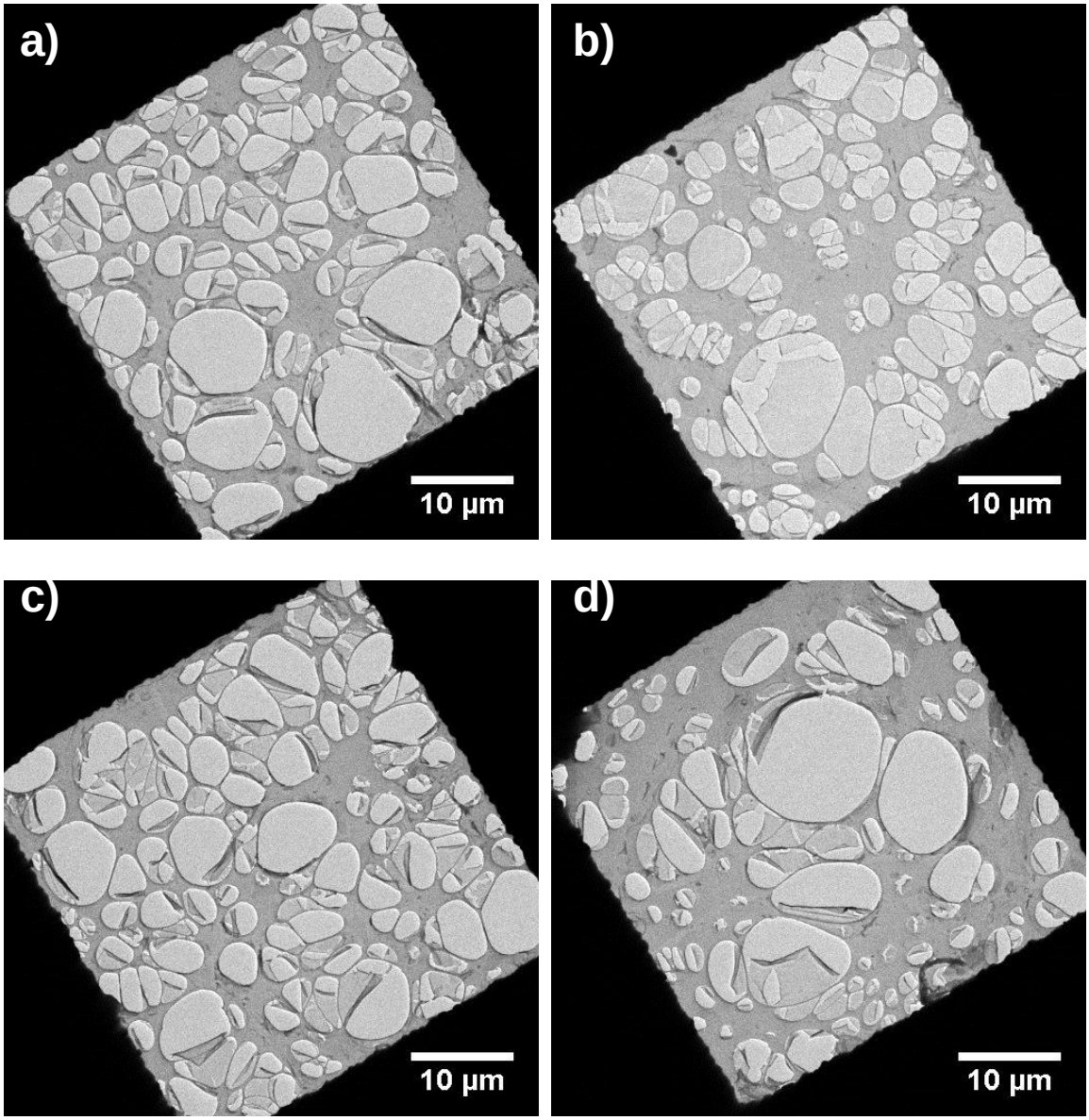

Figure 31: TEM-images of a) **10+CB[8]+15**, b) **10+CB[8]+13**, c) **10+CB[8]+22**, and d) **10+CB[8]+24**.

31+CB[8] as the remaining acceptor complex gave three different morphologies and therefore showed the highest diversity in combination with the different donor molecules. On the one hand, **31+CB[8]+15** (Figure 32a) and **31+CB[8]+13** (Figure 32b) both featured grainy structures with a high number of defects, appearing to be interconnected randomly to provide a certain stability to sustain over gaps of ~4 µm², although not homogeneously. **31+CB[8]+22** revealed sheets, comparable to those of **10+CB[8]+15** or **10+CB[8]+24** (Figure 31a or d) in terms of their free-standing ability (Figure 32c). In contrast, **31+CB[8]+24** (Figure 32d) showed remarkably large and

homogeneous layers, which free-standingly covered gaps of over ~80 µm², therefore measuring up with the combination of **28+CB[8]+24** (Figure 30d).

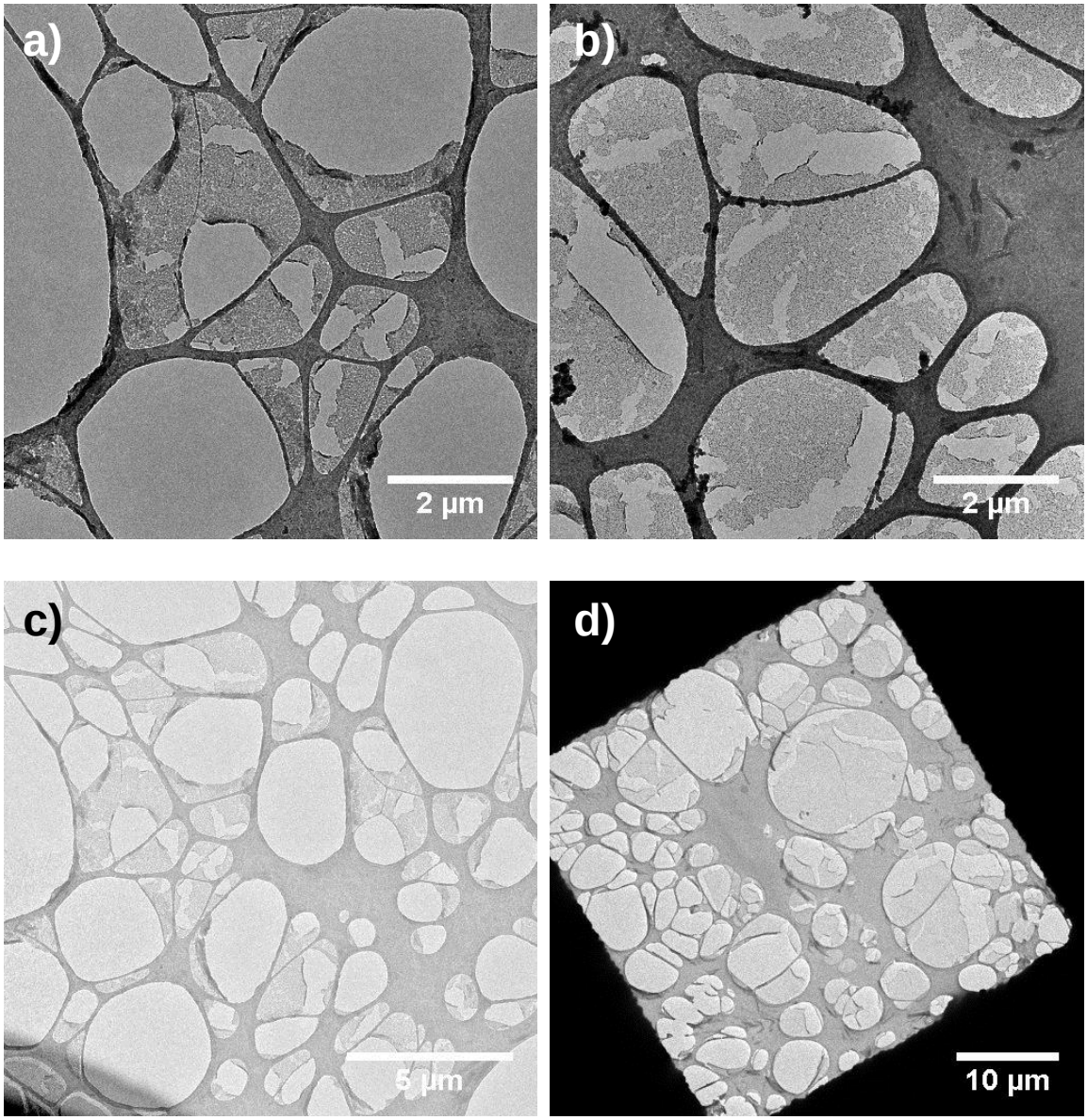

Figure 32: TEM-images of a) **31+CB[8]+15**, b) **31+CB[8]+13**, c) **31+CB[8]+22**, and d) **31+CB[8]+24**.

UV/Vis Measurements of Processed Layers With Different Donor-Acceptor Combinations

Samples for UV/Vis spectroscopy were prepared according to the elaborated procedure in 2.2.2.2. Quartz wafer pieces were provided as substrates. The solutions were let at rest for 24 h to produce thicker layers of polymer material. For comparison, the bare donor compounds and precomplexed acceptor molecules with **CB[8]** were drop-cast onto quartz wafers and measured. The measurements were carried out by solid-state reflectance in an integrating sphere to minimize scattering effects in accordance to the measurements in 2.2.2.4. For comparability, the spectra were normalized.

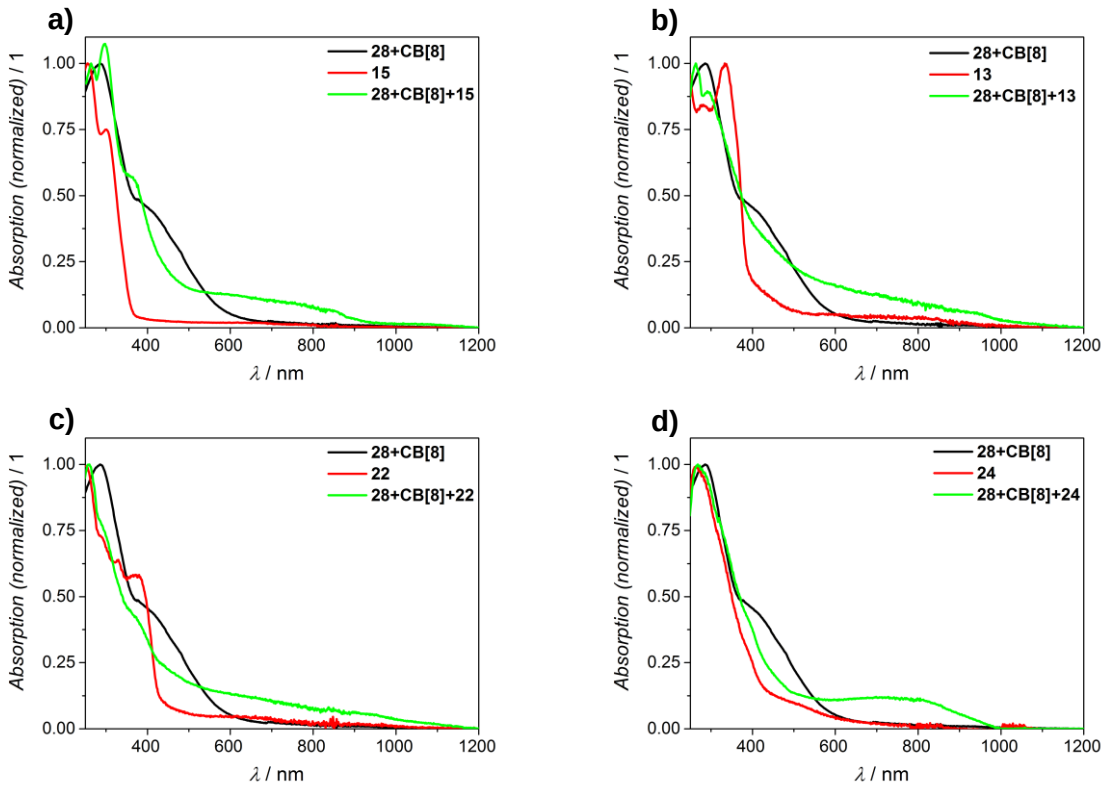

Figure 33: UV/Vis spectra of a) **28+CB[8]** (black), **15** (red), and **28+CB[8]+15** (green), b) **28+CB[8]** (black), **13** (red), and **28+CB[8]+13** (green), c) **28+CB[8]** (black), **22** (red), and **28+CB[8]+22** (green), d) **28+CB[8]** (black), **24** (red), and **28+CB[8]+24** (green).

The four combinations of donor molecules **13**, **15**, **22**, and **24** with **28+CB[8]** revealed superpositions of their monomeric units, however peaks were slightly shifted, therefore indicating certain interactions of the molecules (Figure 33). Furthermore, all spectra showed an enhanced absorption in the area between 400-1000 nm, which significantly

exceeded the shoulder of **28+CB[8]**, indicating a certain degree of self-assembly of the donor and acceptor groups in the cavity of **CB[8]**.[88] The assembly of **28+CB[8]+22** showed the least significant changes from a superposition of **22** with **28+CB[8]** and only a small enhancement in the region > 400 nm, therefore indicating the weakest assembly of these four donor molecules (Figure 33c).

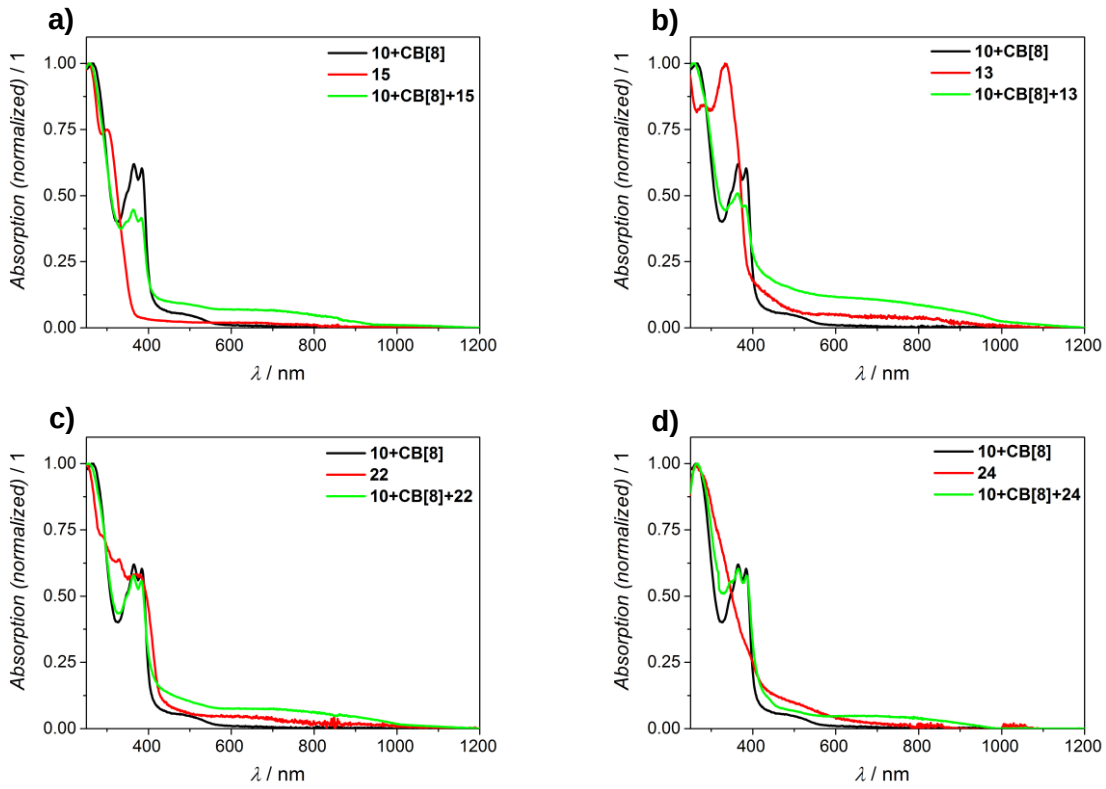

Figure 34: UV/Vis spectra of a) **10+CB[8]** (black), **15** (red), and **10+CB[8]+15** (green), b) **10+CB[8]** (black), **13** (red), and **10+CB[8]+13** (green), c) **10+CB[8]** (black), **22** (red), and **10+CB[8]+22** (green), d) **10+CB[8]** (black), **24** (red), and **10+CB[8]+24** (green).

Complexes of **15**, **22**, and **24** with **10+CB[8]** in Figure 34 exhibited similar characteristics as the assembly of **28+CB[8]+22**. Therefore, they furnished superpositions of their monomeric compounds with minor peak shifts accompanying an enhanced absorption in the range > 400 nm, however less significant as visible e.g. in Figure 34d. **13** showed a slightly higher absorption in the area of 400-1000 nm, suggesting a similar degree of interaction as **28+CB[8]+15**. In all four cases, the characteristic naphthalene diimide absorption at ~400 nm remained unshifted, providing proof for the nonexistence of a generally possible complexation with the naphthalene diimide core. Therefore and consistent with previous measurements and

the literature, the enhanced broad absorption > 400 nm indicates successful complexations of each combination.

Combinations of **13**, **15**, **22**, and **24** with **31+CB[8]** are visible in Figure 35. The spectra corroborate the diverging behavior of **31**, as already discovered in TEM measurements. Therefore, the three combinations with **13**, **15**, and **22** produced layers with a high fragility. In their UV/Vis spectra, only slightly increased absorptions in the area between 400-1000 nm were visible. In contrast, the combination with **24** unambiguously provides a significant and broad absorption between 500-1000 nm, indicating a strong interaction with **CB[8]**. Although still broader than the absorption visible in the assembly in aqueous solution, this peak with λ_{max} = 698 nm appeared with a bathochromic shift compared to the one in solution at λ_{max} = 617 nm. This effect could either be caused by a higher conjugation of the monomers, or a stronger intermolecular interaction.

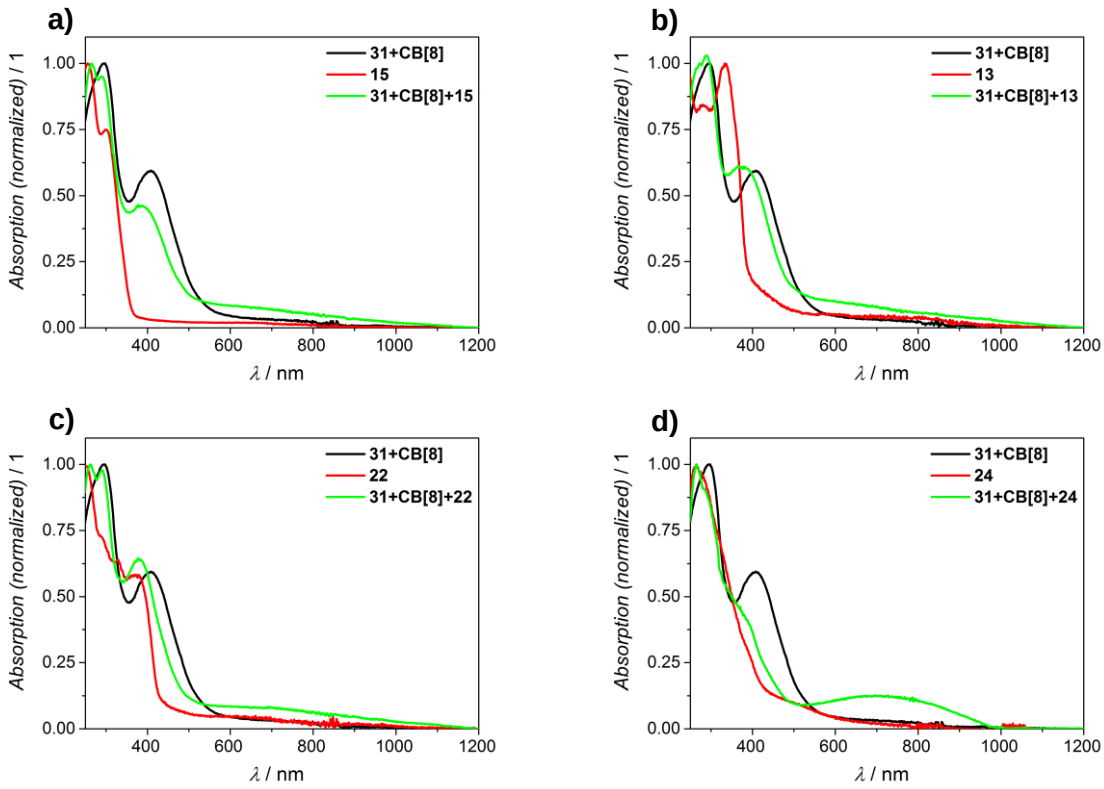

Figure 35: UV/Vis spectra of a) **31+CB[8]** (black), **15** (red), and **31+CB[8]+15** (green), b) **31+CB[8]** (black), **13** (red), and **31+CB[8]+13** (green), c) **31+CB[8]** (black), **22** (red), and **31+CB[8]+22** (green), d) **31+CB[8]** (black), **24** (red), and **31+CB[8]+24** (green), respectively. .

Remarkably, the combinations revealing larger and more homogeneous monolayers under TEM measurements provided more distinct absorptions in the area between 400-1000 nm. This corroborated the additional UV/Vis absorptions of the complexes in this area to correlate with the strength of complexation of the respective donor and acceptor molecule with **CB[8]**.

GIWAXS Measurements of Processed Layers With Different Donor-Acceptor Combinations

Self-assembled multilayers of the different donor and acceptor combinations with **CB[8]** were prepared by resting the aqueous solution of acceptor molecules with **CB[8]** and subsequently being overlayed with the donor monomers in toluene for 7 d. The prepared layers were processed onto SiO_2/Si wafer pieces by horizontal deposition and featured thicknesses between 90-140 nm. The layers were subsequently analyzed by GIWAXS measurements in collaboration with [redacted], using Synchotron irradiation at the DELTA beamline from TU Dortmund. The diffraction patterns of the measured combinations are shown in Figure 36 - Figure 38. Below each pattern, the one-dimensional horizontal and meridional integrations are plotted.

Figure 36 includes the combinations of the different donor monomers **15**, **13**, **22**, and **24** with **28** and **CB[8]**. These combinations revealed defined diffraction patterns of the measured materials, indicating the presence of a high order in the material. In the appearance and intensity of signals, minor differences were visible. While **28+CB[8]+24** (Figure 36d) showed the most distinct as well as the highest number of signals, **28+CB[8]+15** (Figure 36a) and **28+CB[8]+13** (Figure 36b) appeared with a slightly lower intensity. As the latter materials both still revealed a high number of defined diffractions and no amorphous areas, the difference in intensities presumably resulted from different layer thicknesses, taking into account the direct proportionality of the material's thickness and the signal intensity. In addition to a number of distinct peaks, **28+CB[8]+22** (Figure 36c) showed an amorphous halo in the range between q = 1.2-2.0 $Å^{-1}$. This demonstrated the presence of both an ordered, crystalline area as well as an amorphous region. Such behavior could generally be caused by two different reasons. On the one hand, residual precursor material, which was found not to produce a regular order under the applied conditions, could remain on the surface.

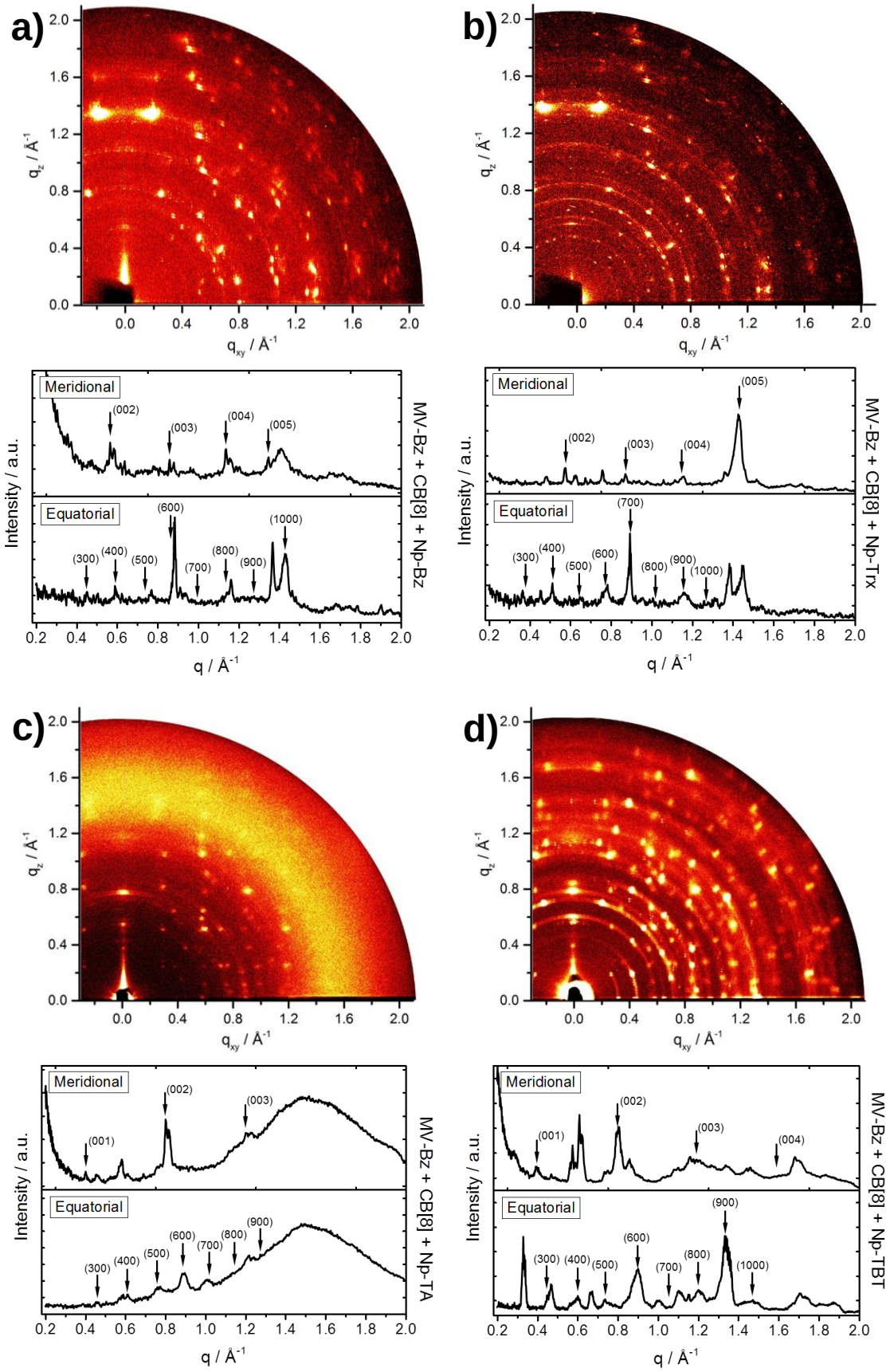

Figure 36: GIWAXS pattern and the respective meridional and equatorial integrations of a) **28+CB[8]+15**, b) **28+CB[8]+13**, c) **28+CB[8]+22**, and d) **28+CB[8]+24**.

As further washing did not change this result, an incomplete complexation was assumed to cause the halo. The regularly assembling solutions then provided the crystalline areas, whereas randomly appearing grain boundaries or small flakes produced amorphous regions. The TEM analysis in Figure 30 corroborated an incomplete complexation, as numerous individual flakes were visible rather than a continuous layer.

Figure 37 shows the GIWAXS pattern of the donor monomers with **10** and **CB[8]**. The GIWAXS pattern of **10+CB[8]+13** from Figure 29 is included in Figure 37b to simplify comparison between the pattern. Apart from the combination of **10+CB[8]+13**, revealing a high number of distinct and intense diffractions, all other combinations revealed low signal-to-noise ratios and only few defined peaks. Within these, **10+CB[8]+15** (Figure 37a) still showed a number of signals also found in the combination **10+CB[8]+13**, which were more diffuse in the case of **10+CB[8]+24** (Figure 37d), and were barely visible for **10+CB[8]+22** (Figure 37c). Remarkably, although the diffraction patterns bore a high signal-to-noise ratio over the whole detector area, the equatorial plane in each case exhibited a higher number of distinct reflections. This behavior accounted for a regular sheet-like structure, although with a certain amount of disorder in the basal plane. This disorder could be explained by the flexible ethylene spacers between the naphthalene diimide spacer and the acceptor moieties in the periphery of **10**. The exceptional case of **10+CB[8]+13**, however, presumably appeared due to different stacking by performing a layer-by-layer deposition (as described in 2.2.2.4) instead of a long-time assembly at the interface. The diffraction pattern of the donor monomers with **31** and **CB[8]** are depicted in Figure 38. In case of **31+CB[8]+24** (Figure 38d) a high number of intensive and defined signals was obtained, comparable to the combination of **28+CB[8]+24** (Figure 36d). Although the signal-to-noise ratio of **31+CB[8]+22** was quite low (Figure 38c), a high number of distinct reflections was visible. **31+CB[8]+15** (Figure 38a) and **31+CB[8]+13** (Figure 38b) showed similarities to **28+CB[8]+22** (Figure 36c) with a number of defined signals additionally to an overlayed, intensive signal. In these two cases, the overlaying signals appeared not to be amorphous, but rather revealed spherical segments in the q_{xy}-direction. These two different kinds of signals indicated two packing behaviors. The spherical segments corresponded to a columnar stacking in the substrate's plane with a short-range order, whereas the underlying, defined signals rather related to a crystalline packing of the material.

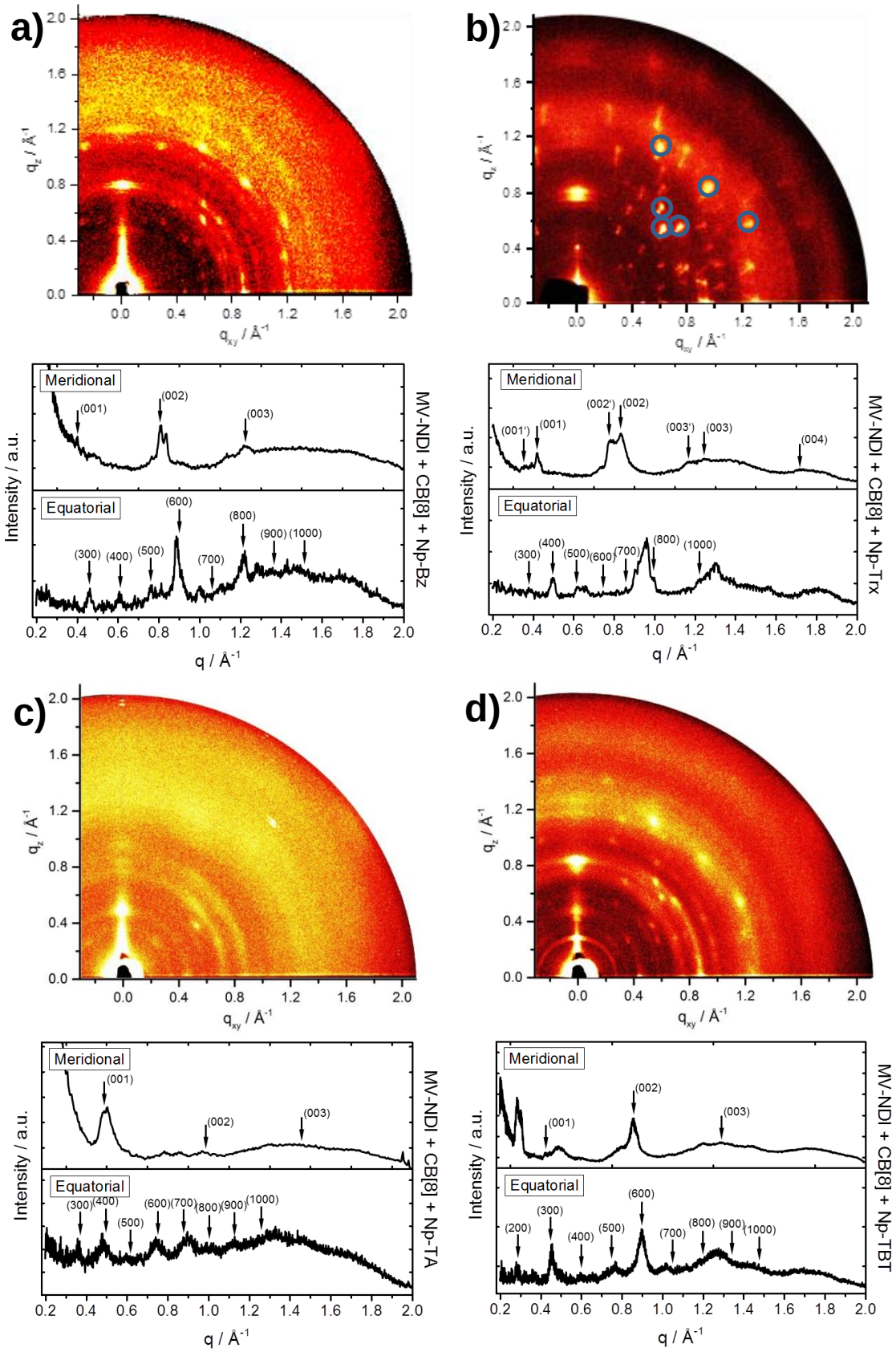

Figure 37: GIWAXS pattern and respective meridional and equatorial integrations of a) **10+CB[8]+15**, b) **10+CB[8]+13**, c) **10+CB[8]+22**, d) **10+CB[8]+24**. The six highlighted signals in b) can be found in each other spectrum.

With regard to the assumption made for the pattern of **28+CB[8]+22**, the incomplete complexation to small-area flakes was explained by the calculated dihedral angle of 9.2 between the planes of the acceptor moieties of each end of **31**. Therefore, the combination of **31+CB[8]+**donor molecule had to provide a sufficient flexibility of the backbone to compensate the 9.2° torsion between each polymerization to stay in plane. If the backbone was too rigid, as it was assumed to be the case of the small **15** and **13**, the assembly stops after small flakes, as an out-of-plane polymerization was prevented by the interface. The TEM-images in Figure 32 showed the same behavior as **28+CB[8]+22**, confirming this assumption. The visibility of spherical reflections in the basal planes instead of an amorphous halo accounted for a columnar stacking of terminal **31** with other **31** units. Such columnar stacking was already reported for aromatic molecules with an ionic periphery.[124-125]

With crystalline material exhibiting a high number of intensive elliptical reflections in GIWAXS patterns, it was possible to evaluate the relative crystallinity between the different donor-acceptor-**CB[8]** combinations. The lowest intensity and number of distinct diffractions was visible with the combination **10+CB[8]+22** (Figure 29c). Its diffraction pattern mainly revealed peaks in the meridional plane, and only a few broad and weak signals in the remaining pattern, leaving a majority of the material to follow no particular order in the basal plane. A slightly higher crystallinity was obtained in the cases of **10+CB[8]+15**, **10+CB[8]+22**, **10+CB[8]+24**, and **31+CB[8]+13**, revealing a number of distinct reflections, which already indicated a regular arrangement of the majority of molecules inside the material. This degree of crystallinity was however exceeded by those patterns obtained from **31+CB[8]+15**, **31+CB[8]+22**, and **28+CB[8]+22**. With their reflections bearing an increased intensity and being more narrow, analysis of these peaks was possible with a higher accuracy. The remaining patterns of **28+CB[8]+15**, **28+CB[8]+13**, **28+CB[8]+24**, **10+CB[8]+13**, and **31+CB[8]+24** however featured a remarkably high number of defined diffractions, accounting for a high crystallinity. Notably, in all diffraction patterns, six signals were visible at the same positions (exemplarily highlighted in Figure 37b), namely at (q,φ) = (1.247 $Å^{-1}$,27.7°); (1.236 $Å^{-1}$,47.7°); (1.316 $Å^{-1}$,65.3°); (0.903 $Å^{-1}$,40.4°); (0.806 $Å^{-1}$,47.7°); (0.904 $Å^{-1}$,53.0°).

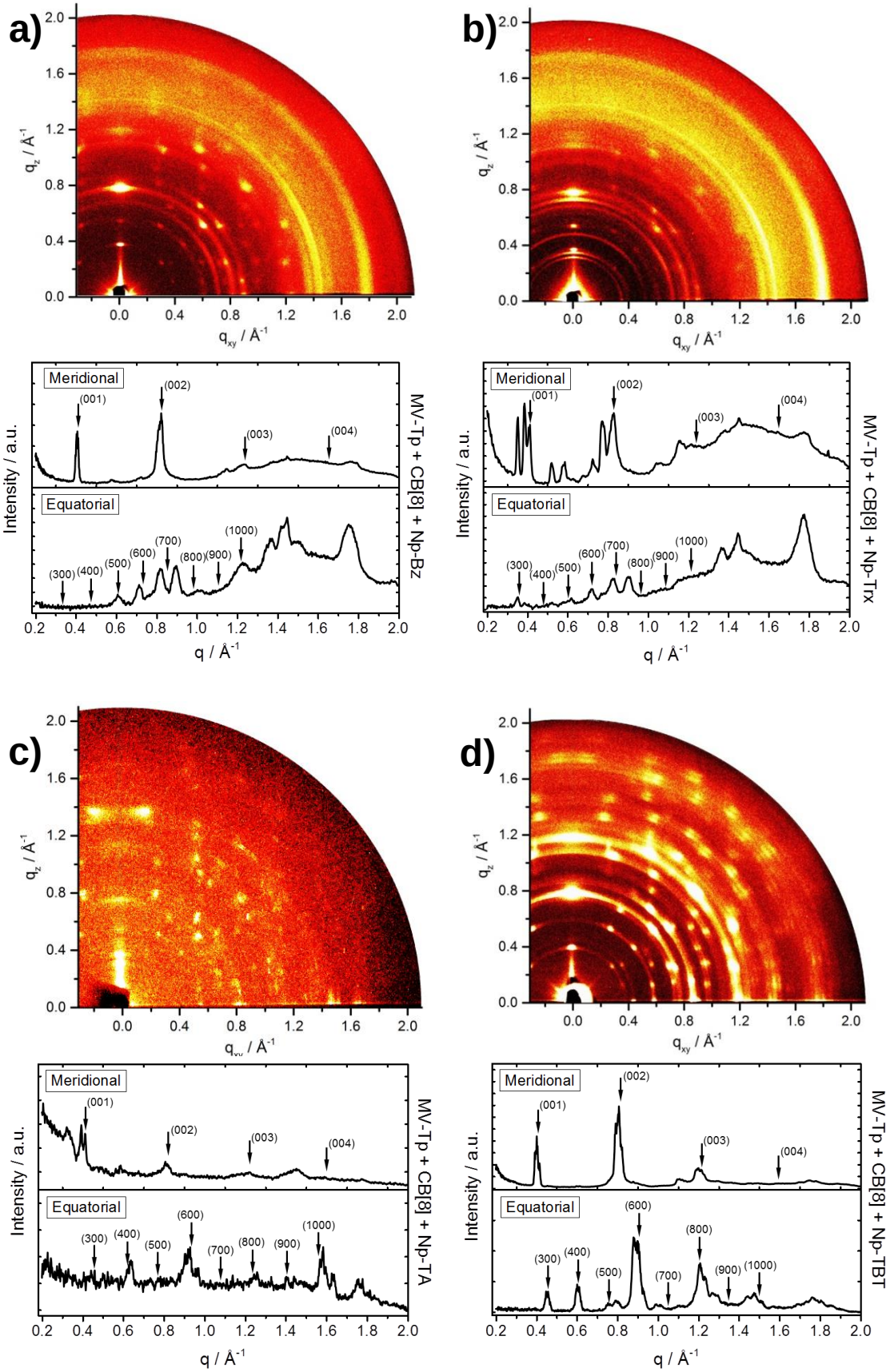

Figure 38: GIWAXS pattern and the respective meridional and equatorial integrations of a) **31+CB[8]+15**, b) **31+CB[8]+13**, c) **31+CB[8]+22**, and d) **31+CB[8]+24**.

As these peaks were visible in all cases, whereas the rest of the signals changed, they had to result either from intramolecular distances in the **CB[8]** ring, from the donor- and acceptor moieties, or from the host-guest enhanced donor-acceptor complex. However, the complexity of the structure left too many possibilities to correlate these diffractions to different regularly reoccurring distances, making it unfeasible to assign the signals unambiguously. Nevertheless, as these particular reflections only occurred in the obtained 2DSPs and were not visible in the monomer diffraction pattern, they could be used as indication for a successful complexation. Having judged the qualitative appearance of the patterns, the obtained crystallinity of the 2DSPs seemed to have a correlation with the applied structures. The assemblies with **22** as donor molecule exhibited lower orders than **13** or **15**, and **24** appeared to be the best donor molecule to promote crystallinity, notwithstanding the lower order of the combination of **24** with **10**. The latter exhibited a significant be influence by the acceptor molecule **10**, which is expected to result in a lower crystallinity regarding its flexible ethylene spacers compared to the unflexible **31** and **28**. The limited flake size and molecular order in case of **31** was expected to be a result of its slightly twisted molecular structure. In contrast, **28** was calculated to furnish a completely planar structure for facilitating planarity and prevent out-of-plane polymerization, therefore enhancing the general order of the assembly.

According to the GIWAXS analysis of **10+CB[8]+13**, information about the packing behavior was obtained by fitting theoretical peak distributions, based on the Bragg equation, to one-dimensional integrations of the equatorial and the meridional plane. For all combinations of **28**, **10**, **31** with **15**, **13**, **22**, **24** in **CB[8]**, except for **28+CB[8]+15** and **28+CB[8]+13**, the reflections in the meridional plane were in accordance to a lamellar structure with equidistant signals with *d*-spacings of 1.48 nm, corresponding to Bernal-stacked arrangement of the individual sheets (Figure 36c,d, Figure 37 - Figure 38, top plots) and suggesting an interlayer distance of 1.48 nm. **28+CB[8]+15** and **28+CB[8]+13** featured a lamellar structure as well, however with a *d*-spacing of 2.20 nm (Figure 36a,b). This interlayer distance was assigned to an arrangement of **CB[8]** not intercalating and not being shifted, but rather standing edge-on-edge on each other. As this only appeared utilizing **28** as acceptor monomer, the latter presumably decreased the available space of the hexagonal structure with small **15** and medium sized **13** so far, that the **CB[8]** molecules were not able to intercalate by shifting the layers. In all cases, however, signal splitting occurred also in the case of **10+CB[8]+13**, indicating the deformation of **CB[8]** as a result of complexing with the donor and acceptor moieties.

Additionally to the presence of a layered structure, all combinations of **28**, **10**, **31** with **15**, **13**, **22**, **Tp-TBT** in **CB[8]** revealed a good match with theoretical peak distributions of a 2D hexagonal cell to the integration of the respective equatorial plane (Figure 36 - Figure 38, bottom plots), indicating a hexagonal arrangement in-plane. The cell parameters were in accordance to considerations regarding the sizes of particular precursors. The resulting lattice parameters are displayed in Table 1. Therefore, the cell parameters followed the sizes of the monomers, namely **13** and **31** as largest molecules giving the largest unit cell parameter. The only exception from these values appeared to be **10+CB[8]+22**, however it has to be mentioned that its parameter has the highest uncertainty due to the diffuse signals.

Table 1: Unit cell parameters of different D-A-CB[8] combinations.

Unit cell parameter [nm]	13	24	22	15
31	6.43	6.27	6.07	5.85
10	5.68	5.41	5.59	5.29
28	4.98	4.82	4.78	4.66

Although different unit cell parameters were obtained from relatively homogeneous structures, which can be synonymous for the presence of a nanoporous structure, the differences in morphology and stability of the TEM measurements assessed not all of these structures being applicable for future use in e.g. size-excluding filters. Therefore, the grainy structure found for **28+CB[8]+22**, **31+CB[8]+15**, and **31+CB[8]+13** featured too many defects between the intrinsically ordered grains for a separation of e.g. quantum dots. Further, the elaborated protocol is applicable for quite a number of different donor-acceptor combinations.

2.2.3. Assembly at the Air-Water Interface

Considering the successful self-assembly of different host-guest enhanced donor-acceptor interactions in water, the formation of stable monolayers over large areas > 20 cm² and related processing procedures still remained elusive. To allow for the formation of larger structures, the system was applied to an air-water interface for assembly. This interface was reported as a 2D template promoting the self-sorting of molecules only along the interface, and at the same time increasing the stability of a 2D structure due to adsorption. According to literature, the air-water interface offers separation between the phases superior to liquid-liquid interfaces[38] and was therefore expected to pave the way for obtaining large monolayers of a host-guest enhanced donor-acceptor interaction.

Although the results obtained from the assembly at the toluene-water interface exceeded the state of art of 2DSPs without using transition metals, the versatility to preadjust the lateral surface pressure of the monomers and beyond that the possibility to extend the lateral dimensions of self-assembled monolayers advocated the utilization of an air-water Langmuir-Blodgett trough.

Initial experiments were performed, trying to deposit the assembled layers of water-soluble **10+CB[8]+7** from a solution of water:methanol = 1:5 onto an air-water interface according to reported attempts with graphene oxide.[126] However, no increase in the surface pressure was observable, probably as a result of diffusion of the layers into the aqueous subphase considering their water-solubility. Further attempts based on the assembly of **10+CB[8]** and **13**, **24**, or **15** at the air-water interface did not succeed as well and suggested different reasons for the absence of self-assembly. Assuming a favored face-on orientation of donor molecules onto the water surface representing a critical point for the successful toluene-water interface approach, the aromatic donor core was considered to be too hydrophobic. Thus the repulsive interactions between the donor molecules and the water surface were expected to spatially prevent self-assembly of the overlayed donor molecules with the acceptor molecules in the subphase. Furthermore, the columnar stacking of donor monomers on top of aqueous solution as suggested for **13** could prevent the self-assembly of the donor monomers **24** and **15** as well. As both reasons can be traced back to the aromaticity of the core, the rational solution was an introduction of polarity to the aromatic core. The latter still had to feature all relevant properties like insolubility in water, planarity, C_3-symmetry, and the ability to enhance the donor effect of the 6-methoxynaphthyl units, while at the same time providing an increased affinity to water. The already synthesized **22**,

although featuring the least order of the resulting 2DSPs according to GIWAXS measurements in 2.2.2.5, but possessing an electron-donating triangulene core, complied with these requirements, whereby the dipole moment induced by the nitrogen at the center of the triangulene was expected to provide an increased interaction with water.

2.2.3.1. General Procedure for the Self-Assembly of Monolayers at the Air-Water Interface

The Langmuir-Blodgett trough was equipped with a Wilhelmy balance to measure the surface tension during the assembly process. With open barriers, the Teflon trough was filled with ultrapure water as subphase. 500 µL of a solution of **22** in toluene (c_{22} = 5.00·10^{-5} mol·L^{-1}) was distributed dropwise over the aqueous subphase, while after each drop complete toluene evaporation was awaited. Subsequently, the barriers were closed until the surface pressure reached a constant value of 3 mN·m^{-1}.

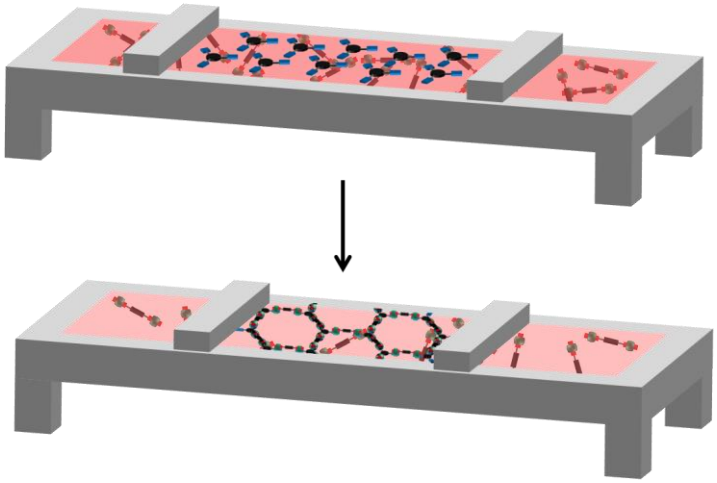

Figure 39: Schematic representation of an assembly experiment at the air-water interface of a Langmuir-Blodgett trough. Top: Distribution of the donor monomer **22** from toluene on top of the aqueous solution of **10+CB[8]**. Bottom: Assembled layer of **10+CB[8]+22** on top of the aqueous subphase after closing the barrier to a surface pressure of 30 mN·m^{-1}

The position of the barriers was held stationary and 15 mL of a preassembled aqueous solution of **CB[8]** ($c_{CB[8]}$ = 2.00·10^{-4} mol/L) and **10** (c_{10} = 1.00·10^{-4} mol·L^{-1}) were injected

into the subphase (Figure 39, top). The surface pressure increased to a constant value of 8.8 $mN \cdot m^{-1}$ during an assembly time of 20 h and subsequently stagnated. After further compressing the assembled layer to 30 $mN \cdot m^{-1}$ (Figure 39, bottom), the aqueous solution was subsequently drained through the bottom, enabling a horizontal deposition of the layer onto a variety of substrates. Eventually, the processed substrates were washed two times with water, ethanol, toluene, and again ethanol.

2.2.3.2. TEM Measurements of Monolayers from the Air-Water Interface

Layers of **10+CB[8]+22** were deposited on Lacey carbon supported grids and analyzed by TEM. Homogeneous layers were visible, covering large areas of the grid revealing a certain fragility, as they did not seem able to be freestanding over gaps of 5 μm^2. Although the homogeneity of the layers appeared to be marginally higher than the one obtained from the toluene-water interface (Figure 31c), the stability could not be enhanced. This corroborated the fragility of the sheets and their rupturing over gaps of 5 μm^2 to originate from intrinsic properties like the limited strength of this particular D-A-CB[8] supramolecular interaction, as already suggested in 2.2.2.5.

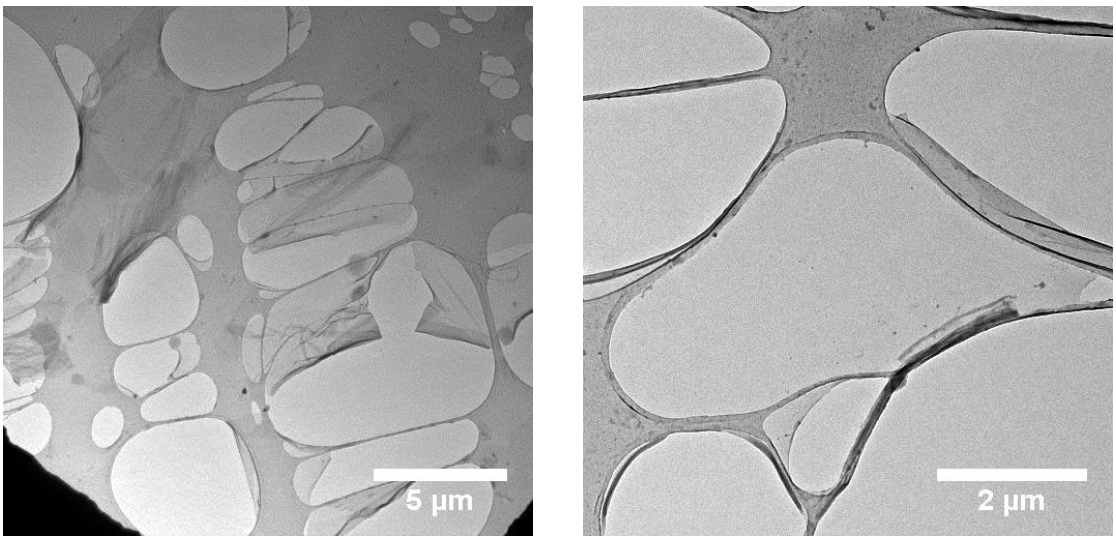

Figure 40: TEM pictures of layers of **10+CB[8]+22** deposited from the air-water interface onto a Lacey carbon grid.

2.2.3.3. *Wear Resistance Measurement of a Si/SiO_2-Wafer Surface Coated with a Self-Assembled Monolayer from the Air-Water Interface*

Friction experiments were performed on a monolayer of **10+CB[8]+22** on Si/SiO_2 following literature known procedures.[127-128] Thus, the AFM device was set to contact mode and a series of measurements was carried out on a small area. The force of the cantilever pressing on top of the layers' surface was controlled with the deflection setpoint. After 100 measurement cycles, a larger area of the surface was scanned in tapping mode, containing the scratched area in direct comparison with its unaltered surrounding (Figure 41a-d). Applying a force of 10 nN, the scratched area showed a complete cleavage of the layer. The height difference of 2.0 nm corroborated the completeness of scratching through the whole layer. A similar effect was visible with a deflection setpoint of 5 nN, revealing a significant damage of the layer. In this case, although residues on the bottom of the scratched area in combination with a smaller height difference of 1.7 nm could be found, a complete removing of the film was assumed. The blur in both cases indicated an abrasive behavior of the surface to the cantilever tip, which was corroborated by scanning electron microscopy (SEM) (Figure 41e). Nevertheless, the resolution of the damaged tip was still sufficient to visualize the abrasive behavior. Reducing the deflection point to 1 nN resulted in a significantly minor damage to the coating. Instead of scratching the whole area, only seven lines with a height difference of 1.0 nm appeared after the measurement. Even further reduction of the deflection setpoint to 0.2 nN did not result in completely undamaged layers from scratching, suggesting a very low wear resistance of this material. Although in the last case only three damaged lines were visible, the applicability for this material in terms of its mechanical stability is improbable, considering comparable coatings with conventional polymers like polystyrene or polyethylene showing wear resistances up to 85 nN.[127-128]

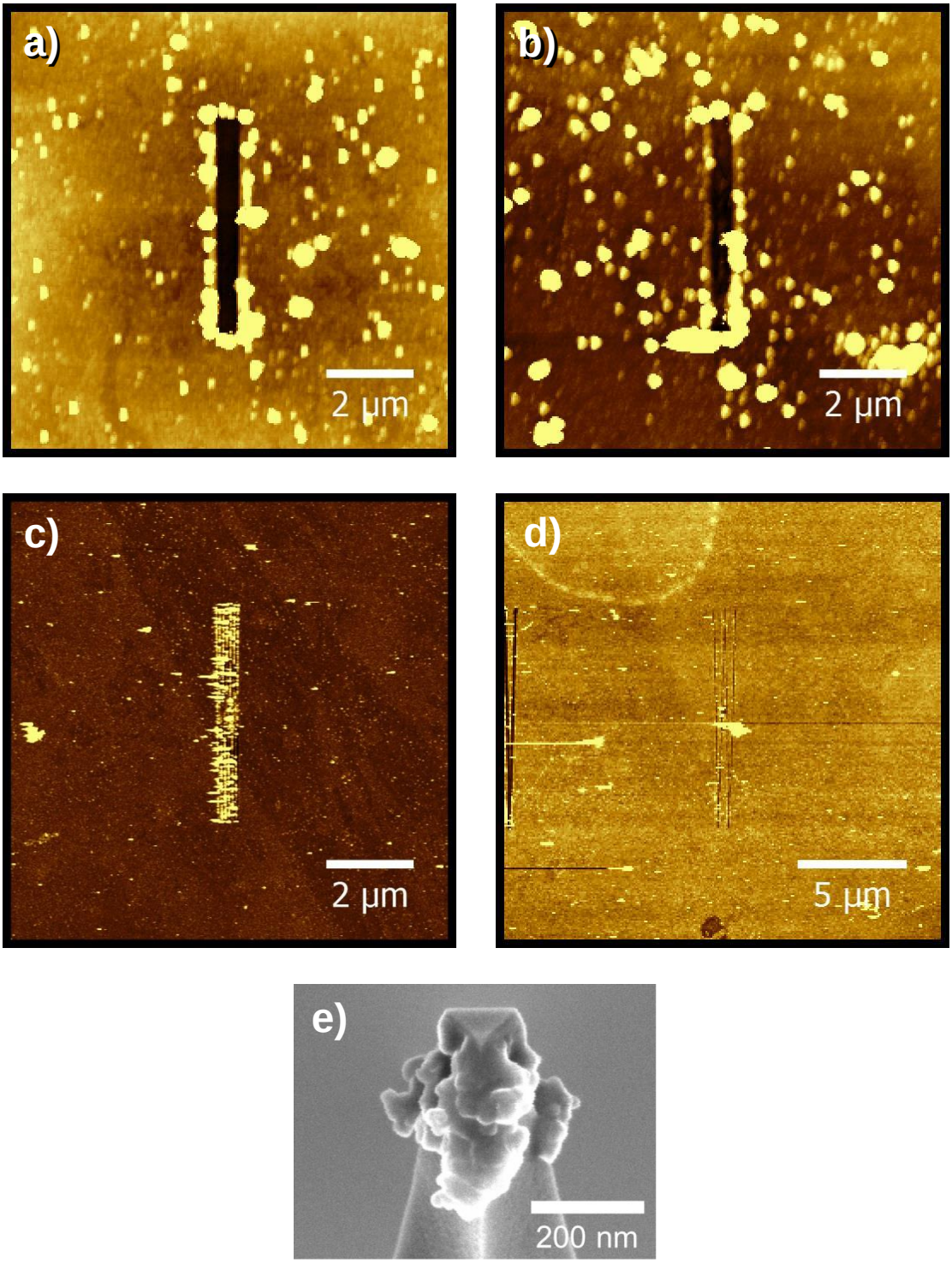

Figure 41: a-d) Tapping mode AFM pictures of a layer of **10+CB[8]+22** after scratching with a cantilever tip with different deflection setpoints. The respective deflection setpoints were a) 100 nm, b) 50 nm, c) 1 nm, d) 0.2 nm. e) exemplarily shows a SEM image of a scraped off cantilever tip after a scratching experiment, which is the reason for the blurry pictures in a) and b), respectively.

2.2.4. Summary

In this project, a reliable procedure for the formation of 2DSPs using host-guest enhanced donor-acceptor interactions was elaborated. However, missing a protocol for analyzing 2DSPs, obtained results had to be validated in comparison with literature known characteristics. Initial experiments with water-soluble monomers in water were thus performed to obtain a transition from the analytical behavior reported for isolated D-A-CB[8] complexes to the behavior of such interactions when used as polymerization motif. NMR, UV/Vis, and PL studies each revealed a peak behavior, which was traced back to a successful complexation of CB[8] with both donor and acceptor moieties inside the cavity. Furthermore, DLS measurements, OM, and TEM analysis showed the formation of sheets and thus indicated the assembly to the anticipated interconnected network. After these promising results, a water-insoluble donor monomer was synthesized to make the polymerization accessible at a liquid-liquid interface. The produced layers at the interface were completely insoluble and were thus analyzed with various methods in solid-state like UV/Vis spectroscopy, IR spectroscopy, $^{13}C\{^{1}H\}$ LG-HETCOR NMR spectroscopy, 2D REPT-HDOR experiments, and GIWAXS measurements. Using such unconventional methods was necessary after unsuccessful HR-TEM and STM attempts, in combination with the insolubility of the 2DSP preventing single-crystal XRD analysis. Although each individual analysis was not able to unambiguously prove the molecular structure of the supramolecular layer, the combination of these methods confirmed the anticipated structure. To expand the versatility of this complexation motif, additional donor and acceptor monomers were synthesized, with varying the spacer units while maintaining the respective donor- and acceptor moieties. The different combinations were then compared by their characteristic behavior in UV/Vis spectroscopy, TEM, and GIWAXS analysis. The degree of molecular order, the unit cell parameters, the optical properties, and occurring differences in layer sizes and morphology of the D-A-CB[8] combinations were consistent to the respective donor and acceptor strength of the spacer units. Eventually, assembly experiments were carried out at the air-water interface in order to further enhance the 2D polymerization process. However, only in the case of **10+CB[8]+22**, layers were obtained at this particular interface, which was attributed to the water-adsorbing properties of the water-insoluble donor monomers. First measurements towards elucidating mechanical properties of an as-processed 2DSP layer were carried out. These, however, featured a low mechanical stability of the layer towards scratching, appraising these kind of 2DSPs to be improbable for application in wear-resistant coatings. Nevertheless, all obtained monolayer 2DSPs

exceed the benchmarks of comparable supramolecular systems, which was accounted to the combination of well-thought molecular design and optimized processing parameters. Based on different approaches without an interface and with different interfaces, the toluene-water interface was found to be the most versatile system for assembly.

2.3. Two-Dimensional Supramolecular Polymers Based on Metal-Organic Interactions

The host-guest enhanced donor-acceptor approach of self-assembling a two-dimensional polymer showed the accessibility of 2DSPs at an interface without the use of metals. Utilizing a different promising supramolecular interaction motif, a 2DSP was planned to be built by metal-organic interactions. Regarding reported association constants of metal-organic complexes in the range of 10^{37}-10^{40} M^{-1},[51] generating a two-dimensional polymer from a metal-organic interaction provides the possibility to feature a higher mechanical stability of the assembled 2DSPs than the D-A-CB[8] approaches and therefore could produce larger and more robust 2D material. Exemplarily, the synthesis of metal-organic iron-terpyridine complexes, assembled at the air-water interface, furnished 2DSPs with lateral dimensions of several mm^2.[70, 81, 129] Taking into account the size of this reported structure in combination with the possibility to apply a functional transition metal in a matrix of rationally designed organic molecules, emphasized metal-coordinated 2DSPs as highly eligible for placing 2DSPs to an application, like hydrogen evolution reaction (HER).[11] In 1991, the work on catalyzed hydrogen evolution using sulfur-coordinated iron(II) complexes with HCl by *Sellmann* et. al.[130] triggered intriguing research on transition-metal dithiolate complexes for the HER.[131-132] For such purposes, π-conjugated metal bis(dithiolene) units are typically provided in aqueous or aqueous/organic medium,[131-132] where they suffer from a loss of stability and reactivity.[133-134] The latter accounts for an immobilization of active centers in a well-defined way onto the surface of an electrode while at the same time providing a large surface area, which are both requirements addressable by 2DSPs. For rationally designing an appropriate metal-organic coordinated 2DSP, several specifications had to be considered:

1) The organic molecule was supposed to bear a π-conjugated unit with a symmetry allowing for 2D polymerization.
2) Dithiol units were to be attached to the periphery for metal-ligand interaction.
3) The assembly was supposed to take place at an interface similar to the host-guest enhanced donor-acceptor approaches, taking advantage of both the stabilizing and templating effect. However, considering the unsuccessful complexation of host-guest enhanced donor-acceptor molecules at the air-water interface, the applied organic monomers should exhibit a certain affinity

to water to be able to interact with the metal ions, which were supposed to be injected to the aqueous phase in excess.

4) The choice of an appropriate metal ion with regard to its respective coordination geometry is inevitable for the successful assembly towards 2DSPs, preventing out-of-plane polymerizations. Considering multidental complexations to be more stable,[135] while at the same time preventing sterical shielding of the coordinating metal ion, a square planar coordination geometry was chosen to be appropriate.

Meeting all these specifications, 1,2,5,6,9,10-triphenylenehexathiol **35** was synthesized. For complexing bis(dithiolene) units, Ni^{2+} was reported to build a square planar coordination sphere.[82, 132] The synthesis of **35**, the assembly process, and the morphological as well as electrochemical characterizations were elaborated in collaboration with [redacted].

2.3.1. Synthesis

The target molecule 1,2,5,6,9,10-triphenylenehexathiol **35** was synthesized in three steps, starting from 1,2,5,6,9,10-hexabromotriphenylene **32**, which was prepared according to literature known procedures.[136] The *in situ* deprotonation of benzyl mercaptane with sodium hydride allowed for a nucleophilic substitution reaction of the bromine units with benzyl protected thiol groups to give **33** in 65% yield. Subsequent deprotection of the thiols was performed by means of a Birch reduction. The crude sodium thiolate intermediate **34** was used without further purification after quenching the reaction with methanol and removing the salts. The protonation of thiolate moieties as final reaction step was done with hydrochloric acid to give **35** in 97% yield (over both steps), whereby oxygen-free conditions had to be maintained to prevent building disulfide bridges by oxidation of **35**.

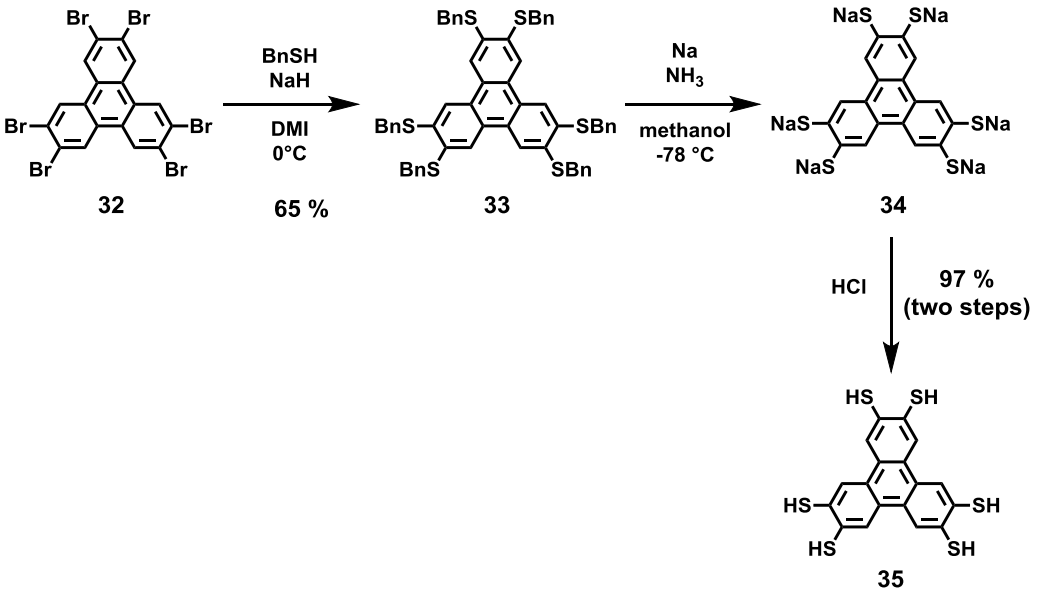

Scheme 10: Synthetic pathway to yield 1,2,5,6,9,10-triphenylenehexathiol **35**, starting from 1,2,5,6,9,10-tribromotriphenylene **32**.

2.3.2. General Procedure for the Self-Assembly of Metal-Organic Layers at the Water-Air Interface

The experiments for assembling host-guest enhanced donor-acceptor complexes demonstrated the advantages of providing a templating effect of an interface to the formation of 2DSPs in combination with a rational monomer design. The protocol for preparing the self-assembled metal-organic sheet was based on the literature reported example of the formation of a 2DSP, built from a metal-organic coordination network of terpyridine monomers with iron(III) species as metal ions, which was prepared at the air-water interface, resulting in monolayers with lateral dimensions of several square millimeters.[70, 81, 129] For the metal-coordination, Ni^{2+} ions were selected, as they previously showed a square planar coordination geometry in combination with thiol-substituted precursors.[82] For a typical experiment, 10 µL of a $2.5 \cdot 10^{-3}$ M solution of **35** in a chloroform/DMF = 1/3 mixture were distributed on the aqueous phase on a Langmuir trough. After evaporation of the solvent, the monomers on the surface were compressed to a surface pressure of 10 mN m^{-1}, generating a submonolayer phase. A 1000-fold excess of Ni^{2+} ions in form of 4 mL of a $5.0 \cdot 10^{-3}$ M solution of $Ni(NO_3)_2$ in water was then submerged into the subphase. The Ni^{2+} ions subsequently spread through the aqueous phase by diffusion, inducing a certain concentration of nickel ions

at the interface triggering the supramolecular coordination polymerization. After an assembly time of 2 h, the resulting 2DSP layers, which are referred to as **Ni-35**, were vertically or horizontally transferred onto various substrates. Excessive or uncomplexed precursors were removed by washing with chloroform and water.

2.3.3. Morphological Characterization

The morphology of resulting 2DSP layers was analyzed using OM, SEM, and AFM.

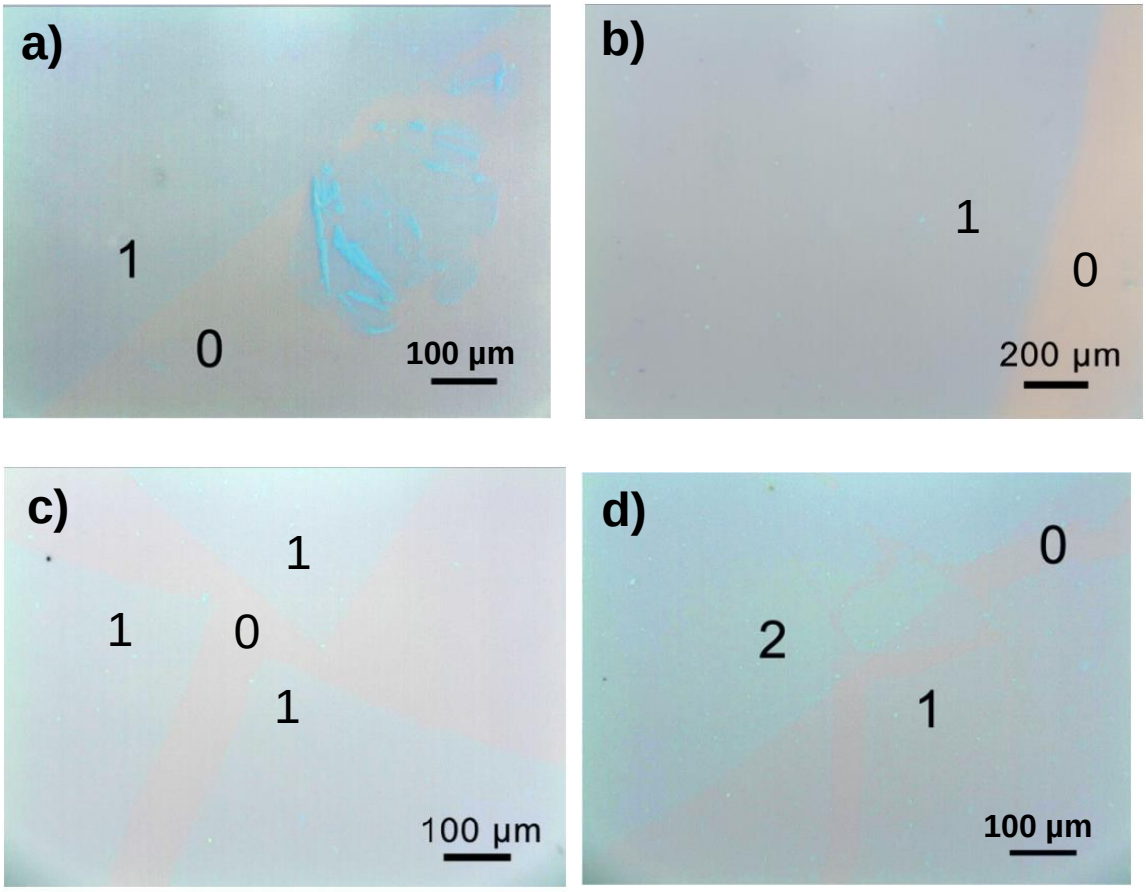

Figure 42: OM pictures of **Ni-35** sheets after vertical transport onto 300 nm Si/SiO_2 wafer pieces. a-b) Single-layer sheets with different magnifications. c) Different layer arrangements. d) A bilayer in addition to a single layer was processed by a repeated transfer step. (0) depicts the bare substrate surface, (1) indicates an area covered with monolayered **Ni-35**, and (2) reveals a bilayer. Reprinted with permission from Ref.[137]. Copyright 2015, John Wiley and Sons.

Images measured by OM revealed thin layers on Si/SiO_2-wafers, exhibiting a significantly different contrast to uncovered areas (Figure 42). The straight edges indicate how far the substrate was dipped into the solution and serve as contrast for distinguishing between covered area and bare substrate surface. The low difference in contrast demonstrates the thin nature of one sheet. Multiple transfer steps were able to produce separated, covered areas (Figure 42c) or multilayer formations (Figure 42d). Remarkably, the depicted layers show large, homogeneous layers over areas of several mm^2.

Further analysis of the fabricated layers by SEM showed comparably homogeneous structures (Figure 43a). The absence of splitting edges indicates the presence of monolayers instead of stacked layers. This was further corroborated by the clearly visible difference in contrast apparent with multilayered structures (Figure 43b).

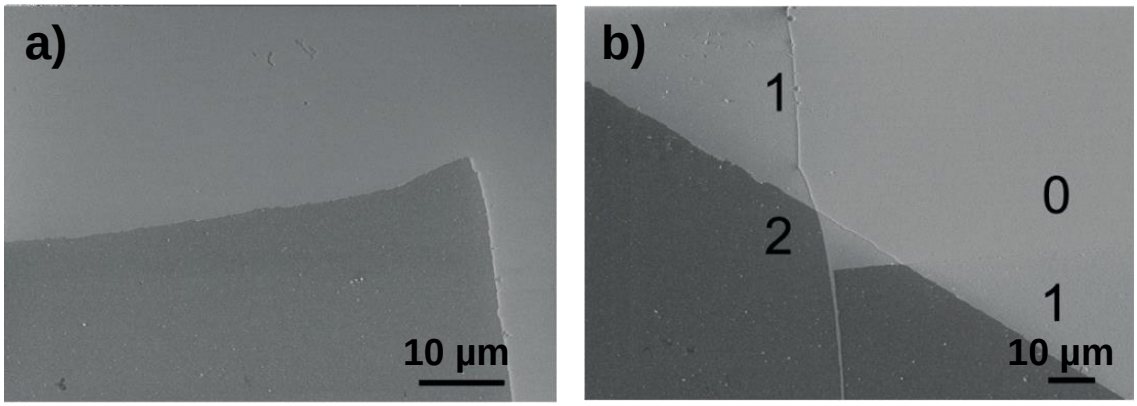

Figure 43: SEM images of **Ni-35** layers. a) Monolayered material with a high homogeneity. b) Multilayered structure, obtained by repeated transfers. The numbers implicate the number of layers visible. Reprinted with permission from Ref.[137]. Copyright 2015, John Wiley and Sons.

As it was already shown with the host-guest enhanced donor-acceptor approach, AFM measurements represent an indispensable tool to draw conclusions as to the numbers of layers present in the obtained material from the layer thickness. Considering the height of comparable, single-atom thick monolayer structures,[83-84] the measured values of 0.6–0.8 nm, obtained from the height difference of cross-sections at the edges of the layers to the bare substrate's surface, proved the produced sheets to be single-layers (Figure 44). The high signal-to-noise ratio during these measurements was caused by the low thickness of the layers, which is near the detection limit of the AFM devices, resulting in a relatively high uncertainty of the absolute layer thickness of 15%. However, considering the necessary complexity and effort for measurements

with a higher sensitivity, these measurements in combination with SEM analysis verified the existence of monolayered species.

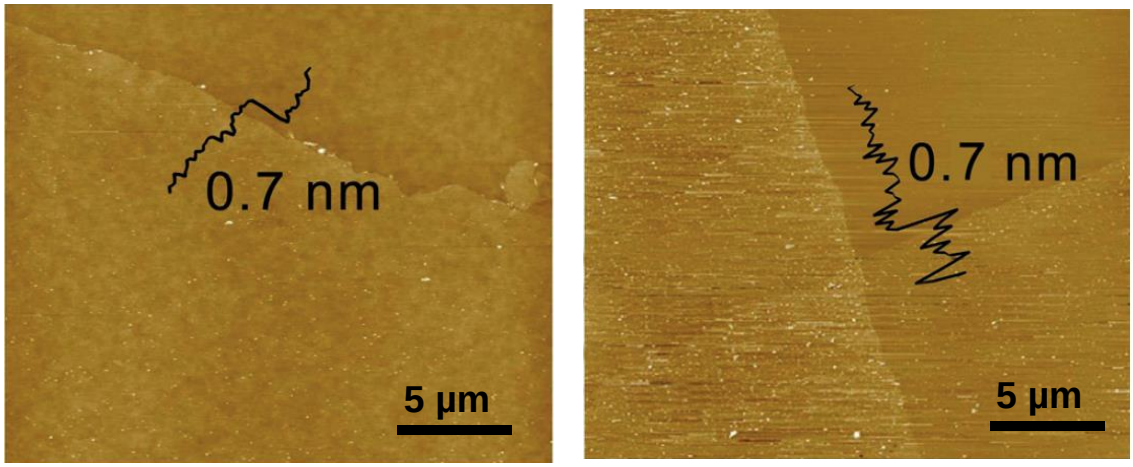

Figure 44: AFM height images, recorded in tapping mode of **Ni-35** sheets processed on mica. Both pictures show a height difference of 0.7 nm, being in good agreement with comparable monolayer structures in literature.[83-84] Reprinted with permission from Ref.[137]. Copyright 2015, John Wiley and Sons.

2.3.4. Structural Characterization

To gain insight into structural properties, UV/Vis spectroscopy, IR spectroscopy, TEM, powder X-ray diffraction (PXRD), and X-ray photoelectron spectroscopy (XPS) measurements were performed.

Ni-35 layers were transferred onto quartz wafer substrates for analysis with UV/Vis and IR spectroscopy. UV/Vis spectra of the **Ni-35** sheets gave a spectrum similar to those of the **34** and **35** precursors (Figure 45). As the absorbance of all three materials was almost identical, a triphenylene-dominated absorption could be assumed, thus indicating the triphenylene building blocks in **Ni-35** sheets. The small bathochromic shift from λ_{max} = 304 nm to λ_{max} = 315 nm visible from comparing the **35** monomer with **34** and **Ni-35** material accounts for similar electronic effects, namely an electron donating effect of sulfur atoms and electron accepting effect of sodium and nickel, respectively, however appearing less distinct in the case of **35**. Increasing the number of layers resulted in a direct proportionality to the UV/Vis absorbance, measured at 315 nm (Figure 45b). The linear regression line crossing the origin upon plotting the layer number against the absorbance (Figure 45b, inset) thus indicating a quantitative,

layer-by-layer stacking of single layers[81] and providing a reliable and fast protocol to monitor the number of layers of each LB experiment. Comparing the **35** monomer with the **Ni-35** sheets by IR spectroscopy furnished a distinct S-H vibrational peak at 2510 cm^{-1} in the spectrum of **35**. This signal disappeared in the **Ni-35** material and was hence accounted to a successful coordination of thiol moieties.[76]

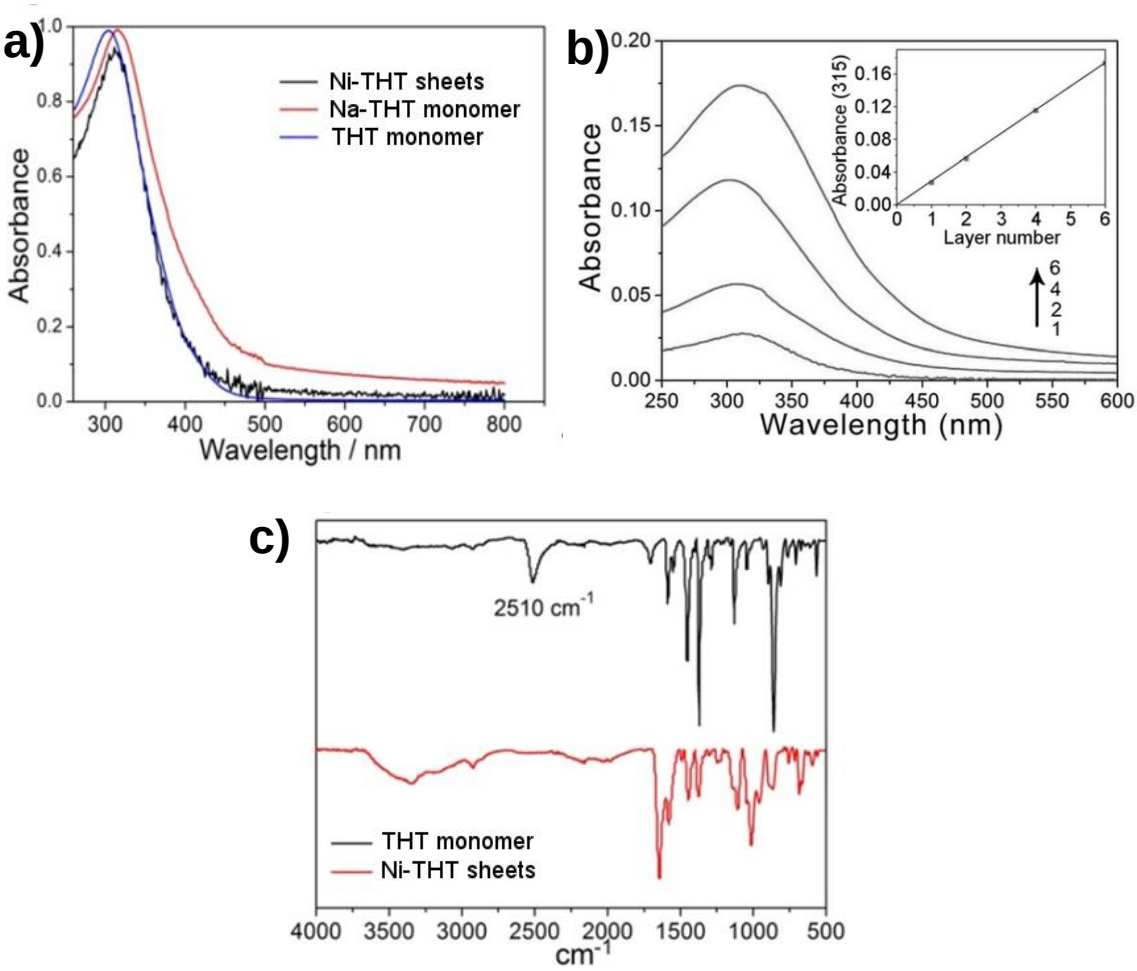

Figure 45: a) UV/Vis spectra of the monomer **35** (blue), the monomer **34** (red), and the assembled **Ni-35** sheets. b) UV/Vis spectra of **Ni-35** with different number of layers. The inset reveals the linear correlation between the number of layers and the absorbance, measured at the maximum at 315 nm. c) IR spectrum of **Ni-35** sheets, compared to the monomer **35** spectrum. The spectra show a clear disappearance of the S-H vibrational peak at 2510 cm^{-1} from the monomer to the assembled sheet. Reprinted with permission from Ref.[137] Copyright 2015, John Wiley and Sons.

For TEM analysis, **Ni-35** monolayers were horizontally deposited onto copper grids with a hexagonal mesh, comprising a side length of 18 µm (Figure 47a-c). The OM picture (Figure 47a) as well as the low resolution TEM image (Figure 47b) show a corrugated layer of **Ni-35** covering the hexagonal holes, which renders these layers as being free-standing.[70, 81, 129] Remarkably, the layer did not break, free-standingly covering the hexagonal holes with an area of ~842 µm² (Figure 46). Further, the sheets revealed many wrinkles, when deposited on top of the copper mesh. These however seemed to have minor influence on the film in terms of stability, as the wrinkles show no rupturing at the bending edges. Considering the different stabilities of supramolecular interactions, e.g. **CB[8]** vs. metal-organic assemblies, the complexation constants of **CB[8]** are with factors between $K_{eq} = 10^4$-10^{15} about 35-45 orders of magnitude lower than metal-organic complexes with constants between 10^{37}-10^{40} (Figure 1).[51] This large difference affects the individual supramolecular bonds, resulting in a tremendous difference in the strength of an ensemble of the respective supramolecular bonds, which builds the monolayered 2DSP.

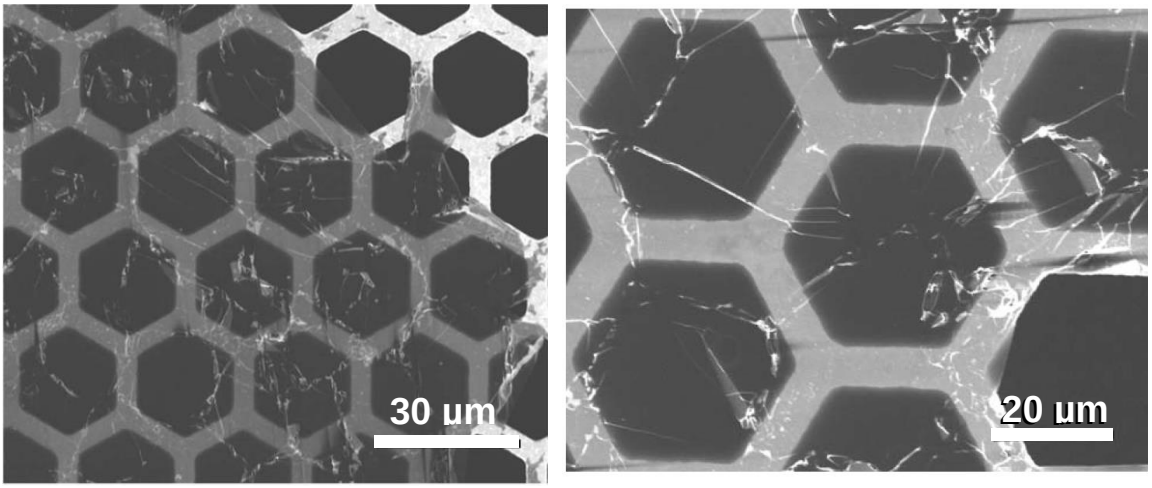

Figure 46: SEM images of a **Ni-35**, showing the homogeneous and intact layer-structure covering hexagonal holes of the copper mesh with areas of 842 µm². The wrinkles in the layer seem to not induce breaking of the film, indicating flexibility of the macroscopic assembly. Reprinted with permission from Ref.[137]. Copyright 2015, John Wiley and Sons.

The occurring wrinkles were reasoned to be caused by evaporation of residual solvents on the wetted sheets, resulting in latter tending to shrink during the transfer process. A representative area of the **Ni-35** layer was measured by selected area

electron diffraction (SAED) with the objective of elucidating its internal structure. Measurements at room temperature, however, did not reveal a defined diffraction pattern, presumably due to thermal fluctuation and a low stability of the sheet under electron irradiation. Therefore, SAED analysis was performed at -175 °C. The diffraction pattern revealed a typical hexagonal structure (Figure 47d), suggesting the presence of a regularly ordered hexagonal network with a unit cell parameter of 2 nm.

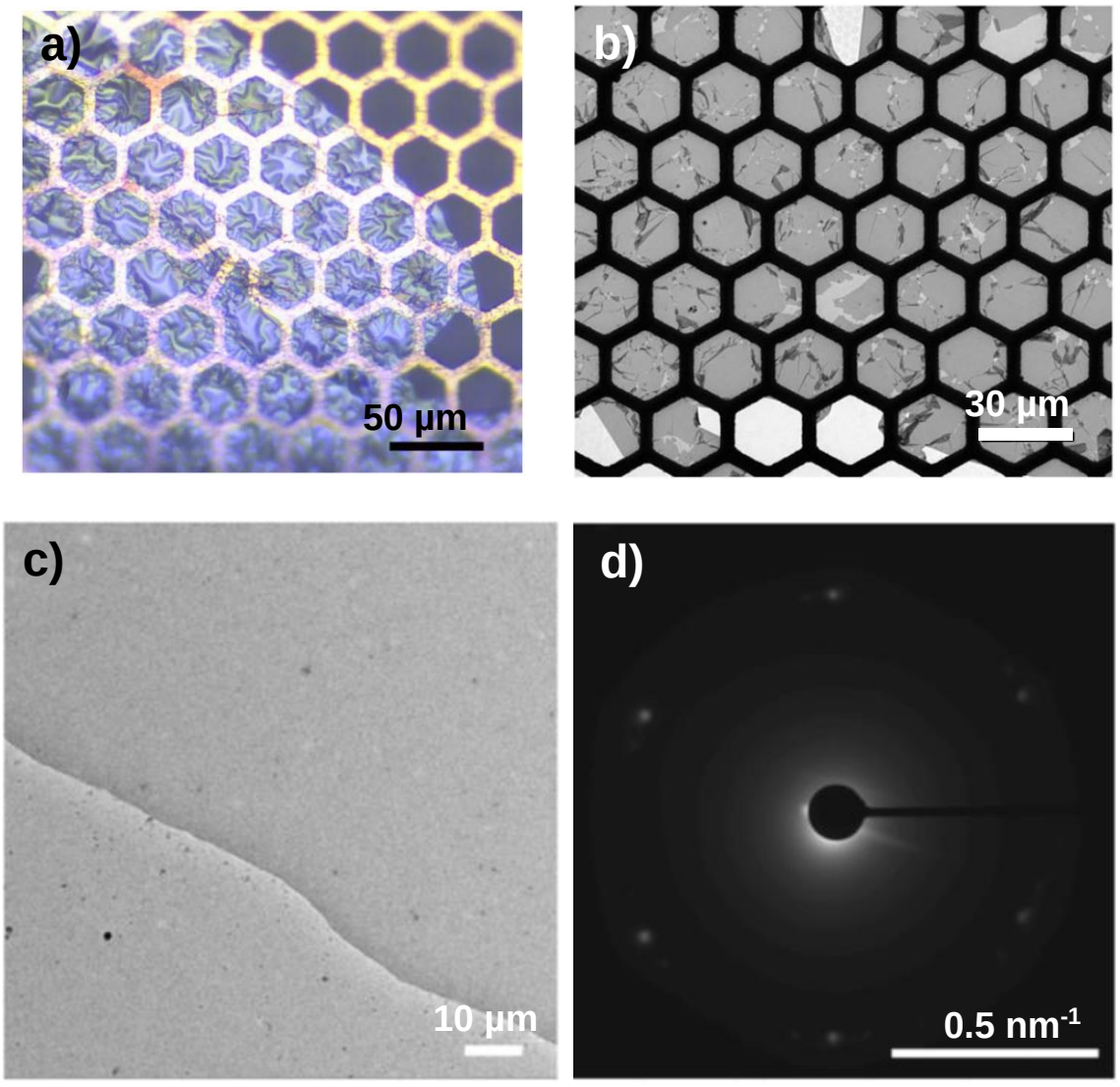

Figure 47: a) Optical microscopy picture of a **Ni-35** layer on a copper grid with a hexagonal mesh. The sheet reveals a high number of wrinkles. b) Low resolution TEM image of the **Ni-35** layer. c) Higher magnification of latter at an edge of the sheet for visualizing the layer by the difference in contrast. d) SAED measurement of the area in c), highlighting a hexagonal diffraction pattern. The diffraction was recorded at -175 °C. Reprinted with permission from Ref.[137]. Copyright 2015, John Wiley and Sons.

Corroborating this regularly ordered hexagonal structure, PXRD was measured. With the amount of material necessary for a PXRD measurement exceeding the obtainable amount of **Ni-35** by the Langmuir-Blodgett technique by far, bulk **Ni-35** powder was produced to provide indirect proof of the internal structure in accordance to the approach used for solid-state NMR measurements in the case of host-guest enhanced donor-acceptor measurements (chapter 2.2.2.4). Thus, a solution of 8.0 mg (0.019 mmol) **35** in 5 mL water was prepared. A solution of 5.1 mg (0.028 mmol) $Ni(NO_3)_2$ in a mixture of 0.7 mL 6 M NH_4OH solution and 5 mL water was added. After slowly stirring the mixture for 2 h at 65 °C, the precipitate was separated. After washing with water and drying, the bulk **Ni-35** material was obtained as black powder.

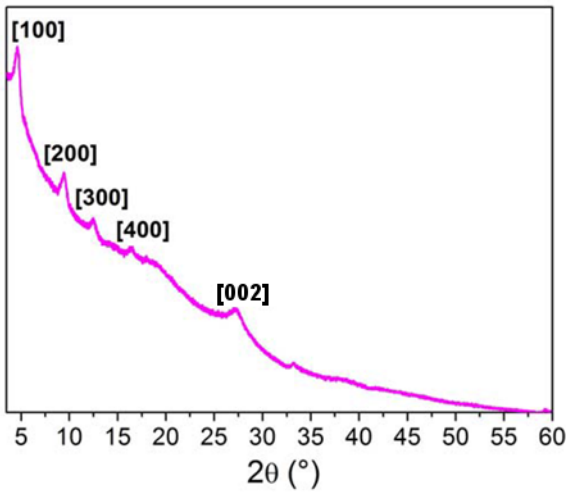

Figure 48: PXRD pattern for bulk **Ni-35** materials. The prominent peak at $2\theta = 4.58°$, with diffractions following up to the 4th order, was assigned to the *(100)* reflection. A second, intensive signal at $2\theta = 27.58°$ was assigned as *(002)* diffraction. Reprinted with permission from Ref.[137]. Copyright 2015, John Wiley and Sons.

The PXRD measurement of this powder indicated the presence of a crystalline structure. Regarding the *(100)* reflection at $2\theta = 4.58°$ with following-up diffractions to the 4th order, a unit cell parameter of a basal hexagonal lattice of 2.1 nm was obtained, standing in good agreement with the value measured from the geometry optimized structure (Figure 48). The intensive signal at $2\theta = 27.58$ was assigned to the *(002)* reflection, whereas the corresponding *(001)* signal, expected at $2\theta = 13.79$, is represented by the shoulder between the *(300)* and *(400)* signals. This *(002)* diffraction accounts for an ordered lamellar stacking along the meridional plane[83-84] with an

interlayer distance of 0.7 nm, as anticipated by related AFM measurements (Figure 44).

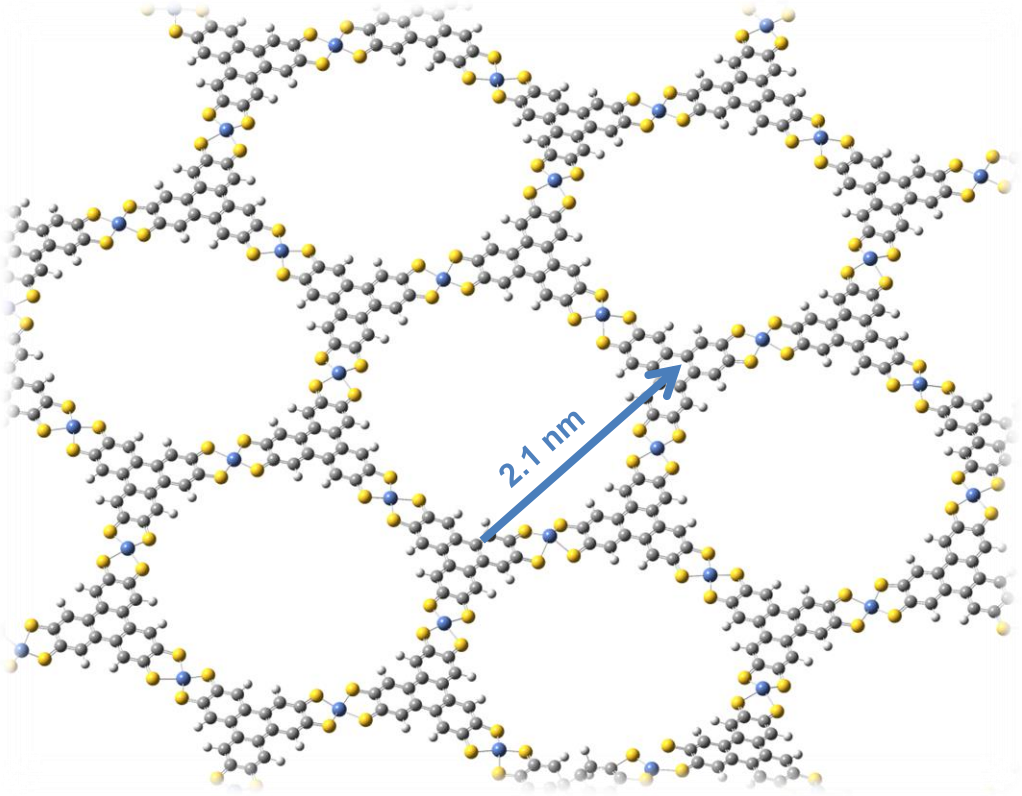

Figure 49: Geometry optimized structure of the **Ni-35** 2DSP, using the semi-empirical PM6 method. The inserted distance shows the expected value of the hexagonal unit cell from this calculated structure.

This strong evidence of TEM and PXRD, proving the proposed regularly ordered, internal hexagonal structure of **Ni-35**, was further corroborated by energy-dispersed X-ray spectroscopy (EDX) and XPS to elucidate the chemical composition, chemical environment and binding environment. EDX analysis detected Na, Ni, C, S, and O as components. The origin of oxygen in this material was assumed to result from residual water by incomplete drying, oxygen adsorption to the **Ni-35** surface after deposition, or the Si/SiO_2 wafer substrate. The residual sodium content was accounted to an imperfect washing procedure with water and chloroform, which could however neither be enhanced by washing with more solvent, nor with using additional solvents. Integration of the EDX signals gave a relative ratio of Ni/S of 1/3.6 according to quantitative contents of Ni with 4.47 at% and S with 16.32 at%, close to the anticipated

Ni/S ratio of 1/4, thus indicating the square planar coordination of thiol units with Ni^{2+} by stoichiometry.

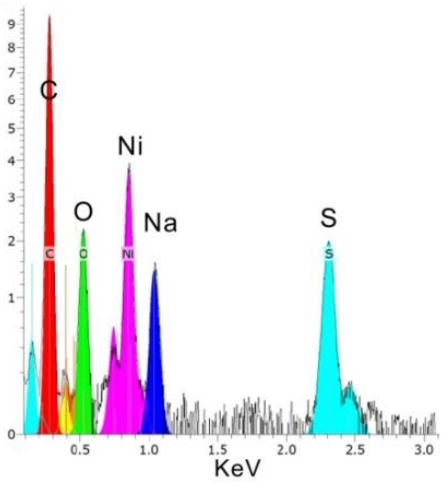

Figure 50: EDX measurement of **Ni-35**, revealing its chemical composition as C, O, Ni, Na, and S. Reprinted with permission from Ref.[137]. Copyright 2015, John Wiley and Sons.

In the XPS spectrum of **Ni-35**, Na 1s, Ni 2s, Ni 2p, O 1s, C 1s, S 2s, and S 2p core levels are visible (Figure 51a-c). The measurement was carried out by [redacted]. Considering the absence of Ni signals in the monomeric spectrum of **35** (Figure 51d-e), the general appearance of Ni species in the sheet is an important corroboration of the inclusion of Ni^{2+}-ions, facilitating the supramolecular polymerization in the 2DSP. The high resolution spectrum of the Ni 2p area reveals two peak sets, one at 855 eV and one at 872 eV, which were assigned to the 2p3/2 and 2p1/2 orbitals, respectively (Figure 51b). These signals prove that only one species of Ni is present in the **Ni-35** 2DSP and therefore excludes any other binding affinities of Ni in the sheet.[82, 138-139] The high resolution spectrum of the S 2p revealed a complex structure of the signal between 160-172 eV. A Ni/S ratio of 1/4.8 by quantitative analysis revealed a slightly higher sulfur composition, than the expected 1/4 ratio for a square planar coordination motif. Deconvolution of the signal gave a superposition of four different contributions. The intensive doublet at 163.8 and 165.1 eV was assigned to a Ni-S species, verifying the successful metal-organic complexation of Ni^{2+} with the thiol ligands.[131-132] Additionally to this species, $S\text{-}O_3$ and $S\text{-}O_4$ were also visible in the region between 166.7-169.5 eV. These sulfur species presumably occurred due to the LB method, not being accessible under inert gas, therefore opening the possibility of oxidizing the thiol moieties.[140]

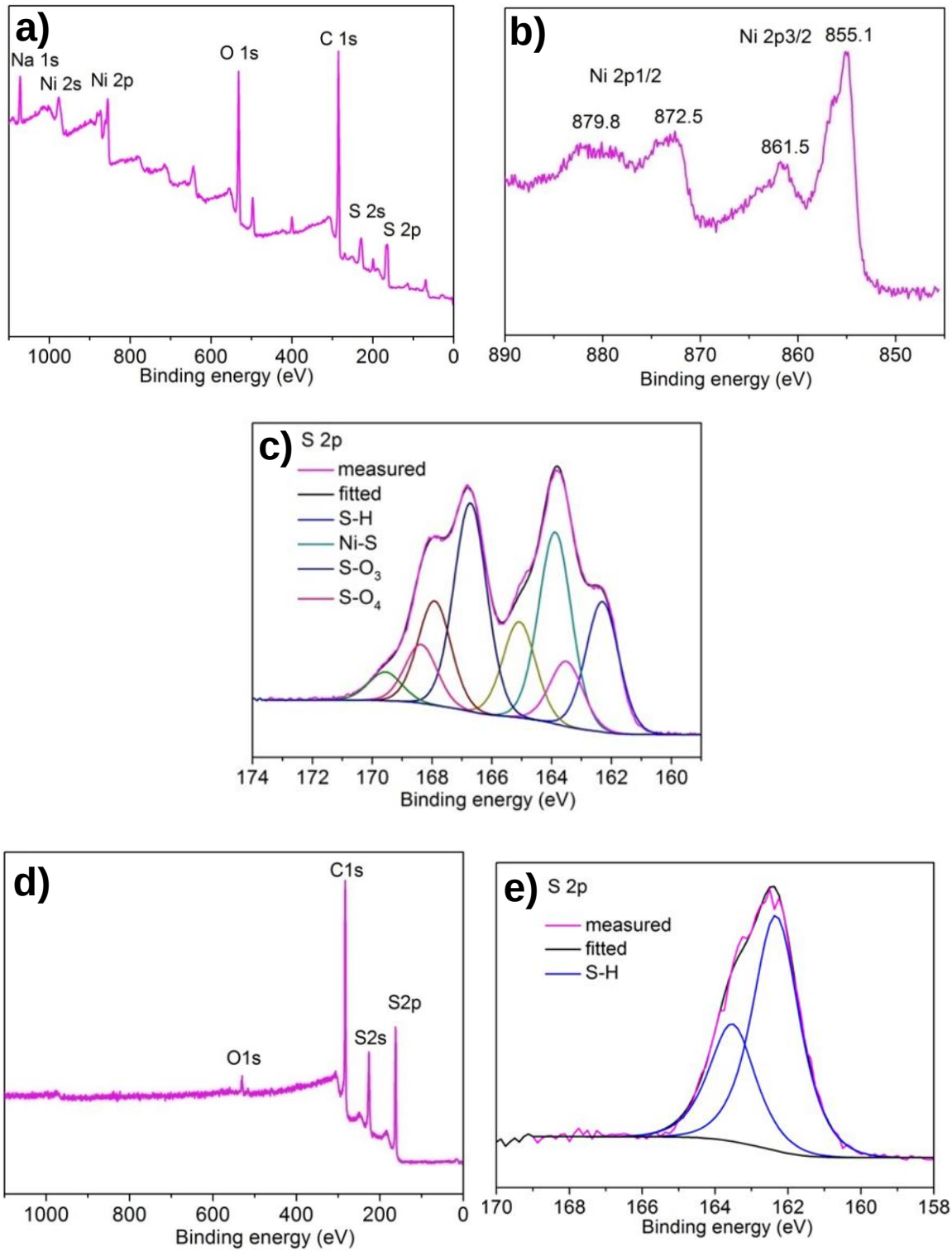

Figure 51: a-c) XPS spectra of **Ni-35** sheets. a) Energy survey spectrum. b) and c) Magnified areas of the Ni 2p area between 850-890 eV and the S 2p area between 160-172 eV, respectively. d-e) XPS spectra of the **35** monomer. d) Energy survey spectrum. e) Magnified area of the spectrum in the range between 160-166 eV, revealing a high resolution of the S 2p region. The S 2p3/2 and 2p1/2 orbitals characteristically resulted in a peak doublet with D = 1.2 eV and an intensity ratio of 1:2, originating from a spin-orbit coupling. Reprinted with permission from Ref.[137]. Copyright 2015, John Wiley and Sons.

The last contribution to the S 2p signals was identified as S-H signals, represented by the weak doublets at 162.3 and 163.5 eV. Quantitative analysis suggested a defect density in the **Ni-35** layer of ~35 at%. The regular order of the layer visible in PXRD measurements and its mechanical strength, which was expressed by the free-standing ability, expected the defects to result e.g. in a trigonal coordination sphere of Ni^{2+} with three thiols, whereby one thiol is assumed to be unavailable for complexation due to oxidation.

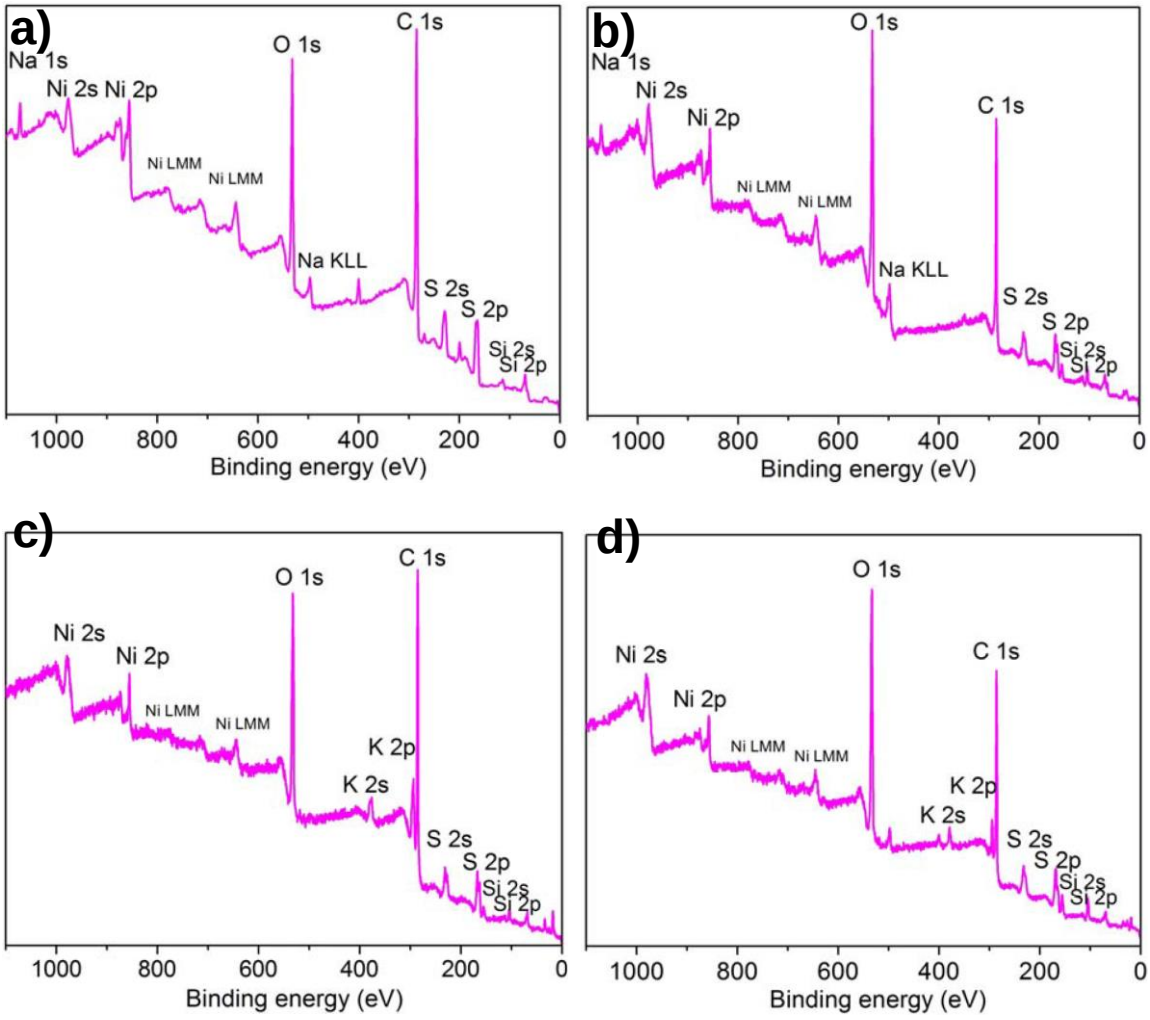

Figure 52: XPS survey spectra of **Ni-35** using Na^+ as compensating ion in a) the layer, and b) the bulk powder. Exchanging the compensating ion to K^+ is shown in c) the layer, and d) the bulk powder. Reprinted with permission from Ref.[137]. Copyright 2015, John Wiley and Sons.

To legitimize the bulk **Ni-35** powder to give comparable results to the **Ni-35** sheet, both samples were measured with XPS (Figure 52a-b). The survey spectra revealed a qualitative conformity of the peak distribution, indicating most similar elemental species in both materials. Quantitative analysis, however, suggested a higher amount of oxygen in the bulk powder, therefore relating for a lower degree of order than in the LB processed monolayers. Sodium residues were found in the **Ni-35** sheet as well as in the bulk **Ni-35** powder. Although more drastic washing procedures in the bulk powder, e.g. washing with boiling water, were able to reduce the sodium content from 1.8 at% to 0.8 at%, it was not possible to completely remove Na from the material. Furthermore, these drastic washing procedures were not applicable to the **Ni-35** layers due to unavoidably rupturing the sheets. Therefore, the addition of $NaNO_3$ was changed to KNO_3 in order to increase the solubility of residual ions. The resulting XPS spectra (Figure 52c-d) revealed the absence of Na signals, however showed an amount of 2.2 at% and 1.2 at% K in the **Ni-35** sheets and bulk powder, respectively. As this amount exceeded the one of Na in both cases, Na was further used as compensating ion.

2.3.5. Application as Active Material in the Hydrogen Evolution Reaction

The regularly ordered structure of catalytically active nickel bis(dithiolene) complexes distributed at a high density in the **Ni-35** 2DSP in combination with the possibility to use the LB technique for processing the **Ni-35** sheets onto arbitrary substrates made this material highly promising for application in HER. HER measurements were carried out in collaboration with [redacted]. After deposition of a **Ni-35** monolayer on a glassy carbon disk, its performance in electrochemical water splitting was measured with the rotating disc electrode (RDE) process in an aqueous solution, which was saturated with argon. The HER polarization plots of the **Ni-35** covered electrode in comparison to a bare electrode, both measured in a 0.5 M H_2SO_4 solution, revealed a drastic increase of current density above an overpotential of 110 mV in the case of the **Ni-35** electrode (Figure 53a, pink). In contrast, the bare electrode did not show an increase in the current density, demonstrating the electrocatalytic effect of **Ni-35** sheets (Figure 53a, black dashed line). At a current density of 10 $mA \cdot cm^{-2}$, an operating potential of 333 mV was achieved. Judging by the Tafel plot, revealing a Tafel slope of 80.5 $mV \cdot dec^{-1}$ (Figure 53a, inset), the rate

determining step of the HER appears to be a Volmer reaction.[141-145] An HER exchange current density of $i_0 = 6 \cdot 10^4$ mA cm^{-2} was calculated based on a linear fit of the Tafel plot.

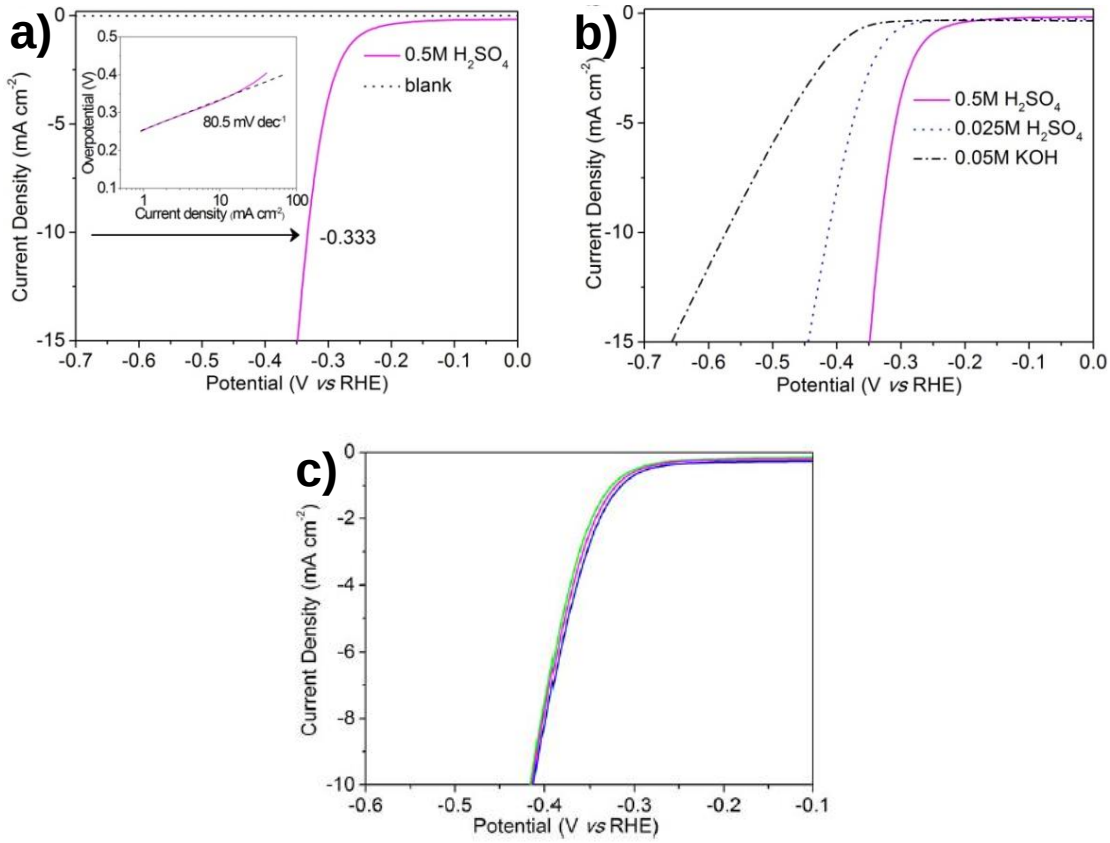

Figure 53: a) HER polarization curves of the **Ni-35** covered electrode (pink) and the bare glassy carbon disc electrode (dashed black), measured in 0.5 M H_2SO_4. The respective Tafel plot is shown as inset in a). b) HER polarization curves of the **Ni-35** covered electrode, measured in different electrolyte solutions. c) Influence of residual Na^+ and K^+ on the HER activity. With Na^+ before further washing (pink) and after washing (blue). With K^+ as compensating ion (green). Reprinted with permission from Ref.[137]. Copyright 2015, John Wiley and Sons.

Further measurements were performed varying the electrolyte solution (Figure 53b). In a 0.05 M KOH solution with a pH value of 15.3, the operating potential increased to 574 mV at 10 mA cm^{-2}. In 0.025 M H_2SO_4 solution with a pH value of 1.3, a lower operating potential of 413 mV at 10 mA·cm^{-2} was achieved. Although the electrocatalytic activity significantly decreased with the pH value, these measurements showed the applicability of the **Ni-35** sheets as HER active material over a wide pH

range. Notably, the electrocatalytic performance was measured by analyzing the effect of residual Na^+ or K^+ on the activity (Figure 53c). The insignificant differences in the obtained plots displayed that both ions have had a negligible influence on the performance of the material in marginal amounts of < 3 at%.

Table 2: Leading results for HER activities in literature. Reprinted with permission from Ref.[137]. Copyright 2015, John Wiley and Sons.

Catalysts	Structure	Onset potential (V, vs. RHE)	Tafel slope (mV dec^{-1})	i_0 (mA $cm^{-2)}$	η (mV) @ 10 mA cm^{-2}	Ref.
Molecular catalysts						
CNTs grafted $Ni(bdp)_2$	1D hybrid	~290	-	-	300 @ 4 mA cm^{-2}	[133]
CNTs grafted CO tetraimine	1D hybrid	~350	~160	-	590 @ 4 mA cm^{-2}	[134]
Metal-free catalysts						
N-graphene	2D sheet	331	116	~$7 \cdot 10^{-5}$	490	[146]
P-graphene	2D sheet	374	133	~$9 \cdot 10^{-6}$	553	[146]
N,P-graphene	2D sheet	289	91	~$2 \cdot 10^{-4}$	422	[146]
S-graphene	2D sheet	240	130	~$6 \cdot 10^{-5}$	391	[147]
N,S-graphene	2D sheet	130	81	~$7 \cdot 10^{-5}$	276	[147]
Non-noble metal catalysts						
CoN_x CNTs	1D hybrid	50	69	0.01	270	[141]
NiN_x CNTs	1D hybrid	-	-	-	~350	[141]
Porous MoS_2	2D film	150-200	50	~$1 \cdot 10^{-4}$	270	[142]
Defect-free MoS_2	2D sheet	180	87	~$3 \cdot 10^{-3}$	~270	[143]
Defect-rich MoS_2	2D sheet	120	50	~$9 \cdot 10^{-3}$	~200	[143]
2H MoS_2	2D sheet	200	110	-	320	[144]
WS_2 sheet	2D sheet	80-100	60	~0.02	~250	[145]

Compared to leading HER activities in literature (Table 2), the highest values obtained with **Ni-35** at pH 15.3 exceeded the ones reported for CNT-supported molecular catalysts,[133-134] and N-, P-, or S-doped graphene.[146-147] The characteristics obtained in a 0.5 M H_2SO_4 electrolyte solution even measure up to the performance of non-noble metal catalysts, e.g. 2D WS_2 sheets,[145] 2D MoS_2 sheets,[142-144] or Ni- and Co-embedded, N-doped CNTs.[141] The importance of providing regularly distributed, easy accessible catalytically active centers in a 2DSP instead of a thin film is corroborated by comparing the results with those of *Marinescu* et. al., which were published at the time this work was elaborated.[83-84] Although the concept of using cobalt bis(dithiolene) fused triphenylenes reveals similarities to the material of **Ni-35**, the reported 360-nm-thick film required a significantly higher operating potential of 530 mV at 10 $mA \cdot cm^{-2}$ (vs. SHE, at pH 1.3).

2.3.6. Summary

Based on the results in chapter 2.2, the formation of a 2DSP based on metal-organic interactions was carried out on an air-water-interface. The design of this 2DSP featured a planar triphenylene core, substituted with six thiol units in the periphery. Those were complexed with nickel(II) ions, whereas the anticipated square planar coordination sphere allowed for limiting the polymerization into two lateral dimensions. By horizontally transferring the layers from the interface, coatings of arbitrary substrates, like TEM grids, Si/SiO_2-wafers, quartz glass, or a glassy carbon disk were achieved. It was further possible to adapt a variety of analytical methods from the D-A-CB[8] attempt for characterizing the metal-organic 2DSP and extend these by measurements specific for this particular 2DSP, like XPS and SAED. In this regard, OM, SEM, and TEM measurements showed monolayer sheets with lateral dimensions of several mm^2. Due to a minor sensitivity against electron irradiation, the possibility to provide proof of the expected hexagonal structure with SAED redundantized the necessity of utilizing a more circumstantial method like GIWAXS. Furthermore, the analyzability of nickel species and their binding behavior in XPS allowed for a more precise measurement of the 2DSP structure. Thereby, a defect density of 35 at% was determined, which implies, that some nickel ions featured a trigonal planar coordination sphere with one thiol group being unavailable for complexation due to oxidation. However, in terms of the mechanical stability of the sheet, the metal-organic interactions appeared strong enough to carry the own weight of the sheet, in contrast

to the host-guest enhanced donor-acceptor approach, hence being free-standing over gaps of ~840 µm². Additionally to solely fabricating this 2DSP, it was applied as active material in the HER by coating a glassy carbon disk with the polymer. The resulting HER characteristics exceeded those of comparable CNT catalysts and heteroatom-doped graphenes. By comparison with HER measurements of a multilayered thin film of a similar structure, a superior activity was achievable in the case of the monolayer. This was judged being a good example for the superior properties of 2D monolayers for certain applications.

3. Hollow Carbon Tubes

3.1. Introduction

These two examples of 2DSPs demonstrated the achievability of 2D monolayers made from supramolecular interactions and the possible utilization of such material in an application. Although there exists a variety of other possible applications for 2DSPs, it is far from being universally implementable. Especially when a three-dimensional structure is requested, 2DSPs typically fail. Nevertheless, 2D structures can still be provided for such cases by furnishing material comprised from stacked layers. Still the two-dimensionality of the individual layers remains of particular importance and can exhibit beneficial properties. Graphite is one of those materials and is an important and widely used carbon allotrope. Historically, the name graphite, meaning “writing stone” was assigned to this naturally occurring allotrope of carbon, as it was found very useful for marking sheep. Today, with deeper understanding of its outstanding properties, namely a high thermal conductivity of 2000 $W \cdot m \cdot K^{-1}$,[148] low thermal expansions between 2-6 $\cdot 10^{-6}$ $m \cdot mK^{-1}$,[149] or beneficial electrical resistivities between 3.5-5.0 $\cdot 10^{-5}$ $\Omega \cdot cm$,[150] its utilization in a large number of applications became part of our everyday life. With an annual amount of 1.1 Mt, the graphite fabricating and crafting organizations form one of the world’s major industries, and they process graphite in a broad variety of applications like pencils, lubricants, shoe polish, conductive rubber, gas-tight barriers, gas adsorbents, catalytic support, carbon fibers, electrodes, or brushes and contacts for electronics, as well as moderator in nuclear reactors.[151-153]

For producing graphitic materials, there exists a variety of procedures, each well adapted for the respective graphite application. These protocols can generally be distinguished between top-down and bottom-up methods. The top-down principle complies with a destructive approach of a macroscopic system to adapt its features on a smaller scale or in a certain shape. In contrast, bottom-up methods assemble fundamental parts towards a desired, more complex system. On the one hand, top-down procedures typically feature the advantageous possibility to fabricate large amounts of material in a short time. On the other hand, bottom-up techniques usually provide less product, though with a better control over structural properties and less waste. Additionally, some components remain elusive for top-down approaches, but

are achievable with bottom-up concepts. This is exemplarily the case for several microscopic structures. They require meticulous abrasive cutting from large blocks, thereby producing excessive waste material and holding the chance of breaking the component due to mechanical stress. One class of these aforementioned microscopic structures, which remain elusive by top-down concepts are micrometer-thin hollow carbon tubes. To prepare those by top-down procedures, the areas to be removed by drilling a hole into a wire would have to be accessible with the respective tool. This is not possible here, as the hollow tube difficile shapes or requires an inaccessible accuracy. Hence, several bottom-up approaches were reported to achieve these hollow carbon tubes. *Chen* et al., *Wang* et al., and *Li* et al. utilized chemical vapor deposition of methane to grow few-layer graphene onto metal substrates like copper or nickel. Although the obtained tubes featured desirable qualities of graphite with only few defects, approaches so far were not able to maintain the hollow structure, but rather collapsed.[154-156] On the contrary, several procedures used the pyrolysis of polymers as organic precursors to obtain hollow carbon tubes. *Qiu* et al., *Yang* et al., *Xie* et al., and *Sun* et al. provided poly(acrylonitrile) fibers as precursors. These were oxidized, with optimization of the temperature and time to achieve oxidation of the exterior and not of the interior. Subsequent pyrolysis resulted in hollow tubes, while the non-oxidized interior was removed by heating and the tube wall was graphitized. All cases provided a porous tube wall, whereby analysis of the tube material revealed amorphous carbon and highly defective graphite material, respectively.[157-160] Instead of oxidation, *Fatema* et al. used iodination to produce randomly crosslinked layers around poly(vinyl alcohol) fibers, which were pyrolyzed after stabilization to give a hollow carbon tube. This approach resulted in graphitic structures with only few defects, however with the necessity to heat to 3000 °C to remove defects in the material.[161-162] *Liu* et al. were able to cut one step of these time-consuming processes by using a bi-component gel-spinning procedure to prepare poly(acrylonitrile) coated poly(methyl methacrylate) fibers in one step with subsequent pyrolysis. The obtained hollow structures featured an equally poor quality of graphite to the other polymer approaches.[163] In 2013, *Zhao* et al. used graphene oxide as precursor to prepare electro-spun hollow fibers. However, they were not able to improve the quality of graphite after reduction compared to other polymer methods.[164] Trying to put hollow carbon tubes into applications, *Jiang* et al. used a poly(sulfone)-beta zeolite fiber, coated with the polymer matrimid 5218. After pyrolysis, a hollow carbon tube with a porous tube was obtained with different selectivities towards O_2/N_2 and CO_2/CH_4, suitable for gas separation.[165] Two different applications were reported by *B. Wang* et al. and *S. Wang* et al., who graphitized natural cotton resulting in hollow tube

structures. These materials were then applied as sorbent for oil removal as well as supercapacitors. It has to be mentioned that the products, although being hollow, revealed random, in most cases not cylindrical, shapes with poor graphite qualities.[166-167] Although all these approaches exhibit their individual benefits, the preparation of hollow tubes with arbitrary shapes, therefore being able to sustain their shape, remained elusive. Due to CVD approaches producing collapsing tubes, and procedures utilizing the pyrolysis of polymers refusing the possibility to influence the resulting structure, e.g. bending or twisting the hollow carbon tube, there was a pressing need for developing a new fabrication procedure for shape-persistent hollow carbon tubes, making the desirable properties of graphite accessible for the improvement of existing applications.

Therefore, a procedure for the fabrication of hollow carbon tubes exhibiting high graphite qualities is to be elaborated in this work. The tubes are to be customizable of their shapes and sizes. Moreover, the hollow carbon tubes must provide stability high enough to sustain their macroscopic shape without bending or collapsing, namely being shape-persistent.

3.1.1. Structure and Conductivity of Graphite

Graphite is composed of trigonal sp^2 bonding carbon atoms arranged in a hexagonal fashion to form a 2D layer. The covalent bonds feature a short length of 0.141 nm and a high strength of 524 kJ/mol, originating from the interaction of three sp^2 valence electrons per atom in combination with the small size of the atom. The basal planes are stacked with a distance of 0.335 nm, based on π-interactions of delocalized electrons of the adjacent plane with an interaction strength of 7 kJ/mol. This fourth valence electron of carbon is located in an orbital perpendicular to the basal plane, which overlaps with adjacent orbitals of the same kind, and therefore resulting in a delocalization of these electrons. The ensemble of these electrons in the valence band overlaps the conduction band by ~36 meV. This overlap is the reason for the electrical conductivity of graphite with anisotropic behavior. The two pathways for charge mobility in graphite material divide into a perpendicular direction to layer planes and in the direction of the basal planes. In accordance to a higher orbital overlap in-plane, this pathway of conductivity features a value of $1.41 \cdot 10^5$ S·m^{-1},[150] whereas the conductivity between the layers is almost two magnitudes lower with $3.30 \cdot 10^3$ S·m.[14]

The outstanding properties of graphite listed above (3.1) correspond to calculated values of ideal graphite, or a material, marginally deviating from an ideal structure. Perfect, defect-free forms of graphite are neither achievable with synthetic approaches nor found in natural sources. Typically, polycrystalline graphite is present, which features a certain number of defects and finite crystallite sizes. Pyrolytic graphite was reported to often reveal large crystallite sizes, demonstrating properties close to those of ideal graphite.[14] Commonly appearing defects include planes not being parallel, missing or additional atoms in the crystal lattice, out-of-plane polymerizations, inclinations or chemical bonding with foreign atoms, or edge dislocations. Such defects in the graphite lattice are more probable to appear during the preparation process, as graphite is chemically inert towards most bases, acids and corrosive gases, especially with its basal plane.[14] Although graphite is a stable allotrope under ambient conditions, its preparation is necessarily carried out at elevated temperatures. Oxidation of graphene with e.g. water or oxygen already appears at 350-400 °C, whereas this temperature is readily exceeded during graphitization. This can be beneficial, e.g. in the case of activated carbon to provide a randomly distributed, high variety of functional groups over the surface for enhancing adsorption interactions. However, it is disadvantageous for obtaining the desired favorable graphite properties. Therefore, graphitization of carbon-containing material has to be performed under protection gas or in vacuum, whereas a high purity of the gas and a high vacuum have to be provided, respectively. Furthermore, the purity and nature of precursor material is decisive for defect structures in resulting graphite, which, apart from minimizing undesired defects, can be used for defect engineering, therefore enhancing or customizing the intrinsic properties of graphite. In this regard, quite a number of intrinsic and extrinsic defects were detected, defined, and correlated with their effect on chemical and electronical properties.[168-172] For example, whereas rationally synthesized graphene nanoribbons were supposed to open the bandgap and produce semiconducting material,[173-174] it is in contrast possible to enhance the conductivity by the inclusion of foreign atoms into the crystal lattice.[168, 175]

3.1.2. Raman Spectroscopy on Graphite Materials

The regularity of the structure of obtained graphite and the sizes of the crystallites basically influence its quality.[176-180] Raman spectroscopy as vibrational technique is extremely sensitive to the geometric occurrence and to molecular bonding, and therefore represents a versatile method for analyzing and evaluating the quality of graphite.[162, 181-183] A typical spectrum exhibits three main bands: the G band is the most prominent feature of graphite and related materials at around 1580 cm^{-1}, which is associated with in-plane vibrations of one graphene layer; the D band at around 1350 cm^{-1}, occurring as a result of the breathing mode of sp^3-hybridized carbon atoms; the 2D band at around 2700 cm^{-1} according to a two phonon process of the graphite layers (Figure 54). Due to the origin of the D band, it is also considered as defect-induced band and is used for draw conclusions about the amount of defects inside the material.

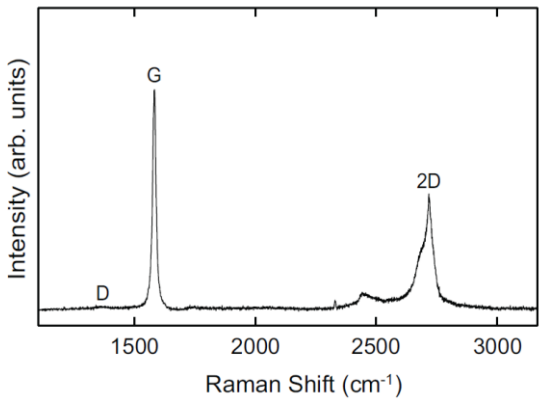

Figure 54: Raman spectrum of nearly defect-free graphite, revealing intense G and 2D peaks, and a barely visible D peak.[184]

Conventionally, the quality of graphite is analyzed by the position and width of the G-band as well as the intensity ratios of the D-band to G-band (I_D/I_G) and of the 2D-band to G-band (I_{2D}/I_G), whereby low I_D/I_G and high I_{2D}/I_G values support a high quality of apparent material.[162, 181-183]

3.2. Results and Disscussion

3.2.1. Solution-Based Approaches

The fabrication of hollow carbon tubes was performed using a solution-based approach (Figure 55). A typical experiment included a three-step procedure: First, dip-coating a metal wire in a hexadodecyl-hexabenzocoronene (hexadodecyl-HBC) solution, followed by carbonization of the coating by pyrolysis, and.third, etching the metal wire to produce a hollow carbon tube. Hexadodecyl-HBC was applied as carbon source to provide aromaticity in the precursor and thus supposed to reduce the necessary steps to obtain graphite to a minimum while at the same time allowing for solubility, facilitating a dip-coating process.

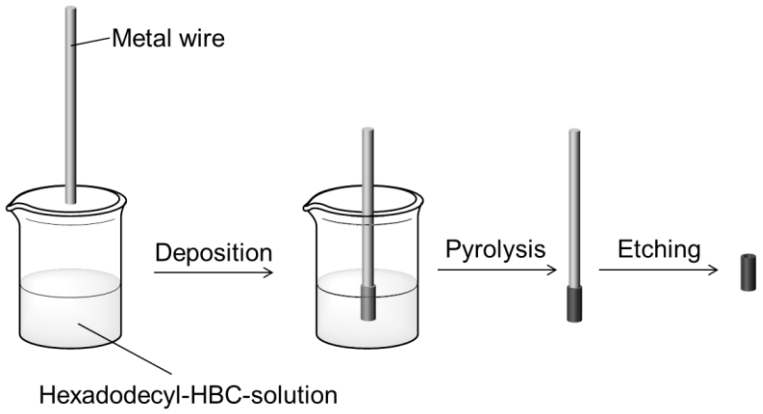

Figure 55: Concept to achieve hollow graphite tubes by dip coating a metal wire into a solution of hexadodecyl-HBC solution, subsequent pyrolysis and final etching.

Dipping copper wires into the hexadodecyl-HBC solution resulted in a 600 nm thick, homogeneous layer on the wires. However, after pyrolysis of the wires at 1000 °C for 10 h, their surface exposed small isles instead of a continuous layer (Figure 56).

Increasing the thickness of the coating and varying the pyrolysis conditions did not enhance the sizes of carbonized isles and was not able to facilitate a continuous carbon layer. Changing the precursor to other small molecules, such as dopamine or coronene, or polymers like poly(methyl methacrylate) did not result in increased areas of carbonized material.

Figure 56: Optical microscopy picture (20x magnification) of a copper wire surface, coated with hexadodecyl-HBC after pyrolysis. The diffuse areas at the top and the bottom appear due to the convex surface.

To decrease the mobility of hexadodecyl-HBC precursor on the surface, it was randomly crosslinked by electron irradiation in accordance to previously reported methods.[185] The random interconnections were supposed to produce a regular graphite structure upon pyrolyzing the material to 1000 °C. Utilizing a focused ion beam device, a 130 µm thick, coated copper wire was irradiated with an electron beam with 0.6 nC/µm² and 1 µs dwell time over a 100 µm broad area around the wire.

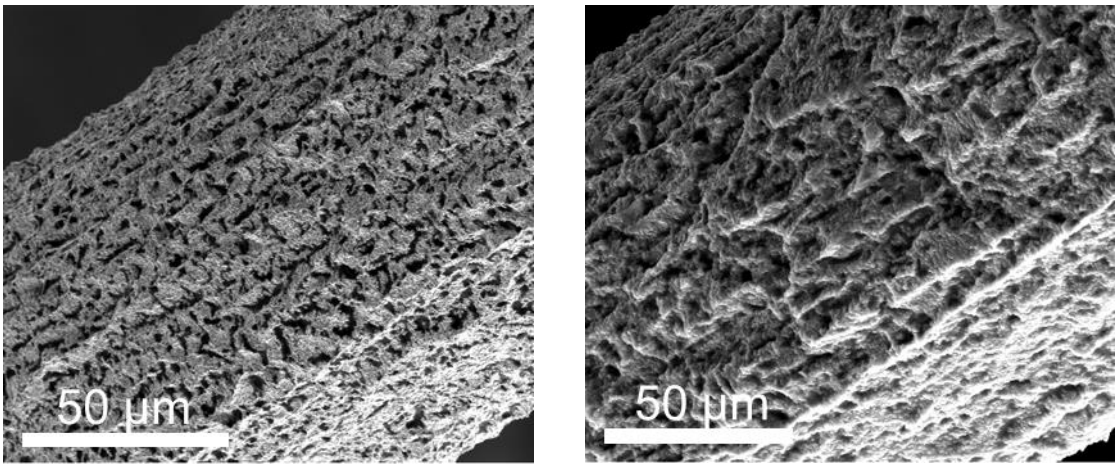

Figure 57: SEM images of the hexadodecyl-HBC covered copper wire before (left) and after (right) irradiation with an electron beam.

The experiment was limited to 100 µm, as the total irradiation time was with 12 h very time-consuming. The SEM images in Figure 57 revealed a changing morphology before (left) and after (right) exposure, which looks like a coalescence of the coating. After subsequent pyrolysis and etching the metal wire with 30% $FeCl_3$-solution, the irradiated piece was too small to be found in the beaker.

Although the irradiation appeared to successfully crosslink the hexadodecyl-HBC molecules on the covered surface, the excessive duration in combination with the low yield was considered not efficient for producing larger components. Therefore, the general concept was reconsidered and changed to a vapor-based approach.

3.2.2. Vapor-Based Approach

The vapor-based approach was therefore designed to utilize the volatility of an organic molecule to cover the wire homogeneously while decomposing. In a typical experiment, iron wires with dimensions of 0.5-3 cm in length and 130 µm or 25 µm in diameter were provided in an evacuated quartz ampoule. Either 100 mg or 50 mg of dichloromethane (DCM) were added as carbon source. Facilitating an evacuation of the ampoule without losing DCM, it was frozen with liquid nitrogen until the ampoule was evacuated and sealed.

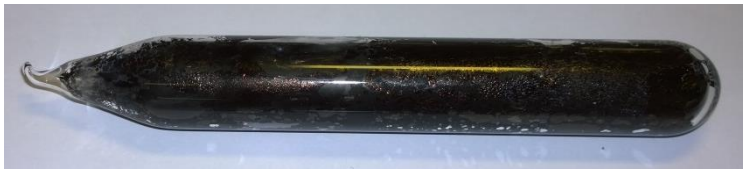

Figure 58: Picture of a quartz ampoule after pyrolysis, revealing carbonized material in its inside.

The sealed ampoule was subsequently heated to 1000 °C for 5 h. Additionally to carbon material on the ampoule wall (Figure 58), it also revealed black structures in the shapes and sizes of the applied metal templates after cooling to room temperature (Figure 59).

Cross-sections by SEM at different positions of such black structures revealed their hollow inner side (Figure 60a).

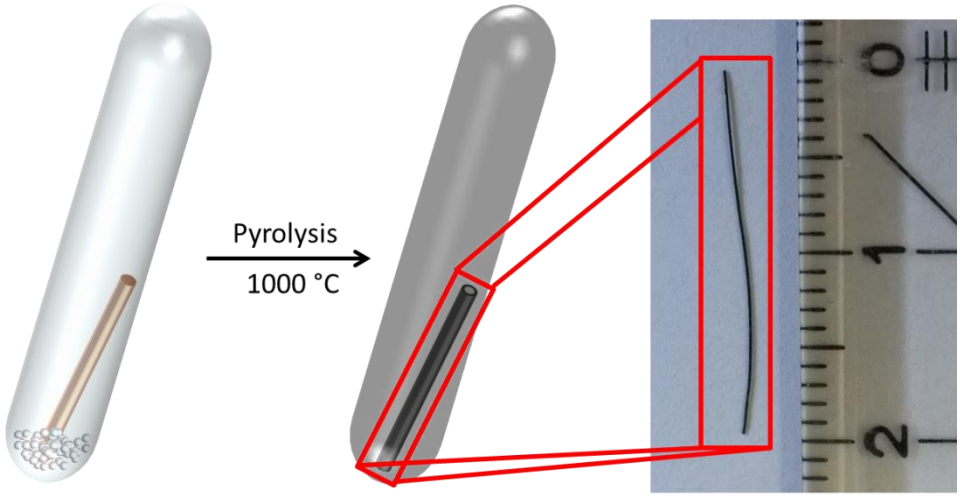

Figure 59: Process for the fabrication of hollow carbon tubes. The left part of the image shows the schematic appearance of the sealed ampoule before and after pyrolysis, visualizing the separated wire template with the precursor (DCM), and the resulting hollow carbon tube. In the right side of the picture, a black structure in the shape and size of an applied wire template is visible, revealing a length of approx. 2 cm.

Additionally to homogeneously covering the wire's surface, the combination of iron and DCM appeared to be able to remove the template, therefore making additional etching steps redundant. Several tubes were randomly broken, corroborating the complete absence of template material (Figure 60b,c). It was possible to influence the wall thickness of resulting tubes by the amount of precursor provided. Therefore, 50 mg of DCM in combination with a 25 µm thick wire resulted in a wall thickness of 1 µm (Figure 60a), whereas the tube wall of 100 mg of DCM with a wire of 130 µm in diameter was 23 µm thick (Figure 60b,c). Remarkably, the inner diameters of the remaining tubes corresponded to the respective templates.

Analyzing the inner side of a hollow tube unveiled a characteristic surface texture (Figure 60c) analog to the template's surface (Figure 61). As these experiments showed the hollow tubes matching the diameters and shapes of the template wires, and the morphology of the inner surface complying with the outer surface of the wires, they were determined to be replica of the applied templates.

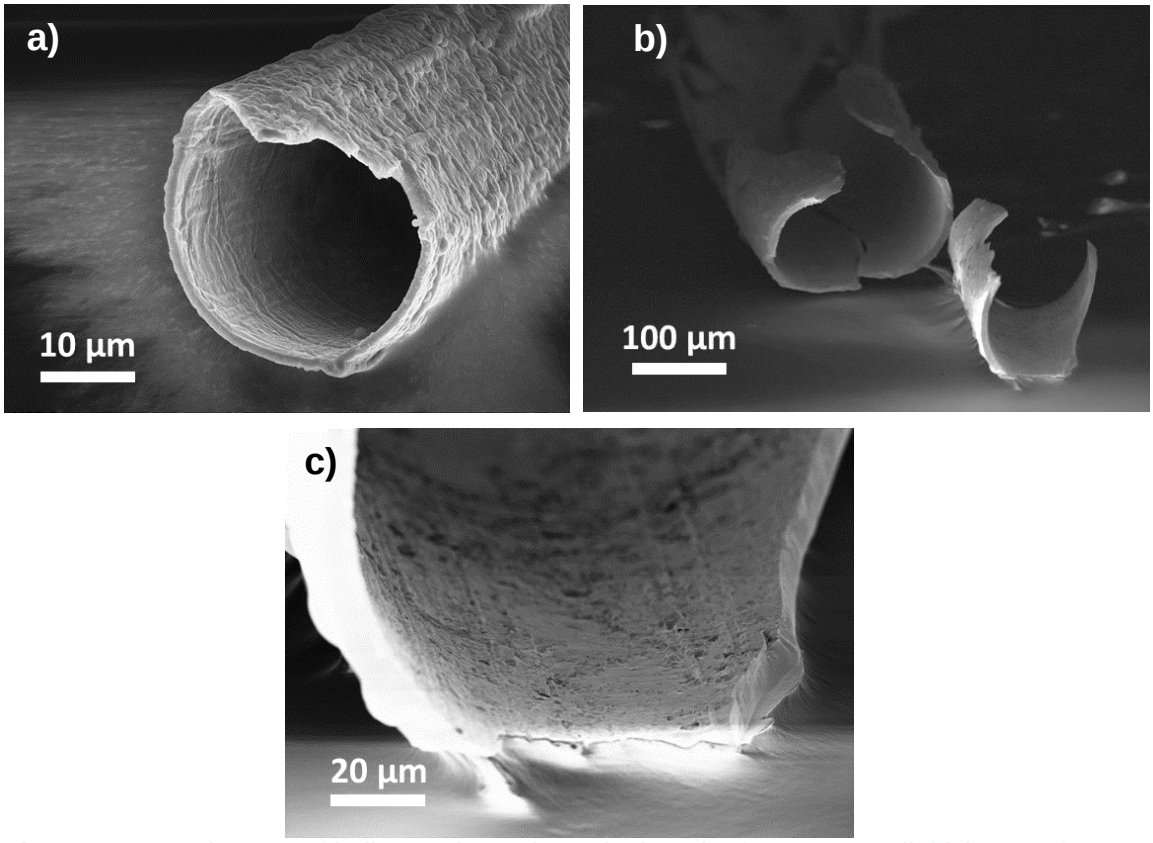

Figure 60: SEM images of hollow carbon tubes. a) The tube features a wall thickness of 1 µm and was produced from an iron wire with a diameter of 25 µm. b) This tube was fabricated from an iron wire of 130 µm in diameter and fractured to reveal its continuous hollowness. The wall thickness amounts to 23 µm. c) The magnified area of the inner side of a broken piece reveals a surface texture matching the surface morphology of the template's surface (Figure 61).

Obtaining the target structures in one step without additional etching leaves the question of where to find the wire leftovers, considering the sealed environment of the tube, which prevents the metal to evade. Therefore, the tube was analyzed by EDX. Instead of measuring the whole tube fragment, only a representative area was analyzed (Figure 62a,b), to avoid influences of the adhesive carbon pad. EDX data suggested a high amount of carbon with 96 atom%, followed by lower contents of oxygen with 1.8 atom%, silicon with 0.5 atom% iron with 0.5 atom%, and chloride with 1.1 atom% (Figure 63). The traces of silicon were identified as residues from the quartz ampoule, originating from destroying the ampoule while opening. Elemental mapping of the measured elements on the surface of the tubes furnished a homogeneous distribution of carbon, oxygen, chloride, and iron over the surface material (Figure 62c-g).

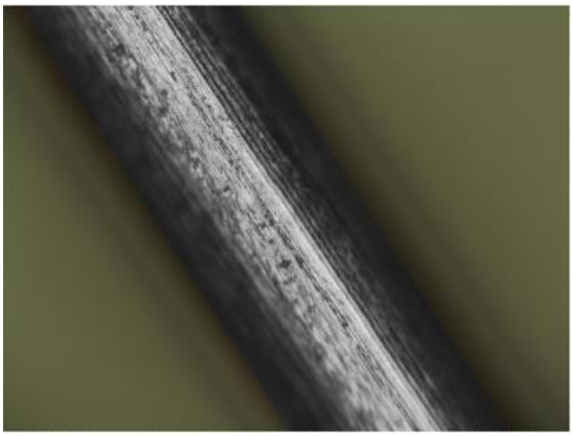

Figure 61: Optical microscopy picture of a bare iron wire with 20x magnification. The surface clearly reflects the characteristic texture, as found inside the hollow tubes in Figure 60c.

In contrast, elemental mapping on the ampoule wall gave separated areas of carbon, oxygen, chloride, and iron (Figure 64). The content of iron and chloride was with 12.1 atom% and 33.8 atom% significantly higher at the ampoule wall than at the obtained tube wall. Both materials were analyzed wet-chemically with potassium hexacyanoferrate(II) and potassium hexacyanoferrate(III), which revealed the presence of iron(II) and iron(III) in both materials. Considering the ratios of iron and chloride obtained from EDX, the in-situ formation of $FeCl_2$ and $FeCl_3$ can be assumed. The higher content of iron and chloride at the ampoule wall can be explained by the metal halides being present in the vapor phase at high temperatures. During cooling down to room temperature, the ampoule wall is cooled faster than the inside of the ampoule, as it is positioned in a continuous nitrogen flow. Therefore, resublimation of the metal halides is supposed to first occur at the ampoule wall than at the tube wall.

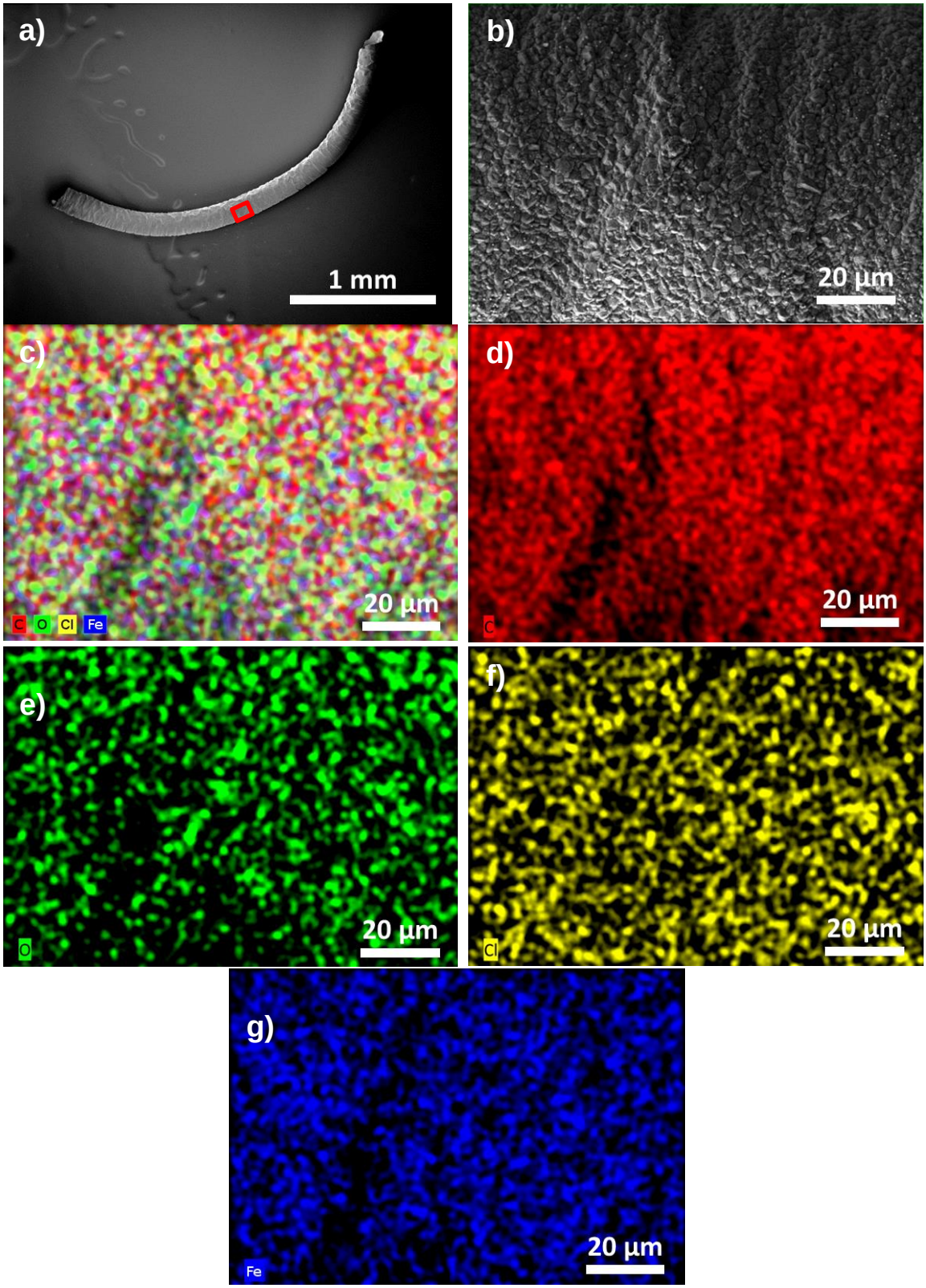

Figure 62: a) SEM image of the produced hollow carbon tube. The red frame highlights the area of higher magnification in b). b) SEM image of the area of the tube used for elemental mapping. Small differences in contrast appear due to a marginal undulation of the tube. c) Elemental mapping of carbon, oxygen, chloride, and iron. d) Elemental mapping of carbon. e) Elemental mapping of oxygen. f) Elemental mapping of chloride. g) Elemental mapping of iron.

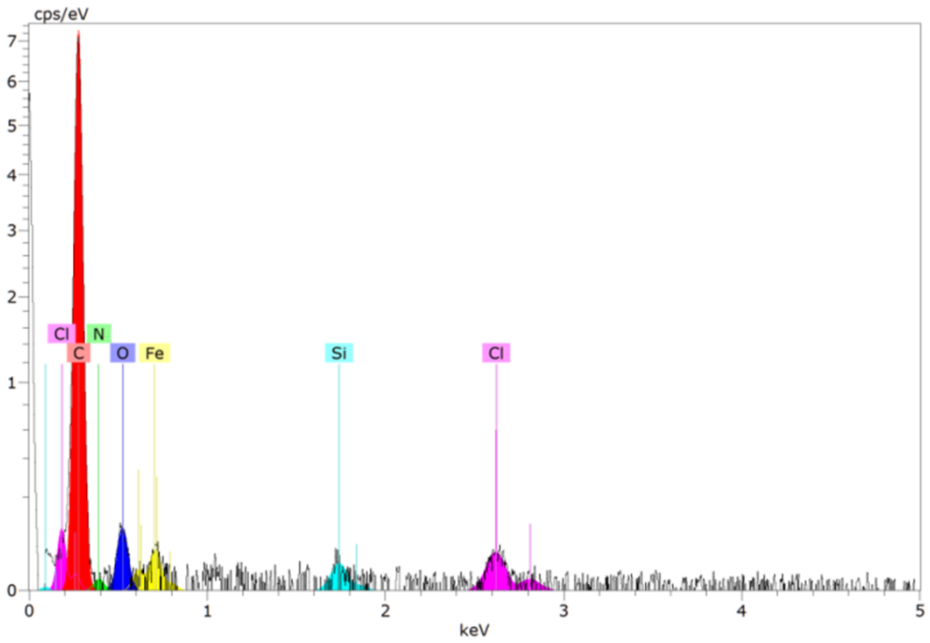

Spectrum: 33

Element	Series	Net	unn. C [wt.%]	norm. C [wt.%]	Atom. C [at.%]	Error (1 Sigma) [wt.%]
Kohlenstoff	K-series	40012	91,29	91,29	95,98	10,98
Stickstoff	K-series	17	0,14	0,14	0,13	0,18
Sauerstoff	K-series	587	2,31	2,31	1,82	0,64
Silizium	K-series	171	1,17	1,17	0,52	0,15
Chlor	K-series	426	3,06	3,06	1,09	0,28
Eisen	L-series	358	2,03	2,03	0,46	0,66
		Total:	100,00	100,00	100,00	

Figure 63: EDX data of the selected area of the hollow carbon tube in Figure 62b. The top plot reveals the intensity vs. the energy of the electrons. The table at the bottom contains the ratios of measured elements, calculated by integration of the EDX plot.

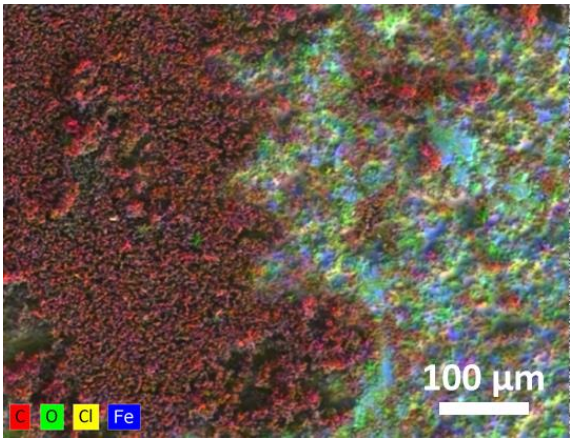

Figure 64: EDX mapping of a representative area of material obtained from the ampoule wall. The picture shows the separation of carbon and a mixture of iron, chloride, and oxygen within this material.

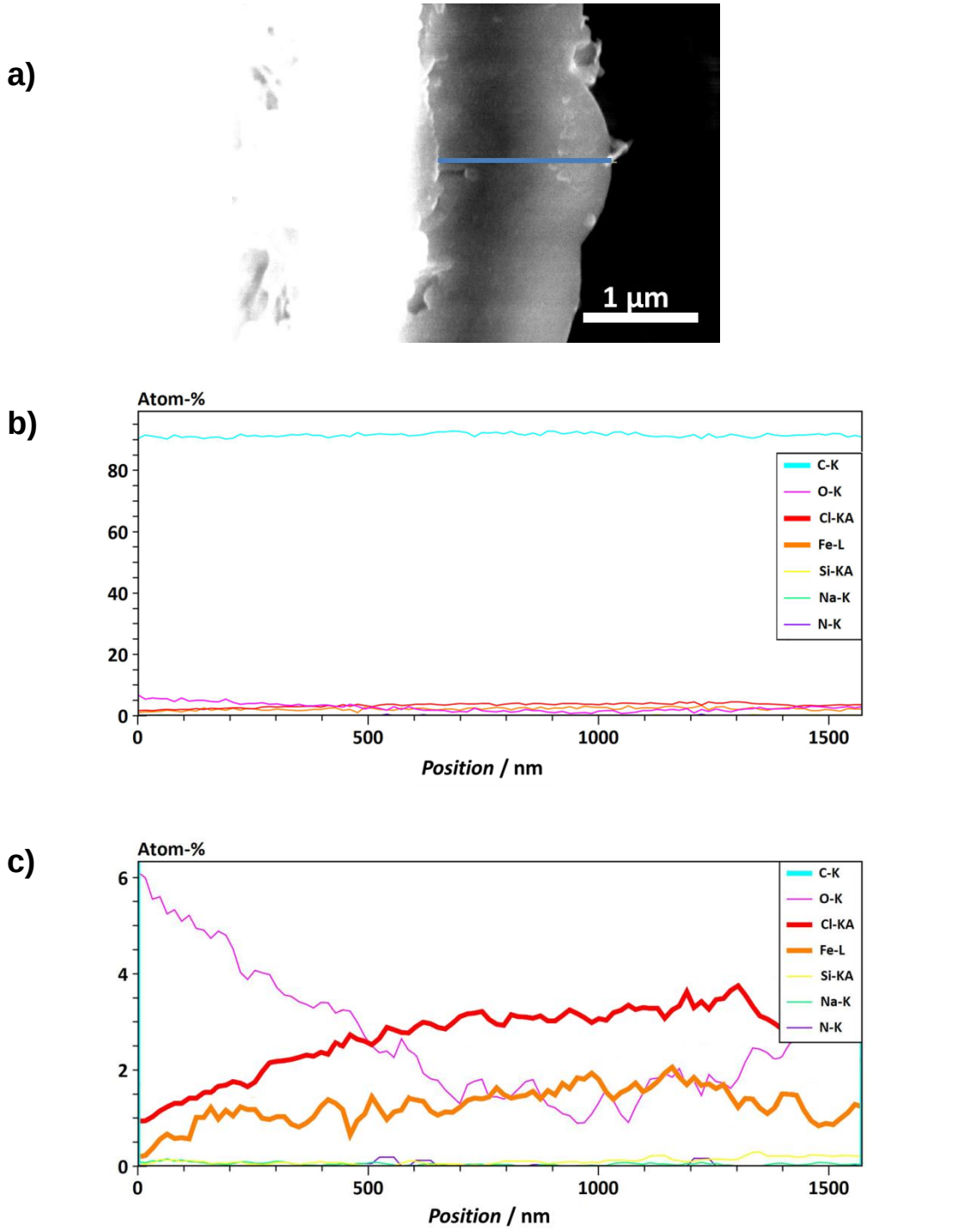

Figure 65: a) SEM image of the measured cross section of a hollow carbon tube wall. Position 0 nm represents the inner part of the tube, 1600 nm presents the exterior. The blue line highlights the area of measurement. b) Plot of the atomic distribution in percent against the position of measurement on the blue line in a). The elements carbon (turquoise), oxygen (pink), chlorine (red), iron (orange), silicon (yellow), sodium (green), and nitrogen (purple) were plotted. The measured traces of silicon, sodium, and nitrogen are not significant for interpretation. c) Magnified plot of b) for the less represented elements.

Analyzing cross-sections of the hollow tube wall by EDX revealed lower contents of iron as well as chloride at the inner tube wall (Figure 65). Thus, the formation of carbon material at the template surface occurs prior to sublimation of the metal halides. The continuous increase of metal halides in the tube wall from 0-700 nm then represents the enhanced sublimation and therefore intercalation of the metal halides in the carbon material. The stagnating contents after 700 nm correspond to a homogeneous distribution of metal halides in the vapor phase and their completed sublimation.

The hollow carbon tubes were produced with different organic halides as precursors and with different metals as templates and analyzed by Raman spectroscopy to gain information about the correlation between the provided materials and the obtained quality of the product graphite. The necessity to provide both an organic halide and a metal wire was corroborated by two control experiments: On the one hand, pyrolyzing hexachlorobenzene (HCB) without a metal wire, and on the other hand, providing benzene with a metal wire without halides present. The Raman spectra of both approaches gave high I_D/I_G values, suggesting the formation of amorphous carbon with a low content of layered sp²-hybridized carbon atoms (Figure 66).

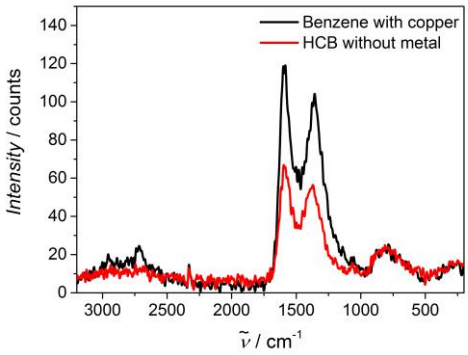

Figure 66: Raman spectra after pyrolysis of benzene with copper (black), and of HCB without the presence of a metal (red).

These experiments determined the necessity of a template and an organic halide for successfully obtaining hollow carbon tubes. As reasonable candidates for organic halides, HCB, hexabromobenzene (HBB), pentachlorocoronene (PCC), DCM, and chloroform ($CHCl_3$) were compared. The Raman spectrum of the carbon tube from pyrolyzed HCB revealed an already promising I_D/I_G ratio of 0.67 and an I_{2D}/I_G ratio of

0.37 (Figure 67, left, red). Providing HBB as precursor significantly increased the number of defects in the obtained graphite material with an I_D/I_G ratio of 1.21, and a broad 2D region (Figure 67, left, turquois). The Raman spectroscopy measurement of material from PCC showed a high I_D/I_G ratio of 0.96 and an undefined, broad 2D region was visible (Figure 67, left, black). In the case of DCM, the same low I_D/I_G ratio of 0.67 as in HCB was found, however it revealed a more distinct 2D peak with a I_{2D}/I_G ratio of 0.61 (Figure 67, left, green). Eventually, the effect of higher chloride contents in the precursor was analyzed by providing $CHCl_3$ as precursor, observing a high I_D/I_G ratio of 1.41 and a weak and broad 2D region in the Raman spectrum (Figure 67, left, pink). These divergent results in the I_D/I_G and I_{2D}/I_G ratios indicated an essential influence of the molecular structure on the resulting graphite material. On the one hand, providing an organic monomer with chloride instead of bromide yields a higher quality of graphite. This was ascribed to differences in the catalytic activity, as $FeCl_3$ was reported to facilitate intermolecular C-C coupling reactions as a moderately active catalyst, and reveals a higher activity than $FeBr_3$.[186-188] On the other hand, aromaticity in the precursor was not facilitating less defects and higher regularities in the produced graphite. In contrast, smaller monomers produced higher qualities of graphite, utilizing the increased mobilities of the molecules for maximizing the possibilities of orientation and organization during carbonization. Last, the carbon/chloride ratio revealed a significant influence on the graphite quality. A lower carbon/chloride ratio was therefore found to increase the amorphous content in the resulting material.

As DCM prevailed over the trialed precursors, it was subsequently provided with different template materials for further optimization. A nonmetallic silicon dioxide template and a metalloid silicon template were tested beside copper, gold, and iron templates (Figure 67, right). In case of silicon dioxide (Figure 67, right, red), a high I_D/I_G value of 0.88 and a broad 2D region were obtained. Using the silicon template (Figure 67, right, black), the measured I_D/I_G ratio of 0.97 was higher, however, the G and D peaks were less broad and a 2D peak with an I_{2D}/I_G ratio of 0.35 was obtained, indicating a slightly higher quality of the graphite material. As anticipated, both templates revealed a carbon coating after pyrolysis and no hollow tubes were obtained. In contrast and corroborating the formation of metal halides, copper, gold, and iron templates produced hollow carbon tubes. Copper (Figure 67, right, blue) and gold (Figure 67, right, orange) revealed similar Raman spectra with I_D/I_G ratios of 0.67 and 0.69, as well as I_{2D}/I_G ratios of 0.37 and 0.46, respectively. Iron, however, significantly increased the quality of graphite with an I_D/I_G ratio of 0.21 and an I_{2D}/I_G ratio of 0.51 (Figure 67, right, green). As the removed metal wire in combination with

EDX measurements and the verification of metal ions being present in the graphite indicated the formation of metal halides, whereby the differences in the obtained graphite quality presumably resulted from using different metals and the reactivity of the respective metal halides. Thus, iron chlorides appear to facilitate the highest regularity in the structure of produced graphite during pyrolysis.

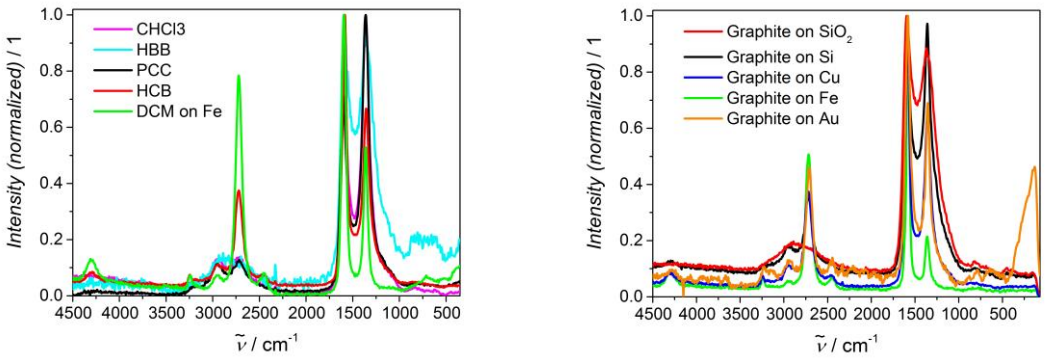

Figure 67: Raman spectra of different precursors in combination with an iron wire template (left), and of the most promising precursor dichloromethane on different surfaces (right). Left graph: Low qualities of graphite were obtained with I_D/I_G of 1.41, 1.21, and 0.96 using perchlorocoronene (black), hexabromobenzene (turquois), and chloroform (pink) as precursors, respectively. This low quality is corroborated by the insignificant and broad 2D regions. Higher qualities were achieved by providing hexachlorobenzene (red), and dichloromethane (green), giving I_D/I_G ratios of 0.67 and I_{2D}/I_G ratios of 0.37 and 0.61, respectively. Right graph: Pyrolysis of DCM achieved an I_D/I_G ratio of 0.88 on silicon dioxide, and I_D/I_G and I_{2D}/I_G ratios of 0.97 and 0.35 on single-crystalline silicon, 0.67 and 0.37 on copper, 0.21 and 0.51 on iron, and 0.69 and 0.46 on gold, respectively.

With the combination of DCM and iron as the most promising precursor and template material, respectively, three different ratios with Fe/Cl = 1/3, 1/2, and 1/6 were tested. A high ratio of chlorine atoms of Fe/Cl = 1/6 (Figure 68, black) resulted in a low graphite quality with I_D/I_G and I_{2D}/I_G ratios of 1.03 and 0.28, respectively. In contrast, a low ratio of chlorine atoms to Fe/Cl = 1/2 (Figure 68, red) gave a low I_D/I_G ratio of 0.20 and an I_{2D}/I_G ratio of 0.35. However, in this case the iron template was not completely removed and therefore the tubes were not entirely hollow. Fe/Cl = 1/3 revealed a high graphite quality with a low I_D/I_G ratio of 0.12 and an I_{2D}/I_G ratio of 0.47. The optimized spectrum revealed an intensive G-peak at 1580.3 cm^{-1}, a small D-peak at 1362.6 cm^{-1},

and a significant 2D-peak at 2732.5 cm^{-1}. Remarkably, in contrast to the decreasing quality of template-assisted graphene formations upon incrementally increasing the numbers of layers,[189-190] the produced hollow carbon tubes featured a high quality of graphite.

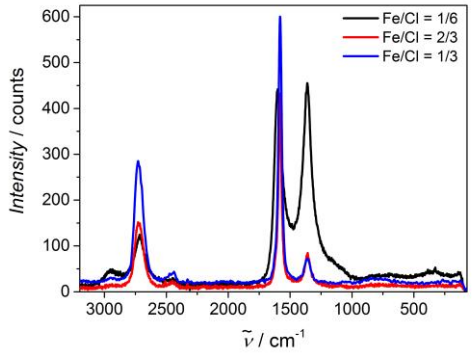

Figure 68: Raman spectra of the pyrolysis of DCM on an iron template with different iron to chloride ratios. The black spectrum shows a ratio of Fe/Cl of 1/6, the red spectrum of 1/2, and the blue spectrum of 1/3. The I_D/I_G and I_{2D}/I_G ratios were obtained as 1.03 and 0.28 for the black spectrum, 0.20 and 0.35 for the red spectrum, 0.12 and 0.47 for the blue spectrum, respectively.

Assessing these results, the following mechanisms during pyrolysis were proposed for the formation of hollow carbon tubes:

1) Initial heating of the mixture inside the ampoule distributes the precursors uniformly in the vapor phase by sublimation.
2) Elevated temperatures then promote surface catalyzed dissociation of the precursor, leading to a thin carbon coating on the template's surface. The metal reacts with the remaining halogens to metal halides, which enhances the formation of graphite.
3) Further heating allows for the sublimation of the in-situ formed metal halides. Their presence in the vapor phase further promotes the formation of regularly ordered graphite even in a micrometer-thick range, and facilitates intercalation between the graphitic layers.
4) By reaching and holding the temperature of 1000 °C for several hours, graphitization is finalized.

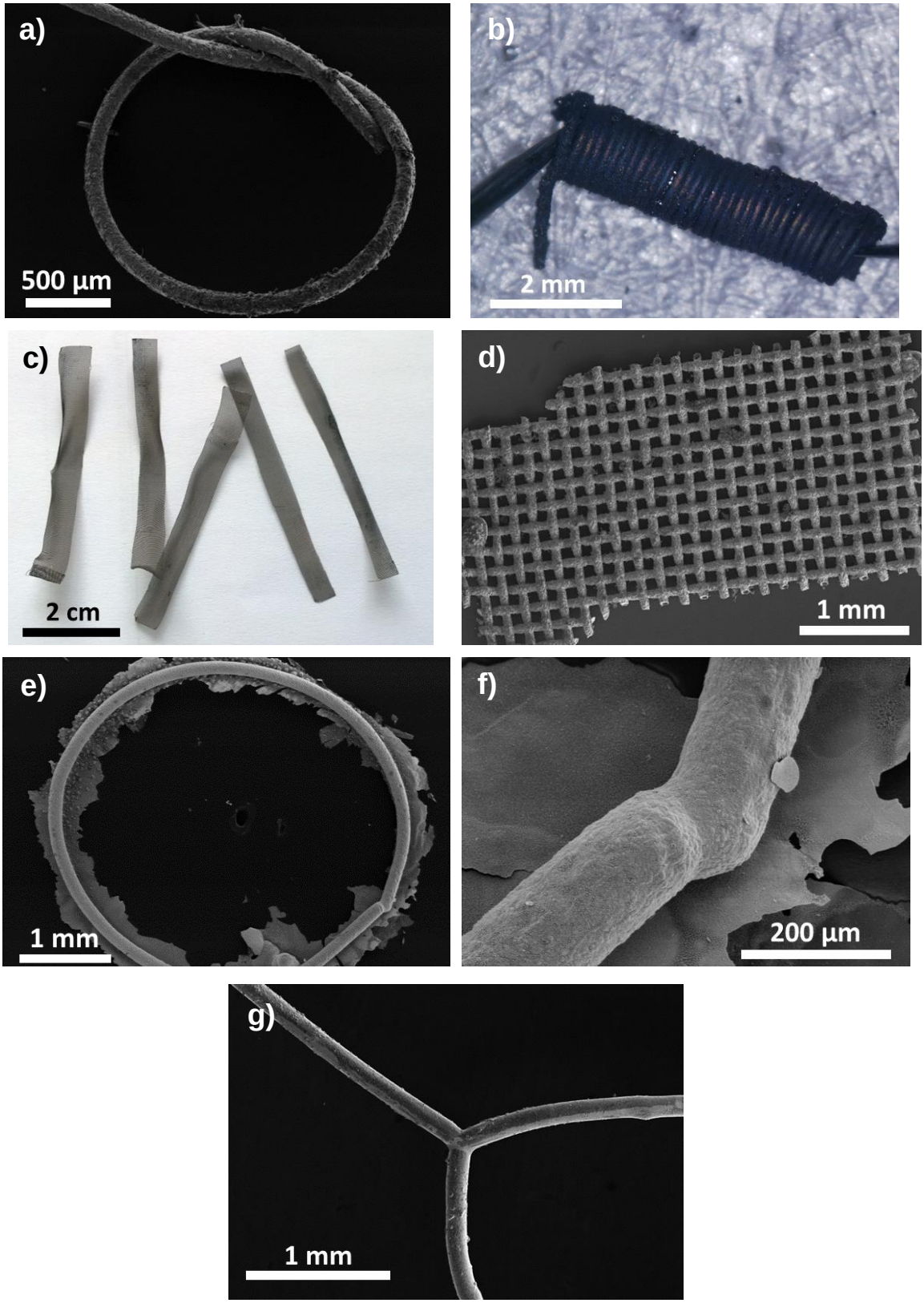

Figure 69: Different shapes of hollow carbon tubes. The figures show a) a SEM picture of a knot, b) an optical microscopy picture of a solenoid, c) a photograph of a mesh, d) SEM image of the hollow graphite mesh. The hollowness is corroborated by the breaking point of the individual tubes. e) A SEM picture of a toroid with an increased magnification of the point juncture in f). g) A SEM picture of a Y-shape.

With the phenomenon of the graphite hollow tubes being obtained as shape-persistent replica of applied metal templates, arbitrary shapes of metal wires were provided to fabricate the respective structures made of graphite materials. Exemplarily, copper templates of a knot, a mesh, a sorenoid, a toroid, and a Y-shape were prepared, with the resulting graphite hollow tubes being shown in Figure 69. The knot shows the possibility to produce twisted and bent shapes (Figure 69a). The solenoid (Figure 69b) featured an inner diameter of 130 µm, a width of 1 mm, and was prepared with 33 turns. The mesh (Figure 69c) was obtained with large dimensions of 5 x 0.5 cm². Its SEM picture revealed the woven structure and the hollow character of the tubes at the breaking points as depicted in Figure 69d. The possibility to fuse the ends of the tubes and therefore producing a closed and separated volume inside the hollow tube, a toroid with a diameter of 3.2 mm was developed (Figure 69e, a magnified image of the junction is visible in Figure 69f). Additionally, a Y-shape was prepared, connecting the ends of three different tube structures (Figure 69g). The different shapes prove the immense potential of this process towards customizing graphite, paving the way to a variety of applications.

With the available high quality of graphite and its high electrical conductivity of $1.41 \pm 0.01 \cdot 10^5$ S·m^{-1},[150] the conductivity of a hollow carbon tube with a wall thickness of 23 µm and an inner diameter of 130 µm was analyzed. Therefore, the electrical resistance of the tube against the tube length was measured with a four-wire resistance measurement configuration. The resulting resistances, plotted against the wire length, featured an Ohmic behavior (Figure 70). Linear fitting revealed a resistance of the hollow tubes of $1.56 \pm 0.07 \cdot 10^{-1}$ Ω·mm^{-1}. Considering the equation

$$\rho = \frac{R \cdot A}{l} \tag{1}$$

with ρ being the resistivity, R as resistance, A being the cross-section area of the wire, and l representing the length, the resistivity of the tube was calculated. According to the small cross-section area of $5.00 \cdot 10^{-3}$ mm², a low resistivity of $\rho_{Tube} = 7.66 \pm 0.35 \cdot 10^{-7}$ Ω·m was obtained. The conductivity as reciprocal value of the resistivity gave $\sigma_{Tube} = 1.31 \pm 0.05 \cdot 10^6$ S·m^{-1}. This conductivity was almost one magnitude higher than the reported value for graphite. The conductivity enhancing effect was ascribed to the intercalation of the metal halides as impurities in the graphite lattice, as similar effects were already reported elsewhere to facilitate lower resistances.[175]

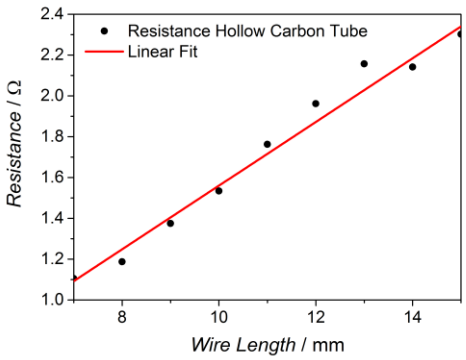

Figure 70: Resistance measurements of a hollow carbon tube at incremental distances. The linear fit reveals a slope of 1.56 ± 0.07 · 10^{-1} Ω·mm^{-1}.

In accordance to the superior conductivity of the graphite material and its ability to adopt arbitrary shapes, it was tried to process transparent layers of graphite onto silicon dioxide surfaces, as there is a basic necessity for transparent, conductive material on dielectric substrates like silicon dioxide for the use as electrodes in photoelectrical devices. As it was shown Figure 67, *right*, providing silicon dioxide as precursor resulted in a poor quality of grahite, whereas copper gave high qualities and was removed throughout the process. Therefore, instead of using bare silicon wafers, the latter were sputtered with a 10 nm thick copper layer prior to applying them to the elaborated procedure (Figure 71, *left* and *middle*).

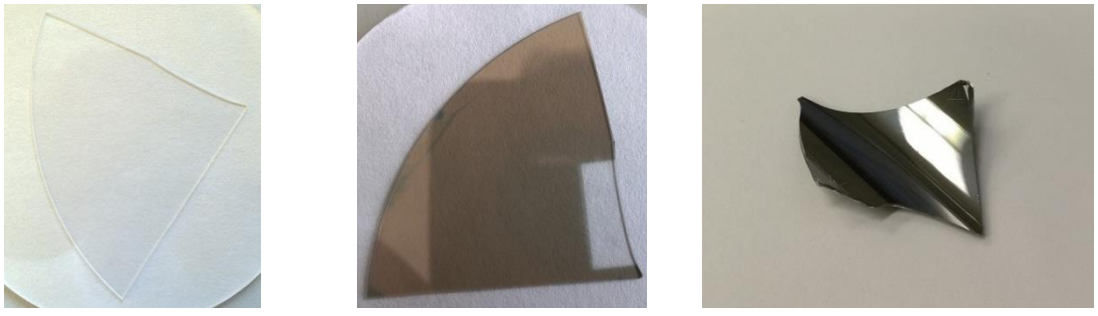

Figure 71: Pictures of a bare silicon dioxide wafer piece (left), of the same wafer piece covered with a 10 nm thick copper layer (middle), and of a wafer piece covered with a ~41 nm thick, metallic reflective graphite layer (right).

The as prepared SiO_2/Cu-wafer pieces were provided as templates with different amounts of DCM as precursor. A typically accrued graphite covered wafer piece is

visible in Figure 71, *right*. The thickness of the graphite layer on the wafer pieces was measured with a profiler, its sheet resistance with a 4-wire measurement device, and the transparency with an UV/Vis device at 500 nm. The different results for applying 50 µL, 25 µL, 10 µL, and 5 µL DCM are summarized in Table 3. As anticipated, with a decreasing amount of provided DCM, the graphite layers became thinner. It was, however, not possible to produce a layer thickness smaller than 40.7 nm, as handling less than one drop of DCM resulted in an irreproducible process due to the low vapor pressure. A desired transparency was only visible in the thinnest case of 40.7 nm, being as low as 2%. Although the thickness was significantly reduced, the low transparency cannot keep up with transparent conductive electrode material, such as indium tin oxide with values of ~95 % and fundamentally prevents the applicability, as the loss of incident light intensity would cause a bad performance of the photoelectric device. All of the produced graphite coatings resulted in a sheet resistance between 1.64–2.41 kΩ·□$^{-1}$, which was relatively high compared to graphene on SiO_2 results in literature with 63 Ω·□$^{-1}$.[191] Remarkably, reducing the provided amount of DCM from 50 µL to 25 µL did not change the sheet resistance of the coating. Further lowering the DCM content to 10 µL and 5 µL, however, resulted in a significant increase of the sheet resistance. This behavior in combination with the high sheet resistance accounts for the formation of small graphite crystallites instead of an interconnected, large graphite crystal. Therefore, the resistance does not change up to a certain thickness, as the interlayer conductivity with a graphite flake overlapping two other flakes is predominant being able bypass these two flakes over their grain boundaries. When the thickness is too low, the amount of graphite layers connecting other crystallites is too low, requiring the electrons to hop over the grain boundary to the adjacent crystallite, therefore increasing the resistance.

Table 3: Layer thicknesses, sheet resistances, and transparencies of graphite layers on silicon dioxide wafer pieces, depending on the amount of applied precursor.

	50 µL DCM	**25 µL DCM**	**10 µL DCM**	**5 µL DCM**
Layer thickness / nm	93.6	63.3	44.0	40.7
Sheet resistance / kΩ·□$^{-1}$	1.64	1.63	1.84	2.41
Transparency /%	0	0	0	2

3.3. Summary

Initial experiments for obtaining hollow carbon tubes were carried out by coating metal wires with hexadodecyl-HBC. However, after pyrolysis a carbon film homogeneously covering the wire surface remained elusive, which also did not change significantly by randomly crosslinking the hexadodecyl-HBC molecules with an electron beam prior to pyrolysis. Furthermore, these approaches classified solution-based approaches for producing hollow carbon tubes as not efficient, due to required preceding time-extensive treatment of the precursor material for graphitization. The thus produced material featured such small dimensions, that it was not found after etching for further characterization. Therefore, an alternative, novel one-step protocol was elaborated, utilizing a vapor-based distribution of precursor material onto an applied metal wire inside an evacuated quartz ampoule. As precursor compounds, different halogenated compounds like hexachlorobenzene or dichloromethane were used. Without further treatment, hollow carbon tubes were received after pyrolysis at 1000 °C. The tubes were obtained as hollow replica of the wires, not collapsing and retaining the shape of the provided metal. This attribute paved the way for producing arbitrary forms like a toroid, a Y-shape, or a mesh. Changes in the diameter of applied wires resulted in the respective inner diameters of the tubes. Increasing the amount of precursor produced thicker tube walls. Characterizations of the produced hollow carbon tubes by means of Raman spectroscopy revealed a high quality of the graphitic material. This quality, however, was found to be fundamentally dependent on the combination of metal and organic halide, and on the ratio of precursor to template. To investigate the whereabouts of the template, the tubes were measured with EDX. Analyzing cross-sections of the wall showed an increasing amount of both metal and halogen from the inside to the outside. The outer surface provided homogeneous distributions of carbon, metal, and halogen and thus suggested incorporation of the metal and halogen atoms in the carbon material. Due to the applied metals not being volatile at 1000 °C and in consideration of the increasing amount of metal and halogen from the inside to the outside of the tube wall, a reaction of the organic halide with the metal at elevated temperatures was assumed, producing carbon and the respective metal halide. As metal halides exhibit significantly lower sublimation temperatures than the bare metals, the pyrolysis conditions allowed for evaporation and incorporation into the carbon material. The formation of metal halides was further corroborated by wet-chemical analyses. Eventually corroborating the regular structure of graphite, a high conductivity

was measured, even exceeding the one for pristine graphite. This behavior was ascribed to the inclusion of metal ions in the material.

4. Disulfide-Bridged Coronenes for Li-S batteries

4.1. Introduction

The previous chapters showed the possibilities lying in 2D materials from two different perspectives. Both topics however were intrinsically based on the two-dimensionality of the structures or the two-dimensionality was presumed as a basic requirement for subsequent utilizability in certain applications. Another option of using the beneficial properties of 2D structures is the implementation in well-established applications to overcome existing disadvantages. One of those issues concerns the supply of sustainable energy as one of the main challenges of today's society. While in the field of energy harvesting systems new and advancing technologies have set steadily increasing benchmarks, progress in the field of energy storage remained restrained in the last decades.[192] Nevertheless, advances in battery technology concerning their chemistry and engineering revolutionized technologies like Li-ion and nickel-metal hydride batteries. Li-ion batteries revealed a longer cycle lifetime, higher energy densities, and were more compact and lightweight than other existing batteries.[193] Typically, Li-ion cells undergo a topotactic intercalation reaction, which is a minimal change to the structure of a solid, being able for reversible uptake of electrons and lithium. Conventionally, lithium phosphates or lithium transition-metal oxides are used as cathode material for deintercalation of lithium ions at high potentials.[194] Due to a topotactic way of operation of the cell at both electrodes, the charge storage capability is intrinsically limited to 300 $mA \cdot h \cdot g^{-1}$, leaving reported benchmark values of up to 180 $mA \cdot h \cdot g^{-1}$.[195]

One of the most promising approaches in the category of Li-ion batteries are Li-S cells. The electrochemical reaction does not follow topotactic processes, but rather dissolves lithium from the anode during discharge, and deposits it back to the electrode during charging, principally not limiting the procedure.[196] The simplest configuration of such a cell consists of lithium as anode material and elemental sulfur as cathode.[197-198] Theoretically, such cells feature remarkably high capacities of 1675 $mA \cdot h \cdot g^{-1}$, high energy densities of 2500 $W \cdot h \cdot kg^{-1}$,[199] and a redox potential of the reaction $S_8 + 16\,Li \leftrightarrow 8\,Li_2S$ of 2.2 V,[200] however assuming a complete reaction to Li_2S. Deviations of these values in devices typically appear due to several disadvantages:

1) Elemental sulfur is ionically and electrically insulating,[201] urging the need for close contact with electrically conductive additives. Those are typically limited in the size of their contact areas.
2) The electrolyte solution has to act as electron as well as ionic conductor to facilitate ion transport inside the cathode.[202]
3) During discharge produced poly(sulfide) anions as intermediates are soluble in polar organic solvents, which are typically applied with electrolytes.[203] These poly(sulfide) anions experience a shuttle effect, describing the process of the anions to diffuse through the separator and reacting at the anode to insoluble Li_2S or Li_2S_2, therefore reducing the amount of active material in the cell.[204-205]

Although advances in research were able to reduce the number of occurring problems by providing new electrolytes[206-209] and by coating the lithium anode with a protecting layer,[210-213] the majority of problems is still caused by the cathode material. A prominent approach to face the problem of shuttle effects is to anchor disulfide units covalently to polymer systems.[214-215] The redox reaction of this chemistry is then based on the reversibility of an oxidation of thiolates, which form the respective radical as an intermediate, subsequently coupling to disulfides.[216-217] Exemplarily, *Xu* et al. prepared cathodes with poly(vinylchloride) disulfide as active material with capacities of 400 $mA{\cdot}h{\cdot}g^{-1}$ and good cyclability.[218] Instead of anchoring disulfide units, other approaches to improve the electrochemical properties of cathode materials include incorporation of sulfur by blending into polymer matrices, adding redox mediators, or nanostructuring.[194, 219-226] For example, *Wang* et al. used a poly(acrylonitrile) matrix to embed sulfur, preventing aggregation of sulfur and the dissolution of poly(sulfide) anions into the electrolyte.[227] However, the performance of the cell was somewhat limited as a maximum of the sulfur loading of 55 wt% into the matrix reduced the energy density of the cell, and occurring polarizations resulted in low operating voltages. *Frischmann* et al. used a substituted polycyclic aromatic hydrocarbon (PAH) perylene diimide-poly(sulfide) gel as redox mediator to enhance limitations regarding charge-transport and for stabilization of the intermediate sulfide adducts. Capacities up to 267 $mA{\cdot}h{\cdot}g^{-1}$ were reported, with Coulombic efficiencies of 81%.[228] Although these electrochemical properties exceed the values obtained for Li-ion batteries, there is still space for improvement according to the theoretical capacity of Li-S batteries.

The disadvantages of the conventional sulfur cathode were to be overcome by using a 2D material. A small PAH unit was selected be modified with redox-active disulfides. Thus, the low conductivity of sulfur should be enhanced by a conductive backbone, and the redox-active surface should be increased while at the same time preventing

the formation of poly(sulfide) anions and the shuttle effect by anchoring the sulfur atoms to the aromatic core. Keeping in mind the theoretically achievable capacity to be mainly influenced by the sulfide content, the ratio of sulfur to carbon was supposed to be as high as possible. Coronene as PAH featuring ion mobilities[229] was planned to be persulfurated. Although sulfur-rich PAH compounds, such as sulfur-annulated HBCs,[230-231] hexathienocoronene,[232] tribenzotetrathienocoronene,[233] hexathiotriphenylene,[234-235] and acene sulfide[236-238] have already been studied extensively in literature,[239] PAHs completely substituted with disulfide units in their periphery remained elusive, hence sulfur contents were limited. Considering their outstanding charge transport and redox properties, which render them suitable for organic photovoltaics and organic field effect transistors, expanding the available library of sulfur-rich PAHs by per(disulfide) substituted coronene is desired. It has to be noted, that *Sülzle* et al. reported on per(disulfide) benzene in 1989, but were not able to synthetically prepare or provide structural proof of this molecules apart from charged fragments in mass spectrometry analysis.[240]

For preparing cathode material for lithium-sulfur batteries, two different approaches were to be followed. First, the small molecule per(disulfide)coronene **40** was designed for synthesis and subsequently was planned for an application as cathode material. Second, a material **42** based on persulfurated coronene was to be prepared by randomly crosslinking the **40** molecules with disulfide bridges. The characterization of **42** should follow the characterization regarding its electrochemical properties in respect to **40**.

4.2. Results and Discussion

4.2.1. Per(disulfide)coronene as Small Molecule Cathode Material in Li-S Batteries

4.2.1.1. Synthesis

Synthesis of **40** was done in collaboration with [redacted]. Starting from commercially available coronene **36**, perchlorination was conducted with iodine monochloride in tetrachloromethane, using aluminium chloride as catalyst to yield 91% of perchlorocoronene **37**. The chlorine units were subsequently replaced by benzyl thiolate in a nucleophilic substitution reaction at room temperature, with the benzyl thiolate being prepared *in situ* by deprotonation of benzyl mercaptan with sodium hydride. After work-up, per(benzylthio)coronene **38** was obtained in 62% yield. Consecutive cleavage of the benzyl protection group under Birch reduction conditions with lithium in liquid ammonia[241] lead to lithium coronene perthiolate **39** as crude product without further purification, due to its high air sensitivity. Further reaction with hydrochloric acid in water gave the target compound **40** after purifying in 10% yield (Scheme 11). The reduction of **40** to perthiol coronene **41** is shown schematically, as it was prepared *in situ* for characterization in 4.2.1.2.

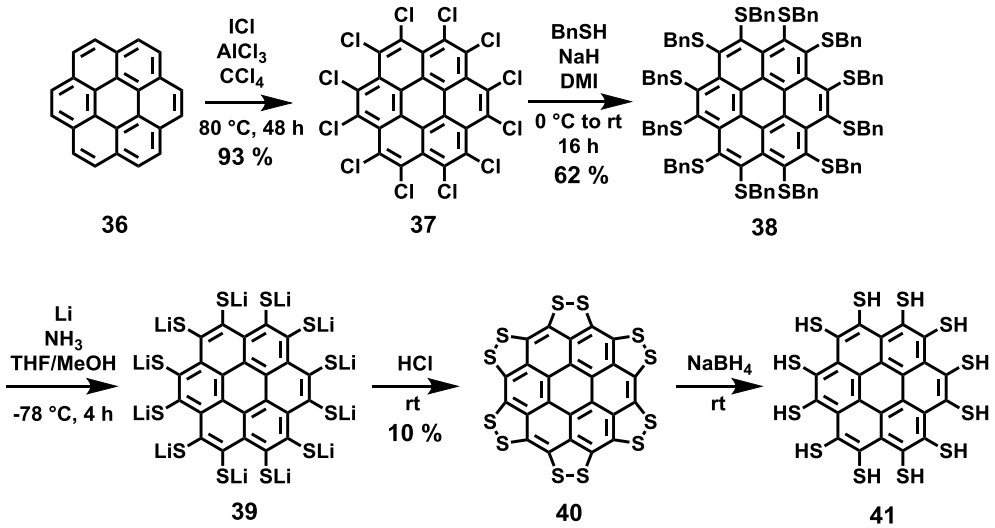

Scheme 11: Reaction path for the synthesis per(disulfide)coronene **40** and its reduced analogon perthiol coronene **41**.

4.2.1.2. Characterization of 40

Characterization of **40** was done in collaboration with [redacted]. Structural characterization of **40** was challenging due to a marginally small solubility in organic solvents, even at elevated temperatures. Therefore, conventional characterization methods like NMR spectroscopy or single crystal XRD were not applicable as the concentrations were too low to obtain an appropriate signal or to prepare a single crystal.

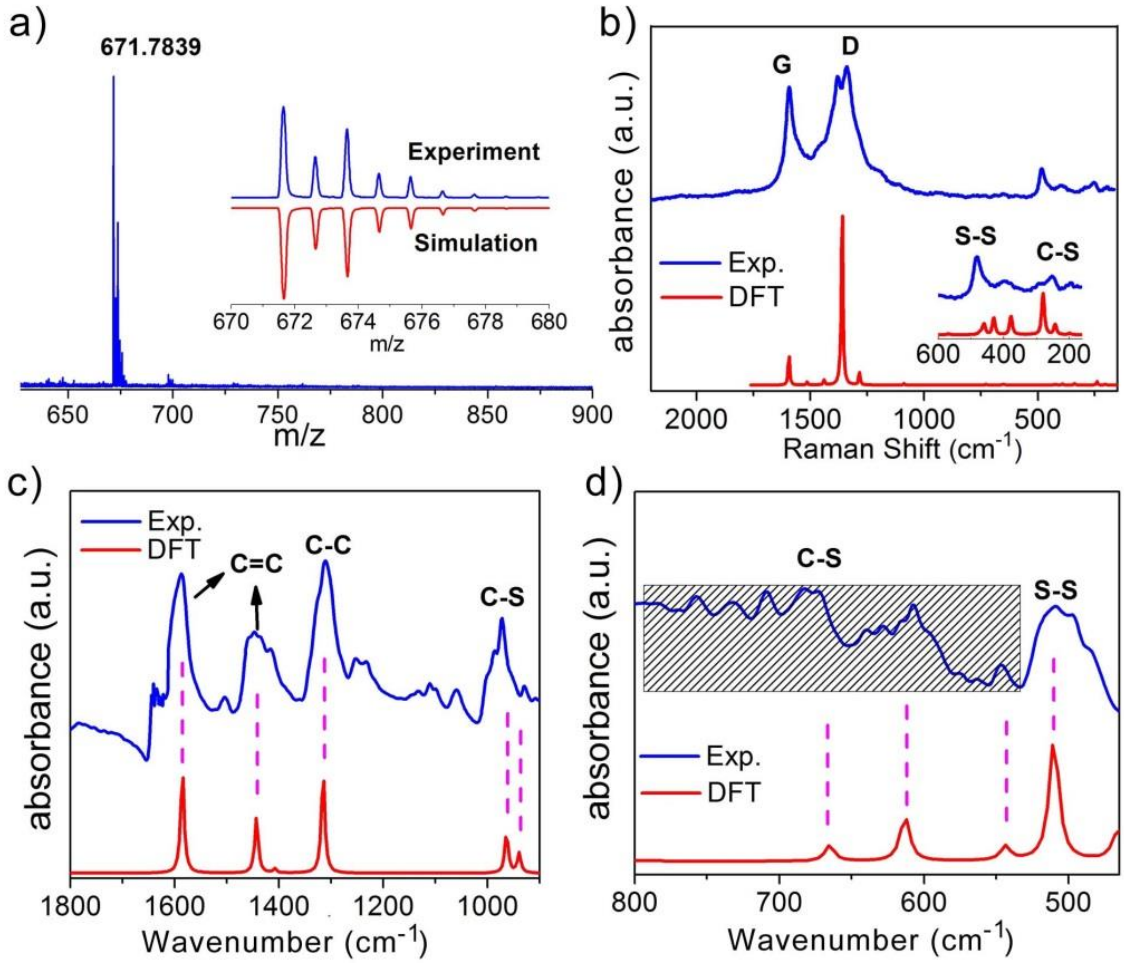

Figure 72: Characterization methods for the structural proof of **40**. a) MALDI-ToF mass spectrum of **40**. The peak is in accordance with the calculated mass of $C_{24}Cl_{12}$ and features an identical isotope pattern. b) Raman spectrum of **40** (blue) and the spectrum derived from DFT calculation (red). The inset reveals a magnified area between 200-600 cm^{-1}. c) IR spectrum of **40** (blue) and the calculated DFT spectrum (red). d) Magnified area from 400-800 cm^{-1} of the spectrum in c).

First structural proof was achieved by MALDI-ToF mass spectrometry with tetracyanochinodimethane (TCNQ) matrix from solid state. The spectrum revealed a single peak at *m/z* = 671.8, which is in good agreement with the calculated mass of $C_{24}Cl_{12}$ with 671.7 u. The characteristic isotope pattern perfectly overlapped the experimental result (Figure 72a). The solid was further analyzed by Raman spectroscopy and compared with its DFT-calculated spectrum (Figure 72b). The measured spectrum featured a D peak at 1382 cm^{-1} and a G peak at 1594 cm^{-1}. In contrast to graphite, the D peak does not indicate the presence of defects rather than appearance due to the edge states of coronene. Additional peaks at lower wavenumbers and with lower intensities were found at 256 cm^{-1} (C-S in-plane bending), 392 cm^{-1}(C-S deformation), and 482 cm^{-1} (S-S bond deformation).[219-220] The good agreement of the experimental Raman shifts in comparison with the calculated ones are shown in Table 4.

Table 4: Raman shifts of **40** found in the spectrum and compared to DFT-calculated values with respective assignments.

Raman Shift (Experiment) [cm^{-1}]	Raman Shift (Calculation) [cm^{-1}]	Vibration Mode
256	279	C-S in plane bending
392	377	C-S deformation
482	458	S-S
1212	1282	ring stretching
1382	1396	D band
1594	1630	G band

40 was further analyzed by IR spectroscopy. A powder sample was measured on an ATR crystal and compared with the spectrum derived from DFT calculation (Figure 72c-d). The experimental spectrum revealed five major peaks at 1588 cm^{-1} (C=C asymmetric stretching), 1447 cm^{-1} (C=C symmetric stretching), 1309 cm^{-1} (C-C deformation), 930 cm^{-1} (C-S stretching), and 509 cm^{-1} (S-S stretching).[219] These signals only deviate marginally from the calculated values (Table 5). The weak signals between 545-757 cm^{-1} were too unincisive to be assigned unambiguously to the anticipated weak C-S vibrations.[242]

Table 5: IR peaks of **40** found in the measured spectrum compared to calculated values with respective assignments.

IR Frequency (Experiment) [cm^{-1}]	IR Frequency (Calculation) [cm^{-1}]	Vibration Mode
1588	1585	C=C asymmetric stretching
1447	1444	C=C symmetric stretching
1309	1312	C-C deformation
971	964	ring breath (side-chain containing S-S)
930	939	C-S stretching
757-545	666	C-S stretching
757-545	612	C-S stretching
757-545	543	C-S stretching
509	510	S-S stretching

STM is a powerful tool to give information about the topology and electronic properties at atomic scale.[243-245] The measurements were performed in collaboration [redacted]. Isolated single molecules of **40** were processed onto an Au(111) surface by thermal vapor deposition at a low rate. During the measurement, the sample was cooled to 5 K to prevent thermal fluctuation of the single molecules on the surface. **40** molecules were found adsorbed to kink sites of the "herringbone" reconstructed gold surface, visible by the bright spots in Figure 73a.[246] Higher magnifications of these spots reveal hexagonal species, being in agreement with an anticipated D_{6h}-symmetry (Figure 73b,c). Desulfurization during depositions can be excluded by the shape of the apparent molecules, as pristine coronene molecules are visible as flower-shaped molecules instead of the rather round shape,[244] and partial desulfuration would result in a shape of lower symmetry The cross-section through the molecular axis reveals a slight decrease of height from the edges of the molecule to its middle, demonstrating the distribution of carbon and sulfur with their different atomic radii in the molecule (Figure 73d). *d*I/*d*V-Spectroscopic analysis was done at different positions of the molecule (Figure 73e). Whereas the bare gold substrate (Figure 73e, blue) exhibits an almost identical behavior as the middle of the molecule (Figure 73e, red), the edge of **40** exhibits a significant resonance at 1.2 V, revealing an increased electronic density of states in the periphery

of **40** compared to its middle.[247-249] Thus, the STM measurements prove the proposed structure of **40**.

The reducibility of the disulfide bonds in the periphery of **40** was tested by reaction with sodium borohydride in THF. After drying, a peak at $\delta = 2.81$ ppm was visible in ^{1}H NMR spectroscopy, which again disappeared upon exposure to the oxidative conditions in air, thus indicating successful reduction of the disulfide units of **40**. The completeness of the reduction of all disulfides of **40** was analyzed by MALDI-ToF MS, revealing one single peak at *m/z* = 685.5, corroborating the presence of **41** with the calculated value of $C_{24}S_{12}H_{12}$ with 685.1 u. The process of reduction of **40** with $NaBH_4$ was followed with UV/Vis spectroscopy (Figure 74a). The low solubility of **40** in NMP was with ~$1 \cdot 10^{-6}$ M nonetheless sufficient for obtaining an absorption spectrum. The latter reveals a broad and weak absorption in the range between 400-600 nm. Addition of 24 eq $NaBH_4$ resulted in an increased absorption, which remained constant after 30 min, revealing a λ_{max} of 314 nm, and two shoulders at 380, and 508 nm, respectively.

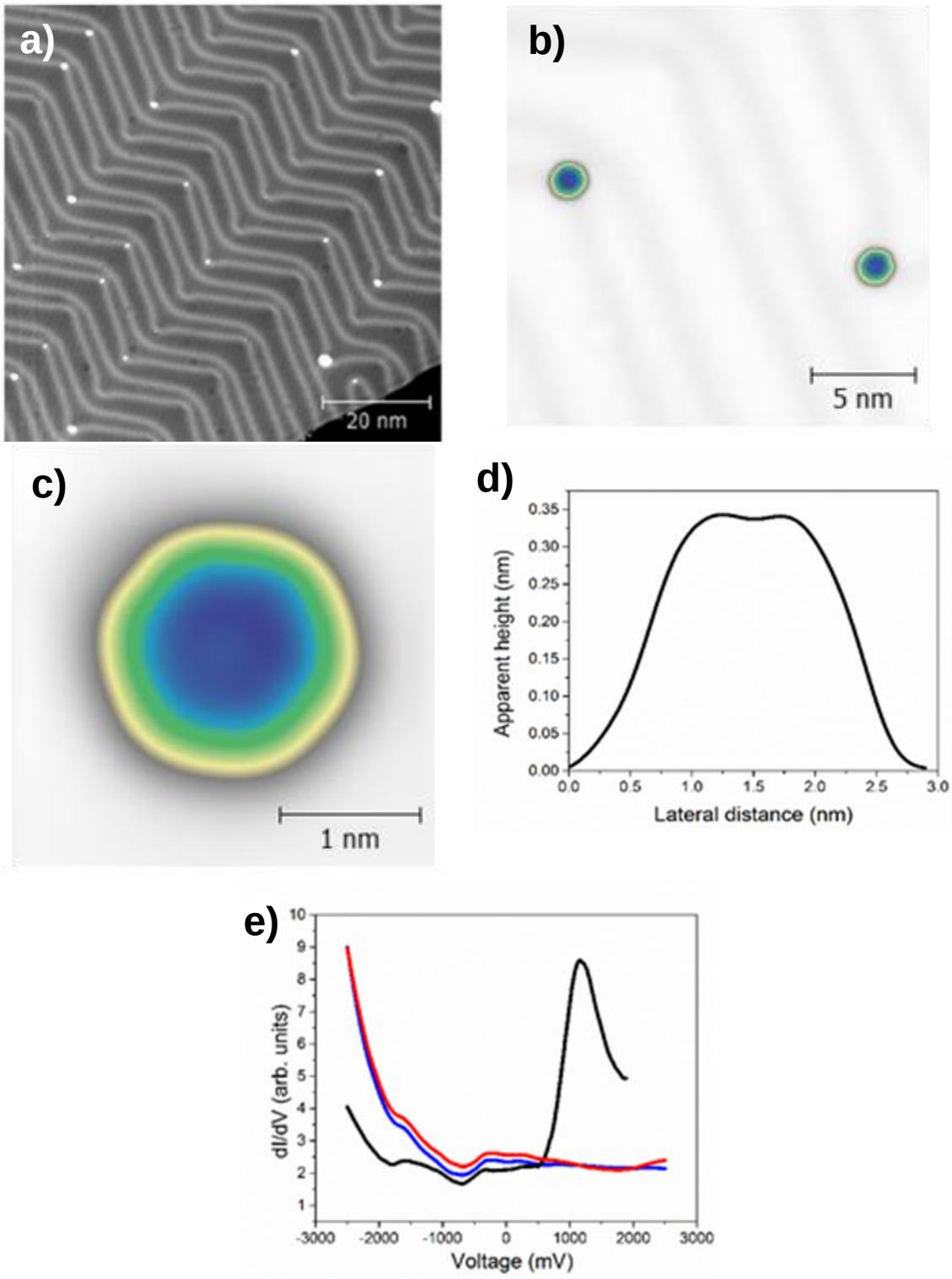

Figure 73: a-c) STM images of **40** on the Au (111) surface. a) Individual molecules are visible at bright spots at the kink sites of the "herringbone" reconstructed gold surface and at the edges of the terraces. b) Two **40** molecules on the surface with a higher magnification. c) Individual **40** molecule, revealing its hexagonal structure. d) Cross-section through **40**. e) *dI*/*dV*-Spectroscopy at different positions. The blue curve was measured as reference on the bare gold surface, the red curve was recorded at the center, and the black spectrum at the edge of the molecule, respectively.

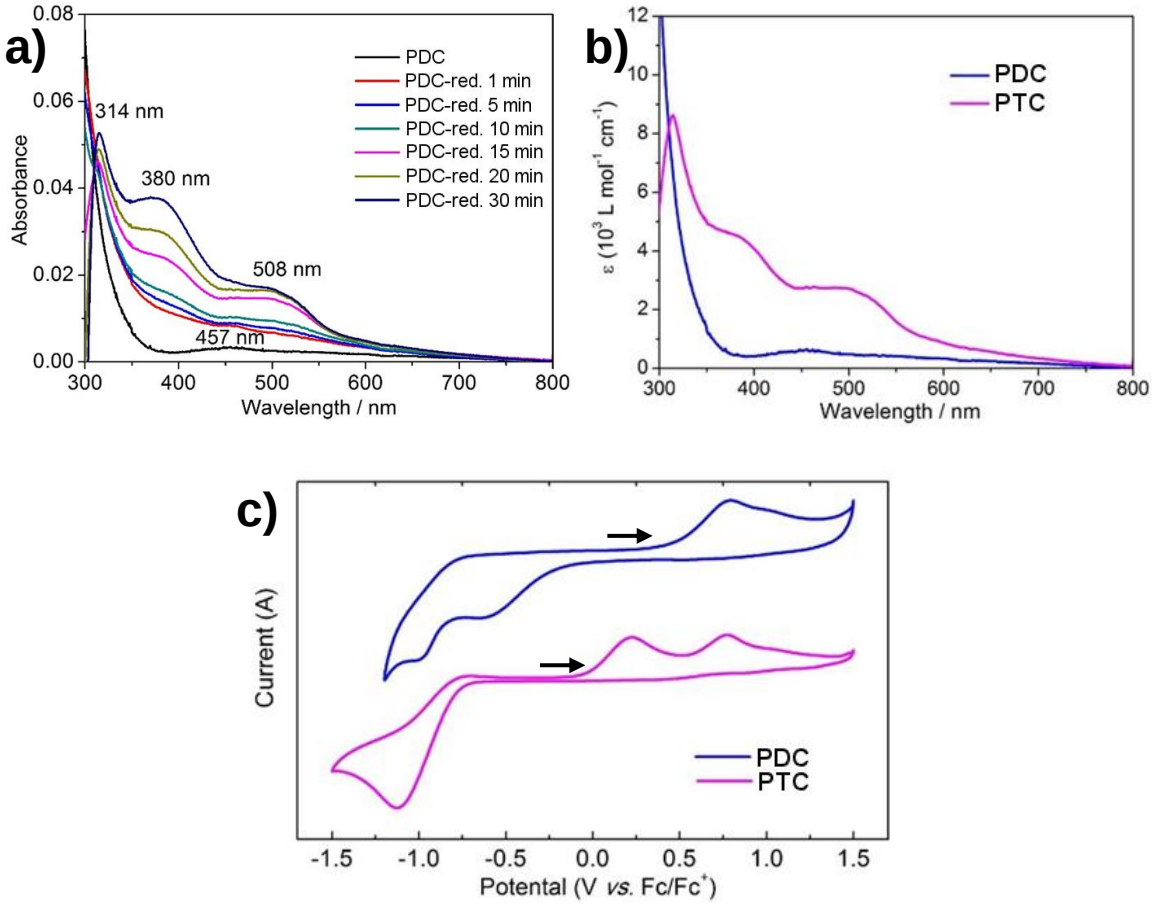

Figure 74: a) Differences in the UV/Vis spectra of **40** with addition of 24 eq of $NaBH_4$ after incremental time spans. The notation **40-red.** denotes the mixture with the reducing agent $NaBH_4$. b) UV/Vis spectrum of **40** (blue) and **41** (pink). c) Cyclic voltammetry measurement of **41** (pink) and **40**(blue) in THF against ferrocene.

According to the spectra of bare **40** and bare **41**, optical bandgaps were estimated using the intersection of a linear regression at the respective absorption peaks at λ_{max} = 457 nm and λ_{max} = 508 nm and the axis of abscissas (Figure 74b). To reduce inaccuracies, the peaks were each fitted with a Lorentz function. As intersections, 588 nm for **40** and 612 nm for **41** were derived. Thus, the optical bandgaps equal to 2.1, and 2.0 eV, respectively. Electrochemical measurements on **40** and **41** in THF by cyclic voltammetry with respect to ferrocene were performed (Figure 74c). Importantly, cycling does not result in irreversible processes like decomposition, therefore indicating feasibility of the materials in battery application. Based on the first oxidation potentials, the HOMO energies were calculated, using the equation:[250]

$$E_{HOMO} = -\left[E_P^{ox} - \frac{1}{2}E^0_{Ferrocene} + 4.8\right] eV \qquad (1)$$

with E_P^{ox} being the first oxidation potential and $E^0_{Ferrocene}$ as the redox potential of ferrocene against the standard hydrogen electrode.[251] The LUMO levels of **40** and **41** were calculated in respect to the HOMO values and band gaps.

Table 6: Band gap values, as well as HOMO and LUMO levels of **40** and **41**, obtained from optical and electrochemical measurements, compared with calculated values.

Substance	$E_{g,opt}$[a] / eV	$E_{HOMO,CV}$[b] / eV	$E_{LUMO,CV}$[c] / eV	$E_{HOMO,cal.}$[d] / eV	$E_{LUMO,cal.}$[d] / eV	$E_{g,cal.}$[d] / eV
40	2.1	-4.7	-2.6	-5.31	-3.27	2.04
41	2.0	-4.27	-2.27	-5.74	-2.79	2.95

[a]Optical band gaps were calculated from the onsets of the UV/Vis-absorption spectra. [b]HOMO levels were obtained from the oxidation potential of CV measurements. [c]LUMO values were calculated from the HOMO levels and the optical band gap. [d]Values were calculated from geometry optimized structures, using DFT with B3LYP/6-31G (d,p) basis set.

The obtained energy gaps and HOMO and LUMO values of both **40** and **41** are listed in Table 6 and compared with theoretical values.

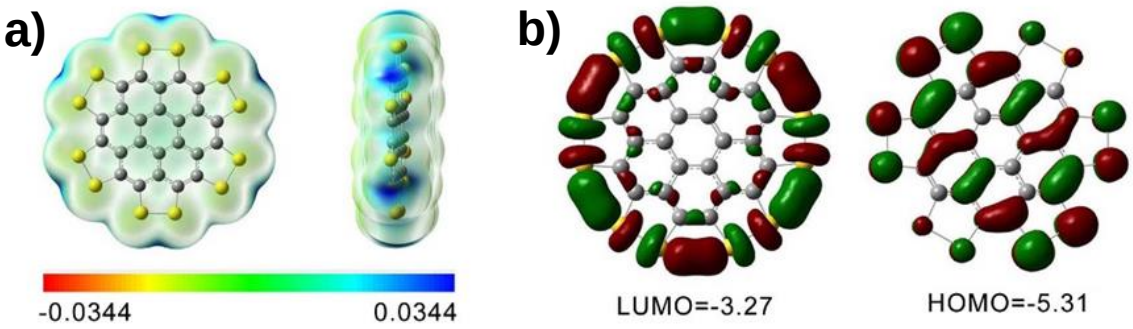

Figure 75: Theoretical results for **40**, calculated using DFT with a B3LYP/6-31G (d,p) basis set. a) Molecular structure and its electrostatic potential surface. b) LUMO (left) and HOMO (right) fragment orbitals with respective orbital energies given in eV.

The influence of disulfide bridges in the periphery of coronene was further investigated with DFT calculations, which were performed by [redacted]. The electrostatic potential surface clearly

corroborates the high electron density located at the disulfide bridges, as already suggested by *d*I/*d*V spectroscopy. Notably, orbital lobes of the LUMO are located exclusively to the periphery instead of being delocalized over the carbon framework.

4.2.1.3. Application of 40 as Cathode Material for Li-S Batteries

The high sulfur content and the redox behavior leave **40** as promising candidate for use in Li-S batteries. Additionally, the low solubility of **40** should provide a good stability during charge-discharge cycles. Figure 76 reveals the suggested charge and discharge mechanism for a one-electron transfer reaction per sulfur atom.

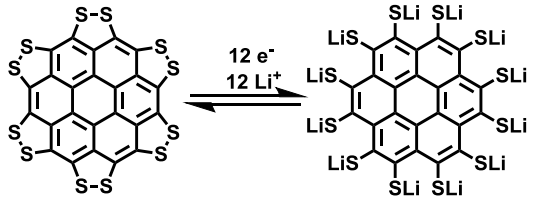

Figure 76: Suggested mechanism for complete charge and discharge cycles with **40** as cathode material, using a one electron transfer per sulfur atom.

If a complete charging and discharging cycle involving 12 electrons is considered, the theoretical capacity ($C_{theoretical}$) of the cell equals to:

$$C_{theoretical} = \frac{n\,F}{MW} = \frac{12\ x\ 96485{,}3{\cdot}10^{3}\,s\ mA\ mol^{-1}\cdot 1\ h}{671.8\ g\ mol^{-1}\cdot 3600\ s} = 478.6\ mA\ h\ g^{-1} \quad (2)$$

n represents the number of electrons available for reaction, F is the Faraday constant, and MW the molecular weight of the active material.

Preparation of the cells and measurements were done in collaboration with [redacted]. Cathodes were prepared by mixing 70 wt% **40** with 20 wt% acetylene black and 10 wt% poly(vinylidene fluoride). The mixture was processed onto an aluminum foil and placed into a coin cell with a diameter of 12 mm. Between the cathode and lithium foil, a porous polypropylene separator was provided. 1.0 M lithium bis-trifluoromethanesulfonylimide (LiTFSI) in a 1:1 mixture of 1,3-dioxolane (DOL) and 1,2-dimethoxyethane (DME) by volume with an additive of 0.1 wt% $LiNO_3$ was used as electrolyte.

The charge-discharge curves using **40** were recorded at 0.6 C. The C-rate represents the charge and discharge current in respect to the specific capacity of the battery cell. Initial cycling resulted in charge and discharge capacities of 496 and 424 $mA \cdot h \cdot g^{-1}$, respectively. Thus, an initially high Coulombic efficiency (ICE) of 85% was achieved. This value already meets the benchmarks of reported S_8-incorporated cathodes and organic matrix/sulfur composites.[194, 219-226] Remarkably, the initial plateau at 1.8 V increased to 2.0 V during subsequent cycles and remained stable. As this change appeared mainly during the first cycle and changed towards a completely reversible charge-discharge behavior, in combination to the electrochemical stability of both **40** as well as **41** suggested by CV analysis, this increasing plateau was ascribed to a change in morphology, which reorganized during the first cycles to a more stable appearance. However, the general presence of only one plateau deviated from comparable S_8-cathodes, typically exhibiting two-steps during the discharge cycle. Thus, the first plateau appeared due to the formation of Li polysulfides at 2.35 V, whereas the second plateau occured at 2.1 V with the formation of Li_2S.[194, 221-223] The absence of the higher plateau suggested a one-electron process per sulfur atom, implying the reversible formation of a lithium sulfide complex from disulfides and vice versa as anticipated in Figure 76. However, during subsequent cycles the **40** material did not only show a stable cycling performance, but rather revealed the specific capacity as well as the Coulombic efficiency to increase to values of 520 $mA \cdot h \cdot g^{-1}$ and 90% ICE. Considering the calculated theoretical capacity with equation (2) of the **40** cell of 478.6 $mA \cdot h \cdot g^{-1}$, a larger amount of electrons has to be included into the process, as the molecular weight of **40** is unlikely to change. With the achieved capacity of 520 $mA \cdot h \cdot g^{-1}$, equation (2) suggests the active participation of 13 electrons in the process. As only twelve sulfur atoms are present in the periphery of coronene, the 13^{th} electron has to react either with coronene, or with an already complexed lithium-sulfur compound. In both cases, an additional plateau would be evident, visualizing the presumed different redox potential. The absence of this second plateau can be explained by the possible charge distribution over the whole molecule, thus being able to stabilize an additional charge via the extended π-system. This was corroborated by the shape of the charge-discharge profiles, which featured a continuous increase for the charge curve and decrease for the discharge curve of voltage instead of a plateau over a large area, as it is e.g. visible for the first charge-discharge curve.

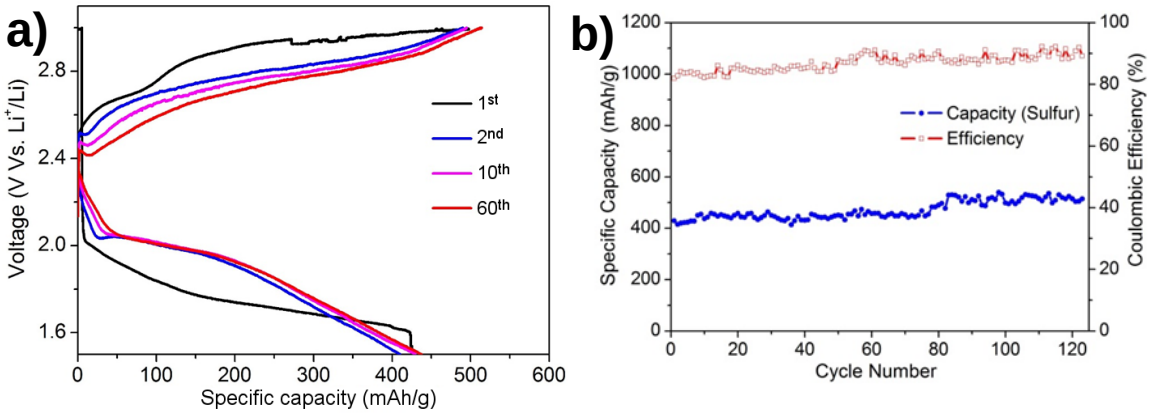

Figure 77: Electrochemical measurements of **40**, applied as cathode material in Li-S batteries. a) Discharge and charge voltage profiles after 1st (black), 2nd (blue), 10th (pink), and 60th (red) cycle. The profiles were measured at a potential rate of 1-3 V vs. Li/Li+. b) Specific capacity relative to the weight (blue) and efficiency (red) of the cell as function of the cycle numbers.

4.2.2. Randomly Disulfide-Bridged Persulfocoronene as Polymer Cathode Material in Li-S Batteries

4.2.2.1. Synthesis

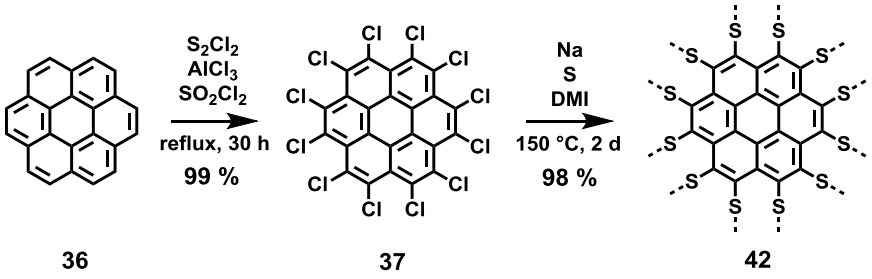

Scheme 12: Reaction scheme to prepare the randomly disulfide-bridged material **42**.

In contrast to the preparation of **40**, synthesis of randomly disulfide-bridged persulfocoronene (**42**) was supposed to be in gram-scale to emphasize its applicability in battery technology. Therefore, synthetic route covering four steps to obtain **40** based on coronene **36** was reduced to a two-step procedure. Furthermore, due to the limited commercial availability of tetrachloromethane, inevitably necessary for the chlorination

with iodine monochloride, the preparation of **37** was altered to the perchlorination under BMC conditions as described in Chapter 4. **37** was reacted with disodium disulfide, being *in-situ* prepared by reaction of elemental sodium with elemental sulfur in 1,3-dimethyl-2-imidazolidinone. After workup under oxidative conditions, **42** was obtained after purification in 98% yield as black solid.

4.2.2.2. Characterization

The resulting **42** was even less soluble in common organic solvents than **40**. Therefore, it was only characterized by solid-state characterization methods. In the MALDI-ToF mass spectrum of **42** three main signals instead of the one found for **40** appeared (Figure 78).

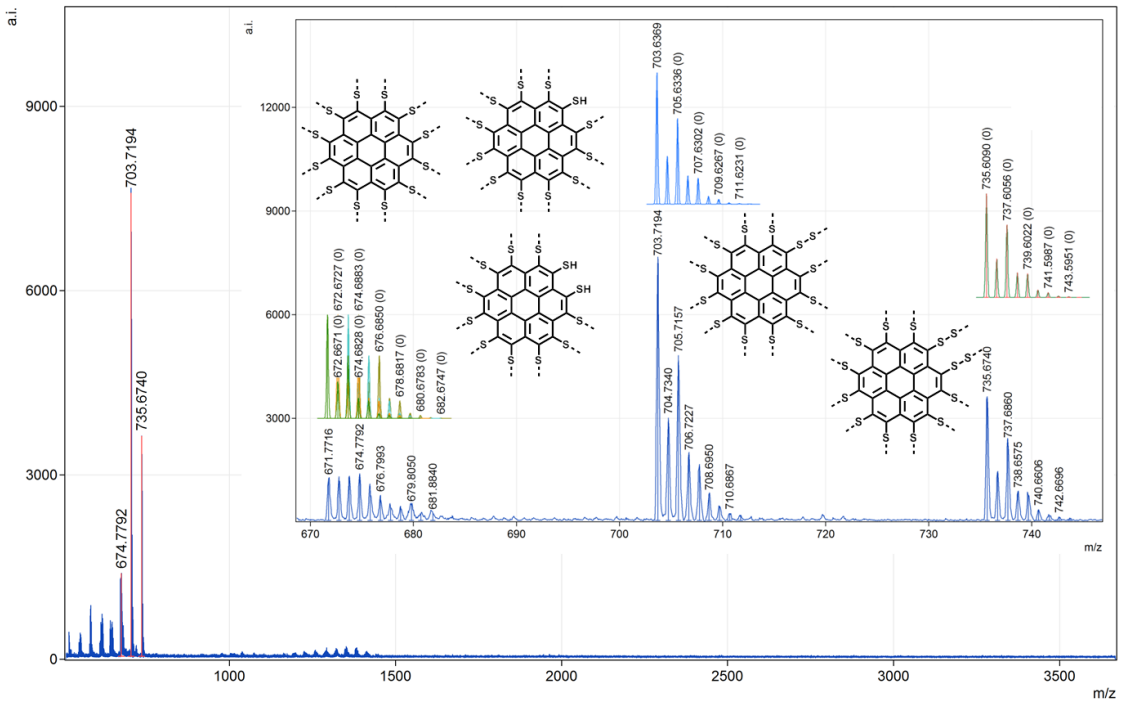

Figure 78: The mass spectrum of **42** shows the material after laser induced fragmentation. The inset shows the isotope pattern of the three main peaks and above the theoretical prediction of the isotope pattern with suggestions of respective molecular structures. The signals below *m/z* = 674.8 appear in intervals of *m/z* = 32 and are the result of cleaving each sulfur atom due to the laser irradiation.

It has to be noted, that at comparably low laser intensities used for **40**, no mass peaks were found. Significantly increasing the laser intensity, the spectrum in Figure 78 appeared. Therefore, it is most probable, that the peaks represent fragments of the **42** instead of the presence of individual molecules. This assumption is corroborated by the additional signals below *m/z* = 674.8. They appear in a regular interval of *m/z* = 32, therefore demonstrating the laser-induced cleavage of sulfur atoms, which was not visible in the spectrum of **40** and proves the laser to provide enough energy to cleave a C-S bond. The three main peaks at *m/z* = 674.8, 703.7, and 735.6 revealed three monomeric fragments. The peak at *m/z* = 674.8 featured an overlap of three different species, additionally to the persulfurated coronene its H- and 2H-adduct, respectively. It was further possible to assign the signals at *m/z* = 703.7 and 735.6 to S- and 2S-adducts of persulfurated coronene species, presumably bearing one and two disulfide bonds in the periphery, respectively. The appearance of these products was assumed to be originated in a non-homolytic cleavage of a C-S-S-C bridge to result in a C-S-S fragment.

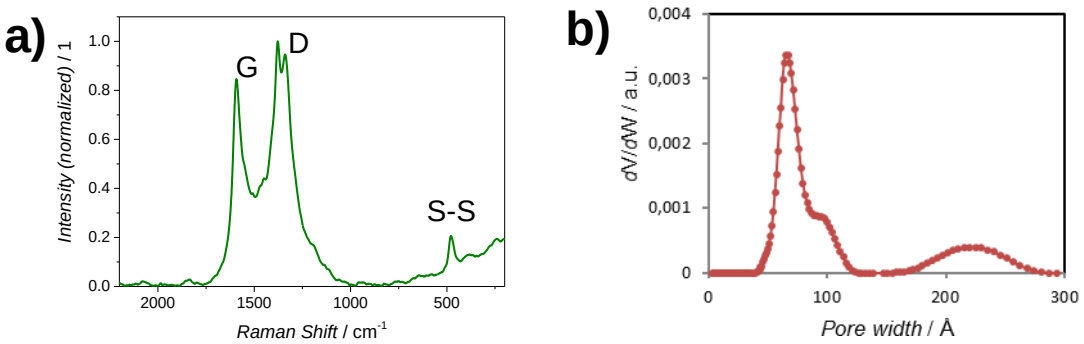

Figure 79: a) Raman spectrum of **42**, revealing a similar structure as **40**. b) Pore size distribution of **42**, calculated with NLDFT method from BET measurement.

Raman spectroscopy of **42** furnished a basically identical spectrum as **40** (Figure 79a). Therefore, the S-S vibration was visible at 479 cm^{-1}, the D peak at 1378 cm^{-1}, and the G peak at 1593 cm^{-1}. Both analyses, MALDI-ToF-MS as well as Raman spectroscopy, provided sufficient proof for the nature of the produced material. **42** was further analyzed by BET measurements. Based on the adsorption isotherm, both pore size distribution and surface area were calculated. The pore size was obtained with a non-local density functional theory (NLDFT) fit featuring the majority of pores between 6-1.2 nm and a small fraction between 1.8-2.8 nm. The surface area was with 28 $m^2 \cdot g^{-1}$

not exceptionally high, therefore still leaving room for improvement. Nevertheless, the material showed extraordinary properties and was hence tested for its characteristics in Li-S batteries.

4.2.2.3. Application of 42 as Cathode Material in Li-S Batteries

Analysis based on the adsorption isotherm and battery measurements with this active material were carried out in collaboration with [redacted].

Cathode laminates were prepared with **42** as active material in combination with conductive carbon C65 as additive, and Kynar® binder, which is a resin based on poly(vinylidenefluoride). The laminates were produced with the ratio 60/30/10 of active material, conductive carbon C65, and binder resin (Figure 80).

Figure 80: Example of a laminate of **42** with conductive carbon C65 and Kynar® binder in the ratio 60/30/10.

Cells were prepared with a diameter of 13 mm. Between the cathode laminate and the lithium metal foil, porous poly(propylene) was applied as separator. The used electrolyte consisted of 1 M LiTFSI with 2 wt% $LiNO_3$ in an DME/DOL mixture of 1:1 by volume. Two similar cells (denoted as cell 1 and cell 2) were prepared and measured to gain information about reproducibility and divergence of the prepared devices. The charge-discharge profiles using **42** were measured at 0.5 C between a potential rate of 1-3 V vs. Li/Li^+ (Figure 81). With obtained initial specific capacities of 120-140 $mA{\cdot}h{\cdot}g^{-1}$, **42** features significantly lower specific capacities than **40**. In contrast to latter, cycling

does not change the shape of the charge-discharge profiles after first cycling and then remains constant during cycling, but instead shows a consistent charge-discharge shape with a low stability, indicated by the decrease in capacity to 90-110 mA·h·g^{-1}.

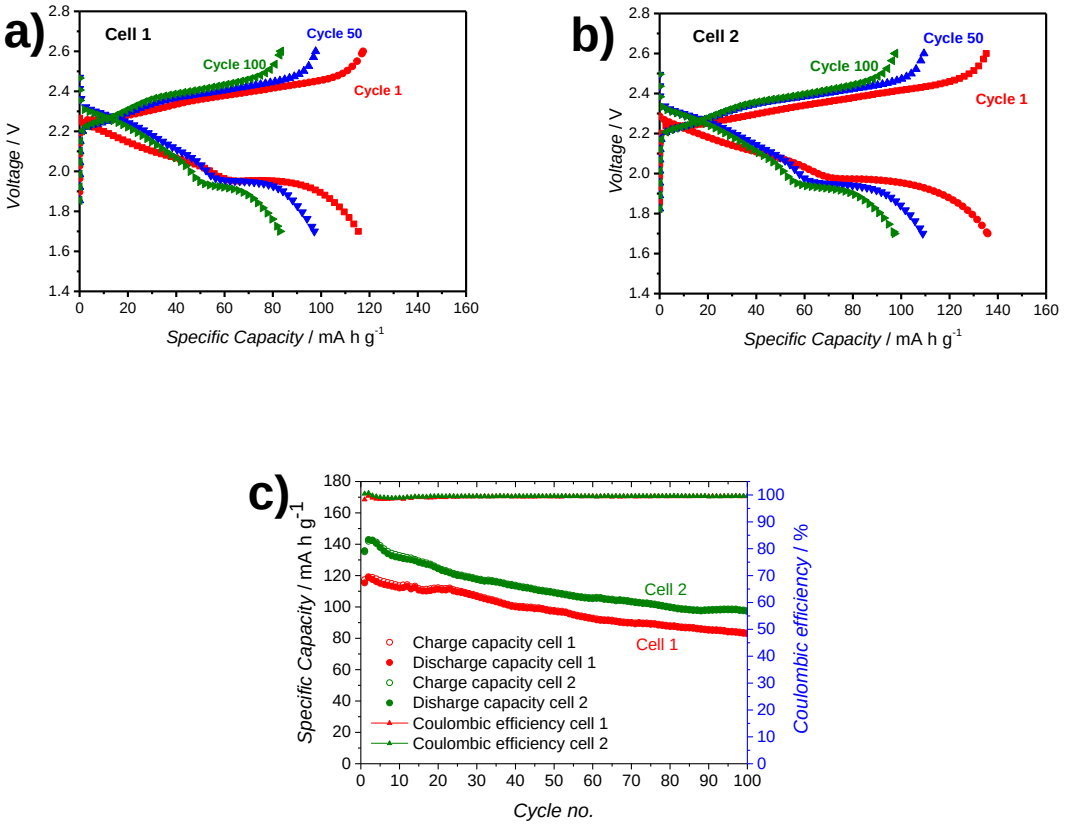

Figure 81: Electrochemical measurements of **42**, applied as cathode material in Li-S batteries, recorded at 0.5 C. a) Discharge and charge voltage profiles of cell 1 after 1st (red), 50th (blue), and 100th (red) cycle. b) Discharge and charge voltage profiles of cell 2 after 1st (red), 50th (blue), and 100th (red) cycle. The profiles were measured at a potential rate of 1-3 V vs. Li/Li^{+}. c) Specific capacity relative to the weight (circles) and Coulombic efficiency (triangles) of cell 1 (red) and cell 2 (green) as function of the cycle numbers.

However, with an excellent ICE of >99%, this material demonstrates that the randomly interconnected backbone increases the reversibility of the redox system and successfully suppresses the shuttle effect. Considering the LUMO orbitals of **40** to be localized at the disulfide units, bridging the persulfurated coronene spacers enlarges the sulfur network and enhances the stabilization of charges by delocalization over the backbone, thus minimizing charge loss/trapping and increasing reversibility. In respect

to the low surface area, the large difference in specific capacity is assumed to result from the morphology of **42** rather than being originated in deviations in the molecular structure.

To elucidate the reason for the decreasing capacity during cycling, electrochemical impedance spectroscopy (EIS) measurements at open circuit voltage (OCV) before and after cycling of the two cells were recorded (Figure 82). The cells were measured at 0.5 C for 100 cycles. The conductivity of the cells increased during cycling, meaning a decrease in terms of resistivity. This behavior is assumed to be caused by a change of the internal structure of the active material in the cell before and after cycling, which may be possible by a reorganization of the molecules during cleavage of the disulfide bonds in the reduced state.

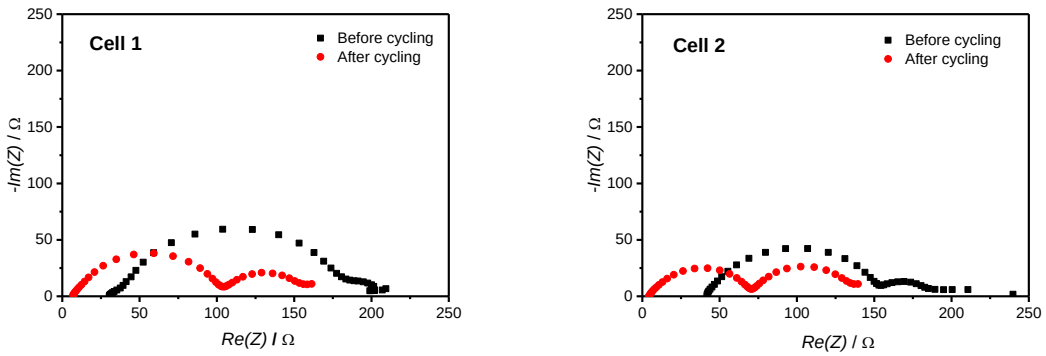

Figure 82: Electrochemical impedance spectroscopy of cell 1 (left) and cell 2 (right) before (black) and after (red) cycling at 0.5 C for 100 cycles. The complex impedance Z is illustrated in a Nyquist plot.

Cycling one cell at different C-rates visualized an essential correlation of the capacity with the C-rate (Figure 83). Reducing the rate to C/10, the specific capacity was obtained as high as 190 $mA \cdot h \cdot g^{-1}$, but also a faster decrease in capacity was visible. In contrast, a high rate of 1 C revealed a low capacity of 55 $mA \cdot h \cdot g^{-1}$, but remained constant through cycling. The measurement further showed that the lower capacity due to a higher rate was not the result of an irreversible process, e.g. decomposition, as decreasing the rate from 1 C to C/2 resulted in restoring the higher capacity of 110 $mA \cdot h \cdot g^{-1}$, but was rather limited due to the small surface area of the active material and a slow charge distribution over the persulfurated coronene backbone. Hence, the high rate of 1 C results in the redox system to kinetically be only able to charge and

discharge the disulfide units the relatively small surface of the active material instead of distributing the charges throughout the complete material.

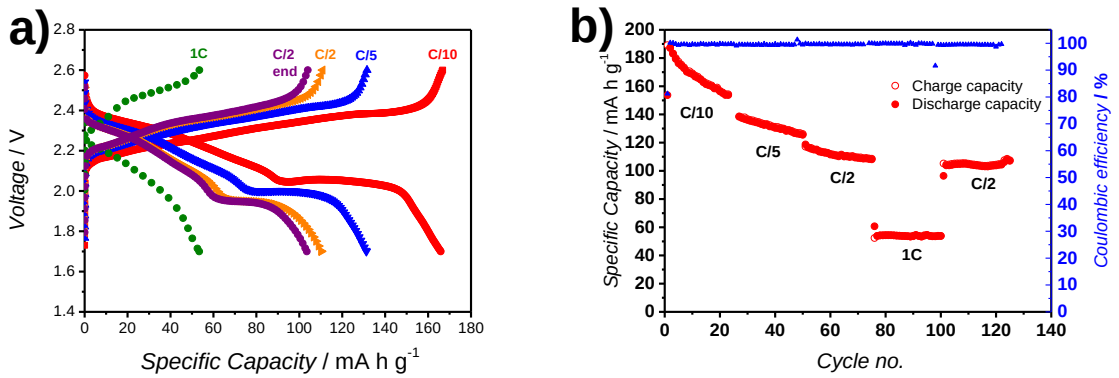

Figure 83: Electrochemical measurements of **42** applied as cathode material in Li-S batteries. a) The charge-discharge profiles, and b) the specific capacity relative to the weight (red circles) and Coulombic efficiency (blue triangles), plotted against the cycle numbers recorded at different C-rates.

Lower rates then allow for the distribution of charges through the sulfurated coronene network, revealing a higher capacity. The decrease in capacity during cycling at lower rates was thus assumed to result from kinetically or spatially trapped charges, being in accordance with the decreased resistivity measured by EIS (Figure 82).

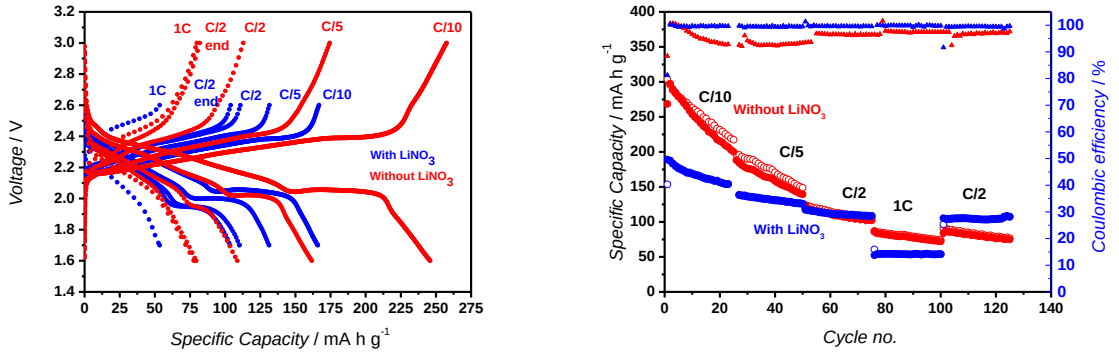

Figure 84: Electrochemical measurements of **42** at different C-rates with (blue) and without (red) $LiNO_3$ in the electrolyte with their respective a) charge-discharge profiles, and b) specific capacity relative to the weight (circles) and Coulombic efficiency (triangles), plotted against the cycle numbers.

For enhancing the stability, the electrolyte composition was changed by relinquishing $LiNO_3$. The corresponding electrochemical measurements are shown in Figure 84. The plots visualize on the one hand the necessity to provide $LiNO_3$ for obtaining an excellent Coulombic efficiency, but on the other hand show a significantly increased stability and specific capacity without $LiNO_3$. Remarkably, the capacity at the first cycle at a rate of C/10 was with 305 $mA \cdot h \cdot g^{-1}$ at 63% of the theoretical value.

To combine this result with the specific capacity being dependent on the C-rate, an optimized process was elaborated:

A sequence of C-rates, starting with an initial rate of C/50 for two cycles, followed by incrementally increased rates of C/20, C/10, C/5, C/2, and 1 C for each 10 cycles, 100 cycles of C/2 were executed on a cell with and without $LiNO_3$ (Figure 85). The plot featured a significantly increased stability of the cell without $LiNO_3$, regarding both the specific capacity degradation and the ICE compared to the C-rate sequence in Figure 84. Thus, the cell without $LiNO_3$ provided a constantly higher capacity than the one with $LiNO_3$. Remarkably, the initial capacity value of 340 $mA \cdot h \cdot g^{-1}$ for the **42** cell without $LiNO_3$ reveals with 71% of its theoretical capacity the potential of achieving a high specific capacity as it was found with **40**. However, the ICE deviating from a desirable, ideal behavior as visible in the case of present $LiNO_3$ in the electrolyte, demands for an optimization of the necessary amount of $LiNO_3$ in the solution to a minimum for an enhanced stability, while retaining an excellent ICE.

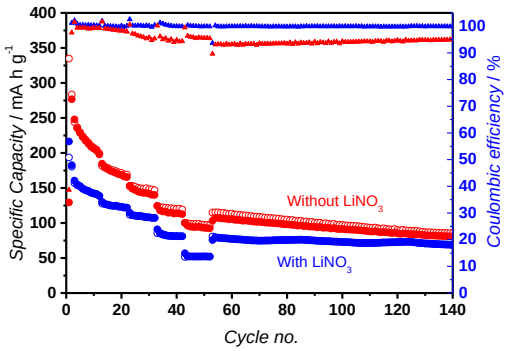

Figure 85: Electrochemical measurements of **42** with (blue) and without (red) $LiNO_3$ using the C-rate sequence C/50 (2 cycles), C/20 (10cycles), C/10 (10cycles), C/5 (10cycles), C/2 (10cycles), 1 C (10cycles), and C/2 (100 cycles). The specific capacity relative to the weight (circles) and Coulombic efficiency (triangles) are plotted against the cycle number.

4.3. Summary

With Li-S batteries facing the problem of dissolving polysulfides in the electrolyte and successively inerting the Lithium electrode, a small 2D molecule was introduced as anchor unit for immobilizing the sulfur atoms. With the specific capacities of a battery increasing with the number of electrons available for electrochemical charging/discharging and decreasing with higher molecular weights, coronene was chosen as a 2D molecule with a moderate molecular weight and the possibility of significantly decreasing the solubility of the sulfur atoms. After synthesis of the per(dithiolated) coronene **40**, its structure analysis was deviating from standard procedures due to a marginally small solubility. However, the structure was elucidated by means of MALDI-ToF MS, Raman spectroscopy, IR spectroscopy, UV/Vis spectroscopy, and STM. Nevertheless, analysis in solution, e.g. with NMR spectroscopy, was indirectly possible by in-situ reduction of the dithiol units in the periphery. After confirming the cyclability of its redox reaction without detectable decomposition or irreversible reactions, **40** was applied as first per(disulfide) PAH as cathode material in a battery. The characteristics revealed a high specific capacity even exceeding the theoretical capacity. This behavior was accounted for the influence of the coronene unit. The high stability of the cell throughout cycling as well as a good ICE value of 90% corroborated successfully reducing conventional problems of Li-S batteries like the shuttle effect as cause for the formation of dendritic and mossy lithium.[252] Based on these beneficial results, this approach was expanded by randomly interconnecting coronene units with via disulfide-bridges **42** and providing them in batteries replacing the individual molecules of **40**. With emphasis on the applicability of this material, the synthesis route was compressed into two steps, each with high yields. **42** was characterized according to elaborated features of **40** and provided in cathode laminates as active material. Although the ICE values were excellent with >99% and thus a further reduced shuttle effect was achieved, the specific capacity of this material was quite low when cycled at 0.5 C, reaching only 31% of the theoretical value. Additional measurements indicated this behavior to be influenced by several parameters. The surface area of produced **42** was found to be low with 28 $m^2 \cdot g^{-1}$. Performing the analysis at low C-rates increased the specific capacity, which indicated the formation of surface charges and a low charge transport through the carbon backbone. The composition of the electrolyte significantly influenced the analysis. Furthermore, impedance measurements suggested a change in the molecular ordering. These parameters were not fully optimized and will be part of future investigations.

5. Conclusion and Outlook

In this thesis, three approaches towards new 2D structures were elaborated.

The first topic used two different methods of noncovalent self-assembly to achieve large-area monolayers. One method utilized host-guest enhanced donor-acceptor interactions of CB[8] with A_3B_2 monomer systems. As the research field of 2DSPs was quite young, there did not exist a large variety of methods or sequences for structural characterization of the produced material. Even more due to insolubility of the fabricated layers, many conventional analyses were not applicable, like single-crystal XRD, NMR measurements in solution, or ITC and other titration experiments. To characterize the insoluble sheets in terms of their internal structure, different solid-state variations of analytical methods were used based on reported measurements, which proved the D-A-CB[8] complexation motif of small molecules. For closing the gap between characterizations of small molecule complexes in solution and respective analysis of polymer layers in solid state, a water-soluble polymer was synthesized to distinguish the behavior of the complexing molecules during measurements resulting from the noncovalent interaction itself, or from the difference between measuring in solid-state and solution. In this regard, ^{1}H-^{13}C HSQC NMR spectra of the soluble polymer were compared with ^{1}H NMR spectra of small molecule D-A-CB[8] complexes and $^{1}H\{^{13}C\}$ LG-HETCOR NMR measurements in solid state, all featuring the same qualitative behavior. However in contrast to the results reported in literature, the peaks obtained in solid state analysis could only be assigned to the whole molecules instead of the individual atoms in the monomers. Therefore, this measurement gave strong indication about the internal structure of the 2DSP, but was not able to solely prove the anticipated complex. A similar conclusion was elaborated for the case of UV/Vis analysis. For all different measurements, an additional broad absorption was visible, bathochromically shifted compared to the spectra of the individual components. Although this peak was identified in literature as a charge-transfer band resulting from the interaction of donor and acceptor in CB[8], e.g. by measurements in solvents with different polarities, this identification was transferred to both the polymer in solution and the polymer in solid state due to qualitative overlaps, however the unambiguous proof for this phenomenon remained elusive, being limited insolubility. Therefore, to further elucidate the structure of the 2DSP, different methods, being novel to this field of research, were applied. 2D REPT-HDOR sideband pattern of CB[8] revealed restrictions in the fluctuation of this molecule, which were assigned to steric

interactions of CB[8] when equipped with two guests. GIWAXS measurements of the layers were able to corroborate the thickness of the sheets as proposed by AFM, and the diffraction patterns were in accordance with an anticipated hexagonal unit cell. Nevertheless it has to be mentioned, that the conclusion to have obtained the 2DSP with the anticipated structure was based on a significant number of investigations, which individually gave strong indication about having achieved this complexation motif in the polymer, but were not able to prove the structure unambiguously. Attempts to achieve the latter included STM and HR-TEM measurements, which failed due to mobility of the layer on the substrates' surface and because of instability against electron irradiation. Efforts to grow single-crystals for XRD were also not successful whereas the required dimensions were not achievable. Therefore, a marginal uncertainty about the structure remained. This uncertainty, however, was further minimalized by providing seven different precursor monomers in different combinations to achieve 12 2DSP materials, which all featured comparable analytical results. Deviations between those, like variations in the unit cell parameters of a hexagonal cell, were reasonable due to different sizes or properties of the monomers. In contrast to elucidating the structure of the 2DSP, it was possible for the morphological characterization to use well-established methods like AFM, STM, TEM, SEM, and OM and to prove the presence of a monolayer as well as analyzing its dimensions. Apart from analytical difficulties, it was possible to overcome the benchmarks of comparable 2DSPs in literature by optimizing the assembly procedure at a toluene-water interface in combination with a rational design of monomers to furnish monolayers with lateral sizes of 0.25 cm^2 and a free-standing ability over gaps of 10 μm^2. In addition to corroborating the analyses, the seven different spacer units demonstrated the possibility of introducing various functionalities to the 2DSP and to change the pore-size of the monolayers. However, the different spacer groups were found to influence the crystallinity of the resulting 2DSP and its mechanical stability. Future research in this area should consider application of appropriate donor and acceptor units, which provide certain functionalities, e.g. beneficial optical or electrical properties, and at the same time promote a crystalline order of the 2DSP. Considering the charge-transfer behavior of D-A-CB[8] combinations in literature,[88, 90, 92] this material could be examined towards semiconducting or optical properties. The regular order of donor and acceptor units could be interesting for Förster or Dexter resonance energy transfer phenomena, as this material is the first example of a 2DSP featuring defined distances between the donor and acceptor moieties. In view of the different hexagonal unit cell parameters between 4.66-6.43 nm derived from GIWAXS measurements, an application of these 2DSPs in nano-size separating membrane technologies could be

achieved. Thus, an extension of the reported nanoporosities from 3.4-4.1 nm of reported 2DPs, which were able to separate CdTe quantum dot mixtures by filtration,[80] to larger porosities could be considered. Furthermore, as one main issue in this research area the limited intrinsic mechanic stability of the 2DSPs should be faced. Increasing the mechanic stability of this supramolecular approach can come collateral with a triggered covalent cross-linking. As *Baek* et al. reported on connecting CB[n] units with thiol-ene click reactions in their periphery,[35] such a concept could be introduced into the monomer design to indirectly combine the donor and acceptor monomers covalently over the CB[8] mediator while leaving the possibility of maintaining the charge-transfer properties. Neglecting the latter and only focusing on the stability, binding the acceptor moiety to the donor unit could be possible after assembling at the interface by providing a radical starter, utilizing the viologen radical cation formation of the acceptor monomer with sodium dithionite.[253]

With the demonstrated implementation of the D-A-CB[8] interaction in the research on 2DSPs, this topic was continued with producing 2DSPs based on a different binding motif. Therefore, the second approach used strong metal-organic noncovalent bonds for the self-assembly. As organic ligand, 1,2,5,6,9,10-triphenylenehexathiol was synthesized. Based on elaborated processing parameters in the previous 2DSP, this precursor was provided at an air-water interface with nickel(II) ions in the aqueous subphase. This interfacial procedure again allowed for the fabrication of large, homogeneous layers of monolayered 2DSPs onto arbitrary substrates. The elucidation of the internal structure was less complicated compared to the D-A-CB[8] approach, as the layer remained stable against electron irradiation. Therefore, analysis by SAED provided unambiguous proof about the hexagonal order of the sheet, which was in agreement with the theoretical calculation of the structure. This characterization was additionally corroborated by XPS, PXRD, UV/Vis, and IR measurements. The morphological properties and dimensions of the monolayers were analyzed by OM and TEM in accordance to the previous attempt, and due to the stability against electron irradiation with additional SEM measurements. The influence of the larger binding strength of the nickel-sulfide complex compared to the D-A-CB[8] interaction was directly found in the increased free-standing ability of the monolayers, covering gaps of 840 µm² and the ability to support the own weight. Considering the large surface with regularly distributed transition metal ions this 2DSP was applied as active material in the HER. Processing onto glassy carbon discs was facile by horizontal deposition from the water-air interface. The HER characteristics were compared to leading HER activities in literature. With optimized conditions, the values exceeded those of N-, P-,

or S-doped graphene and CNT-supported molecular catalysts, and were comparable with the performance of non-noble metal catalysts, like 2D MoS_2 sheets, 2D WS_2 sheets, or Co- and Ni-embedded, N-doped CNTs. These results corroborated the anticipated beneficial distribution of the transition metal ions to the catalytic activity. In addition to exceeding HER characteristics of comparable CNT catalysts, the metal-organic 2DSPs can be fabricated at much lower costs, considering e.g. the extensive effort necessary for separating CNTs.[254] In deliberation of the facile preparation at the interface in large sizes, future studies can focus on the application of this and related 2DSPs in a variation of e.g. electric or catalytic devices. In this regard, experiments should be carried out exploring the influence and utilizability of different transition metals incorporated into the 2DSPs for applications. In particular, the relation of the effects of Ni and Co in a monolayered 2DSP on the HER activity have to be examined, as the comparison with the work of *Marinescu* et al.[83-84] cannot unambiguously exclude the advantageous HER characteristics of **Ni-35** to be a result of using Ni instead of Co and not exceeding its performance due to providing a monolayer instead of a thin multilayer. The assembly protocol further leaves the possibility to prepare monolayers with different metal-organic interactions. For example with maintaining **35** as organic monomer, injecting two competing metal salts to the subphase could prepare a bifunctional 2DSP or manipulate the band gap of the resulting structure. In contrast, providing different metals successively to the self-assembly procedure could furnish separated areas of each transition metal, applicable as one-material alternative for catalytic cascade reactions, usually requiring two different catalysts. Apart from varying the transition metal, the influence of providing different PAHs should be investigated. The elaborated protocol for sulfurization of coronene and its applicability to other PAHs paves the way for utilization of such material in metal-organic 2DSPs. Therefore, monolayers with customizable pore sizes and optical and electrical properties could be achieved.

In the second approach towards 2D structures, hollow carbon tubes were produced, which prior remained elusive in size and shape due to limited workability of graphite as basic material. The protocol for producing these structures featured only one facile step, namely providing the precursor materials in an ampoule and their pyrolysis. Organic halides were applied as carbon source and metal wires served as template. After pyrolysis, the resulting hollow carbon tubes were replica of applied wires, whereby the wires were removed during the preparation and redundantized an additional etching step. Control experiments using organic molecules without halides did not result in hollow carbon tubes. The tubes were analyzed by Raman

spectroscopy, which revealed fundamental influences of the provided organic halide, of the applied metal, and of the ratio between template and organic precursor on the resulting graphite material of the tube. The highest quality of graphite was obtained using dichloromethane as organic halide and iron as template in an atomic ratio of 3/1 in respect to the amount of chlorine atoms in DCM to iron. Further investigations were made to elucidate the whereabouts of the metal wire, as pyrolyzing in a closed system required the metal to remain inside the ampoule. EDX measurements on cross-sections and of the surface of the tube walls suggested an evaporation of metal halides at elevated temperatures to cause increasing amounts of both metals and halogens from the inside to the outside. With the tubes featuring a replica effect of the template, arbitrary shapes and diameters were achievable by providing the corresponding metal template. Apart from a high quality of graphite of the hollow carbon tubes, a high conductivity was measured, exceeding the one of pristine graphite. As the intercalation of graphite with metal atoms was basically supposed to influence its conductivity, subsequent research should investigate the effect of various atoms to the conductivity. In this regard – apart from providing a different metal as template – a postprocessing addition or exchange of metal ions in solution or by sputtering could be considered. Even more possibilities for tuning the properties of hollow carbon tubes could be accessible by contemplation of different methods. On the one hand, two different organic halides as precursors could be provided, whereby one organic halide could feature a heteroaromatic ring. Due to variations in their decomposition temperatures, a two-material hollow carbon tube bearing phase-separation could be achieved. With similar decomposition temperatures of the organic halides, intrinsic doping of the graphite material could be possible. Furthermore, the morphology of the produced material was not defect free. Using different precursor monomers incorporating alkyl chains in the periphery, e.g. 2,3,4,5,6-pentachlorotoluene, can provide a local carbon source in the area of defects and could thus be able to heal structural imperfections. The hollow carbon tubes could also be treated by coating or incorporating with heterolayers, such as MoS_2, WS_2, $MoSe_2$, $NbSe_2$, or BN, to tune properties like the band structure as demonstrated for MoS_2-graphite[255] or suggested for BN-graphite.[256] Coating with a heterolayer could be achieved after preparation of the hollow carbon tubes by Langmuir-Blodgett deposition from an interface. If the heterolayer was supposed to be incorporated, additional graphite layers could be grown by reestablishing pyrolysis conditions with organic halides. Additionally, providing heterolayer-coated metal wire templates could be imagined for obtaining hollow carbon tubes with a different functionality at the inside of the tubes. However, the influence of the heterolayer on the graphite formation should be considered, leading to either a

more or a less ordered structure. Demonstrating the possibility to produce arbitrary shapes, further experiments should prove the utilization of these tubular structures in various applications. The solenoid could be used for example as an electromagnet. The hollow interior would in this case allow for establishing a cooling system, e.g. by gas flow through the tube, thus enabling larger currents, which typically raise the temperature of the conductor. The mesh might provide desirable electrolytic performances when applied as electrode, or could be provided as heat protecting cover and electronic shielding, respectively. The Y-shape demonstrates the possibility to merge two canals and therefore opens applicability of graphite in microfluidics. In this regard, an electrochemical mixing chamber is conceivable. Considering reported superconductive properties of graphitic materials,[257-259] the toroid structure could potentially be used as object of research on quantization of magnetic flux,[260] or be applied as superconducting energy storage.[261] Regarding the transparent graphite coatings on dielectric substrates, it was possible to provide a proof of concept for coating a SiO_2 substrate with graphite. However, the yet high thickness and high sheet resistance demand for further optimization of the conditions. Therefore, continuing experiments should utilize a mass flow controller for the possibility of providing even less amounts of precursor. With an ampoule possessing two openings, the precursor could be introduced at one end, its amount controlled over the gas flow, then being condensated at the ampoule wall under low temperatures, and the ampoule subsequently be sealed. Optimization of the applied copper layer on the SiO_2 surface in combination with the amount of precursor should facilitate higher graphite qualities and thus higher conductivities. In combination with improving the thickness of the copper sputtering on silicon dioxide, transparent graphite electrodes with high conductivities could be achieved for further use e.g. in solar panels. Notwithstanding these beneficial properties and promising utilization in applications, the hollow carbon tubes lacked mechanical stability, as anticipated regarding well-established carbon fibers.[262-263] Commercially available carbon fibers are conventionally graphitized at temperatures between 3000-3300 °C. Thus post-processing annealing experiments should be performed at high temperatures to increase the stability of obtained hollow carbon tubes. Another possibility to mechanically stabilize the hollow carbon tubes could be subsequent coating with a heterolayer like MoS_2, or the implementation in a polymer matrix, such as PMMA.[264] Although making the outer surface of the tubes inaccessible, the hollowness remains intact, thus sustaining the possibility to use them as material for microfluidics.

In the third topic of this work with the target of producing 2D structures, the small PAH **40**, containing an entirely disulfide-bridged periphery, as well as its randomly crosslinked analogon **42** were synthesized. The synthesis of **40** was facilitated based on the sulfurization procedure elaborated in chapter 2.3. Similar to the first topic, the low solubility of the analyte complicated the structure elucidation. In this particular case, STM provided unambiguous proof of the structure of **40**, which was corroborated by measurements like MALDI-ToF MS, Raman spectroscopy, and IR spectroscopy. Additionally, the reduced compound **41**, accessible in-situ with $NaBH_4$ and soluble in common organic solvents, was able to support the structural analysis by providing indirect proof. Structural investigations of randomly crosslinked **42** were thus facile by comparison of the Raman spectra and MALDI-Tof MS. After characterization, both materials **40** and **42** were applied as active material into Li-S batteries. The small molecule **40** exhibited a high specific capacity and a good ICE of 90%. These characteristics in combination with a stable cycling performance corroborated the anticipated reduction of typical problems of Li-S batteries. Although **42** on the contrary revealed an excellent ICE of > 99%, the specific capacity was low, reaching only 31% of the theoretical value. The differences in the performance of both materials were suggested to be caused by different morphologies, considering the structural similarities of **42** and **40**. Continuing studies should therefore increase the surface area of **42** and optimize the composition in the cathode laminate. To increase the surface area, both extremes of self-assembly prior to disulfide bridging should be tried. For achieving a regularly ordered structure, hydrothermal conditions should be applied. Contrarily, for obtaining a low order, the solution of **42** could be snap-freezed during workup with subsequent freeze-drying to utilize the diffusion of molecules in solution for a low self-assembly. Both methods were reported in literature being able to produce porous materials with high surface areas.[265-266] To optimize the composition in cathode laminates, the amount of conductive additive should be the main focus. In both cases of **40** and **42**, conductive additives were added by amounts of 20 and 30 wt%, respectively. Current investigations elucidate the influence of different laminate compositions to further increase the specific capacities, e.g. by optimization of the ratio between active material to conductive additive. Furthermore, the elaborated protocol should be applied to larger PAHs for enhancing the conductivity in the backbone of the active material and for the possibility to make conductive additives in the laminates redundant. Additionally, as the capacity of **40** exceeding its theoretical value was traced back to the redox process including more than 12 electrons, charging and discharging conditions in a larger voltage range should be tested to verify the inclusion of the coronene spacer in the process without degradation of the material and to test

the limit of latter. Eventually, the utilization of both **40** and **42** should be further extended to various applications suitable for persulfurated aromatic compounds, like ion-selective membranes, electronics, lubricants, or antioxidants.[267]

6. Experimental Part

6.1. Materials

All starting materials were purchased from Sigma-Aldrich, Acros, ABCR, Alfa Aesar, Merck, Fisher Scientific, Combi-Blocks, Manchester Organics, or Strem and if not stated otherwise used without further purification. Hexadodecyl-HBC was received from [redacted] and benzenetrithiophene was obtained from [redacted]. Reactions under protective atmosphere (Argon 4.6, Linde AG) were done with standard Schlenk techniques. During sample preparation as well as during final reaction steps towards target molecules, purified water (Milli-Q® Type 1 Water purification system, Merck KGaA) was used.

6.2. Methods

Assembly of D-A-CB[8] Monolayers in the Custom-Made Glass Trough

A custom-made glass trough with a diameter of 5 cm, a height of 4 cm, a glass bottom with a porosity of 00, an outlet with a valve at the bottom, and a lid with a valve was positioned on an active vibration isolation desktop unit (*halcyonics i4 series*, *Accurion GmbH*), which was itself placed on a passive vibration isolation table. In a typical experiment, 19 mL of the respective preassembled, aqueous solution of **CB[8]** ($6 \cdot 10^{-4}$ mol/L) and acceptor monomer ($3 \cdot 10^{-4}$ mol/L) was provided in the trough. Different substrates were then positioned in the aqueous phase on a PTFE substrate holder with a 5° slope, placed on the porous bottom. The aqueous solution was carefully overlayed with 19 mL of a respective donor solution in toluene ($1.7 \cdot 10^{-5}$ mol/L). After sealing the trough with a lid, the system was let at rest. Releasing the solutions through the bottom with a flow rate of 50 µL/s resulted in a deposition of the assembled 2DP onto the substrates. To prevent the presence of residual precursors, the substrates were washed with toluene, ethanol, and water by dipping the substrate into the solution. In case of the TEM-grids bearing the free-standing layers, washing was performed by a

drop-wise exposure of the grids to the respective solvent utilizing capillary forces of the tips of a tweezer.

Atomic Force Microscopy (AFM)

AFM measurements were performed on a *Multimode PicoForce*, a *Multimode Torsion TUNA*, or a *Veeco Dimension 3100* in tapping mode. Silicon cantilevers (Olympus, Japan) with a resonance frequency of ~300 kHz and a spring constant of 19 Nm^{-1} were equipped. Scratches for height measurements were applied by scratching the SiO_2 surface of the SiO_2/Si wafer with a cannula tip. The height measurements were carried out perpendicular to the scratching direction.

Wear resistance was obtained after several steps of measurement: First, the surface of the coating was imaged in tapping mode. The mode was then switched to contact mode and a section of this surface with 1/10 of the width and 1/2 of the height was measured at different deflection setpoints, each with 100 iterations. Eventually, the initial measurement was repeated in tapping mode.

Column Chromatography

Glas columns were wet-filled with silica gel (particle size 0.063–0.200 mm), purchased from *Macherey-Nagel*. The eluents were varied in respect to the retention of the particular substances.

Conductivity Measurements

Resistances were measured with a *Keithley model 4200 semiconductor characterization* system, whereas contacting was performed under a *Nikon SMZ1000* microscope. The resistance of a hollow carbon fiber with an inner diameter of 127 µm and a wall thickness of 23 µm was measured. The wire was fixed on one side with silver varnish to reduce the contact resistance. One needle of the micromanipulator was positioned to this silver contact, the other was contacted directly to the fiber in incremental distances of 1 mm. The measured resistances were plotted against the distances in Figure 70: Resistance measurements of a hollow carbon tube at incremental distances. The linear fit reveals a slope of 1.56 ± 0.07 · 10-1 Ω·mm-1.

Fitting the measurement with a linear fit revealed the contact resistance as intersection with $1.02 \pm 0.87 \cdot 10^{-1}\ \Omega$, and a resistance of the hollow fiber of $1.56 \pm 0.07 \cdot 10^{-1}\ \Omega \cdot mm^{-1}$. Regarding a cross-section area of $5.00 \cdot 10^{-3}\ mm^2$, the resistivity ρ_{Fiber} of the fiber was calculated using the equation

$$\rho = \frac{R \cdot A}{l} \tag{1}$$

with R being the resistance, A as cross-section area, and l as length of the fiber, to be $\rho_{Fiber} = 7.66 \pm 0.35 \cdot 10^{-7}\ \Omega \cdot m$.

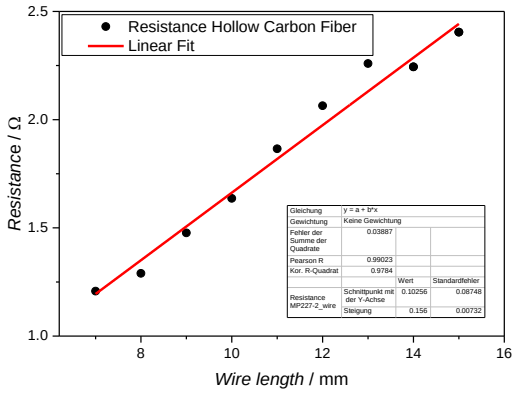

Figure 86: Resistance measurements of a hollow carbon fiber at incremental distances. The linear fit reveals an intersection of $1.02 \pm 0.87 \cdot 10^{-1}\ \Omega$ and an inclination of $1.56 \pm 0.07 \cdot 10^{-1}\ \Omega \cdot mm^{-1}$.

Cyclic Voltammetry (CV)

For CV measurements, a three-electrode configuration with platinum as counter electrode, silver as reference electrode, and glassy carbon as working electrode, respectively, was applied in 0.1 M Bu_4NPF_6 solution in THF. A *CHI 600 device* (*CH Instruments, Inc.*) was used for controlling and measuring. The working electrode was coated with the active material and measured at room temperature with a scan rate of $50\ mV \cdot s^{-1}$.

Dynamic Light Scattering (DLS)

DLS measurements were executed on a *Malvern Zetasizer 3000*, operating at 632.8 nm with a fixed scattering angle of 90°.

Electrochemical Analysis of Li-S Batteries

Preparation and measurements of the cells containing small molecule **40** were performed in collaboration with [redacted]. Cathode laminates were prepared by grinding 70 wt% **40** with 20 wt% acetylene black and 10 wt% poly(vinylidene fluoride). The mixture was processed with Doctor Blade onto an aluminum foil and placed into a coin cell with a diameter of 12 mm. Between the cathode and lithium foil, a porous polypropylene separator was provided. 1.0 M lithium bis-trifluoromethanesulfonylimide (LiTFSI) in a 1:1 mixture of 1,3-dioxolane (DOL) and 1,2-dimethoxyethane (DME) by volume with an additive of 0.1 wt% $LiNO_3$ was used as electrolyte.

Preparation and measurements of the cells containing the randomly crosslinked **42** were executed in collaboration with [redacted]. Cathode material was prepared by grinding 60 wt% **42** with 30 wt% C_{65}, and 10 wt% Kynar® binder. The laminates were produced with Doctor Blade with a wet thickness of 300 µm. After drying under vacuum at 50 °C for 16 h they were punched, achieving discs with a diameter of 13 mm. The cells were assembled with the following set-up:

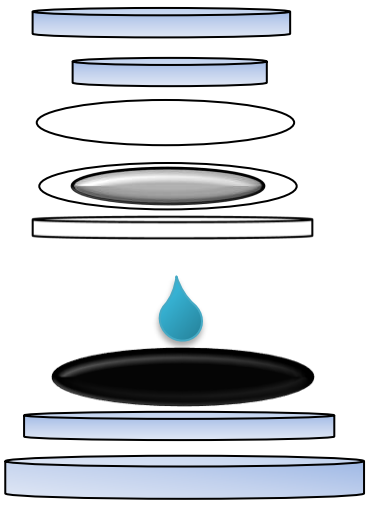

Cap
Wave Spring
16 mm Ø Spacer
16 mm Ø Spacer + 14 mm Ø Lithium
16 mm Ø Celgard 3501 as separator
20 µL 1 M LiTFSI + 2 wt.% $LiNO_3$ in DME/DOL or 1M LiTFSI in DME/DOL as electrolyte
13 mm Ø cathode laminate
Gasket
Bottom

Figure 87: Schematic assembly of a coin cell as produced with the active material **42**.

The cells were measured at room temperature with galvanostatic discharge and charge cycles using a *Landt Battery CT2001* device.

Elemental Analysis

Elemental analysis was measured at the Institute for Organic Chemistry (Johannes Gutenberg-Universität Mainz) on a *Foss Heraeus Vario EL* instrument.

Fluorescence Spectroscopy

Fluorescence spectra were measured in a 10 mm quartz cuvette in a *SPEX-Fluorolog II* device.

Grazing-Incidence Wide-Angle X-Ray Scattering (GIWAXS)

GIWAXS experiments were carried out in collaboration with [redacted] under Synchotron irradiation by means of a solid anode X-ray tube (*Siemens Kristalloflex X-ray source*, copper anode X-ray tube operated at 35 kV and 40 mA), Osmic confocal MaxFlux optics. The X-ray beam was adjusted with pinhole collimation to a size of 0.5 x 0.5 mm and detected with a MAR345 image plate detector. Samples were placed in the beam just below the critical angle for total reflection with respect to the incoming X-ray beam (~0.18°). To increase the intensity of diffraction signals, samples were either prepared by layer-by-layer deposition of monolayers, or after 7 d of assembly time onto 300 nm SiO_2/Si-wafer pieces by horizontal deposition.

Hydrogen Evolution Reaction (HER) Measurements

Electrochemical measurements regarding the HER were performed by [redacted] on an CHI 760C electrochemical workstation (CH Instruments Inc.). Conventional three-electrode cells were used at room temperature and a *WaveDriver 20 bipotentiostat* was applied (*Pine Instrument Company*). Ag/AgCl was provided as reference electrode. A graphite rod acted as counter electrode instead of a platinum wire to avoid tampering the results with the possibility of dissolvable Pt-species present. All potentials were determined relative to the reversible hydrogen electrode (RHE). The system was calibrated measuring the potential difference in a H_2-saturated electrolyte between the RHE and Ag/AgCl

electrode. For producing the working electrode, glassy carbon discs with diameters of 5.0 mm were polished with aqueous alumina suspensions. Then, the assembled Ni-35 layer was processed onto these discs by horizontal deposition (surface area 0.196 cm^2) and washed with chloroform and water. The glassy carbon discs were applied to a rotating disc electrode (RDE) and provided as working electrode. The electrolyte was saturated with Ar and the HER polarization measurement performed at 1600 rpm at a scan rate of 10 mV^{-1} between -0.8 -0.0 V. All polarization curves are capacity-corrected by using the average values of forward and backward scans.

Infrared Spectroscopy

Infrared spectroscopy experiments were performed with a *Nicolet FT-IR 730* device in solid state with an ATR unit (Zn-Se crystal).

Langmuir-Blodgett Experiments

Langmuir-Blodgett experiments were performed using an *KSV NIMA air-water Langmuir-Blodgett Minitrough* or a *KSV NIMA liquid-liquid Langmuir-Blodgett trough*. The troughs were placed onto passive anti-vibration tables to prevent excessive ambient vibrations.

Mass Spectrometry (MS)

Field desorption (FD) mass spectrometry was carried out on a *VG Instruments ZAB 2-SE-FPD*, using an acceleration voltage of 8 kV.

Matrix-assisted laser desorption/ionization time of flight (MALDI-ToF) mass spectra were obtained using a *Bruker Reflex II-ToF Spectrometer* with a 337 nm nitrogen laser. High resolution spectra were calibrated using C_{60} (720 m/z) and C_{70} (720 m/z) fullerenes, respectively. Solid samples were prepared for measurement by mixing with either dithranol or tetracyanoquinodimethane (TCNQ)[268] in THF as matrix in a ratio of 1/250.

High resolution ESI-TOF mass spectra were measured on a *Micromass/Waters QTof Ultima 3 Spectrometer* at the Institute for Organic Chemistry (Johannes Gutenberg-Universität Mainz).

Melting Point Determination

Melting points were measured in open capillars with a *Büchi B-545*. All melting points are uncorrected.

Nuclear Magnetic Resonance (NMR) Spectroscopy

^{1}H and ^{13}C NMR spectra were measured with a *Bruker Avance 250*, a *Bruker Avance 300*, a *Bruker Avance 500*, or a *Bruker Avance 700* spectrometer in the respective deuterated solvents. The chemical shifts δ are noted in ppm with respect to trimethylsilane (TMS). Residual solvent peaks were used as internal standard. Multiplets are entitled as s (singlet), bs (broad singlet), d (duplet), t (triplet), m (multiplet) and denoted values are positioned in the center of a peak.

^{13}C{^{1}H} LG-HETCOR NMR and REPT-HDOR spectroscopic measurements were performed on a *Bruker Avance 850* with 850 MHz ^{1}H Larmor frequency, 3 ms LG-CP contact time and 18 kHz MAS.

Optical microscopy (OM)

For optical microscopy, a *Zeiss Axioplan 2* with a *Hitachi KP-D50* color digital CCD camera was used.

Powder X-Ray Diffraction (PXRD)

PXRD measurements were recorded at room temperature with a *Siemens D5000 X-ray diffractometer* using Cu Kα (1.5406 Å) radiation.

Preparation of Hollow Carbon Tubes

In a typical experiment, metal wires were provided in a cylindrical quartz ampoule (1.5 cm diameter, 12 cm height) under Ar atmosphere. In case of a solid organic halide, the substance was added and the ampoule evacuated and sealed. In contrast, for providing a liquid organic halide the ampoule was first evacuated and cooled to -196 °C for at least 30 min. Subsequently, the cooling was interrupted for flushing with Ar to prevent condensation and sublimation, and the liquid precursor was injected to freeze on the ampoule wall. Then the ampoule was simultaneously evacuated and cooling restored. While maintaining the cooling, the ampoule was sealed. In both cases, the ampoule was then subjected to an oven and heated up to 1000 °C with a heating rate of 5 °C·min^{-1}. After maintaining this temperature for 5 h, the oven was slowly cooled to room temperature with a cooling rate of 2 °C·min^{-1}. The ampoules were wrapped into ~10 layers of aluminum foil and this again in an 80 x 20 cm² cloth as safety precaution due to possible high pressure inside the quartz tube. Its sealed end was treated with a hammer until the glass broke. The glass was removed carefully and separated from the hollow carbon tubes.

Raman Spectroscopy

Raman experiments were performed with a *Bruker RFS 100/S* device at a laser wavelength of 488 or 532 nm and an intensity of 2 mW. The laser beam was positioned on the sample with a *Senterra Dispersive Raman Microscope*. The peak positions and intensities were obtained from fitting the peaks with Lorentz functions.

Scanning Electron Microscopy (SEM)

SEM experiments were performed on a *Zeiss LEO Gemini 1530* or a *Hitachi SU8000* with samples attached with conductive carbon pads to aluminum stubs. Energy dispersed X-ray spectroscopy (EDX) measurements and elemental mappings were carried out with a *Bruker AXS XFlash Detector 5010* attached to the Hitachi SU8000 device using a monochromatic Al Kα radiation source (1486.6 eV).

Scanning Tunneling Microscopy (STM)

Measurements were performed in collaboration with [redacted]. Au(111)-coated mica substrates were used and cleaned by Ne^+ sputtering and annealing at 723 K. Individual molecules of **40** were sublimed at elevated temperatures of 600 K from a Knudsen cell with a sublimation time of 30 s. During deposition, the sample was kept at room temperature. During the measurement, the sample was cooled to 5 K and ultra-high vacuum < 10^{-10} mbar was provided. Topographic imaging was performed using low voltages or low currents, e.g. U = 0.1 V and I = 0.1 nA, to prevent manipulations of the sample.

Template Preparation for Hollow Carbon Tubes

Applied templates were purchased as available at Alfa Aesar, Sigma Aldrich, or Goodfellow. All templates were cleaned by ultrasonication with aceton, toluene, and isopropanol prior to providing them in an ampoule. Copper templates were additionally treated with an aqueous 2 M hydrochloric acid solution for the removal of copper oxides on the surface.

For preparing the copper toroids, a copper wire with a diameter of 127 µm was cut into pieces of 0.6 cm. The wire pieces were bent in such a way, that the cutting edges touch each other. The bent pieces were placed into a custom made graphite template (Figure 88Figure 88: Pictures of the graphite templates used for fusing the cutting edges (top) to obtain copper toroids (left), and copper Y-shapes (right), respectively. Below every template, an example of the produced copper shape is shown., left), which was positioned into an oven. The oven was permanently flushed with a nitrogen flow of 1300 sccm to prevent oxidation of the copper. After heating the oven to 1100 °C with a heating rate of 5 °C/min, the temperature was kept constant for 18 min. Letting the oven cool to room temperature and removing the copper wires from the template resulted in the cutting edges being fused to a toroid in nine of ten cases.

The Y-pieces were prepared similar to the copper toroids, however with copper wire pieces of 0.4 cm. Fusing the cutting edges in the oven was performed under similar conditions as with the toroids, however with a temperature plateau of 7 min at 1100 °C and an appropriate graphite template (Figure 88Figure 88: Pictures of the graphite templates used for fusing the cutting edges (top) to obtain copper toroids (left), and

copper Y-shapes (right), respectively. Below every template, an example of the produced copper shape is shown., right).

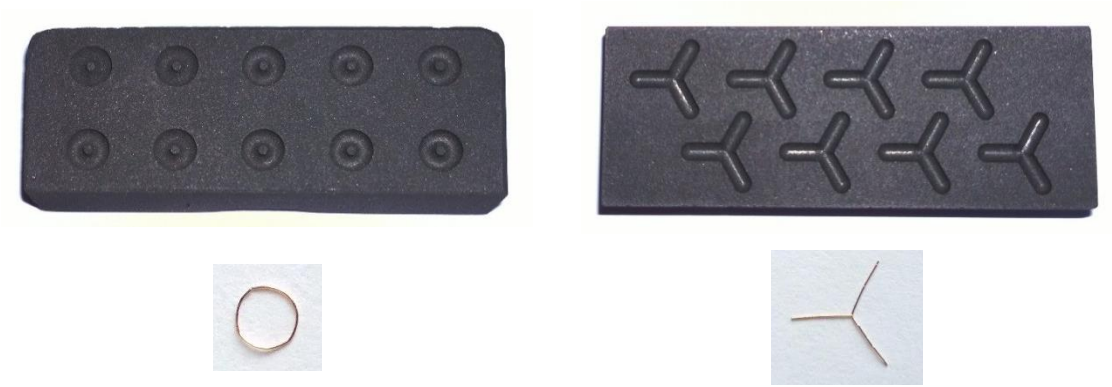

Figure 88: Pictures of the graphite templates used for fusing the cutting edges (top) to obtain copper toroids (left), and copper Y-shapes (right), respectively. Below every template, an example of the produced copper shape is shown.

Transmission Electron Microscopy (TEM)

TEM measurements were measured on Lacey carbon supported copper grids (3.05 mm, 400 mesh, *Plano GmbH*) with a *JEOL JEM-1400* at 120 kV, or with a *Zeiss Libra 120* at 80 kV.

HR-TEM experiments were performed by [redacted] on a *FEI Titan 80-300* instrument, operated at 80 kV. As substrates, Quantifoil® R 0.6/1 or Quantifoil® R 1.2/1.3 gold grids were used.

UV/Vis Spectroscopy

UV-visible spectra were recorded using a *Perkin-Elmer Lambda 900* spectrophotometer at room temperature. The samples were typically provided in a 10 mm quartz cell in concentrations between $1 \cdot 10^{-5}$-$1 \cdot 10^{-7}$ M dissolved in an appropriate solvent and measured down to a lower wavelength limit of 20 nm above the respective UV-cutoff.

Solid state UV/Vis spectra were recorded with a *Perkin Elmer Lambda 900* equipped with a 120 mm integrating sphere at room temperature. The samples were measured on quartz-wafer substrates (thickness 525 µm, roughness < 0.5 nm, *Plan Optik AG*) in reflection mode.

X-Ray Photoelectron Spectroscopy (XPS)

Measurements were performed by [redacted] on an *ESCALAB 250* device (*Thermo Scientific*) under low pressure (1-10 mbar). As X-ray beam origin, a monochromatic Al (Kα) source was equipped in the measurement chamber. The beam diameter was adjusted to 100 µm for both survey and high-resolution measurements. Calibration of the device was done using the ISO 15472 protocol. As internal standard, the $Au_{47/2}$ signal at 84 eV was used. The spectra were processed and analyzed with CasaXPS software.

6.3. Synthesis

6.3.1. Synthesis of 1,3,5-tribromo-2,4,6-trimethylbenzene (2)

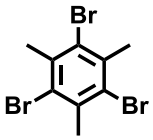

1,3,5-Tribromo-2,4,6-trimethylbenzene was synthesized after a literature known procedure.[269] 5.02 g (89.9 mmol, 0.32 eq.) iron powder was provided in a flask with a gas outlet to a washing solution of aqueous sodium hydroxide. 78.0 mL (243 g, 1.52 mol, 5.5 eq.) bromine were added slowly and the mixture stirred for 10 min. 29.9 mL (33.4 g, 278 mmol, 1 eq.) mesitylene were added over a time of 3.5 h and the mixture subsequently stirred at room temperature for 3 d. 500 mL water was added and the precipitating crude product was filtered. Repeated recrystallization from chloroform gave **2** as colorless needles in 64% (63.4 g, 178 mmol) yield. ^{1}H NMR (300 Mhz, CD_2Cl_2): δ = 2.65 (s, 9H); Elemental analysis: C 30.46, H 2.74 (theoretical: C 30.29, H 2.54).

6.3.2. Synthesis of 2',4',6'-trimethyl-4,4''-dinitro-5'-(4-nitro-phenyl)-1,1':3',1''-terphenyl (3)

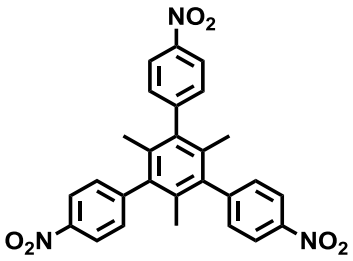

3.50 g (9.81 mmol, 1 eq.) **2** were provided under argon atmosphere with 9.82 g (58.84 mmol, 6 eq.) of commercially available 4-nitrophenylboronic acid in a solution of 100 mL toluene, 130 mL ethanol and 150 mL 2 M aqueous K_2CO_3. 1.70 g (1.47 mmol, 0.15 eq.) tetrakis(triphenylphosphine)palladium(0) were added slowly under stirring and the protective atmosphere was ensured by three “freeze-pump-thaw” cycles. After heating to 90°C for 1 d the reaction mixture was cooled to room temperature, quenched with water and extracted with ethyl acetate. The solvent of the combined

organic phases was removed and the mixture subjected to column chromatography. The first three fractions were collected with PE/DCM = 2/1 as eluent. The fourth fraction, containing the product, was received after increasing the polarity of the eluent to PE/DCM = 1/3. **3** was obtained after precipitation with hexane, followed by filtration, and drying as a colorless solid in 67% (3.18 g, 6.57 mmol). ^{1}H NMR (300 Mhz, CD_2Cl_2): δ = 8.31 (d, 6H), 7.41 (d, 6H), 7.19 (s, 6H), 1.66 (s, 9H); MS (FD): *m/z* 483.0 $[M]^+$ (calc. for $C_{27}H_{21}N_3O_6$ 483.14); Elemental analysis: C 67.23, H 4.22, N 8.60 (theoretical: C 67.08, H 4.38, N 8.69).

6.3.3. Synthesis of 5'-(4-aminophenyl)-2',4',6'-trimethyl-[1,1':3',1''-terphenyl]-4,4''-diamine (4)

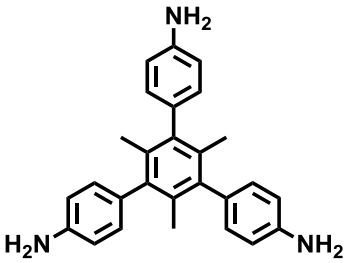

1.00 g (2.07 mmol, 1 eq.) **3** was provided in a mixture of 10 mL ethanol and 90 mL 6 M hydrochloric acid. 3.68 g (31.03 mmol, 15 eq.) tin powder were added to the suspension and the mixture heated to 115 °C for 2 d. The clear solution was cooled to room temperature and 10% aqueous potassium hydroxide solution was added until precipitation occurred. The solid was filtrated and washed with 10% aqueous potassium hydroxide solution. The crude product was dissolved in 5 mL ethanol and 15 mL hexane were added. The solution was concentrated and precipitated with hexane. After filtration, **4** was obtained as a colorless solid in 63% (510 mg, 1.30 mmol) yield. ^{1}H NMR (300 Mhz, CD_2Cl_2): δ = 6.93 (d, 6H), 6.73 (d, 6H), 3.71 (bs, 6H), 1.71 (s, 9H); Elemental analysis: C 82.61, H 7.09, N 10.47 (theoretical: C 82.41, H 6.92, N 10.68).

6.3.4. Synthesis of 4,4''-diiodo-5'-(4-iodophenyl)-2',4',6'-trimethyl-1,1':3',1''-terphenyl (5)

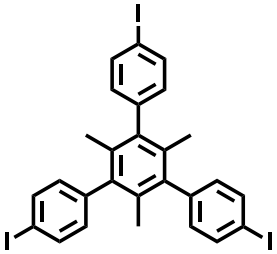

1.57 g (3.99 mmol, 1 eq.) **4** were provided in 7.50 mL concentrated hydrochloric acid and stirred at 0 °C for 10 min. 908 mg (13.2 mmol, 3.3 eq.) sodium nitrite were added slowly and the mixture stirred for 1 h until a color change to yellow-orange was observed. The mixture was poured into a solution of 15.9 g (95.8 mmol, 24 eq.) potassium iodide in 25 mL water in a flask covered in aluminium foil and stirred over night at room temperature. The reaction mixture was quenched with sodium sulfite and extracted with DCM. After removing the solvent, the mixture was subjected to column chromatography. With hexane/DCM = 10/1 as eluent, **5** was obtained as colorless solid in 33% (879 mg, 1.21 mmol) yield. ^{1}H NMR (300 Mhz, CD_2Cl_2): δ = 7.77 (d, 6H), 6.94 (d, 6H), 1.66 (s, 9H); Elemental analysis: C 45.72, H 3.42 (theoretical: C 44.66, H 2.91).

6.3.5. Synthesis of 6,6'-(5'-(4-(6-methoxynaphthalen-2-yl)phenyl)-2',4',6'-trimethyl-[1,1':3',1''-terphenyl]-4,4''-diyl)bis(2-methoxynaphthalene) (6)

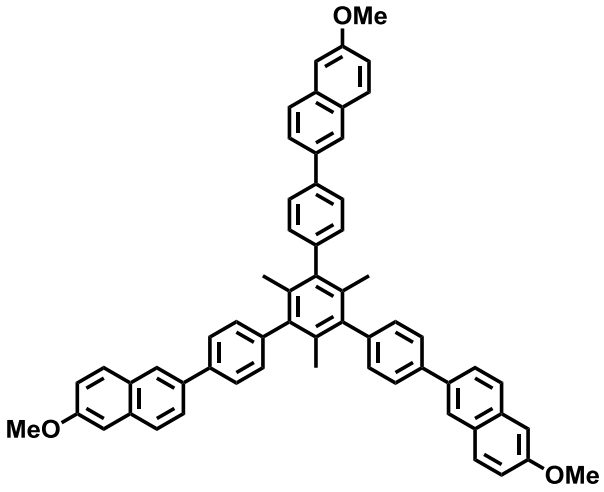

800 mg (1.10 mmol, 1 eq.) 5 were provided under argon atmosphere with 2.00 g (9.91 mmol, 9 eq.) 6-methoxy-2-naphthaleneboronic acid in a solution of 20 mL toluene, 25 mL ethanol and 25 mL 2 M aqueous K_2CO_3. 191 mg (165 µmol, 0.15 eq.) tetrakis(triphenylphosphine)palladium(0) were added slowly under stirring and the protective atmosphere was ensured by three “freeze-pump-thaw” cycles. After heating to 90°C for 2 d the reaction mixture was cooled to room temperature, quenched with water and extracted with DCM. The solvent of the combined organic phases was removed and the mixture subjected to column chromatography. The first two fractions were collected with DCM/hexane = 1/1 as eluent. The third fraction, containing the product, was received after increasing the polarity of the eluent to pure DCM. Evaporation of the solvent yielded **6** as colorless needles by 89% (807 mg, 988 µmol). ^{1}H NMR (300 Mhz, $CD_2Cl_{4^-2}$): δ = 8.08 (s, 3H), 7.90-7.76 (m, 15H), 7.37 (d, 6H), 7.23-7.12 (m, 6H), 3.94 (s, 9H), 1.86 (s, 9H); MS (FD): *m/z* 817.7 $[M]^+$ (calc. for $C_{60}H_{48}O_3$ 817.4). Elemental analysis: C 88.32, H 6.00 (theoretical: C 88.20, H 5.92).

6.3.6. Synthesis of 4,4''-bis(6-methoxynaphthalen-2-yl)-5'-(4-(6-methoxynaphthalen-2-yl)phenyl)-[1,1':3',1''-ter-phenyl]-2',4',6'-tricarboxylic acid (7)

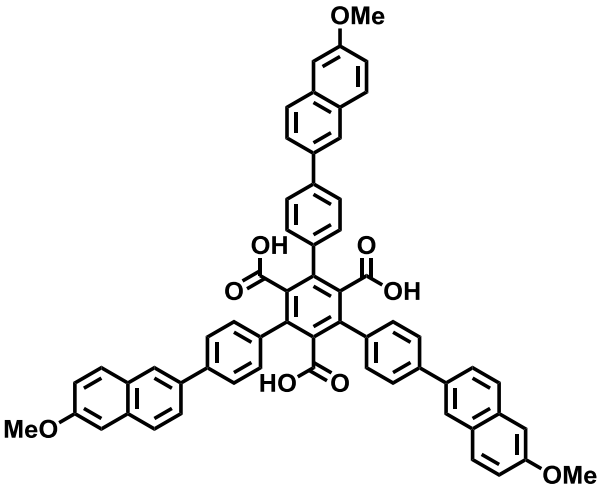

296 mg (363 µmol, 1 eq.) **6** was provided in a solution of 38.2 mg (142 µmol, 0.4 eq.) dodecyltrimethylammonium chloride in 5 mL 0.2 M aqueous sodium hydroxide. The mixture was heated to 95 °C and 371 mg (2.36 mmol, 6.5 eq.) potassium permanganate were added over a time of 3 h. After refluxing the solution for 3 d, the mixture was cooled to room temperature and the occurring precipitate filtered. The filtrate was acidified with concentrated hydrochloric acid and the precipitate filtrated and dried. **7** was obtained as orange solid in 8% (30.2 mg, 29.0 µmol) yield. ^{1}H NMR (500 Mhz, D_2O): δ = 8.10–7.72 (m, 18H), 7.58 (s, 6H), 3.36 (s, 9H); ^{13}C NMR (176 Mhz, D_2O): δ = 129.67, 129.46, 129.27, 127.07, 127.01, 124.38, 124.20, 123.77, 56.72 (due to low solubility, the ^{13}C-signals were derived from ^{1}H-^{13}C HSQC measurements); Elemental analysis: C 79.92, H 4.27 (theoretical: C 79.46, H 4.67).

6.3.7. Synthesis of *N,N*-bis(2-bromoethyl)naphthalene diimide (8)

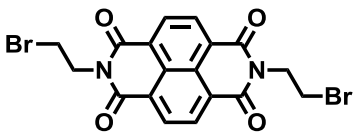

10.00 g (37.3 mmol, 1 eq.) 1,4,5,8-naphthalenetetracarboxylic dianhydride and 91.8 g (1.50 mol, 40 eq.) 2-aminoethanol were reacted under argon atmosphere at 110 °C for 2 d. The reaction was quenched by pouring the mixture into water. The red precipitate

was filtered off and washed with water. The crude intermediate was further provided in 100 mL ethyl acetate under argon atmosphere and stirred for 30 min. Subsequently, a mixture of 65.6 g (410 mmol, 11 eq.) bromine and 22.5 g (164 mmol, 4.4 eq.) phosphorous trichloride was added dropwise and the resulting solution refluxed for 7 h. After cooling to room temperature, the red precipitate was filtered and washed with ethyl acetate, yielding **8** as a bright red powder in 69% (12.4 g, 25.9 mmol) yield. Melting Point: 282°C (decomposition); ^{1}H NMR (250 Mhz, DMSO-d_6): δ = 8.72 (s, 4H), 4.47 (t, 4H, ^{3}J = 7.2 Hz), 3.72 (t, 4H, ^{3}J = 7.2 Hz); ^{13}C NMR (125.7 Mhz, DMSO-d_6): δ = 162.76, 130.67, 126.70, 126.25, 57.72, 28.68; MS (MALDI-TOF, CH_2Cl_2): *m/z* 482.50 $[M+H]^+$ (calc. for $C_{18}H_{13}Br_2N_2O_4$ 481.93), 400.60 $[M-Br-H]^+$ (calc. for $C_{18}H_{12}BrN_2O_4$ 401.00). The fine structure of the mass spectrum at 482.50 m/z suggests an equimolar presence of both $[M+H]^+$ and $[M+2H]^+$.

6.3.8. Synthesis of 1',1'''-((1,3,6,8-tetraoxo-1,3,6,8-tetrahydro-benzo[lmn][3,8]phenanthroline2,7-diyl)bis(ethane-2,1-diyl))bis(1-methyl-[4,4'-bipyridine]-1,1'-diium) chloride (10)

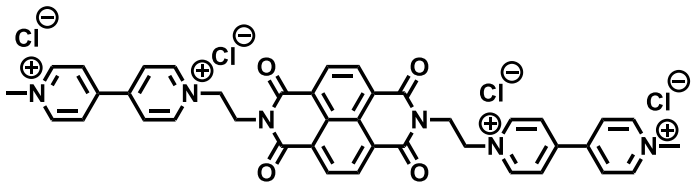

4.00 g (8.33 mmol, 1 eq.) of **8** were provided in 250 mL DMF. After addition of 23.4 g (150 mmol, 18 eq.) 4,4'-bipyridine, the solution was heated to 100 °C for 2 d. After letting the mixture cool to room temperature, it was poured into diethyl ether. The resulting crude intermediate was filtered and washed with diethyl ether and dried. The obtained solid was provided in 200 mL DMF and 59.1 g (416 mmol, 50 eq.) methyl iodide were added dropwise. After heating the reaction mixture to 100 °C for 2 d, it was cooled to room temperature and poured into diethyl ether. The occurring red precipitate was filtered and washed with acetone, ethyl acetate, toluene and DMF. The crude product was subjected to HPLC with acetonitrile:water = 1:1 as eluent and a triethylamine:ammonium acetate buffer. The resulting red solid was dissolved in methanol:HCl = 10:1 for anion exchange and subsequently precipitated in diethyl ether. Filtration gave **10** in 39% (3.49 g, 3.25 mmol) yield. Melting Point: 274°C (decomposition); ^{1}H NMR (300 Mhz, DMSO-d_6): δ = 9.54 (d, 4H, ^{3}J = 6.5 Hz), 9.29 (d,

4H, ^{3}J = 6.5 Hz), 8.79 (d, 8H, ^{3}J = 6.6 Hz), 8.60 (s, 4H), 5.06 (bs, 4H), 4.71 (bs, 4H), 4.44 (s, 6H); ^{13}C NMR (125.7 Mhz, $C_2D_2Cl_4$): δ = 162.40, 148.57, 147.57, 146.01, 130.04, 125.97, 125.78, 59.22, 47.75, 40.55; MS (MALDI-TOF, TCNQ-matrix): *m/z* 662.39 $[M]^+$ (calc. for $C_{40}H_{35}N_6O_4$ 662.62), 685.14 $[M+Na]^+$ (calc. for $C_{40}H_{35}N_6O_4$ 685.25), 720.16 [M-H+acetate]$^+$ (calc. for $C_{42}H_{36}N_6O_6$: 720.27), 815.62 [M+2x acetate+Cl^-]$^+$ (calc. for $C_{44}H_{40}ClN_6O_8$: 815.26). The acetate ions can be found in the mass spectrum due to the use of triethylammonium acetate as buffer during HPLC; (HR-ESI, H_2O): *m/z* found 331.1320 $[M]^{2+}$ (calc. for $C_{40}H_{34}N_6O_4^{2+}$ 331.1321).

6.3.9. Synthesis of 2,7,12-tribromotruxene (10)

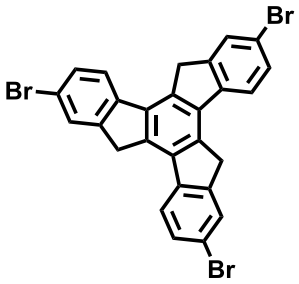

2,7,12-Tribromotruxene **10** was synthesized according to a literature known procedure.[108] 3.28 g (15.6 mmol, 1 eq.) of commercially available 5-bromo-1-indanone were provided with 12.7 g (66.6 mmol, 4.3 eq.) of *p*-toluenesulfonic acid monohydrate and 3.69 g (49.7 mmol, 3.2 eq.) propionic acid in 15 mL *o*-dichlorobenzene. After heating the mixture to 105 °C for 16 h, the crude product was precipitated with methanol and the suspension neutralized with 2 M aqueous sodium hydroxide solution. The filtrated solid was washed with ethanol and methanol. Repeated recrystallization from tetrachloroethane yielded pure **10** as pale yellow solid in 84% (2.54 g, 4.38 mmol). Melting Point: >395°C (decomposition); ^{1}H NMR (500 Mhz, $C_2D_2Cl_4$, 110°C): δ = 7.91 (s, 3H), 7.84 (d, 3H, ^{3}J = 8.2 Hz), 7.71 (d, 3H, ^{3}J = 8.2 Hz), 4.33 (s, 6H); MS (MALDI-TOF, TCNQ-matrix): *m/z* 575.82 $[M]^+$ (calc. for $C_{27}H_{15}Br_3$ 575.87); Conventional ^{13}C NMR experiments were not performable due to the low solubility of the compound. Thus, ^{13}C signals were derived from C-H correlations in a HSQC NMR experiment with δ = 122.50, 128.08, 130.37, 36.00.

6.3.10. Synthesis of 2,7,12-tris(6-methoxynaphthalene-2-yl)truxene (13)

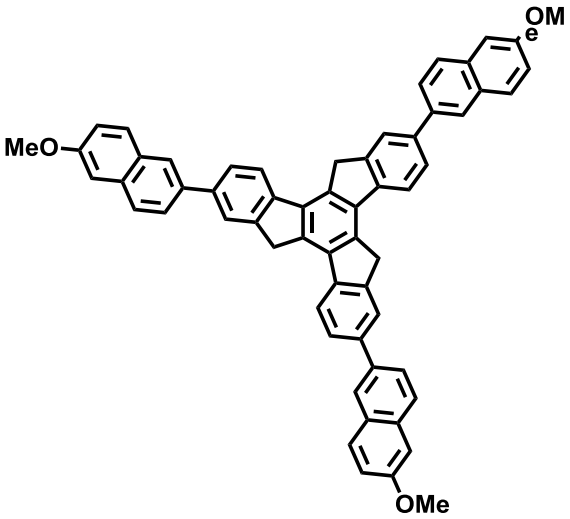

Under argon atmosphere, 2.29 g (11.4 mmol, 6.5 eq.) of commercially available 6-methoxy-2-napthaleneboronic acid were provided with 1.01 g (1.75 mmol, 1 eq.) **10** in a mixture of 50 mL ethanol, 40 mL toluene, and 17 mL 2 M aqueous K_2CO_3 solution. 299 mg (259 µmol, 0.15 eq.) of tetrakis(triphenylphosphine)palladium(0) were added slowly under stirring and the protective atmosphere was ensured by three “freeze-pump-thaw” cycles. After heating the mixture to 90 °C for 2 d, the solution was allowed to cool to room temperature. The suspension was filtrated and the solid washed with ethanol, methanol and aceton. Further recrystallization, first from toluene, then from 1,1,2,2-tetrachloroethane, gave pure **13** in yields of 70°% (1.00 g, 1.23 mmol) as pale yellow powder. Melting Point: 329°C (decomposition); ^{1}H NMR (300 Mhz, $C_2D_2Cl_4$): δ = 8.08–7.99 (m, 9H), 7.90–7.78 (m, 12H), 7.19 (s, 6H), 4.29 (s, 6H), 3.98 (s, 9H); ^{13}C NMR (125.7 Mhz, $C_2D_2Cl_4$): δ = 157.85, 145.76, 140.51, 140.22, 139.52, 136.41, 135.37, 133.73, 130.02, 129.55, 129.32, 128.25, 127.15, 125.95, 125.38, 123.70, 118.84, 106.43, 55.37, 36.54; MS (MALDI-TOF, TCNQ-matrix): *m/z* 810.21 $[M]^+$ (calc. for $C_{60}H_{42}O_3$ 810.31), 809.18 $[M-H]^+$ (calc. for $C_{60}H_{41}O_3$ 809.30).

6.3.11. Synthesis of 1,3,5-tris(6-methoxynaphthalen-2-yl)benzene (15)

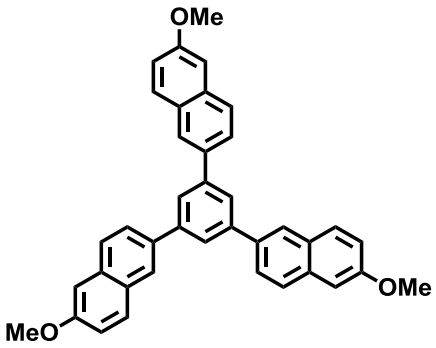

1.00 g (3.18 mmol, 1 eq.) 1,3,5-tribromobenzene and 3.85 g (19.1 mmol, 6 eq.) 6-methoxynaphthalene-2-boronic acid were provided under Ar-atmosphere in a mixture of 24 mL 2 M aqueous Na_2CO_3-solution with 55 mL toluene and 65 mL ethanol. After purging for 1 h, 551 mg (477 µmol, 0.15 eq.) of tetrakis(triphenylphosphine)palladium(0) were added and the mixture heated to 90 °C for 2 d. After cooling to room temperature, water was added and the organic phase extracted with DCM. The solvent was removed and the crude product subjected to column chromatography. The first fraction was collected with DCM/hexane = 1/3 and discarded. The second fraction contained the product and was obtained with DCM/hexane = 2/1 as eluent. Crystallization from DCM, overlayed with EtOH gave pristine **15** as colorless needles in 94% yield (1.63 g, 2.99 mmol). ^{1}H NMR (300 Mhz, CD_2Cl_2): δ = 8.20 (bs, 3H), 8.06 (s, 3H), 7.94-7.83 (m, 9H), 7.27-7.17 (m, 6H), 3.96 (s, 9H); ^{13}C NMR (75.4 Mhz, CD_2Cl_2): δ = 158.39, 142.73, 136.61, 134.44, 130.07, 129.59, 127.72, 126.34, 126.17, 125.27, 119.60, 55.72; MS (FD): *m/z* 546.3 $[M]^+$ (calc. for $C_{39}H_{30}O_3$ 546.22); Elemental analysis: C 85.67, H 5.46 (theoretical: C 85.69, H 5.53).

6.3.12. Synthesis of trimethyl-2,2',2''-nitrilotribenzoat (14)

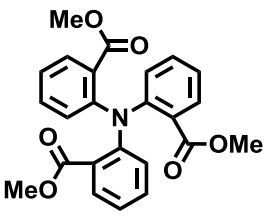

Trimethyl-2,2',2''-nitrilotribenzoat was synthesized according to a literature known procedure.[270] 27.0 mL (31.3 g, 207 mmol, 1 eq.) methyl anthranilate, 122 mL (217 g,

829 mmol, 4 eq.) methyl-2-iodobenzoate, 65.9 g (477 mmol, 2.3 eq.) potassium carbonate, 3.95 g (20.7 mmol, 0.1 eq.) copper iodide, and 2.76 g (43.5 mmol, 0.2 eq.) copper were heated in 250 mL diphenyl ether to 190 °C for 3 d under argon atmosphere. The diphenyl ether was removed by distillation and the remaining solid dissolved in DCM and subjected to column chromatography. The first fractions were collected with DCM as eluent, the product was obtained by using DCM/ethyl acetate = 3/1 as eluent as yellow solid in yields of 60% (52.0 g, 226 mmol). ^{1}H NMR (300 Mhz, CD_2Cl_2): δ = 7.55 (dd, ^{3}J = 7.77 Hz, ^{4}J = 1.62 Hz, 3H), 7.41-7.30 (ddt, ^{3}J = 7.74 Hz, ^{4}J = 1.74 Hz, ^{4}J = 0.88 Hz 3H), 7.10 (dt, ^{3}J = 7.42 Hz, ^{4}J = 1.08 Hz 3H), 7.02 (dd, ^{3}J = 8.22 Hz, ^{4}J = 0.88 Hz, 3H), 3.33 (s, 9H); MS (FD): *m/z* 419.8 $[M]^+$ (calc. for $C_{24}H_{21}NO_6$ 419.1).

6.3.13. Synthesis of 2,2',2''-(nitrilotris(benzene-2,1-diyl))tris-(propan-2-ol) (15)

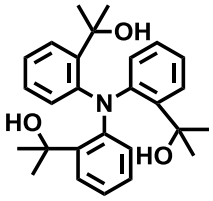

2,2',2''-(Nitrilotris(benzene-2,1-diyl))tris(propan-2-ol) was synthesized according to a literature known procedure.[270] 24.5 mL (55.7 g, 392 mmol, 18.5 eq.) methyl iodide were provided in 200 mL anhydrous ether. This solution was added slowly to 9.14 g (376 mmol, 18 eq.) magnesium chips with little I_2 in 40 mL of anhydrous ether. The mixture was refluxed for 1 h. 8.92 g (21.2 mmol, 1 eq.) **14** in 250 mL dry toluene were added slowly to the reaction mixture and the resulting solution was heated to reflux for 15 h. After cooling down to room temperature, the mixture was poured into 40 mL conc. H_2SO_4 in 1100 mL ice water. The organic phase was extracted with 3x300 mL DCM and dried. The crude product was purified by column chromatography using DCM/Et_2O = 4/1 (2nd fraction). **15** was obtained as yellow-white solid in 32% (2.85 g, 6.80 mmol) yield. Due to sensitivity of the substance to air, it was only characterized with FD-MS and directly provided for further reaction. MS (FD): m/z 420.9 $[M+H]^+$ (calc. for $C_{27}H_{34}NO_3$ 420.3).

6.3.14. Synthesis of 4,4,8,8,12,12-hexamethyl-8,12-dihydro-4H-benzo[9,1]quinolizino[3,4,5,6,7-defg]acridine (16)

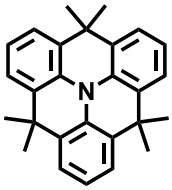

4,4,8,8,12,12-Hexamethyl-8,12-dihydro-4H-benzo[9,1]quinolizino[3,4,5,6,7-defg]acridine was synthesized according to a literature known procedure.[270] 1.87 g (4.46 mmol, 1 eq.) **15** were dispersed in 19 mL (16.2 g, 165 mmol, 37 eq.) 85% H_3PO_4 and stirred for 2 h at room temperature. The mixture was neutralized with 2 M aqueous NaOH solution. The crude product was collected by extraction with 2x50 mL DCM and subjected to column chromatography. Pure **16** was obtained as white solid with the eluent hexane/DCM = 5/1 by yields of 62% (1.01 g, 2.77 mmol). ^{1}H NMR (300 Mhz, CD_2Cl_2): δ = 7.39 (d, ^3J = 7.73 Hz, 6H), 7.12 (t, ^3J = 7.76 Hz, 3H), 1.61 (s, 18H); ^{13}C NMR (75.4 Mhz, CD_2Cl_2): δ = 132.31, 130.18, 123.85, 123.40, 35.83, 33.23; MS (FD): *m/z* 366.2 $[M+H]^+$ (calc. for $C_{27}H_{28}N$ 366.2).

6.3.15. Synthesis of 2,6,10-tribromo-4,4,8,8,12,12-hexamethyl-8,12-dihydro-4H-benzo[9,1]quinolizino[3,4,5,6,7-defg]acridine (17)

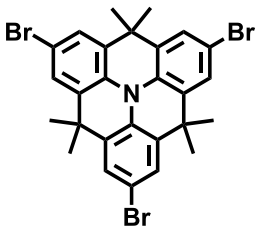

2.00 g (5.47 mmol, 1 eq.) **16** were provided in 50 mL $CHCl_3$ and cooled to 0 °C. 3.12 g (17.5 mmol, 3.2 eq.) *N*-bromosuccinimide were added successively in five equivalent doses. The reaction flask was covered with aluminum foil to avoid photodegradation. The mixture was allowed to reach room temperature and the reaction was completed by stirring for 16 h. The solution was filtered through silica gel and the solvent was removed. Residual oil was collected with 5 mL DCM and mixed with 15 mL EtOH. The DCM was removed by distillation and the solution cooled to -18 °C for 16 h. The resulting colorless precipitate was filtered and dried, giving **17** in 60% (1.98 g,

3.28 mmol) yield. ^{1}H NMR (300 Mhz, CD_2Cl_2): δ = 7.47 (s, 6H), 1.58 (s, 18H); MS (FD): *m/z* 598.7 $[M]^+$ (calc. for $C_{27}H_{24}Br_3N$ 599.0); Elemental analysis: C 53.89, H 3.99, N 2.35 (theoretical: C 53.85, H 4.02 N 2.33).

6.3.16. Synthesis of 2,6,10-tris(6-methoxynaphthalen-2-yl)-4,4,8,8,12,12-hexamethyl-8,12-dihydro-4H-benzo[9,1]quinolizino[3,4,5,6,7-defg]acridine (22)

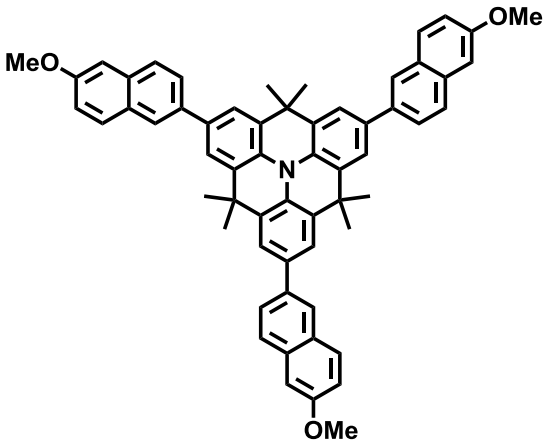

100 mg (166 µmol, 1 eq.) **17** was provided with 201 mg (996 µmol, 6 eq.) 6-methoxynaphthalene-2-boronic acid and 24 mL of a 2 M aqueous Na_2CO_3 solution in 55 mL toluene and 65 mL ethanol under argon atmosphere. After purging for 1 h, 28.8 mg (24.9 µmol, 0.15 eq.) tetrakis(triphenylphosphine)palladium(0) catalyst were added and the mixture heated to 90 °C for 2 d. After cooling to room temperature, 50 mL of water were added and the organic phase extracted with 3x50 mL DCM. The crude product was subjected to column chromatography. The first three fractions were collected using hexane/DCM = 3/1 and hexane/DCM = 1:1 as eluent, respectively. The third fraction contained the product, which was obtained after evaporation of the solvent as yellow-white powder in 52% (71.6 mg, 85.8 µmol) yield. ^{1}H NMR (300 Mhz, CD_2Cl_2): δ = 8.07 (bs, 3H), 7.89-7.82 (m, 15H), 7.22-7.18 (m, 6H), 3.95 (s, 9H), 1.85 (s, 18H); ^{13}C NMR (125.7 Mhz, CD_2Cl_2): δ = 157.28, 134.41, 133.38, 131. 77, 131.22, 130.56, 129.23, 126.73, 126.19, 124.15, 124.02, 123.88, 116.53, 105.17, 35.83, 33.23; MS (FD): *m/z* 834.2 $[M]^+$ (calc. for $C_{60}H_{51}NO_3$ 834.4); Elemental analysis: C 86.66, H 6.49, N 1.56 (theoretical: C 86.40 H 6.16, N 1.68).

6.3.17. Synthesis of 2,5,8-tris(6-methoxynaphthalen-2-yl)benzo[1,2-b:3,4-b':5,6-b'']trithiophene (24)

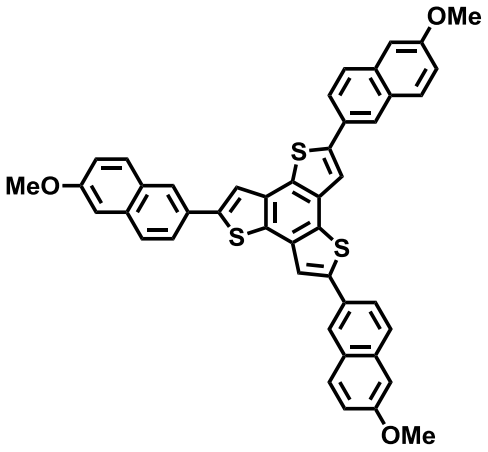

100 mg (207 µmol, 1 eq.) 2,5,8-tribromobenzo[1,2-b:3,4-b':5,6-b'']trithiophene, gratefully received from [redacted] was provided with 251 mg (1.24 mmol, 6 eq.) 6-methoxynaphthalene-2-boronic acid and 24 mL of a 2 M aqueous Na_2CO_3 solution in 55 mL toluene and 65 mL ethanol under argon atmosphere. After purging for 1 h, 35.9 mg (31.1 µmol, 0.15 eq.) tetrakis(triphenylphosphine)palladium(0) catalyst were added and the mixture heated to 90 °C for 2 d. After cooling to room temperature, 50 mL of water were added and the organic phase extracted with 3x50 mL DCM. The crude product was subjected to column chromatography. The first three fractions were collected using hexane/DCM = 3/1 and hexane/DCM = 1:1 as eluent, respectively. The third fraction contained the product, which was obtained after evaporation of the solvent as yellow-white powder in 73% (108 mg, 151 µmol) yield. ^{1}H NMR (300 Mhz, $C_2D_2Cl_4$): δ = 8.11 (bs, 3H), 7.90-7.78 (m, 12H), 7.22-7.13 (m, 6H), 3.96 (s, 9H); ^{13}C NMR (125.7 Mhz, $C_2D_2Cl_4$ @ 373 K): δ = 158.47, 144. 24, 134.57, 132.68, 131.00, 129.73, 129.69, 127.61, 127.35, 126.15, 125.58, 125.17, 125.04, 119.50, 119.04, 117.65, 106.80, 74.24, 55.57; MS (FD): *m/z* 715.5 $[M+H]^+$ (calc. for $C_{45}H_{30}N_3S_3$ 715.1).

6.3.18. Synthesis of 2,4-dinitrophenyl-4,4'-bispyridinium chloride (20)

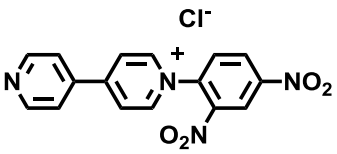

20.0 g (128 mmol, 1 eq.) 4,4'-bipyridine was provided with 26.0 g (128 mmol, 1 eq.) 2,4-dinitrochlorobenzene in 200 mL ethanol. After refluxing the mixture for 24 h, 1 L Et_2O was added. The precipitate was filtered and washed with Et_2O. **20** was obtained as yellow-brown solid in 78% (36,1 g, 101 mmol) yield. ^{1}H NMR (250 Mhz, MeOD): δ = 9.42 (d, ^3J = 7.16 Hz, 2H), 9.31 (d, ^4J = 2.45 Hz, 1H), 8.98-8.91 (m, 3H), 8.83 (d, ^3J = 7.16 Hz, 2H).

6.3.19. Synthesis of 1,1''-(1,4-phenylene)bis(([4,4'-bipyridin]-1-ium)) chloride (21)

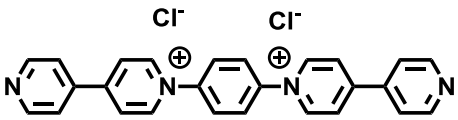

To 10.9 g (30.4 mmol, 2 eq.) **20** in 180 mL ethanol were added 1.67 g (15.4 mmol, 1 eq.) of 1,4-diaminophenyl. The solution was refluxed for 2 d and subsequently cooled to room temperature. 1.2 L of water were added and the precipitate filtered off. The filtrate was collected and the solvent removed. The resulting solid was dissolved in 0.7 L ethanol and precipitated with 4 L Et_2O. **21** was obtained as dark red solid after filtration and drying in 99% (5.92 g, 15.2 mmol) yield. ^{1}H NMR (300 Mhz, DMSO-d_6): δ = 9.60 (dd, ^3J = 22.05 Hz, ^4J = 6.85 Hz, 4H), 9.34 (d, ^3J = 7.15 Hz, 4H), 8.99-8.87 (m, 4H), 8.67 (d, ^3J = 7.11 Hz 4H), 8.37 (s, 4H); Elemental analysis: C 67.26, H 4.11, N 12.12 (theoretical: C 67.98, H 4.39, N 12.20).

6.3.20. Synthesis of 1',1'''-(1,4-phenylene)bis(1-methyl-[4,4'-bipyridine]-1,1'-diium) dichloride diiodide (28)

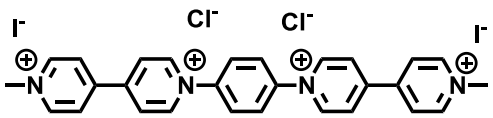

4.13 g (9.00 mmol, 1 eq.) **21** were dissolved in 400 mL DMF. 12 mL (27.1 g, 171 mmol) methyl iodide were added and the mixture stirred at 100 °C for 16 h. After cooling to room temperature, solution was poured into 1.5 L Et_2O. The resulting precipitate was filtered and washed with EtOH and DCM. After recrystallization from MeCN/H_2O = 10/1, pure **28** was obtained as red solid in yields of 32% (2.14 g, 2.88 mmol). ^{1}H NMR (300 Mhz, DMSO-d_6): δ = 9.79 (d, ^3J = 5.77 Hz, 4H), 9.37 (d, ^3J = 5.55 Hz, 4H), 9.03 (d, ^3J = 5.55 Hz, 4H), 8.93 (d, ^3J = 5.55 Hz, 4H), 8.42 (s, 4H), 4.49 (s, 6H); ^{13}C NMR (125.7 Mhz, DMSO-d_6): δ = 153.45, 149.43, 145.39, 131.51, 130.64, 128.44, 125.23, 51.39; Elemental analysis: C 44.78, H 3.31, N 7.49 (theoretical: C 45.25, H 3.53, N 7.54).

6.3.21. Synthesis of 1,1''-([1,1':4',1''-terphenyl]-4,4''-diyl)bis-(([4,4'-bipyridin]-1-ium)) chloride (23)

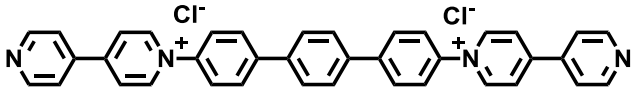

7.96 g (22.2 mmol, 2.3 eq.) **20** were dissolved in 100 mL ethanol under argon atmosphere. 2.47 g (9.49 mmol, 1 eq.) [1,1':4',1''-terphenyl]-4,4''-diamine were added and the mixture refluxed for 2 d. The suspension was filtrated and the filtrate collected. After pouring the filtrate into 5 L EtOAc, the occurring precipitate was filtrated and washed with water and EtOAc. **23** was obtained as yellow solid after hot filtration from water with subsequent evaporation of the solvent in 34% (1.99 g, 3.25 mmol) yield. ^{1}H NMR (300 Mhz, DMSO-d_6): δ = 9.59 (d, ^3J = 6.96 Hz, 4H), 8.94 (d, ^3J = 6.05 Hz, 4H), 8.84 (d, ^3J = 6.96 Hz, 4H) 8.21-8.03 (m, 16H).

6.3.22. Synthesis of 1',1'''-([1,1':4',1''-terphenyl]-4,4''-diyl)bis-(1-methyl-[4,4'-bipyridine]-1,1'-diium) dichloride diiodide (31)

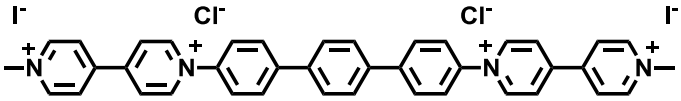

1.00 g (1.64 g, 1 eq.) **23** were heated with 5.09 mL (11.6 g, 81.8 mmol, 50 eq.) methyl iodide in 50 mL DMF under argon atmosphere to 100 °C for 2 d. The precipitate was filtered and washed with DMF and aceton. The crude product was recrystallized from isopropanol to give **31** in 98% yield (1.44 g, 1.61 mmol). ^{1}H NMR (300 Mhz, DMSO-d_6): δ = 9.74 (d, ^{3}J = 6.92 Hz, 4H), 9.33 (d, ^{3}J = 6.92 Hz, 4H), 8.99 (d, ^{3}J = 6.92 Hz 4H), 8.90 (d, ^{3}J = 6.92 Hz, 4H), 8.24 (d, ^{3}J = 8.82 Hz, 4H), 8.11 (d, ^{3}J = 8.82 Hz, 4H), 8.04 (s, 4H), 4.47 (s, 6H); ^{13}C NMR (125.7 Mhz, DMSO-d_6): δ = 151.49, 147.99, 143.58, 142.14, 142.05, 131.41, 129.87, 128.62, 128.35, 127.01, 126.66, 124.31, 49.46; Elemental analysis: C 52.81, H 3.61, N 6.10 (theoretical: C 53.65, H 3.83, N 6.26).

6.3.23. Synthesis of 2,3,6,7,10,11-hexabenzothiotripheny-lene (25)

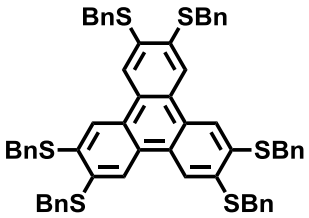

288 mg sodium hydride (12 mmol) were provided in 20 mL *N,N*'-dimethylimizolidinone in a two-neck flask under argon atmosphere. After cooling the flask to 0 °C with an ice bath, 1.49 g benzyl mercaptan (12 mmol) were added slowly to avoid foaming. After letting the mixture react for 30 min, 0.701 g 2,3,6,7,10,11-hexabrommotriphenylene[136] (1 mmol) were added. After stirring for 10 min, cooling was removed and the reaction completed at room temperature for 4 h. The reaction was then quenched with 150 mL saturated Na_2CO_3 solution and extracted with 150 mL toluene. The organic phase was washed with saturated Na_2CO_3 solution and the solvent was removed. Hexabenzothiotriphenylene was obtained after column chromatography (eluent: DCM/hexane = 1/1) as white solid in 65% yield (625 mg, 0.65 mmol). ^{1}H NMR (250

MHz, CD_2Cl_2): δ = 7.98 (s, 6H), 7.25-7.41 (m, 30H), 4.03 (s, 12H). MALDI-MS (m/z): 961.01 (calc. for $C_{60}H_{48}S_6$: 961.41).

6.3.24. Synthesis of hexasodium-2,3,6,7,10,11-triphenylene-hexathiolate (34)

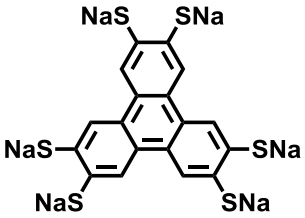

10 mL of anhydrous liquid ammonia were provided at -78 °C. 0.331 g (14.4 mmol) sodium were added slowly. After letting the reaction mixture stir for 20 min, 0.192 g (0.22 mmol) 2,3,6,7,10,11-hexabenzothiotriphenylene were added slowly. The reaction was completed by stirring while maintaining -78 °C for 4 h, before it was quenched with methanol. Cooling was removed and the mixture was allowed to reach room temperature. 10 mL degassed water (the water was degassed with several freeze-pump-thaw cycles) were added and washed with ethyl ether. The aqueous phase was freeze-dried to give the crude product, which was provided without further purification.

6.3.25. Synthesis of 2,3,6,7,10,11-triphenylenehexathiol (35)

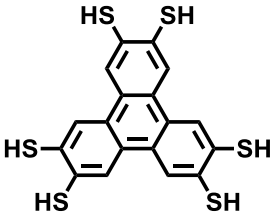

Crude hexasodium-2,3,6,7,10,11-triphenylenehexathiolate was dissolved in 10 mL degassed water and reacted with 20 mL of a degassed 5% HCl solution, which was added dropwise. After filtration of the occurring precipitate, the target compound 2,3,6,7,10,11-triphenylenehexathiol was obtained as white solid in yields of 97 °% (82.3 mg, 0.20 mmol, yield given over two steps). MALDI-MS (m/z): 419.93 (calc. for $C_{18}H_{12}S_6$: 419.93), 387.98 (calc. for $C_{18}H_{12}S_5$: 387.95).

6.3.26. Synthesis of perchlorocoronene (37)

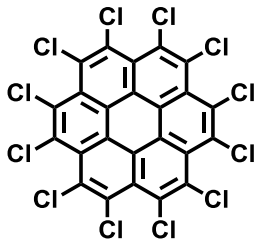

480 mg (1.61 mmol, 1 eq.) coronene were refluxed with 426 mg (3.24 mmol, 2 eq.) $AlCl_3$ and 15 g (192 mmol, 120 eq) ICl in 40 ml CCl_4 for 2 d. The reaction was quenched with 50 mL of methanol. The precipitate was filtered and washed with 1 M HCl solution, methanol, and aceton. **37** was obtained as yellow powder in yields of 93% (1.00 g, 1.41 mmol). MALDI-MS (m/z): 713.69 (calc. for $C_{24}Cl_{12}$: 713.84).

6.3.27. Synthesis of per(benzylthio)coronene (38)

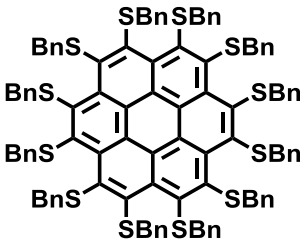

120 mg (5.10 mmol, 24 eq.) sodium hydride were provided in 10 mL dry DMI under argon atmosphere. The reaction mixture was cooled to 0 °C and 596 mg (4.89 mmol, 23 eq.) were added drop-wise. After stirring for 1 h, 143 mg (212 µmol, 1 eq.) of **37** were added. The reaction was stirred at room temperature for 4 h. The mixture was quenched with 150 mL saturated Na_2CO_3 solution and extracted with toluene (3x50 mL). The crude product was subjected to column chromatography using DCM/hexane = 1/1 as eluent. The last fraction contained **38**, which was obtained after evaporation of the solvent as red solid in 62% (232 mg, 131 µmol) yield. ^{1}H NMR (250 MHz, $CDCl_3$): δ = 6.80-6.84 (m, 60H), 4.36 (s, 24H); ^{13}C NMR (250 MHz, $CDCl_3$): δ = 137.31, 129.01, 128.22, 127.11, 122.28, 44.05; FD MS (m/z): 1766.8 (calc. for $C_{108}H_{84}S_{12}$: 1766.6026).

6.3.28. Synthesis of per(lithiumthiolate)coronene (39)

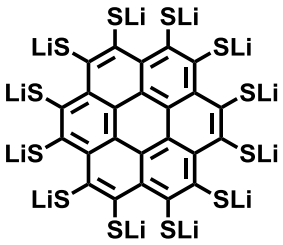

200 mg (0.12 mmol, 1 eq) **38** were provided in 10 mL liquid ammonia at -78 °C. 190 mg (27.2 mmol, 270 eq) lithium were added in five equivalent portions and the solution reacted for 1 h. The reaction was quenched with 10 mL dry methanol and 10 mL degassed water. The mixture was extracted with 3x20 mL Et_2O and crude **39** was obtained as red solid after evaporation of the solvent. This intermediate was reacted without further purification or characterization due to air-sensitivity.

6.3.29. Synthesis of per(disulfide)coronene (40)

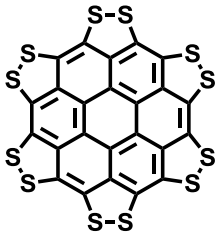

39 was dissolved in 10 mL degassed water and 200 mL degassed 2 M aqueous HCl solution were added. After the precipitate was filtrated and washed with water, it was purified by hot filtration from toluene, giving **40** as dark red solid in yields of 10% (8 mg, 11.9 µmol) over both steps. MALDI-ToF MS (m/z): 671.8 (calc. for $C_{24}S_{12}$: 671.7).

6.3.30. Synthesis of perthiolcoronene (41)

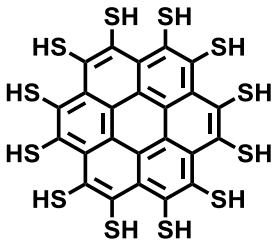

Under argon atmosphere, 3.0 mg (4.46 µmol, 1 eq.) **40** were stirred for 30 min with 1.0 mg (26.4 µmol, 6 eq.) $NaBH_4$ in 10 mL dry THF. After filtration, the solvent of the filtrate was evaporated to provide **41** as dark red solid in quantitative yield (3.1 mg, 4.46 µmol). ^1H NMR (250 MHz, CD_2Cl_2): δ = 2.81 (s, 12H); MALDI-ToF MS (m/z): 685.48 (calc. for $C_{24}H_{12}S_{12}$: 685.13).

6.3.31. Alternative synthesis of perchlorocoronene (37)

Perchlorocoronene was synthesized by perchlorination under BMC conditions[271] of commercially available coronene. 750 mg (5.63 mmol, 0.56 eq.) $AlCl_3$ were refluxed in 280 mL sulfuryl chloride. 3.00 g (9.99 mmol, 1 eq.) coronene was dispersed with 1.50 g (11.1 mmol, 0.89 mL, 1.1 eq.) disulfur dichloride in 120 mL sulfuryl chloride and slowly added to the reaction. The mixture was refluxed for 30 h and 50 mL sulfuryl chloride were added for dissolving occurring precipitation. Subsequently, the solvent was evaporated and the residue poured into ethanol. The occurring precipitate was filtered and washed with ethanol, aqueous 1 M hydrochloric acid solution, water, and aceton to give **37** as yellow powder in quantitative yields (7.23 g, 9.99 mmol). ^{13}C NMR (125.7 MHz, $C_2D_2Cl_4$, δ): 132.8 (C4), 126.4 (C4), 121.1 (C4); MALDI-MS (m/z): 713.2 [M^+] (calc. for $C_{24}Cl_{12}$: 713.84).

6.3.32. Synthesis of randomly disulfide-bridged material (42)

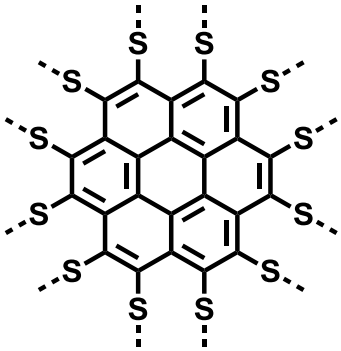

674 mg (21.0 mmol, 15 eq.) sulfur and 483 mg (21.0 mmol, 15 eq.) sodium were heated in 150 mL of DMI to 110 °C for 1 h. 1.00 g (1.4 mmol, 1 eq.) **37** were added and the solution was further heated to 150 °C for 2 d. The reaction mixture was quenched with 200 mL of 5 M aqueous HCl solution. After filtration of the precipitate with water, methanol, and aceton, the crude product was purified by washing with hot toluene, producing **42** in 98% yield as black solid.

7. References

[1] "The Nobel Prize in Physics 2010". *Nobelprize.org*. Nobel Media AB 2014. 26 Jul 2016. <http://www.nobelprize.org/nobel_prizes/physics/laureates/2010/advanced.html>

[2] M. Osada, T. Sasaki, *Adv. Mater.* **2012**, *24*, 210-228.

[3] K. I. Bolotin, K. J. Sikes, Z. Jiang, M. Klima, G. Fudenberg, J. Hone, P. Kim, H. L. Stormer, *Solid State Communications* **2008**, *146*, 351-355.

[4] S. V. Morozov, K. S. Novoselov, M. I. Katsnelson, F. Schedin, D. C. Elias, J. A. Jaszczak, A. K. Geim, *Physical Review Letters* **2008**, *100*, 016602.

[5] K. S. Novoselov, A. K. Geim, S. V. Morozov, D. Jiang, Y. Zhang, S. V. Dubonos, I. V. Grigorieva, A. A. Firsov, *Science* **2004**, *306*, 666-669.

[6] Y. Zhang, Y.-W. Tan, H. L. Stormer, P. Kim, *Nature* **2005**, *438*, 201-204.

[7] X. Li, X. Wang, L. Zhang, S. Lee, H. Dai, *Science* **2008**, *319*, 1229-1232.

[8] A. A. Balandin, S. Ghosh, W. Bao, I. Calizo, D. Teweldebrhan, F. Miao, C. N. Lau, *Nano Letters* **2008**, *8*, 902-907.

[9] C. Lee, X. Wei, J. W. Kysar, J. Hone, *Science* **2008**, *321*, 385-388.

[10] J. Sakamoto, H. J. van, O. Lukin, A. D. Schlüter, *Angew. Chem., Int. Ed.* **2009**, *48*, 1030–1069.

[11] X. Zhuang, Y. Mai, D. Wu, F. Zhang, X. Feng, *Adv. Mater.* **2015**, *27*, 403-427.

[12] P. Payamyar, B. T. King, H. C. Ottinger, A. D. Schluter, *Chemical Communications* **2016**, *52*, 18-34.

[13] M. F. Brigatti, A. Mottana, *Layered Mineral Structures and their Application in Advanced Technologies*, Mineralogical Society of Great Britain and Ireland, **2010**.

[14] H. O. Pierson, in *Handbook of Carbon, Graphite, Diamonds and Fullerenes*, William Andrew Publishing, Oxford, **1993**, pp. 43-69.

[15] F. J. Maile, G. Pfaff, P. Reynders, *Progress in Organic Coatings* **2005**, *54*, 150-163.

[16] J. N. Coleman, M. Lotya, A. O'Neill, S. D. Bergin, P. J. King, U. Khan, K. Young, A. Gaucher, S. De, R. J. Smith, I. V. Shvets, S. K. Arora, G. Stanton, H.-Y. Kim, K. Lee, G. T. Kim, G. S. Duesberg, T. Hallam, J. J. Boland, J. J. Wang, J. F. Donegan, J. C. Grunlan, G. Moriarty, A. Shmeliov, R. J. Nicholls, J. M. Perkins, E. M. Grieveson, K. Theuwissen, D. W. McComb, P. D. Nellist, V. Nicolosi, *Science (Washington, DC, U. S.)* **2011**, *331*, 568-571.

[17] H.-C. Zhou, J. R. Long, O. M. Yaghi, *Chemical Reviews* **2012**, *112*, 673-674.

[18] X. Feng, X. Ding, D. Jiang, *Chem. Soc. Rev.* **2012**, *41*, 6010-6022.

[19] A. P. Côté, H. M. El-Kaderi, H. Furukawa, J. R. Hunt, O. M. Yaghi, *J. Am. Chem. Soc.* **2007**, *129*, 12914-12915.

[20] C. Wu, X. Lu, L. Peng, K. Xu, X. Peng, J. Huang, G. Yu, Y. Xie, *Nat. Commun.* **2013**, *4*.

[21] K. Xu, P. Chen, X. Li, C. Wu, Y. Guo, J. Zhao, X. Wu, Y. Xie, *Angew. Chem., Int. Ed.* **2013**, *52*, 10477-10481.

[22] W. J. Roth, P. Nachtigall, R. E. Morris, J. Cejka, *Chem. Rev. (Washington, DC, U. S.)* **2014**, *114*, 4807-4837.

[23] X. Huang, S. Tang, X. Mu, Y. Dai, G. Chen, Z. Zhou, F. Ruan, Z. Yang, N. Zheng, *Nat. Nanotechnol.* **2011**, *6*, 28-32.

[24] J. Niu, D. Wang, H. Qin, X. Xiong, P. Tan, Y. Li, R. Liu, X. Lu, J. Wu, T. Zhang, W. Ni, J. Jin, *Nat. Commun.* **2014**, *5*.

[25] M. Chhowalla, H. S. Shin, G. Eda, L.-J. Li, K. P. Loh, H. Zhang, *Nat. Chem.* **2013**, *5*, 263-275.

[26] Z. Sun, T. Liao, Y. Dou, S. M. Hwang, M.-S. Park, L. Jiang, J. H. Kim, S. X. Dou, *Nat. Commun.* **2014**, *5*, 3813.

[27] F. Xia, H. Wang, D. Xiao, M. Dubey, A. Ramasubramaniam, *Nat. Photon.* **2014**, *8*, 899-907.

[28] P. K. Kannan, D. J. Late, H. Morgan, C. S. Rout, *Nanoscale* **2015**, *7*, 13293-13312.

[29] C. N. R. Rao, H. S. S. Ramakrishna Matte, U. Maitra, *Angew. Chem., Int. Ed.* **2013**, *52*, 13162-13185.

[30] R. Mas-Balleste, C. Gomez-Navarro, J. Gomez-Herrero, F. Zamora, *Nanoscale* **2011**, *3*, 20-30.

[31] M. Bieri, M.-T. Nguyen, O. Groning, J. Cai, M. Treier, K. Ait-Mansour, P. Ruffieux, C. A. Pignedoli, D. Passerone, M. Kastler, K. Mullen, R. Fasel, *J. Am. Chem. Soc.* **2010**, *132*, 16669-16676.

[32] M. Abel, S. Clair, O. Ourdjini, M. Mossoyan, L. Porte, *J. Am. Chem. Soc.* **2011**, *133*, 1203-1205.

[33] N. A. A. Zwaneveld, R. Pawlak, M. Abel, D. Catalin, D. Gigmes, D. Bertin, L. Porte, *J. Am. Chem. Soc.* **2008**, *130*, 6678-6679.

[34] D. N. Bunck, W. R. Dichtel, *J. Am. Chem. Soc.* **2013**, *135*, 14952-14955.

[35] K. Baek, G. Yun, Y. Kim, D. Kim, R. Hota, I. Hwang, D. Xu, Y. H. Ko, G. H. Gu, J. H. Suh, C. G. Park, B. J. Sung, K. Kim, *J. Am. Chem. Soc.* **2013**, *135*, 6523–6528.

[36] P. Kissel, R. Erni, W. B. Schweizer, M. D. Rossell, B. T. King, T. Bauer, S. Goetzinger, A. D. Schlüter, J. Sakamoto, *Nat. Chem.* **2012**, *4*, 287–291.

[37] R. Bhola, P. Payamyar, D. J. Murray, B. Kumar, A. J. Teator, M. U. Schmidt, S. M. Hammer, A. Saha, J. Sakamoto, A. D. Schluter, B. T. King, *J. Am. Chem. Soc.* **2013**, *135*, 14134–14141.

[38] D. J. Murray, D. D. Patterson, P. Payamyar, R. Bhola, W. Song, M. Lackinger, A. D. Schluter, B. T. King, *J. Am. Chem. Soc.* **2015**, *137*, 3450-3453.

[39] A. M. Brockway, J. Schrier, *J. Phys. Chem. C* **2013**, *117*, 393-402.

[40] J. W. Steed, J. L. Atwood, Editors, *Supramolecular Chemistry, Second Edition*, John Wiley & Sons, Ltd., **2009**.

[41] Lehn, *Supramolecular Chemistry - Concepts and Perspectives*, Wiley-Blackwell, **1995**.

[42] K. Ariga, *Supramolecular Chemistry — Fundamentals and Applications Advanced Textbook*, Springer Berlin Heidelberg, Berlin, Heidelberg, **2006**.

[43] E. Fischer, *Berichte der deutschen chemischen Gesellschaft* **1894**, *27*, 2985-2993.

[44] S. Sivakova, S. J. Rowan, *Chemical Society Reviews* **2005**, *34*, 9-21.

[45] G. M. Whitesides, J. P. Mathias, C. T. Seto, *Science* **1991**, *254*, 1312-1319.

[46] R. G. Chapman, J. C. Sherman, *Tetrahedron* **1997**, *53*, 15911-15945.

[47] J. D. Dunitz, *Pure Appl. Chem.* **1991**, *63*, 177-185.

[48] C. B. Aakeroy, K. R. Seddon, *Chemical Society Reviews* **1993**, *22*, 397-407.

[49] M. O. Sinnokrot, C. D. Sherrill, *J. Phys. Chem. A* **2006**, *110*, 10656-10668.

[50] P. Metrangolo, G. Resnati, *Chemistry – A European Journal* **2001**, *7*, 2511-2519.

[51] E. A. Appel, J. del Barrio, X. J. Loh, O. A. Scherman, *Chemical Society Reviews* **2012**, *41*, 6195-6214.

[52] J. R. R. Tolkien, *The Lord of the Rings*, Houghton Mifflin, Boston, **1987**.

[53] J. Kim, I.-S. Jung, S.-Y. Kim, E. Lee, J.-K. Kang, S. Sakamoto, K. Yamaguchi, K. Kim, *J. Am. Chem. Soc.* **2000**, *122*, 540-541.

[54] F. H. Beijer, H. Kooijman, A. L. Spek, R. P. Sijbesma, E. W. Meijer, *Angew. Chem. Int. Ed.* **1998**, *37*, 75-78.

[55] Y.-M. Jeon, J. Kim, D. Whang, K. Kim, *J. Am. Chem. Soc.* **1996**, *118*, 9790-9791.

[56] D. Whang, Y.-M. Jeon, J. Heo, K. Kim, *J. Am. Chem. Soc.* **1996**, *118*, 11333-11334.

[57] D. Whang, K. Kim, *J. Am. Chem. Soc.* **1997**, *119*, 451-452.

[58] W. L. Mock, T. A. Irra, J. P. Wepsiec, T. L. Manimaran, *J. Org. Chem.* **1983**, *48*, 3619-3620.

[59] M. V. Rekharsky, T. Mori, C. Yang, Y. H. Ko, N. Selvapalam, H. Kim, D. Sobransingh, A. E. Kaifer, S. Liu, L. Isaacs, W. Chen, S. Moghaddam, M. K. Gilson, K. Kim, Y. Inoue, *Proceedings of the National Academy of Sciences* **2007**, *104*, 20737-20742.

[60] K. I. Assaf, W. M. Nau, *Chemical Society Reviews* **2015**, *44*, 394-418.

[61] W. M. Nau, M. Florea, K. I. Assaf, *Israel Journal of Chemistry* **2011**, *51*, 559-577.

[62] F. Biedermann, V. D. Uzunova, O. A. Scherman, W. M. Nau, A. De Simone, *J. Am. Chem. Soc.* **2012**, *134*, 15318-15323.

[63] U. Rauwald, F. Biedermann, S. Deroo, C. V. Robinson, O. A. Scherman, *J. Phys. Chem. B* **2010**, *114*, 8606–8615.

[64] U. Rauwald, O. A. Scherman, *Angew. Chem., Int. Ed.* **2008**, *47*, 3950–3953.

[65] C. J. Pedersen, *J. Am. Chem. Soc.* **1967**, *89*, 7017-7036.

[66] C. J. Pedersen, *J. Am. Chem. Soc.* **1967**, *89*, 2495-2496.

[67] S. L. James, *Chemical Society Reviews* **2003**, *32*, 276-288.

[68] J. C. Bailar, Jr., *Reinhold Publishing Corp., New York, N.Y.* **1956**, 834 pp.

[69] J. J. Zuckerman, *Journal of Chemical Education* **1966**, *43*, 224.

[70] T. Bauer, Z. Zheng, A. Renn, R. Enning, A. Stemmer, J. Sakamoto, A. D. Schlüter, *Angew. Chem., Int. Ed.* **2011**, *50*, 7879–7884.

[71] M. J. Kory, D. A. Schlueter, **2015**.

[72] Q. Sun, Y. Dai, Y. Ma, X. Li, W. Wei, B. Huang, *J. Mater. Chem. C* **2015**, *3*, 6901-6907.

[73] M. Vybornyi, A. V. Rudnev, S. M. Langenegger, T. Wandlowski, G. Calzaferri, R. Haener, *Angew. Chem., Int. Ed.* **2013**, *52*, 11488-11493.

[74] S. Shin, S. Lim, Y. Kim, T. Kim, T.-L. Choi, M. Lee, *J. Am. Chem. Soc.* **2013**, *135*, 2156-2159.

[75] X. Hou, Z. Wang, M. Overby, A. Ugrinov, C. Oian, R. Singh, Q. R. Chu, *Chemical Communications* **2014**, *50*, 5209-5211.

[76] K.-D. Zhang, J. Tian, D. Hanifi, Y. Zhang, A. C.-H. Sue, T.-Y. Zhou, L. Zhang, X. Zhao, Y. Liu, Z.-T. Li, *J. Am. Chem. Soc.* **2013**, *135*, 17913-17918.

[77] L. Zhang, T.-Y. Zhou, J. Tian, H. Wang, D.-W. Zhang, X. Zhao, Y. Liu, Z.-T. Li, *Polymer Chemistry* **2014**, *5*, 4715-4721.

[78] S.-Q. Xu, X. Zhang, C.-B. Nie, Z.-F. Pang, X.-N. Xu, X. Zhao, *Chem. Commun.* **2015**, *51*, 16417-16420.

[79] T. Y. Zhou, Q. Y. Qi, Q. L. Zhao, J. Fu, Y. Liu, Z. Ma, X. Zhao, *Polymer Chemistry* **2015**, *6*, 3018-3023.

[80] L. Yue, S. Wang, D. Zhou, H. Zhang, B. Li, L. Wu, *Nat. Commun.* **2016**, *7*:10742.

[81] R. Sakamoto, K. Hoshiko, Q. Liu, T. Yagi, T. Nagayama, S. Kusaka, M. Tsuchiya, Y. Kitagawa, W. Y. Wong, H. Nishihara, *Nat. Commun.* **2015**, *6*, 6713.

[82] T. Kambe, R. Sakamoto, K. Hoshiko, K. Takada, M. Miyachi, J.-H. Ryu, S. Sasaki, J. Kim, K. Nakazato, M. Takata, H. Nishihara, *J. Am. Chem. Soc.* **2013**, *135*, 2462–2465.

[83] A. J. Clough, J. W. Yoo, M. H. Mecklenburg, S. C. Marinescu, *J. Am. Chem. Soc.* **2015**, *137*, 118-121.

[84] M. G. Campbell, D. Sheberla, S. F. Liu, T. M. Swager, M. Dincă, *Angew. Chem. Int. Ed.* **2015**, *54*, 4349-4352.

[85] W. Eck, A. Küller, M. Grunze, B. Völkel, A. Gölzhäuser, *Advanced Materials* **2005**, *17*, 2583-2587.

[86] A. Becker, T. R. Kannan, A. B. Taylor, O. N. Pakhomova, Y. Zhang, S. R. Somarajan, A. Galaleldeen, S. P. Holloway, J. B. Baseman, P. J. Hart, *Proceedings of the National Academy of Sciences* **2015**, *112*, 5165-5170.

[87] M. Suga, F. Akita, K. Hirata, G. Ueno, H. Murakami, Y. Nakajima, T. Shimizu, K. Yamashita, M. Yamamoto, H. Ago, J.-R. Shen, *Nature* **2015**, *517*, 99-103.

[88] H.-J. Kim, J. Heo, W. S. Jeon, E. Lee, J. Kim, S. Sakamoto, K. Yamaguchi, K. Kim, *Angew. Chem., Int. Ed.* **2001**, *40*, 1526–1529.

[89] Y. J. Jeon, P. K. Bharadwaj, S. Choi, J. W. Lee, K. Kim, *Angew. Chem. Int. Ed.* **2002**, *41*, 4474-4476.

[90] T. Mori, Y. H. Ko, K. Kim, Y. Inoue, *J. Org. Chem.* **2006**, *71*, 3232-3247.

[91] D. Jiao, F. Biedermann, O. A. Scherman, *Organic Letters* **2011**, *13*, 3044-3047.

[92] F. Biedermann, O. A. Scherman, *J. Phys. Chem. B* **2012**, *116*, 2842−2849.

[93] F. Biedermann, E. Elmalem, I. Ghosh, W. M. Nau, O. A. Scherman, *Angew. Chem. Int. Ed.* **2012**, *51*, 7739-7743.

[94] P. W. Sutter, J.-I. Flege, E. A. Sutter, *Nat. Mater.* **2008**, *7*, 406-411.

[95] X. Li, C. W. Magnuson, A. Venugopal, R. M. Tromp, J. B. Hannon, E. M. Vogel, L. Colombo, R. S. Ruoff, *J. Am. Chem. Soc.* **2011**, *133*, 2816-2819.

[96] B. Lee, I. Park, J. Yoon, S. Park, J. Kim, K.-W. Kim, T. Chang, M. Ree, *Macromolecules* **2005**, *38*, 4311-4323.

[97] P. Müller-Buschbaum, *Analytical and Bioanalytical Chemistry* **2003**, *376*, 3-10.

[98] K. Nakamoto, in *Handbook of Vibrational Spectroscopy*, John Wiley & Sons, Ltd, **2006**.

[99] J. B. Hodgson, G. C. Percy, *Spectrochimica Acta Part A: Molecular Spectroscopy* **1978**, *34*, 777-780.

[100] R. D. Feltham, P. Brant, *J. Am. Chem. Soc.* **1982**, *104*, 641-645.

[101] J.-C. Dupin, D. Gonbeau, P. Vinatier, A. Levasseur, *Physical Chemistry Chemical Physics* **2000**, *2*, 1319-1324.

[102] J. del Barrio, P. N. Horton, D. Lairez, G. O. Lloyd, C. Toprakcioglu, O. A. Scherman, *J. Am. Chem. Soc.* **2013**, *135*, 11760-11763.

[103] K. J. Hartlieb, A. N. Basuray, C. Ke, A. A. Sarjeant, H.-P. Jacquot de Rouville, T. Kikuchi, R. S. Forgan, J. W. Kurutz, J. F. Stoddart, *Asian Journal of Organic Chemistry* **2013**, *2*, 225-229.

[104] D. Das, O. A. Scherman, *Israel Journal of Chemistry* **2011**, *51*, 537-550.

[105] F. Tian, M. Cziferszky, D. Jiao, K. Wahlström, J. Geng, O. A. Scherman, *Langmuir* **2011**, *27*, 1387-1390.

[106] Y. Liu, H. Yang, Z. Wang, X. Zhang, *Chemistry – An Asian Journal* **2013**, *8*, 1626-1632.

[107] D. Kuenzel, T. Markert, A. Gross, D. M. Benoit, *Phys. Chem. Chem. Phys.* **2009**, *11*, 8867-8878.

[108] A. W. Amick, L. T. Scott, *J. Org. Chem.* **2007**, *72*, 3412–3418.

[109] J. P. Rane, V. Pauchard, A. Couzis, S. Banerjee, *Langmuir* **2013**, *29*, 4750–4759.

[110] X. Zhang, C.-B. Nie, T.-Y. Zhou, Q.-Y. Qi, J. Fu, X.-Z. Wang, L. Dai, Y. Chen, X. Zhao, *Polym. Chem.* **2015**, *6*, 1923-1927.

[111] L. Yang, X. Liu, X. Tan, H. Yang, Z. Wang, X. Zhang, *Polymer Chemistry* **2014**, *5*, 323–326.

[112] F. Lin, T.-G. Zhan, T.-Y. Zhou, K.-D. Zhang, G.-Y. Li, J. Wu, X. Zhao, *Chem. Commun. (Cambridge, U. K.)* **2014**, *50*, 7982-7985.

[113] D. Jiao, F. Biedermann, F. Tian, O. A. Scherman, *J. Am. Chem. Soc.* **2010**, *132*, 15734-15743.

[114] Y. Liu, Z. Huang, X. Tan, Z. Wang, X. Zhang, *Chem. Commun.* **2013**, *49*, 5766–5768.

[115] K.-D. Zhang, J. Tian, D. Hanifi, Y. Zhang, A. C.-H. Sue, T.-Y. Zhou, L. Zhang, X. Zhao, Y. Liu, Z.-T. Li, *J. Am. Chem. Soc.* **2013**, *135*, 17913–17918.

[116] K. Saalwachter, R. Graf, H. W. Spiess, *J. Magn. Reson.* **1999**, *140*, 471-476.

[117] K. Saalwachter, R. Graf, H. W. Spiess, *J. Magn. Reson.* **2001**, *148*, 398-418.

[118] P. Payamyar, K. Kaja, C. R. Vargas, A. Stemmer, D. J. Murray, C. J. Johnson, B. T. King, F. Schiffmann, J. Van de Vondele, A. Renn, S. Goetzinger, P. Ceroni, A. Schuetz, L.-T. Lee, Z. Zheng, J. Sakamoto, A. D. Schlueter, *Adv. Mater.* **2014**, *26*, 2052-2058.

[119] Z. Zheng, C. S. Ruiz-Vargas, T. Bauer, A. Rossi, P. Payamyar, A. Schuetz, A. Stemmer, J. Sakamoto, A. D. Schlueter, *Macromol. Rapid Commun.* **2013**, *34*, 1670-1680.

[120] J. van Heijst, M. Corda, O. Lukin, *Polymer* **2015**, *70*, 1-7.

[121] L. Zhang, N. S. Colella, F. Liu, S. Trahan, J. K. Baral, H. H. Winter, S. C. B. Mannsfeld, A. L. Briseno, *J. Am. Chem. Soc.* **2013**, *135*, 844-854.

[122] Q. Yuan, S. C. B. Mannsfeld, M. L. Tang, M. Roberts, M. F. Toney, D. M. DeLongchamp, Z. Bao, *Chem. Mater.* **2008**, *20*, 2763-2772.

[123] Z. Fang, V. Chellappan, R. D. Webster, L. Ke, T. Zhang, B. Liu, Y.-H. Lai, *J. Mater. Chem.* **2012**, *22*, 15397-15404.

[124] J. Lydon, *Journal of Materials Chemistry* **2010**, *20*, 10071-10099.

[125] S.-W. Tam-Chang, L. Huang, *Chemical Communications* **2008**, 1957-1967.

[126] F. Kim, L. J. Cote, J. Huang, *Advanced Materials* **2010**, *22*, 1954-1958.

[127] R. Berger, Y. Cheng, R. Förch, B. Gotsmann, J. S. Gutmann, T. Pakula, U. Rietzler, W. Schärtl, M. Schmidt, A. Strack, J. Windeln, H. J. Butt, *Langmuir* **2007**, *23*, 3150-3156.

[128] S. A. Pihan, S. G. J. Emmerling, H.-J. Butt, J. S. Gutmann, R. Berger, *Wear* **2011**, *271*, 2852-2856.

[129] Z. Zheng, L. Opilik, F. Schiffmann, W. Liu, G. Bergamini, P. Ceroni, L.-T. Lee, A. Schutz, J. Sakamoto, R. Zenobi, J. VandeVondele, A. D. Schluter, *J. Am. Chem. Soc.* **2014**, *136*, 6103-6110.

[130] D. Sellmann, M. Geck, M. Moll, *J. Am. Chem. Soc.* **1991**, *113*, 5259-5264.

[131] W. R. McNamara, Z. Han, C.-J. Yin, W. W. Brennessel, P. L. Holland, R. Eisenberg, *Proceedings of the National Academy of Sciences* **2012**, *109*, 15594-15599.

[132] A. Das, Z. Han, W. W. Brennessel, P. L. Holland, R. Eisenberg, *ACS Catalysis* **2015**, *5*, 1397-1406.

[133] A. Le Goff, V. Artero, B. Jousselme, P. D. Tran, N. Guillet, R. Métayé, A. Fihri, S. Palacin, M. Fontecave, *Science* **2009**, *326*, 1384-1387.

[134] E. S. Andreiadis, P.-A. Jacques, P. D. Tran, A. Leyris, M. Chavarot-Kerlidou, B. Jousselme, M. Matheron, J. Pécaut, S. Palacin, M. Fontecave, V. Artero, *Nat. Chem.* **2013**, *5*, 48-53.

[135] G. Hunter, R. Mukundan, Editors, *Nanotechnology (General). [In: ECS Trans., 2007; 3(30)]*, Electrochemical Society, **2007**.

[136] T. Yatabe, M. A. Harbison, J. D. Brand, M. Wagner, K. Mullen, P. Samori, J. P. Rabe, *Journal of Materials Chemistry* **2000**, *10*, 1519-1525.

[137] R. Dong, M. Pfeffermann, H. Liang, X. Zhu, J. Zhang, J. Hao, Z. Zheng, X. Feng, *Ahead of Print* **2015**.

[138] J. Cui, Z. Xu, *Chemical Communications* **2014**, *50*, 3986-3988.

[139] D. Sheberla, L. Sun, M. A. Blood-Forsythe, S. Er, C. R. Wade, C. K. Brozek, A. Aspuru-Guzik, M. Dinca, *J. Am. Chem. Soc.* **2014**, *136*, 8859-8862.

[140] J. Baltrusaitis, D. M. Cwiertny, V. H. Grassian, *Physical Chemistry Chemical Physics* **2007**, *9*, 5542-5554.

[141] X. Zou, X. Huang, A. Goswami, R. Silva, B. R. Sathe, E. Mikmeková, T. Asefa, *Angew. Chem. Int. Ed.* **2014**, *53*, 4372-4376.

[142] J. Kibsgaard, Z. Chen, B. N. Reinecke, T. F. Jaramillo, *Nat. Mater.* **2012**, *11*, 963-969.

[143] J. Xie, H. Zhang, S. Li, R. Wang, X. Sun, M. Zhou, J. Zhou, X. W. Lou, Y. Xie, *Advanced Materials* **2013**, *25*, 5807-5813.

[144] M. A. Lukowski, A. S. Daniel, F. Meng, A. Forticaux, L. Li, S. Jin, *J. Am. Chem. Soc.* **2013**, *135*, 10274-10277.

[145] D. Voiry, H. Yamaguchi, J. Li, R. Silva, D. C. B. Alves, T. Fujita, M. Chen, T. Asefa, V. B. Shenoy, G. Eda, M. Chhowalla, *Nat. Mater.* **2013**, *12*, 850-855.

[146] Y. Zheng, Y. Jiao, L. H. Li, T. Xing, Y. Chen, M. Jaroniec, S. Z. Qiao, *ACS Nano* **2014**, *8*, 5290-5296.

[147] Y. Ito, W. Cong, T. Fujita, Z. Tang, M. Chen, *Angew. Chem. Int. Ed.* **2015**, *54*, 2131-2136.

[148] G. Fugallo, A. Cepellotti, L. Paulatto, M. Lazzeri, N. Marzari, F. Mauri, *Nano Letters* **2014**, *14*, 6109-6114.

[149] E. Fitzer, *Carbon* **1989**, *27*, 621-645.

[150] X. Luo, R. Chugh, B. C. Biller, Y. M. Hoi, D. D. L. Chung, *J. Electron. Mater.* **2002**, *31*, 535–544.

[151] H. O. Pierson, in *Handbook of Carbon, Graphite, Diamonds and Fullerenes*, William Andrew Publishing, Oxford, **1993**.

[152] Y. Wei, Z. Sun, *Curr. Opin. Colloid Interface Sci.* **2015**, *20*, 311–321.

[153] P. Yu, S. E. Lowe, G. P. Simon, Y. L. Zhong, *Curr. Opin. Colloid Interface Sci.* **2015**, *20*, 329–338.

[154] T. Chen, L. Dai, *Angew. Chem. Int. Ed.* **2015**, *54*, 14947–14950.

[155] R. Wang, Y. Hao, Z. Wang, H. Gong, J. T. L. Thong, *Nano Lett.* **2010**, *10*, 4844–4850.

[156] X. Li, P. Sun, L. Fan, M. Zhu, K. Wang, M. Zhong, J. Wei, D. Wu, Y. Cheng, H. Zhu, *Sci. Rep.* **2012**, *2*, 395.

[157] J. Qiu, T. Qiu, *Carbon* **2015**, *81*, 20–28.

[158] W. Xie, H. Cheng, Z. Chu, Z. Chen, C. Long, *Ceram. Int.* **2011**, *37*, 1947–1951.

[159] J. Sun, X. Wang, C. Wang, Q. Wang, *J. Appl. Polym. Sci.* **2006**, *99*, 2565–2569.

[160] M.-C. Yang, D.-G. Yu, *Text. Res. J.* **1996**, *66*, 115–121.

[161] U. K. Fatema, C. Tomizawa, M. Harada, Y. Gotoh, *Carbon* **2011**, *49*, 2158–2161.

[162] U. K. Fatema, F. Okino, Y. Gotoh, *J. Mater. Sci.* **2013**, *49*, 1049–1057.

[163] Y. Liu, H. G. Chae, Y. H. Choi, S. Kumar, *J. Mater. Sci.* **2015**, *50*, 3614–3621.

[164] Y. Zhao, C. Jiang, C. Hu, Z. Dong, J. Xue, Y. Meng, N. Zheng, P. Chen, L. Qu, *ACS Nano* **2013**, *7*, 2406–2412.

[165] L. Y. Jiang, T.-S. Chung, R. Rajagopalan, *Carbon* **2007**, *45*, 166–172.

[166] S. Wang, Z. Ren, J. Li, Y. Ren, L. Zhao, J. Yu, *RSC Adv.* **2014**, *4*, 31300–31307.

[167] B. Wang, R. Karthikeyan, X.-Y. Lu, J. Xuan, M. K. H. Leung, *Ind. Eng. Chem. Res.* **2013**, *52*, 18251–18261.

[168] A. H. Castro Neto, F. Guinea, N. M. R. Peres, K. S. Novoselov, A. K. Geim, *Reviews of Modern Physics* **2009**, *81*, 109-162.

[169] D. W. Boukhvalov, M. I. Katsnelson, *Nano Letters* **2008**, *8*, 4373-4379.

[170] X. Peng, R. Ahuja, *Nano Letters* **2008**, *8*, 4464-4468.

[171] G. Cantele, Y.-S. Lee, D. Ninno, N. Marzari, *Nano Letters* **2009**, *9*, 3425-3429.

[172] E. J. Duplock, M. Scheffler, P. J. D. Lindan, *Physical Review Letters* **2004**, *92*, 225502.

[173] S. Osella, A. Narita, M. G. Schwab, Y. Hernandez, X. Feng, K. Müllen, D. Beljonne, *ACS Nano* **2012**, *6*, 5539-5548.

[174] M. G. Schwab, A. Narita, Y. Hernandez, T. Balandina, K. S. Mali, S. De Feyter, X. Feng, K. Müllen, *J. Am. Chem. Soc.* **2012**, *134*, 18169-18172.

[175] H. Zabel, S. A. Solin, *Graphite Intercalation Compounds. II. Transport and Electronic Properties, Vol. 18*, Springer-Verlag Berlin Heidelberg, **1992**.

[176] M. A. Pimenta, G. Dresselhaus, M. S. Dresselhaus, L. G. Cancado, A. Jorio, R. Saito, *Phys. Chem. Chem. Phys.* **2007**, *9*, 1276–1290.

[177] A. C. Ferrari, J. Robertson, *Phys. Rev. B* **2000**, *61*, 14095–14107.

[178] I. Rannou, V. Bayot, M. Lelaurain, *Carbon* **1994**, *32*, 833–843.

[179] H. Wilhelm, M. Lelaurain, E. McRae, B. Humbert, *J. Appl. Phys.* **1998**, *84*, 6552–6558.

[180] F. Tuinstra, J. L. Koenig, *J. Chem. Phys.* **1970**, *53*, 1126–1130.

[181] A. C. Ferrari, *Solid State Commun.* **2007**, *143*, 47–57.

[182] L. M. Malard, M. A. Pimenta, G. Dresselhaus, M. S. Dresselhaus, *Physics Reports* **2009**, *473*, 51–87.

[183] P. Lespade, R. Al-Jishi, M. S. Dresselhaus, *Carbon* **1982**, *20*, 427–431.

[184] Y. Kim, Dissertation thesis, Florida State University (Tallahassee, Florida), **2012**.

[185] P. Angelova, H. Vieker, N.-E. Weber, D. Matei, O. Reimer, I. Meier, S. Kurasch, J. Biskupek, D. Lorbach, K. Wunderlich, L. Chen, A. Terfort, M. Klapper, K. Muellen, U. Kaiser, A. Goelzhaeuser, A. Turchanin, *ACS Nano* **2013**, *7*, 6489-6497.

[186] G. A. Olah, S. Kobayashi, M. Tashiro, *J. Am. Chem. Soc.* **1972**, *94*, 7448-7461.

[187] B. Plietker, *Iron Catalysis: Fundamentals and Applications, Vol. 33*, Springer-Verlag Berlin Heidelberg, **2011**.

[188] S. Cenini, F. Ragaini, *Catalytic Reductive Carbonylation of Organic Nitro Compounds, Vol. 20*, Springer-Science+Business Media, B.V., **1997**.

[189] M. Bayle, N. Reckinger, J.-R. Huntzinger, A. Felten, A. Bakaraki, P. Landois, J.-F. Colomer, L. Henrard, A.-A. Zahab, J.-L. Sauvajol, M. Paillet, *Phys. Status Solidi B* **2015**, *252*, 2375–2379.

[190] H. J. Park, J. Meyer, S. Roth, V. Skakalova, *Carbon* **2010**, *48*, 1088–1094.

[191] Z. Liu, X. Zhou, *Graphene: Energy Storage and Conversion Applications*, CRC Press, **2014**.

[192] J. M. Tarascon, M. Armand, *Nature* **2001**, *414*, 359-367.

[193] I. Hadjipaschalis, A. Poullikkas, V. Efthimiou, *Renewable and Sustainable Energy Reviews* **2009**, *13*, 1513-1522.

[194] X. Ji, K. T. Lee, L. F. Nazar, *Nat. Mater.* **2009**, *8*, 500-506.

[195] K. Kang, Y. S. Meng, J. Bréger, C. P. Grey, G. Ceder, *Science* **2006**, *311*, 977-980.

[196] F. B. Tudron, J. R. Akridge, V. J. Puglisi, *Proceedings of the 41st Power Sources Conference* **2004**, 341-344.

[197] R. D. Rauh, K. M. Abraham, G. F. Pearson, J. K. Surprenant, S. B. Brummer, *Journal of The Electrochemical Society* **1979**, *126*, 523-527.

[198] J. Shim, K. A. Striebel, E. J. Cairns, *Journal of The Electrochemical Society* **2002**, *149*, A1321-A1325.

[199] M. Y. Chu, US5686201, **1997**.

[200] E. Peled, H. Yamin, *Prog. Batteries Sol. Cell* **1984**, *5*, 56-58.

[201] J. A. Dean, *Materials and Manufacturing Processes* **1990**, *5*, 687-688.

[202] J.-W. Choi, J.-K. Kim, G. Cheruvally, J.-H. Ahn, H.-J. Ahn, K.-W. Kim, *Electrochimica Acta* **2007**, *52*, 2075-2082.

[203] R. D. Rauh, F. S. Shuker, J. M. Marston, S. B. Brummer, *Journal of Inorganic and Nuclear Chemistry* **1977**, *39*, 1761-1766.

[204] S.-E. Cheon, K.-S. Ko, J.-H. Cho, S.-W. Kim, E.-Y. Chin, H.-T. Kim, *Journal of The Electrochemical Society* **2003**, *150*, A800-A805.

[205] Y. V. Mikhaylik, J. R. Akridge, *Journal of The Electrochemical Society* **2004**, *151*, A1969-A1976.

[206] J. H. Shin, E. J. Cairns, *Journal of The Electrochemical Society* **2008**, *155*, A368-A373.

[207] L. X. Yuan, J. K. Feng, X. P. Ai, Y. L. Cao, S. L. Chen, H. X. Yang, *Electrochemistry Communications* **2006**, *8*, 610-614.

[208] H.-S. Ryu, H.-J. Ahn, K.-W. Kim, J.-H. Ahn, K.-K. Cho, T.-H. Nam, J.-U. Kim, G.-B. Cho, *Journal of Power Sources* **2006**, *163*, 201-206.

[209] J. Wang, S. Y. Chew, Z. W. Zhao, S. Ashraf, D. Wexler, J. Chen, S. H. Ng, S. L. Chou, H. K. Liu, *Carbon* **2008**, *46*, 229-235.

[210] M. M. Islam, V. S. Bryantsev, A. C. T. van Duin, *Journal of The Electrochemical Society* **2014**, *161*, E3009-E3014.

[211] K.-i. Chung, W.-S. Kim, Y.-K. Choi, *Journal of Electroanalytical Chemistry* **2004**, *566*, 263-267.

[212] S. J. Visco, Y. S. Nimon, B. D. Katz, US7282296 B2, **2007**.

[213] T. A. Skotheim, C. J. Sheehan, Y. V. Mikhaylik, J. Affinito, US7247408, **2007**.

[214] M. Liu, S. J. Visco, L. C. De Jonghe, *Journal of The Electrochemical Society* **1989**, *136*, 2570-2575.

[215] S. J. Visco, C. C. Mailhe, L. C. De Jonghe, M. B. Armand, *Journal of The Electrochemical Society* **1989**, *136*, 661-664.

[216] Y. Kiya, J. C. Henderson, G. R. Hutchison, H. D. Abruna, *Journal of Materials Chemistry* **2007**, *17*, 4366-4376.

[217] Y. Kiya, A. Iwata, T. Sarukawa, J. C. Henderson, H. D. Abruña, *Journal of Power Sources* **2007**, *173*, 522-530.

[218] G.-x. Xu, L. Qi, B.-t. Yu, L. Wen, *Chinese Journal of Polymer Science* **2006**, *24*, 307-313.

[219] S. Wei, L. Ma, K. E. Hendrickson, Z. Tu, L. A. Archer, *J. Am. Chem. Soc.* **2015**, *137*, 12143-12152.

[220] S. N. Talapaneni, T. H. Hwang, S. H. Je, O. Buyukcakir, J. W. Choi, A. Coskun, *Angew. Chem. Int. Ed.* **2016**, *55*, 3106-3111.

[221] H. Wang, Y. Yang, Y. Liang, J. T. Robinson, Y. Li, A. Jackson, Y. Cui, H. Dai, *Nano Letters* **2011**, *11*, 2644-2647.

[222] G. Bruce Peter, A. Freunberger Stefan, J. Hardwick Laurence, M. Tarascon Jean, *Nat. Mater.* **2012**, *11*, 172-172.

[223] A. Manthiram, Y. Fu, S.-H. Chung, C. Zu, Y.-S. Su, *Chemical Reviews* **2014**, *114*, 11751-11787.

[224] Y. Yang, G. Yu, J. J. Cha, H. Wu, M. Vosgueritchian, Y. Yao, Z. Bao, Y. Cui, *ACS Nano* **2011**, *5*, 9187-9193.

[225] C. Zhang, H. B. Wu, C. Yuan, Z. Guo, X. W. Lou, *Angew. Chem.* **2012**, *124*, 9730-9733.

[226] D. S. Jung, T. H. Hwang, J. H. Lee, H. Y. Koo, R. A. Shakoor, R. Kahraman, Y. N. Jo, M.-S. Park, J. W. Choi, *Nano Lett.* **2014**, *14*, 4418-4425.

[227] J. Wang, J. Yang, J. Xie, N. Xu, *Advanced Materials* **2002**, *14*, 963-965.

[228] P. D. Frischmann, L. C. H. Gerber, S. E. Doris, E. Y. Tsai, F. Y. Fan, X. Qu, A. Jain, K. A. Persson, Y.-M. Chiang, B. A. Helms, *Chemistry of Materials* **2015**, *27*, 6765-6770.

[229] D. Young, K. M. Douglas, G. A. Eiceman, D. A. Lake, M. V. Johnston, *Analytica Chimica Acta* **2002**, *453*, 231-243.

[230] Y.-Z. Tan, S. Osella, Y. Liu, B. Yang, D. Beljonne, X. Feng, K. Müllen, *Angew. Chem. Int. Ed.* **2015**, *54*, 2927-2931.

[231] J. Cao, Y.-M. Liu, X. Jing, J. Yin, J. Li, B. Xu, Y.-Z. Tan, N. Zheng, *J. Am. Chem. Soc.* **2015**, *137*, 10914-10917.

[232] L. Chen, S. R. Puniredd, Y.-Z. Tan, M. Baumgarten, U. Zschieschang, V. Enkelmann, W. Pisula, X. Feng, H. Klauk, K. Müllen, *J. Am. Chem. Soc.* **2012**, *134*, 17869-17872.

[233] Q. Zhang, H. Peng, G. Zhang, Q. Lu, J. Chang, Y. Dong, X. Shi, J. Wei, *J. Am. Chem. Soc.* **2014**, *136*, 5057-5064.

[234] R. Dong, M. Pfeffermann, H. Liang, Z. Zheng, X. Zhu, J. Zhang, X. Feng, *Angew. Chem. Int. Ed.* **2015**, *54*, 12058-12063.

[235] R. Sakamoto, T. Kambe, S. Tsukada, K. Takada, K. Hoshiko, Y. Kitagawa, M. Okumura, H. Nishihara, *Inorganic Chemistry* **2013**, *52*, 7411-7416.

[236] E. P. Goodings, D. A. Mitchard, G. Owen, *Journal of the Chemical Society, Perkin Transactions 1* **1972**, 1310-1314.

[237] P. J. Nigrey, A. F. Garito, *Journal of Chemical & Engineering Data* **1978**, *23*, 182-183.

[238] J. E. Anthony, *Angew. Chem. Int. Ed.* **2008**, *47*, 452-483.

[239] A. Narita, X.-Y. Wang, X. Feng, K. Mullen, *Chemical Society Reviews* **2015**, *44*, 6616-6643.

[240] G. Frenking, *Angew. Chem. Int. Ed.* **1990**, *29*, 1410-1412.

[241] J. A. Harnisch, R. J. Angelici, *Inorganica Chimica Acta* **2000**, *300–302*, 273-279.

[242] J. J. Colman, W. C. Trogler, *J. Am. Chem. Soc.* **1995**, *117*, 11270-11277.

[243] P. Sautet, C. Joachim, *Chemical Physics Letters* **1991**, *185*, 23-30.

[244] C. Manzano, W. H. Soe, M. Hliwa, M. Grisolia, H. S. Wong, C. Joachim, *Chemical Physics Letters* **2013**, *587*, 35-39.

[245] R. Ohmann, J. Meyer, A. Nickel, J. Echeverria, M. Grisolia, C. Joachim, F. Moresco, G. Cuniberti, *ACS Nano* **2015**, *9*, 8394-8400.

[246] W. Chen, V. Madhavan, T. Jamneala, M. F. Crommie, *Physical Review Letters* **1998**, *80*, 1469-1472.

[247] N. V. Smith, *Physical Review B* **1985**, *32*, 3549-3555.

[248] S. Fölsch, P. Hyldgaard, R. Koch, K. H. Ploog, *Physical Review Letters* **2004**, *92*, 056803.

[249] J. Lagoute, X. Liu, S. Fölsch, *Physical Review Letters* **2005**, *95*, 136801.

[250] A. Shafiee, M. M. Salleh, M. Yahaya, *Sains Malaysiana* **2011**, *40*, 173-176.

[251] H. M. Koepp, H. Wendt, H. Stkehlow, *Zeitschrift für Elektrochemie, Berichte der Bunsengesellschaft für physikalische Chemie* **1960**, *64*, 483-491.

[252] W. Li, H. Yao, K. Yan, G. Zheng, Z. Liang, Y.-M. Chiang, Y. Cui, *Nat. Commun.* **2015**, *6*.

[253] E. M. Kosower, J. L. Cotter, *J. Am. Chem. Soc.* **1964**, *86*, 5524-5527.

[254] N. Komatsu, F. Wang, *Materials* **2010**, *3*.

[255] M. Adrian, A. Senftleben, S. Morgenstern, T. Baumert, *Ultramicroscopy* **2016**, *166*, 9-15.

[256] S. B. Cho, Y.-C. Chung, *Sci. Rep.* **2016**, *6*, 27986.

[257] L. Grover, V. Yuriy, H. Kiar, *Supercond. Sci. Technol.* **2016**, *29*, 015015.

[258] J. Zhou, Q. Sun, Q. Wang, P. Jena, *Phys. Rev. B* **2015**, *92*, 064505.

[259] R. P. Smith, T. E. Weller, C. A. Howard, M. P. M. Dean, K. C. Rahnejat, S. S. Saxena, M. Ellerby, *arXiv.org, e-Print Arch., Condens. Matter* **2015**, 1–22.

[260] R. D. Parks, *Science* **1964**, *146*, 1429–1435.

[261] H. Yamamoto, H. Nasu, H. Kameno, *Physica C* **2003**, *392–396, Part 1*, 759–763.

[262] J. L. Figueiredo, C. A. Bernardo, R. T. K. Baker, K. J. Hüttinger, *Carbon Fibers Filaments and Composites*, Springer-Science+Business Media, B.V. , **1990**.

[263] M. S. Dresselhaus, G. Dresselhaus, K. Sugihara, I. L. Spain, H. A. Goldberg, *Graphite Fibers and Filaments, Vol. 5*, Springer-Verlag Berlin Heidelberg, **1988**.

[264] S. Thomas, G. E. Zaikov, S. V. Valsaraj, A. P. Meera, Editors, *Recent Advances In Polymer Nanocomposites: Synthesis And Characterisation*, VSP, **2010**.

[265] N. Fechler, S.-A. Wohlgemuth, P. Jaker, M. Antonietti, *Journal of Materials Chemistry A* **2013**, *1*, 9418-9421.

[266] K. R. N. Pai, G. S. Anjusree, T. G. Deepak, D. Subash, S. V. Nair, A. S. Nair, *RSC Advances* **2014**, *4*, 36821-36827.

[267] M. Gingras, J.-M. Raimundo, Y. M. Chabre, *Angew. Chem. Int. Ed.* **2006**, *45*, 1686-1712.

[268] L. Przybilla, J.-D. Brand, K. Yoshimura, H. J. Räder, K. Müllen, *Analytical Chemistry* **2000**, *72*, 4591-4597.

[269] D. Bruns, H. Miura, K. P. C. Vollhardt, A. Stanger, *Organic Letters* **2003**, *5*, 549-552.

[270] X. Zheng, X. Wang, Y. Qiu, Y. Li, C. Zhou, Y. Sui, Y. Li, J. Ma, X. Wang, *J. Am. Chem. Soc.* **2013**, *135*, 14912-14915.

[271] M. Ballester, C. Molinet, J. Castañer, *J. Am. Chem. Soc.* **1960**, *82*, 4254–4258.

8. List of Publications

Dong, R.; Pfeffermann, M.; Liang, H.; Zheng, Z.; Zhu, X.; Zhang, J.; Feng, X., "Large-Area, Free-Standing, Two-dimensional Supramolecular Polymer Single-Layer Sheets for Highly Efficient Electrocatalytic Hydrogen Evolution." *Angew. Chem.*, *Int. Ed.*, **2015**, *54*, 12058–12063.

Pfeffermann, M.; Dong, R.; Graf, R.; Zajaczkowski, W.; Gorelik, T.; Pisula, W.; Narita, A.; Müllen, K.; Feng, X., "Free-Standing Monolayer Two-dimensional Supramolecular Organic Framework with Good Internal Order." *J. Am. Chem. Soc.*, **2015**, *45*, 14525–14532.

Pfeffermann, M.; Wuttke, M.; Feng, X.; Narita, A.; Müllen, K., "Shape-persistent Graphite Replica of Metal Wires." Submitted to *Adv. Mater.*

Dong, R.; Pfeffermann, M.; Skidin, D.; Wang, F.; Fu, Y.; Narita, A.; Tommasini, M.; Moresco, F.; Cuniberti, G.; Berger, R.; Müllen, K.; Feng, X.; "Persulfurated Coronene: A New Generation of "Sulflower"." Submitted to *J. Am. Chem. Soc.*

Müller, P.; Grünker, R.; Bon, V.; Pfeffermann, M.; Senkovska, I.; Weiss, M.; Feng, X.; Kaskel, S.; "Topological control of 3,4-connected frameworks based on the Cu_2-paddle-wheel node: tbo or pto, and why?" *CrystEngComm* **2016**, *ASAP*.

9. Curriculum Vitae

10. Acknowledgement

Vielen Dank!